A META-ANALYSIS OF GEOSPATIAL ESTIMATES IN THE CASE OF MALAYSIAN AIRLINES FLIGHT MH370

By

PETER OLIVER LARGE

Bachelor of Science in Surveying & Mapping Science
University of Newcastle Upon Tyne
Newcastle Upon Tyne, United Kingdom
1994

Postgraduate Diploma in Strategy & Innovation
University of Oxford
Oxford, United Kingdom
2015

Master of Science in Management
Stanford University, Graduate School of Business
Stanford, CA
2008

Submitted to the Faculty of the
Graduate College of the
Oklahoma State University
in partial fulfillment of
the requirements for
the Degree of
DOCTOR OF EDUCATION
May, 2019

A META-ANALYSIS OF GEOSPATIAL ESTIMATES IN THE CASE OF MALAYSIAN AIRLINES FLIGHT MH370

Dissertation Approved:

Dr. Jon Loffi
Dissertation Adviser

Dr. Mwrumba Mwavita
Committee Member

Dr. Samuel Matthew Vance
Committee Member

Dr. Kathryn Gardner-Vandy
Committee Member

Dr. Jamey Jacob
Outside Committee Member

ACKNOWLEDGEMENTS

"..whilst the great ocean of truth lay undiscovered before me."

- Sir Isaac Newton (1642-1727)

Perhaps, in the subject case of this study, we might paraphrase that an important truth lays undiscovered beneath a great ocean. Newton also famously spoke of standing on the shoulders of giants, which I undoubtedly do in the completion of this work; those at Inmarsat whose forward thinking in recording BTO and BFO data and subsequent pioneering early analysis led us to the Indian Ocean in the first place, the expert prior research of all those acting in an official capacity in Australia and elsewhere, and the work conducted by the Independent Group; the crowd has once again shown its wisdom. I am enormously grateful to my doctoral committee members for their support, insight and collegial challenges, and not least to my Chair, Dr. Jon Loffi. Most of all, the extent of my gratitude to my wife Amanda and sons Jack and Craig for their love and support simply cannot be expressed in words.

Two hundred and thirty-nine souls were lost along with MH370 on March 7th, 2014, the youngest of whom was less than two years old. Their lost opportunity for a life lived and fulfilled is the profound and enduring tragedy of the MH370 case. This work is dedicated to their memory and to their families, loved ones, friends and colleagues whose loss has yet to be fully explained. Aerospace has a long and important tradition of learning from both triumph and disaster; the MH370 case should be no exception.

"To strive, to seek, to find, and not to yield" – Alfred, Lord Tennyson (1809-1892)

Acknowledgements reflect the views of the author and are not endorsed by committee members or Oklahoma State University.

Name: PETER OLIVER LARGE

Date of Degree: MAY, 2019

Title of Study: A META-ANALYSIS OF GEOSPATIAL ESTIMATES IN THE CASE OF MALAYSIAN AIRLINES FLIGHT MH370

Major Field: APPLIED EDUCATIONAL STUDIES

Abstract: This study performs a meta-analysis of 38 studies providing geospatial estimates for the final location of MH370, investigates the spatial characteristics of antennas as a potential source of additional useful spatial information and direction sensing, and makes an independent assessment of the impact of the Global Aeronautical Distress and Safety System implementation on the reduction of the probability of future oceanic hull loss accidents with high spatial uncertainty. The meta-analysis finds that those studies derived from ocean drift modelling are statistically homogenous, while those derived from satellite communications observations are statistically heterogenous. This heterogeneity may be explained by the multimodal nature of the solution space when making use of the Doppler-based Burst Frequency Offset measurements. Inclusion in a physical model of the known variation in peak gain for the MH370 aircraft's MSS antenna as a function of apparent satellite elevation and azimuth, as an additional direction sensing technique, is shown to reduce the bimodality and multimodality of the BFO-only solutions when the two are combined, however the technique is not sufficiently powerful under the present model to isolate a single trajectory for the flight. The most coherent trajectories terminate around 34-37S latitude. Probability distributions are estimated for future oceanic hull losses with high spatial uncertainty during the period 2020-2030, through Monte Carlo simulation of scenarios related to the GADSS implementation. The risk of a loss with high spatial uncertainty such as was encountered with Air France 447 and Malaysian Airlines 370 is forecast to be reduced but far from eliminated.

TABLE OF CONTENTS

Chapter Page

LIST OF TABLES

Table Page

LIST OF FIGURES

CHAPTER I

INTRODUCTION

The global commercial air transport system is remarkably safe; as CNN's Jon Ostrower is quoted by Twombly (2018) as saying, "..how extraordinary it is that humanity has created a method of transportation that is literally safer than walking on your own two feet" (p. 6). Indeed, according to data from the National Safety Council (2016) loss of one's life as a pedestrian is multiple orders of magnitude more likely than as a commercial air transport passenger.

Fundamental to this safety record is a culture in aerospace of learning from incidents and accidents and applying those lessons learned in such a way as to avoid future recurrences and thus to continuously improve safety. Flight recorders, consisting of the Flight Data Recorder (FDR) which records data collected from the aircraft systems and the Cockpit Voice Recorder (CVR), which creates a record of sampled audio signals, play an essential role in the accident investigation process. Flight recorders, together with many other sources of information, enable investigators to systematically and objectively arrive at a probable cause and contributing factors for an accident or incident under investigation, and to subsequently make recommendations intended to prevent future, similar occurrences. As embodied in the International Convention on Civil Aviation (ICAO, 1944), *the purpose of accident investigation is prevention*.

Although less than 20% of air transport accidents occur in the cruise phase of flight (Boeing, 2017), the long-term average implies approximately one hull loss in water per year (Flight safety Foundation, 2018), and one instance approximately every four and a half years (IPFS, 2016; ARIAB, 2015) where the recorders are not recovered, notwithstanding the significant expense incurred in many cases where the recorders have been recovered.

Regulatory Environment and the Global Aeronautical Distress and Safety System

Annexes to the ICAO Convention on International Civil Aviation (ICAO, 1944) or 'Chicago Convention', as amended, provide the international framework for flight recorders, search-and-rescue operations and for air accident investigation, while publications of ICAO and the IMO provide more detailed procedures relevant to aeronautical and search-and-rescue operations. The ICAO Procedures for Air Navigation Services, Air Traffic Management (PANS-ATM) Doc 4444 (ICAO, 2016) provides, inter alia, detailed procedures including position reporting, emergency communications, procedures and alerting, while the International Aeronautical and Maritime Search and Rescue manuals (IAMSAR) provide detailed guidance and procedures for search and rescue operations (IMO, 2016).

The Global Aeronautical Distress and Safety System (GADSS) Concept of Operations document (ICAO, 2017) describes concepts developed following Air France Flight 447 and Malaysian Airlines Flight 370, intended to improve search-and-rescue and recovery efforts. The GADSS Concept of Operations is being implemented in phases, through amendments to Annex 6 of the Convention on International Civil Aviation (ICAO, 2017b), which in turn have been, or are expected to be, adopted by ICAO Contracting States their national laws and civil aviation regulations.

The Specific Case of Malaysian Airlines Flight 370 (MH370)

In the case of Malaysian Airlines Flight 370, a Boeing 777-200ER registered in Malaysia as 9M-MRO, the aircraft was lost with 239 souls on board and, at the time of writing five years after the loss, neither the flight recorders nor the wreckage of the aircraft have been located despite an extensive search, with the exception of multiple items of debris recovered from island beaches in the Indian Ocean and along the south-eastern African coast.

The *Safety Investigation Report* (Malaysian Government, 2018), while noting many important facts and making multiple recommendations, concluded that the investigation was "unable to determine the real cause for the disappearance of MH370" (p.443). This conclusion has significance for aviation safety, given the importance of understanding the exact circumstances and probable cause of a hull loss of this magnitude and significance, and in order to have confidence in the efficacy of recommendations for future preventative action.

Salient Factors in The Case of Malaysian Airlines Flight 370 from 2014-2018.

The specific events relating to the flight, in so far as they are known, are well documented in the official reports of the safety investigation team and the search team (ATSB, 2017; Malaysian Government, 2018). Although much still remains unknown about the exact circumstances surrounding the loss of this aircraft, some factors are known to a relatively high degree of confidence, while many other factors can only be inferred through the available evidence.

Following departure from Kuala Lumpur International Airport (WMKK) at 16:42Z (where the Z suffix indicates Zulu Time or Co-ordinated Universal Time), 00:42 local time on March 7th, 2014, the aircraft was under normal surveillance, with normal voice and data communications established, until the point of handover from Malaysian to Vietnamese air traffic control as the aircraft approached the Vietnam Flight Information Region (FIR) approximately 40 minutes after departure, at 17:21Z, in the vicinity of waypoint IGARI. From this point, the aircraft was unresponsive to voice communications, aircraft generated data communications ceased, and the aircraft's transponder became inoperative.

While no longer under secondary radar surveillance from that point, subsequent forensic examination of civil and military primary radar data revealed partially complete information about the trajectory of the aircraft for approximately one hour after this initial deviation from the flight plan, for the phase of flight between 17:21Z and 18:22Z. After that time, between 18:25Z and 00:19Z the next morning, intermittent exchanges were recorded between the aircraft's L-band mobile satellite service (MSS) terminal and the Inmarsat communications network, via the I-3 F1 spacecraft located in a geosynchronous equatorial orbit (GEO) nominally stationed above the equator at 64.5E longitude and received at the Inmarsat Ground Earth Station (GES) in Perth, Western Australia.

Although these exchanges do not include any normal 'payload' data such as the routine Aircraft Communications Addressing and Reporting System (ACARS) messages which would normally be expected during the flight, nor were two satellite telephony attempts successful, these network management and signaling exchanges provide a set of measurements useful for making spatio-temporal inferences about the flight after 18:22Z, beyond the most striking fact that the flight continued for almost five hours after the final primary radar contact when the aircraft was located between the Malacca Strait and the Andaman Sea, at which time the aircraft had already been airborne for 104 minutes.

As was first described by Ashton, Schuster-Bruce, College and Dickinson (2014), the log files from the satellite communication network contain, among other things, timing offset and frequency offset measurements which can be combined with other known information, such as the dynamics of the Inmarsat spacecraft with which the AES was communicating and details of algorithms used in the GES and AES systems, to make inferences relating to aircraft location, heading and velocity at the times that the measurements were made. When combined with known aircraft performance characteristics and limitations, feasible aircraft dynamics, and the known fuel-on-board (FOB) the aircraft at departure and upon reaching cruise altitude (via ACARS messages), these inferences have been extended to geospatial estimation for the purposes of search area definition for the location of the aircraft wreckage, including the flight recorders and other physical evidence.

Following recovery of multiple items of debris, either confirmed to be from the aircraft in question or determined as likely to be from that aircraft, reverse ocean surface drift models based on time of debris arrival at the point of discovery, combined with knowledge and estimation of ocean surface or near-surface dynamics and windage factors, have yielded additional geospatial estimates for the likely origin of the debris. Satellite imagery has also been made available which could contain objects from the aircraft, although not which have been positively identified as such.

Ocean Search for MH370, 2014-2018.

Following a surface search immediately after the loss of the aircraft, an extensive subsea search effort – the largest of its kind in history - covering approximately 232,000km^2 of the ocean floor (Malaysian Government, 2018) with high resolution sonar data, based on geospatial parameter estimates derived using the available information, has proven unsuccessful at the time of writing.

The official search area for part of the search was defined with reference to a posterior probability density function estimated by Davey, Gordon, Holland, Rutten and Williams (2015), employing sequential Markov Chain Monte Carlo, particle filter methods (Doucet, de Freitas & Gordon, 2001) and Bayesian inference. The posterior probability density reflects the estimated likelihood of the aircraft state vector taking a particular value given the available observational data and its inherent uncertainty, constrained by plausible flight dynamics during the particle filter proposal distribution generation. Of particular note is that the combined area searched covers, and in fact extends beyond, the area from the posterior probability density function described by the ATSB (2017) to contain the aircraft debris with an estimated probability in the range of p=0.85-0.90.

The confidence in the ability of the subsea search to locate the debris field if contained within the search is assessed as p=0.94 (ATSB, 2017). That is, it is possible for the ocean floor survey to miss the debris field due to small gaps in the data, areas of terrain shadowing on the ocean floor, or the failure of the means of detection to identify the debris.

Fundamentally, there are a limited number of possible explanations for why the search determined, to a level of confidence reported as p=0.94, that the wreckage was *not* in the area in which the posterior probability density function from the Bayesian estimation predicted it would be, to a reported p=0.85 to 0.90 level of confidence (ATSB, 2017). Either, (a) The wreckage is located in the area outside the p=0.85-0.90 region but still within the estimated PDF i.e. in a remaining p=0.10-0.15 area which was not searched, (b) if the defined search area and hence the p=0.85-0.90 pdf area *did* include the wreckage but it was not detected by the survey, for which the probability of this occurring is estimated to be p=0.06; or, (c) the area of the estimated posterior PDF does not contain the aircraft wreckage. The latter case includes the possibility that the wreckage is on or close to a different part of the 7th BTO arc to that searched, or elsewhere. This could be due to a combination of factors, for example the assumptions and techniques used in the dynamic model, both during the flight and at the end of the flight, the presence of biases both in the BTO and BFO observations, the characterization of the stochastic properties of the observations, etc.

Davey et al. (2015) state that "The factors that do make a significant difference to the output pdf are the assumed spread of Mach number and the end of flight model" (p.98). The Mach number was sampled between M0.73 and M0.84 and the end of flight model assumed no human control, which together have a significant impact on the search area due to their narrowing effect, both along the arcs and orthogonally to the 7th arc.

Emergence of an Independent Group and Alternative Geospatial Estimates.

Although the search was primarily informed by the work of those acting in an official capacity, a number of other geospatial estimates have been derived for the location of the aircraft wreckage, including an extensive body of work conducted by an independent group of experts which emerged via the internet during the period 2014-2018. In the typology of Geiger, Rosemann and Fielt (2011), this ad hoc and diverse group including members with extensive expertise in relevant areas could be viewed as a specific manifestation of the crowd-solving phenomenon in society, as a distinct typological subset of the crowdsourcing phenomenon (Howe, 2006).

Members of the independent group have conducted substantial analysis of the available data and have produced independent spatial estimates based on the available information. These analyses, together with estimates from various other studies conducted by independent researchers using the same data, exhibit significant variation in their resulting geospatial parameter estimations, reflecting differing assumptions, methodologies, results and conclusions, yet drawn from the same underlying information.

Potential Use of Antenna Spatial Characteristics in Geospatial Estimates.

The available data in the case, including primary radar data during the period 17:21Z-18:22Z and the L-band satellite log files during the period 18:25Z-00:19Z, includes information which has generally been assumed not to be useful in the formulation of geospatial estimates, or which has only been partially made use of. For the satellite data, this includes records of the received power levels and carrier-to-noise density ratio (C/No) at the Perth Ground Earth Station (GES) for each transmission received from the aircraft. In theory, if all the parameters of the communications link budget from the aircraft earth station (AES) to the GES via the satellite were known, knowledge of the spatial characteristics of the AES antenna could potentially be used to make coarse inferences about aircraft orientation and attitude at the point of transmission, although the precision and reliability with which this could be achieved in practice is not well known.

In particular, the specific type of side-mounted antenna installed on the 9M-MRO aircraft exhibits a known variation in the peak gain of the antenna as a function of elevation and azimuth, which could conceivably be used to discriminate direction, provided that the effect is detectable within the inherent noise and fading of the received power observations. Other opportunities to make use of the spatial characteristics of antennas include the phase of the MH370 flight during which the aircraft was found to have been recorded by primary civilian and military radar, and during the brief interaction of a crew member's mobile phone in the vicinity of Penang (for which a preliminary analysis is provided in the Appendix).

Meta-Analysis

Meta-analysis, a term neologized by Glass (1976), refers to the "analysis of analyses" (p.3) and "the statistical analysis of a large collection of analysis results from individual studies for the purpose of integrating the findings" (p.3). Although the original context was in the field of educational research, and the techniques are today applied in diverse fields such as high energy and particle physics (Baker & Jackson, 2012), or information systems research (Weigel, Hazen, Cegielski & Hall, 2014), meta-analytic methods have found the most extensive application in the medical sciences (Schwarzer, Carpenter & Rücker, 2015), where it is quite common for effect sizes of some intervention to have been measured across different studies and the purpose of meta-analysis is to combine and compare those studies. However, as pointed out by O'Rourke (2007), the underlying techniques of mathematical statistics used in present day meta-analysis date back to seminal works such as that of Airy (1861), who drew on the work of Laplace (1749-1827) and Gauss (1777-1855), in his epic treatise on the combination of multiple observations in the presence of uncertainty, applied to the fields of astronomy and geodesy. In the context of the present study, meta-analysis techniques are applied to two sub-groups of studies as shown in Table 1, each of which provides an estimate of the final location of the aircraft along, or in the vicinity of, the 7th BTO arc and which collectively offer wide diversity of estimation methodology, as well as wide diversity of estimated location (from 12 degrees south to 40 degrees south latitude). The first sub-group incorporates the use of the satellite communications data while the second sub-group uses ocean drift analysis relating to the recovered items of debris.

Table 1

Studies Selected for Meta-Analysis

		7th Arc-Latitude Range	
	Author(s)	Lower Bound (Degrees South)	Upper Bound (Degrees South)
	Satellite Communications Sub-Group of Studies		
1	ATSB (2014) Wide Area	16.4	39.0
2	ATSB (2014) Priority Area	27.4	32.1
3	ATSB (2014) Medium Area	24.4	34.7
4	ATSB (2014, Oct) Flight Path Analysis Update	33.5	38.3
5	Ashton et al. (2014)	34.7	34.7
6	Anderson et al (2014)	37.5	37.7
7	Spinor (2014)	38.5	38.5
8	Ulich (2014)	40.2	40.2
9	Martin (2014)	40.6	40.6
10	Pleter, Constantinescu and Jakab (2015)	38.2	39.9
11	Fah (2015)	34.5	40.5
12	Davey et al. (2015)	34.0	40.0
13	GlobusMax (2015)	40.0	40.0
14	ATSB (2015)	36.0	39.3
15	ATSB (2016)	32.5	36.0
16	Ianello and Godfrey (2016)	26.9	26.9
17	SK999 (2016)	22.0	37.0
18	Ianello (2017)	28.0	39.0
19	Godfrey (2017)	29.0	31.0
20	Nederland (2017)	31.0	31.0
21	Gilbert (2017)	31.0	34.0
22	Marchand, Gasser, Delarche and Garot (2018)	12.0	12.0
23	Ulich (2018)	31.6	31.6
24	Ianello (2018)	22.0	22.0
25	Kristensen (2018)	13.3	13.3
26	Kristensen (2018) 2nd minima	34.6	34.6
	Ocean Drift Sub-Group of Studies		
27	Pattiaratchi & Wijeratne (2016)	28	33
28	Rydberg (2015)	12	38
29	Daniel (2016)	25	35
30	Jansen et al. (2016)	28	35
31	Durgadoo et al. (2016)	14	33
32	Trinanes et al. (2016)	26	38
33	Griffin, Oke & Jones (2016)	26	38
34	Godfrey (2017)	19	37
35	Nesterov (2018)	25	35
36	Godfrey (2018)	19	35
37	Griffin & Oke (2018)	25	36
38	Miron et al (2019)	17	33

Statement of the Problem

The search for the flight recorders and other physical evidence in the case of MH370 concluded without location of the wreckage and without a probable cause being adopted for the oceanic loss of a 777-200ER aircraft with 239 souls on board, despite an extensive search based on estimates and inferences made from the available data. Furthermore, multiple independent studies result in widely varying geospatial estimates for the aircraft trajectory and end of flight location, spanning a range of almost 2,000 nautical miles along the 7th arc.

From a spatial perspective, the case depends on two critical aspects: (a) the aircraft trajectory and fuel flow up until the point of crossing the 6th and 7th arcs, and (b) the three-dimensional trajectory between the top of descent point and the final ocean floor location of the debris field. In turn, estimates of these critical aspects depend on a set of assumptions and prior information, for which those used to date have not resulted in location of the recorders. The 232,000km^2 area searched itself acts as an observation regarding where the debris field is probably *not* located; the question remains of whether the totality of information currently available is sufficient to determine a plausible future search effort, or whether the specific MH370 case will remain a mystery indefinitely. Beyond this specific case, the question also remains of the probability of future oceanic hull losses with high degrees of spatial uncertainty and the likely efficacy of new GADSS legislation in reducing that probability.

Purpose of the Study

The purpose of this study is threefold. First, to provide a systematic review of multiple geospatial estimates for the final location of MH370 during the period 2014-2018, including investigation of the reasons why these studies reach such geospatially diverse conclusions from the same observed data, through meta-analysis of multiple independent estimates for location of the wreckage. Secondly, to investigate a previously unused source of information, namely the spatial characteristics of antennas, combined with measurements made during the flight, as a potential source of additional useful spatial information, to combine that technique with Doppler based direction sensing and to perform sensitivity analysis and probability density function estimation using the combined model. Finally, to make an independent and forward-looking assessment of the potential impact of the GADSS implementation on the reduction of the probability of future occurrences of oceanic hull loss accidents with high spatial uncertainty.

Research Questions

RQ-1. Meta-Analysis: For the studies identified in Table 1, which provide geospatial estimates of the MH370 trajectory and/or end of flight vicinity:

(a): Is the observed variation in estimated probable impact location for MH370 across these studies likely due to random variation within the range of uncertainty of the observed data and propagated error, or do the studies exhibit statistical heterogeneity?

(b): To which factors are the arc-latitude estimates most sensitive?

RQ-2. The Spatial Characteristics of Antennas: Can the spatial characteristics of antennas be used to reduce the uncertainty in the geospatial estimates in the MH370 case?

RQ-3. Effect of GADSS on Future Occurrences: In the absence of an adopted probable cause for the loss of MH370, what is an estimate of the probability of an oceanic hull loss with high spatial uncertainty (>5NM last known position or LKP) as a function of time, during the period 2020 to 2030?

Significance of the Study

Published research to date on the specific case of MH370 has contributed to the body of knowledge regarding the available data and information relating to the flight and regarding how that data has been interpreted and acted upon. Currently absent from the literature is a systematic review and meta-analysis of that research; this study is significant in that it attempts to perform such a meta-analysis, intended to provide insight into the causes of the wide variation of geospatial estimates for the case in question.

The use of recorded received power observations for the satellite data combined with knowledge of the peak gain variation in the aircraft's MSS antenna has not been incorporated into any of the studies selected for the meta-analysis, nor any study found in the literature review. The study is significant in respect of the inclusion of this data into a physical estimation model, and subsequent combination with the BFO observable in a joint probability density function estimation.

Published work to date on the Global Aeronautical Distress and Safety System (GADSS) is generally technical, conceptual and operational in nature. This significance of this study is in exploring the question of the estimated future impact of this new system and its associated legislation on aviation safety, particularly in terms of the potential effect on the probability of future occurrences of oceanic hull loss accidents with a high degree of spatial uncertainty.

Acronyms and Abbreviations

ACARS – Aircraft Communications, Addressing and Reporting System

ADS-C – Aircraft Dependent Surveillance - Contract

ADFR – Automatically Deployable Flight Recorder

AES – Aircraft Earth Station

AF447 – Air France Flight 447

AMS(R)S – Aeronautical Mobile Satellite (Route) Service

APU – Auxiliary Power Unit

ATC – Air Traffic Control

ATSB – Australian Transportation Safety Bureau

BFO – Burst Frequency Offset

BTO – Burst Timing Offset

CDF – Cumulative Density Function, also equivalently lower case ‘cdf’

C/No – Carrier-to-Noise Density Ratio (referenced to a 1Hz Bandwidth)

CNS – Communications, Navigation and Surveillance

ConOps – Concept of Operations

CPDLC – Controller Pilot Data Link Communications

CSIRO – Commonwealth Scientific and Industrial Research Organisation (Australia)

CVR – Cockpit Voice Recorder

dB – Decibel

dBic – Decibel referenced to an isotropic antenna with circular polarization (measure of gain)

dBm – Decibel milliwatts, equal to 10 x Log$_{10}$ (Power / 1 milliwatt)

dBW – Decibel Watts, equal to 10 x Log$_{10}$ (Power / 1 Watt)

dB-Hz – Decibel-Hertz, e.g. carrier-to-noise density ratio C/No in a 1Hz bandwidth.

DSTG – Defence Science and Technology Group (Australia)

ECEF – Earth Centered Earth Fixed (Co-ordinate reference frame)

EIRP – Effective Isotropic Radiated Power

ELT – Emergency Locator Transmitter

ELT-DT - Emergency Locator Transmitter – Distress Tracking (GADSS ADT compliant)

ETA – Estimated Time of Arrival

FAA - Federal Aviation Administration

FANS – Future Air Navigation System

FDR – Flight Data Recorder (or Flight Data Recovery in the GADSS context).

FIR – Flight Information Region

FL – Flight Level (with three-digit suffix representing feet x 100 e.g. FL350 = 35,000ft)

fpm – Feet per Minute

GADSS – Global Aeronautical Distress and Safety System

GEO – Geosynchronous Equatorial Orbit, may also be referred to as Geostationary.

GES – Ground Earth Station

GNSS – Global Navigation Satellite System

GPS – Global Positioning System

HDG – Heading, three digits suffixed with ‘T’ for true and ‘M’ for magnetic heading.

HPA – High Power Amplifier

I3 – Inmarsat I3 Constellation or Satellite

I3 F1 – Inmarsat I3 Constellation, Flight 1.

IAMSAR – International Aeronautical and Maritime Search and Rescue (Manuals)

ICAO – International Civil Aviation Organisation

IFC – In-Flight Connectivity (Passenger Cabin)

IFEC - In-Flight Entertainment and Connectivity (Passenger Cabin)

IMO – International Maritime Organisation

IOR – Indian Ocean Region

KIAS – Knots indicated airspeed

KLIA – Kuala Lumpur International Airport

Kts – Knots or Nautical Miles per Hour

LIDU - Link Interface Data Unit, a link layer class of data in the Inmarsat network.

LKP – Last Known Position

MADGE - Malaysian Air Defense Ground Environment

MCMC – Markov Chain Monte Carlo (simulation or sampling)

MH370 – Malaysian Airlines Flight 370

MDT – Malaysian Daylight Time (UTC + 0800 hrs)

M_{MO} – Mach, maximum operating for the aircraft type.

MOTM – Ministry of Transport, Malaysia

MSL – Above Mean Sea Level

MSS – Mobile Satellite Service

NM – Nautical Miles

OCXO – Oven-Controlled Crystal Oscillator

OEM – Original Equipment Manufacturer

PDF – Probability Density Function (or equivalently, lower case ‘pdf’)

PEK – IATA airport identifier for Beijing Capital Airport

PGV – Peak Gain Variation

POR – Pacific Ocean Region

PSR – Primary Surveillance Radar

PSTN – Public Service Telecommunications Network

P_{rx} – Power received, the received signal power at the GES channel unit, in dBm in this case.

RMAF - Royal Malaysian Air Force, or Tentera Udara Diraja Malaysia (TUDM)

SAR – Search-and Rescue (or, alternatively, Search-and-Recovery)

SARPs – Standards and Recommended Procedures (ICAO)

SAT – Static Air Temperature

SatCom – Satellite Communications (in this case L-band)

SDU – Satellite Data Unit

SID – Standard Instrument Departure (procedure)

SoG – Speed over Ground (ground track velocity)

SSR – Secondary Surveillance Radar

TAS – True Air Speed

TAT – Total Air Temperature

TT&C – Tracking, Telemetry and Command (or, equivalently, Control)

TUDM - Tentera Udara Diraja Malaysia (Malay for RMAF as above)

UWB - Underwater Locator Beacon(s)

UTC - Universal Time Coordinated or Coordinated Universal Time (Z)

V_{LO}/V_{LE} – Maximum speed for a type with gear operated/extended

WMKC – ICAO airport identifier for Kota Bharu Airport.

WMKK – – ICAO airport identifier for Kuala Lumpur Airport

WMKP – – ICAO airport identifier for Penang Airport.

XYZ – Co-ordinate vector in 3-dimensional Cartesian space

Z – Suffix for ‘Zulu Time’ e.g. 00:00Z, equivalent to UTC above.

Assumptions

For the purposes of the study, it is assumed that the underlying cause of the loss of Malaysian Airlines Fight 370 is undetermined and would be best determined by recovery of the flight recorders and other physical evidence. It is assumed that the available measurements from the satellite communications system are genuine and are reliable within their normal statistical uncertainty and that the available primary radar data relate to the MH370 aircraft and not to another aircraft in the vicinity.

It is assumed that the 00:19Z satellite communication, eight minutes after the hourly log on/log off request at 00:11Z, was the result of fuel exhaustion to the last operative engine, where the aircraft's auxiliary power unit (APU) briefly provided electrical power to the L-band terminal prior to total fuel exhaustion. It is assumed that the peak gain variation model used in the calculations is representative of the antenna installed on the 9M-MRO aircraft.

Limitations

The research depends on data which is generally in the public domain at the time of writing. Consequently, it is possible either that materially important data or information may exist which is consequential to the study but which is not publicly available, or that new data or information will become available in the fullness of time.

Although part of the research is conducted in the manner of a meta-analysis, the unusually sparse and highly incomplete nature of the data in question leads to certain limitations of this study in comparison with most meta-analyses, where a broader range of statistical techniques can be used due to the more abundant and complete data. The sparsity of data and the need for imputation of certain parameters also affects the uncertainty, margin of error and potential robustness of any statistical analysis carried out as part of the study.

CHAPTER II

REVIEW OF THE LITERATURE

This chapter begins with a review of the literature pertaining to the history of oceanic losses, the salient regulatory and economic factors, and a review of the ‘wisdom of crowds’ phenomenon relevant to the emergence of an independent group in the MH370 case. The literature specific to the MH370 case is reviewed, beginning with the phase of flight after the loss of communications and prior work on the radar data during that phase, where there is general consensus on the approximate lateral path but less so on the vertical trajectory and velocity profile. For the phase of flight after loss of primary radar contact until the end of flight, the literature pertaining to the satellite communications system and use of measurements from it is reviewed, followed by a review of the literature pertaining to the characteristics of the antenna used on the MH370 aircraft. Prior studies are reviewed which have estimated the location of the end of flight using a combination of the radar data, satellite data, drift analysis on debris and aircraft performance limitations and characteristics. Several key assumptions and areas of broad dispersion in the estimates are identified

History of Oceanic Hull Losses

Although 80% of air transport accidents occur during the takeoff, initial climb, initial/final approach and landing phases of flight (Boeing, 2017), a number of hull loss accidents have occurred over large bodies of water during the cruise phase of flight, presenting significant challenges in the subsequent investigation due to the difficulties associated with localization and recovery of flight recorders and other physical evidence in a deep water, offshore environment.

Schuster-Bruce (2017) identifies twenty-one oceanic hull losses of commercial air transport aircraft in the twenty-year period from 1996-2016; an implied average of just over one such loss per year. Data from the Aviation Safety Network (Flight Safety Foundation, 2018) shows that 9 of these occurred more than 12 miles offshore, i.e. outside of territorial waters, while the remaining 12 occurred within 12 miles of shore.

Table 2

Air Transport Hull Loss Accidents Over Water, 1996-2016 (Flight Safety Foundation, 2018)

Year	Operator	Type	>12 Miles Offshore
2016	Egypt Air	A320	Yes
2014	Air Asia	A320	No
2014	Malaysian Airlines	B777	Yes
2013	Lion Air	B737	No
2011	Asiana Airlines	B747	Yes
2010	Ethiopian Airlines	B737	No
2009	Air France	A330	Yes
2007	Adam Air	B737	No
2006	Armavia	A320	No
2003	Flash Airlines	B737	No
2002	China Airlines	B747	Yes
2001	Siberia Airlines	Tu154	Yes
2000	Gulf Air	A320	No
2000	Kenya Airways	A310	No
2000	Alaska Airlines	MD83	No
1999	Egypt Air	B767	Yes
1998	Swiss Air	MD11	No
1996	Aeroperú	B757	Yes
1996	Birgenair	B757	Yes
1996	Ethiopian Airlines	B767	No
1996	Trans World Airlines	B747	No

Of these oceanic losses, the flight recorders were recovered (albeit at significant expense in some cases) in all but two of these cases at the time of writing, namely Asiana Flight 991 lost in 2011 and Malaysian Airlines Flight 370 lost in 2014. In the former case, a Boeing 747-400F cargo aircraft lost with its two crew members in the Korea Strait, the aircraft wreckage was located and sufficient physical evidence found to identify the probable cause of the accident (ARIAB, 2015), however the FDR and CVR were not recovered, despite an effort reported to have incurred costs of US$14,000,000 (p. 169).

During the forty-year period from 1975-2015, eight air transport accidents in oceanic or remote areas for which the flight recorders were not recovered (this does not include destroyed flight recorders, only those where recovery was not successful) have been identified (IPFS; 2016; ARIAB, 2015), for which the implied average is one such loss approximately five years where either the FDR, CVR, or both, were unrecoverable.

Regulatory Environment and the Global Aeronautical Distress and Safety System

The International Civil Aviation Organization (ICAO), through a process of consensus among its 192 Member States, defines over 12,000 Standards and Recommended Practices (SARPs), contained within the annexes, as amended, of the Convention on International Civil Aviation (ICAO, 1944), commonly referred to as the ‘Chicago Convention’ (ICAO, 2018). The Standards and Recommended Practices (SARPs) for flight recorders are provided within Annex 6, *Operation of Aircraft*, where new provisions for aircraft tracking and flight data recovery are embodied in recent Amendments 39, 40-A and 42 to Annex 6 (ICAO, 2017).

ICAO Contracting States generally embody the provisions of the ICAO Convention within the laws, regulations, standards and practices of their sovereign state. For example, the

European Commission adopted flight tracking amendments to Annex 6 through Commission Regulation (EU) 2015/2338 (European Commission, 2015), effective December 2018, while the U.S. Federal Aviation Administration has not yet implemented the ICAO recommendation at the time of writing (Pichavant, 2018). Some attempts at parallel legislation have been made in the U.S., for example a proposed Bill in the United States Congress (Bill HR 79, 2016), although no such Bill has yet been passed on this topic.

The Standards and Recommended Practices for Search and Rescue Operations are provided within Annex 12. In general, ICAO Contracting States are responsible for search-and-rescue operations within their sovereign territory and in areas of international waters where they have agreed to do so within regional air navigation agreements which have been approved by the ICAO Council (ICAO, 2012).

Accident investigation provisions are contained within Annex 13, while Annexes 2,8,10 and 11 provide provisions related to distress signals, safety equipment, communications systems, and alerting, respectively (ICAO, 2016). Publications of ICAO and the IMO provide more detailed procedures relevant to aeronautical and search-and-rescue operations. The ICAO Procedures for Air Navigation Services, Air Traffic Management (PANS-ATM) Doc 4444 (ICAO, 2016) provides detailed of recommended practices regarding position reporting, emergency communications procedures, and alerting. The International Aeronautical and Maritime Search and Rescue manuals (IAMSAR) provide detailed guidance and procedures for search and rescue services (IMO, 2016).

The Global Aeronautical Distress and Safety System (GADSS) Concept of Operations document (ICAO, 2017) describes the concepts developed after the losses of Air France Flight 447 and Malaysian Airlines Flight 370, intended to improve search-and-rescue and recovery efforts. The set of recommendations includes, for the existing and future fleet, extensions and improvements of Underwater Locator Beacons (UWBs), including 90-day operation, and new aircraft tracking standards under normal and abnormal conditions (ICAO, 2017; Pichavant, 2018).

For forward fit, the recommendations also extend the duration of the Cockpit Voice Recorder to 25 hours, the addition of new Autonomous Distress Tracking (ADT) requirements for new aircraft with a Certificate of Airworthiness issued after 1/1/2021 and, for new aircraft for which the Type Certificate is first applied for after 1/1/2021, new means of flight data recovery, either real time transmission of data via a communication link, or the use of an automatically deployable flight recorder or ADFR (ICAO, 2017; Pichavant, 2016).

Although these are the recommended implementation dates, it is possible that new technologies will be implemented as standard or optional features on aircraft for which the new standards do not strictly apply. For example, new means of flight data recovery could be installed on aircraft for which the type certificate was applied for prior to January 2021, on a voluntary or optional basis; Airbus (2017) has stated that 25-hour CVRs and ADFRs will be available on certain types of aircraft by 2019 and which will eventually be available on all Airbus types, in both cases examples of GADSS compliant solutions being made optionally available beyond the minimum requirements as per the dates and conditions above.

The GADSS Concept of Operations is being implemented in phases, through the amendments to Annex 6 of the Convention on International Civil Aviation, dependent on embodiment in the civil aviation regulations of ICAO Member States, as noted above. The relevant amendments to ICAO Annex 6, Part 1 Standards and Recommended Practices being

Amendments 39 and 42 for normal aircraft tracking, Amendment 40 for autonomous distress tracking (ICAO, 2016) and flight data recovery.

Economic Factors

The GADSS Concept of Operations (ICAO, 2017) identifies three specific issues to be addressed in forming the high level objectives for the system, namely: "(a) the late notification of SAR services when aircraft are in distress (as defined in ICAO Annex 11), (b) missing or inaccurate end of flight aircraft position information i.e. the location of wreckage and (c) lengthy and costly retrieval of flight data for accident investigation" (p.11).

Items (a) and (b) first and foremost address the single highest priority in any search-and-rescue mission, namely, to attempt to locate and rescue any survivors as quickly as possible within a short time window. During this phase of an operation, humanitarian considerations naturally take general priority over economic considerations and in any case the duration of this phase is by nature time-limited.

Item (c) relates more to the recovery of flight data for the purposes of investigation and also introduces an economic factor, in the stated consideration of the length and cost of such retrieval efforts. The GADSS Concept of Operations document also refers to one function of the IAMSAR manual as aiding the provision of "effective and economical SAR services" (p.9).

A fundamental trade-off exists between the rare but expensive SAR efforts which can be incurred by nation states, essentially borne by the taxpayer, versus increasing routine airline operating costs by changing requirements intended to reduce the search time, and thus cost, in those rare events. In the latter case, the cost is ultimately borne by the passenger. The U.S. FAA, addressing this trade-off directly, has noted in its position on the ICAO amendments that global tracking, “while cost-relieving for States, implementation of new tracking and reporting systems may be economically burdensome to manufacturers and operators who realize little or no return on investment” (Parfitt, 2016. p.16).

The search for Air France Flight 447 is reported to have incurred costs of $44,000,000 (Wardell, 2014), and $39,000,000 for Swiss Air Flight 111 in Canadian waters (Mohney, 2014), while that for MH370, by far the largest of its kind in history, is in excess of US$150,000,000; the ATSB (2017) reports Aus$198,000,000 (US$145,000,000), of which Malaysia contributed 58%, Australia 32% and the People’s Republic of China 10%, however this does not include subsequent costs incurred by the company Ocean Infinity in their part of the search to date, a speculative no-find-no-fee effort carried out under agreement with the Malaysian Government (Rodzi, 2018). Although those costs have not been officially reported, it has been estimated that the vessel used would incur costs in the order of US$70,000-$100,000 per day, plus the cost of the teams to operate the equipment used and the cost of access to that equipment (De Changy, 2018), which together implies unknown additional costs likely to be in excess of US$10,000,000, putting the total to well over US$150,000,000m, yet still excluding the costs associated with the airborne and naval surface searches conducted in the South China Sea, Malacca Strait and Indian Ocean in the days immediately following the initial loss of the aircraft.

While the United States has not incurred such costs in recent history, the recovery and investigation of TWA Flight 800 in 1996-2000 and Egypt Air Flight 990 in 1999 are reported to have cost US$40,000,000 and $4,000,000, respectively (Marks, 2000).

Nonetheless, as illustrated in Figure 1, the exposure based on U.S. search and rescue obligations is substantial, with a particularly large exposure in the Pacific Ocean, where the US SAR region extends as far as the Philippine Sea.

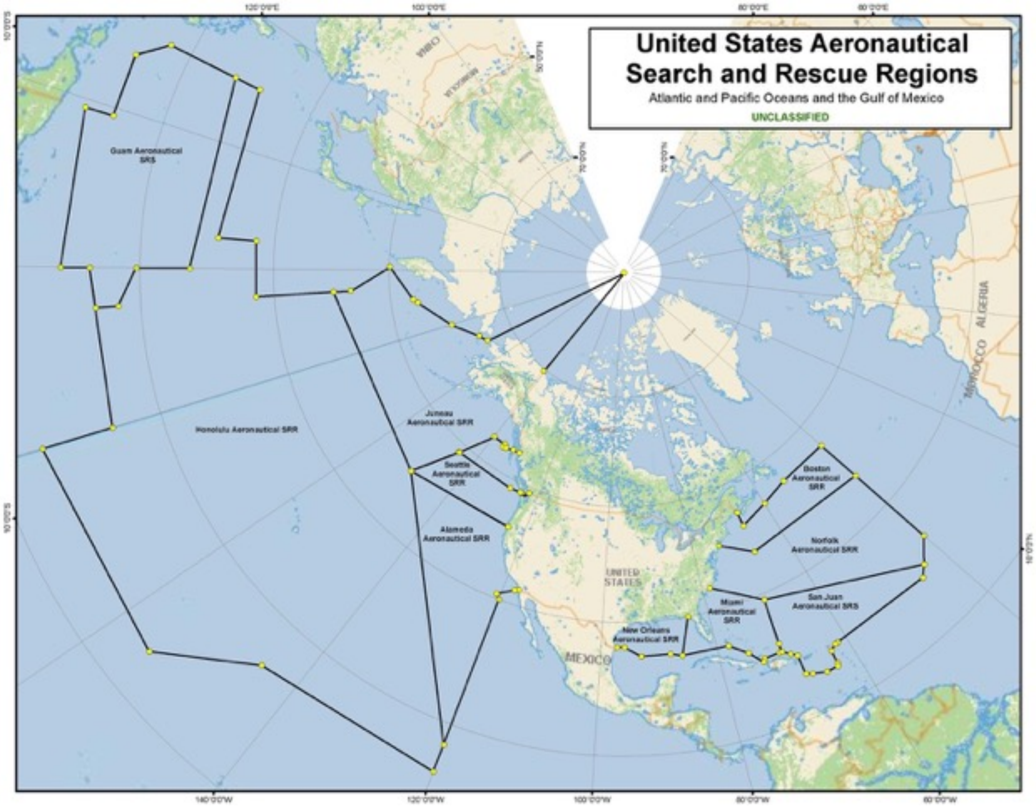

Figure 1. United States Aeronautical Search and Rescue Regions (USCG, 2016).

From the viewpoint of economic theory, the economically efficient solution (Lumsden, 2003) would be where the resources available to society are allocated in such a way as to produce the desired output – i.e. the timely recovery of flight data – with the minimum allocation of resources. This is essentially a view of production efficiency where the desired output is recovery of flight data in the least time and at the least cost. From the perspective of allocation efficiency, it is assumed that society desires a safe air transport system which is continually improving, where SAR efforts to rescue survivors are as effective as possible, and where entire airliners are not lost in the world's oceans for prolonged periods, together with resolution of the true cause for their loss.

It should be noted, however, that not everyone agrees that the prolonged search for MH370 or any other lost aircraft represents efficient allocation of society's resources; Cook (2015), after Cohen (2015) suggests that US$100,000,000 could save over 52,000 lives if the funds were instead spent on vaccinating children, specifically citing the MH370 case as a bioethics question and an example of our bias toward *identifiable lives* versus *statistical lives* (Singer, 2010).

The fundamental challenges of all these economic trade-offs mean that society will not necessarily automatically achieve the most economically efficient outcome. Thus, the question of economic efficiency is a pertinent one both to the specific MH370 case and to the general question of improvements in flight data recovery following oceanic losses and the implementation of the GADSS.

A second relevant economic factor relates to the area of innovation economics and industry evolution in the supply of products and technology for flight data recovery. The introduction of performance-based GADSS requirements creates an opportunity for technological innovation, which may in turn create new ways to achieve the aforementioned economically efficient outcomes. Furthermore, since the advent of flight recorders in the second half of the twentieth century, technological advancements have been largely competence-enhancing (Tushman & Anderson, 1986) to the incumbents. New GADSS related innovations may prove to be more discontinuous in nature (Utterback, 1996) and potentially competence-destroying (Tushman & Anderson, 1986) for some incumbents, which could in turn potentially reshape the industry landscape for the provision of flight data recovery technology in the twenty first century concept of operations.

The Independent Group and Crowdsourcing or Crowd-Solving Phenomena

The *wisdom of crowds* phenomenon (Surowiecki, 2005) has been known for centuries; Galton, as cited in Surowiecki (2005), observed in 1906 after a competition to estimate the weight of an Ox at an English country fair that the crowd's estimate – as measured by the arithmetic mean of the 800 participants' estimates - was within 1lb or 0.1% of the actual weight of 1,198lbs. Chilton (2009) suggests that the Longitude Prize organized by the British Government in 1714 and famously claimed by John Harrison for his novel chronometer design was in fact an early example of crowdsourcing, which Sobel (1995) characterizes as the solution to the greatest scientific problem of that age, solved by a lone genius who was an unlikely candidate for the winner and who would have almost certainly not have been involved in the official effort had the open prize not been established.

At the turn of the nineteenth century the astronomer Piazzi discovered what he believed to be a new planet, Ceres (the largest known object in the Asteroid belt, today classified as a dwarf planet or plutoid, IAU, 2006), which he observed for several weeks before the object passed behind the sun, after which he failed to re-observe it (Diaconis, 1998). Despite intense effort in calculation and observation among the astronomical and contemporary scientific community, the object appeared to be lost until Piazzi's observations were published in a newspaper (Diaconis, 2018), in an act somewhat analogous to modern day crowdsourcing. A twenty-four year old, as-yet largely unknown, Carl Friedrich Gauss (1777-1855) happened upon the newspaper observations and set about estimating a solution; in doing so, he applied Newton's and Kepler's laws to the problem, set the foundation for least squares estimation methods including statistical orbit determination, proved the Gauss-Markov Theorem, applied the Gaussian distribution to observational errors, and invented the method of Gaussian elimination (Diaconis, 1998; 2018). As Gauss (1857) himself put it, “This first application of the method was made in the month of October 1801, and the first clear night when the planet was sought for as directed by the numbers deduced from it, restored the fugitive to observation” (p.xv).

Although crowdsourcing may have a long and storied history, the rise of the internet and its ability to connect well over 3 billion people (ITU, 2016), creates a whole new environment for tapping into the wisdom of crowds via the internet to source ideas, solutions, information, even the funding of new ventures. The term ‘crowdsourcing’ was neologized by Howe (2006) to express this idea and the phenomenon has found application, to varying degrees, across many fields of human endeavor (Chilton, 2009; Franzoni & Sauermann, 2014; Guillot, 2013).

Geiger, Rosemann and Fielt (2011) draw typological distinctions between classes of crowdsourcing phenomena by assessing (a) the degree to which the external sources are treated as homogeneous by the system and (b) the degree to which the system aggregates the external sources, collective or individual. Thus, crowdsourcing systems can be categorized into four categories: *crowd-rating* (homogenous and collective), *crowd-creating* (heterogeneous and collective), *crowd-processing* (homogenous and individual), *crowd-solving* (heterogeneous and individual). In contrast to a crowd-rating system such as eBay seller ratings or TripAdvisor, where all the inputs from the crowd are generally treated as equally valid and where all the results are aggregated into a single answer, a crowd-solving (heterogeneous and individual) system does not treat all the inputs as equal, nor does it aggregate them; rather, it seeks to find the best individual inputs from a large sample by differentiating them on some dimension. These kinds of systems are typically used when an organization is seeking a novel solution to a particular problem (Marjanovic et al., 2012; Passig, Cohen & Bareket-Bojmel, 2015).

A common assumption in the general literature on the subject is that crowd-solving solutions are orchestrated by an organization, for example Brabham (2013), defines crowdsourcing as "an online, distributed problem solving and production model that leverages the collective intelligence of online communities for specific purposes set forth by a crowdsourcing organization -- corporate, government, or volunteer." (p.2). Marjanovic, Fry and Chataway (2012) assume that the crowd is 'tasked' by an organization (p.318), while Nickerson, Wuebker and Zenger (2017) define crowdsourcing as a governance choice. This assumption is pertinent to the case in question, as the MH370 Independent Group emerged untasked, so to speak, by the organizations officially tasked with solving the problem, as did others who have made contributions to the effort but are not directly associated with the Independent Group, a salient counter-example to the common assumption of orchestration in the current literature.

Comparisons of the quality of crowdsourced results to that of conventional solutions have shown equal or better results in many cases (Lee, Zhang and Shi, 2011; Tripathi, 2017), yet as Brabham (2013, p.42) points out in referring to the "misconception of the amateur participant", common psychological biases, such as authority bias (Milgram, 1963), can lead to misconceptions about the quality of participants not endowed with an official capacity to the task in hand, at the risk of discarding good data, information or solutions. In the case of the Independent Group, Thomas (2018) notes that it "includes experts in physics, radar, satellite technology, mobile satellite communications, avionics designers (GPS) and airline flight simulators. And a number are pilots". (p.1). Not that the Australian Transportation Safety Board can by any measure be accused of discarding the input of the crowd; in fact, the ATSB (2017) specifically acknowledges the 'external contributions' (p.119) of the Independent Group and other individual contributors, stating that much credible analysis was considered from such sources, alongside the work of those acting in an official capacity and noting the remarkable efforts of one individual in the location of debris across multiple countries. The literature review for this study has revealed a substantial amount of independent analysis, information and expert opinion, much of it published informally, which may either individually or in aggregate serve to refine estimates, or their underlying assumptions and which provide diversity of methodology, assumptions and conclusions.

Factual Information and Official Reports Specific to the Case of Flight MH370

For the purposes of this review, the chronology of publications by organizations responsible for the official investigation and search effort for MH370 begins with the *Preliminary Report* issued by the Malaysian Government in accordance with ICAO guidelines approximately 30 days after the loss of MH370 (Malaysian Government, 2014) and ends with the publication of the *Safety Investigation Report* in July of 2018 (Malaysian Government, 2018). Between those two dates, the Malaysian Government issued a series of annual *Interim Reports* (Malaysian Government, 2015; 2016; 2017) in accordance with guidelines in Annex 13 to the Convention on International Civil Aviation (ICAO, 2016).

The Australian Transport Safety Bureau (ATSB), acting in support of the Malaysian investigation as an *accredited representative* as defined under Annex 13 to the Convention on International Civil Aviation (ICAO, 2016) issued a series of publications commencing with the *Definition of Underwater Search Areas* in June, 2014 (ATSB, 2014) and concluding for the purposes of this study with the final report for the operational search published in October of 2017 (ATSB, 2017).

ATSB publications between those dates include multiple updates to the search area and flight path analysis (ATSB 2014; 2015; 2016), a series of five reports on analysis of recovered debris (ATSB, 2016), a *First Principles Review* (ATSB, 2016), and a series of five reports concerning drift analysis for the debris (ATSB 2016;2017). In addition to these primary sources of information issued by the official safety investigation team and its accredited representatives, a large body of additional factual information and analysis has been published by a range of other sources, including by the MH370 Independent Group, and other independent researchers, as further explored in this literature review.

Primary Radar Data - 1721-1822Z Phase of Flight MH370

The Malaysian Government (2018) reports that, after the final voice communication at 17:19:30Z, the aircraft is observed on radar records as crossing waypoint IGARI as per the operational flight plan, sixty-one seconds later at 17:20:31Z, slightly ahead of ETA, with loss of the Mode S symbol at 17:20:36Z, six seconds after passage of IGARI. Complete loss of Secondary Surveillance Radar (SSR) was recorded at 17:21:13Z, where it is possible that the SSR was coasting for at least part of that last 37 second period. The loss of SSR was also recorded at approximately the same time by radar facilities located in Thailand and Vietnam (Malaysian Government, 2018).

From Malaysian sources, the primary radar data after this point consists of two types of radar data after 17:22Z; that obtained from primary civil aviation approach radar facilities, i.e. Primary Surveillance Radar or PSR used in the vicinity of terminal areas (typically operated in C-band with a range of 50-60NM from the terminal), and that obtained from Royal Malaysian Air Force long-range primary radar sites in Malaysia (typically L-band or C-band with a detection range in the order of 250NM).

Beyond its immediate value in the days immediately after the incident in determining that the aircraft was not lost in the South China Sea as initially thought, this radar data is an important input to geospatial estimation models for the final aircraft location as it can, through estimation of the trajectory during this phase of the flight, potentially serve to reduce the uncertainty about the aircraft state, including the remaining fuel on board as well as position, track and velocity, for up to an hour after the initial diversion at 17:22Z. Any reduction in the uncertainty of the fuel state at the 18:22Z point of last primary radar contact can translate into reduced uncertainty of the region along the 7th arc where fuel exhaustion is likely have taken place.

Malaysian Military Primary Radar Data

Prior to the loss of secondary surveillance radar contact at 17:21Z, civil aviation radar sources, both primary and secondary, provide a record of the trajectory of the aircraft until that point. In concordance with the civil radar records, the loss of SSR capability was recorded by Malaysian military radar, as well as by radar facilities located in Thailand and Vietnam (Malaysian Government, 2018).

An unspecified RMAF military radar facility maintained primary radar contact after the point of loss of SSR contact at 17:21Z, and this military primary radar data has been used to establish that the aircraft proceeded only briefly from the waypoint IGARI toward BITOD as per the flight plan, departing from that plan in a left hand turn to a heading of 273 degrees, at an observed rate of turn which has been assessed through simulation to be beyond the operating envelope of the 777 autopilot and which is therefore believed to have been performed under manual control (Malaysian Government, 2018).

Overall, the RMAF primary radar data consists of intermittent returns from what is believed to be the aircraft of interest for approximately one hour after the initial turn near waypoint IGARI, with a final return at 18:22Z approximately 10NM northwest of waypoint MEKAR, heading northwesterly on or close to airway N571, out of the Malacca Strait toward the Andaman Sea, at a registered altitude of 29500 ft. (Malaysian Government, 2018).

Military Primary Radar Data from Thailand and Indonesia

The Malaysian Government (2018) report notes that Thai radar recorded the loss of SSR at 17:21:13Z but contains no mention of Thai military radar contact. Press reports, however, suggest that such contact was made; Thai Air Vice Marshal Montol Suchookorn was quoted as stating that Thai military radar "was able to detect a signal, which was not a normal signal, of a plane flying in the opposite direction from the MH370 plane, back toward Kuala Lumpur. The plane later turned right, toward Butterworth, a Malaysian city along the Strait of Malacca. The radar signal was infrequent and did not include any data such as the flight number" (Doksone, 2014, p.1). Thailand's Air Chief Marshal was quoted as identifying the Surat Thani radar facility as that which detected the aircraft (The Nation, 2014).

However, it is more likely that the radar information was sourced from that facility, based on radar feeds from antenna locations at Khok Muang, Ko Samui, and Phuket (Ianello, Thompson & Workman, 2017). Hall (2015) provides an estimate of the radar field of view for seven military radar facilities within range of the flight segment from 17:21Z-18:22Z; two in Malaysia, three in Thailand and two in Indonesia. So far as Thailand is concerned, the description of the radar contact with the aircraft of interest, which mentions the location of

Butterworth but nothing beyond that, would be broadly consistent with the extent of coverage for the Ko Samui and Khok Muang radar antenna locations. In theory, a known Thai radar location near Phuket should have been able to track the aircraft well beyond Butterworth and, in fact, well beyond the last reported point of primary radar contact at 18:22Z (Ianello, 2017), although no record of such contact exists in the literature. Workman (2017) suggests that the Phuket radar may have been inactive at the time.

Among the most salient of the gaps in the military radar records is the absence of any reported radar contact from Indonesian facilities, through the coverage of which the MH370 aircraft almost certainly flew (Hall, 2015). Ianello (2015) suggests that the fact that the Indonesian Government is reported to have stated that the aircraft was observed on radar prior to reaching waypoint IGARI but not afterwards (Malayasian Government, 2018) could be explained if the Indonesian radar facilities were shut down at midnight local time; such closure of radar facilities at night could explain the significant gap in radar contact with Indonesian facilities during the phase of flight in the Malacca Straight, including the civil radar facilities at Medan and multiple military facilities with range extending well into that area. It is also possible that the facilities may have been operating but the data were not recorded, or that the owners of the data elected not to share it due to the sensitive nature of military radar coverage.

For its part, Indonesia has indicated that the aircraft did not transit its territory; Indonesian Defense Minister Purnomo Yusgiantoro initially stated that on the morning of March 8, “We did not get any detection from any of our radars. There was no detection of any strange plane; there was none” (Jacques & Gantan, 2014, p. 1). He subsequently stated that the air defense radar facility located at Sabang did not detect an airplane “flying over

Indonesian territory" (Antara News, 2014, p. 1) and later that this facility did not detect MH370 flying over "Indonesian airspace" (SSIG, 2014). It should be noted that there is an important semantic distinction between the first statement and the latter two; detection of an aircraft is quite distinct from an aircraft flying over Indonesian territory or in Indonesian airspace. The Indonesian PSR capability extends well beyond Indonesian territory and airspace; for example, it is possible that the aircraft was detected on radar but that it remained north of the Indonesian FIR while on a northwesterly heading and turned south at a point which would have avoided the Indonesian FIR, therefore did not transit either Indonesian airspace or territory. A clear explanation for why the aircraft was not detected by Indonesian PSR during the period of flight when it is believed to have transited the coverage of that facility remains absent from the extant literature, yet it remains as potentially important information relating to the trajectory of the aircraft at that time and the resulting fuel state at the time of lost radar contact.

Primary Civil Radar Data

The initial loss of SSR contact at 17:22Z occurred in an area which is within the 200NM SSR range but beyond civil PSR coverage. Accordingly, after 17:22Z, this loss of SSR capability meant that civil radar contact was lost for around 8 minutes, until 17:30:37Z when the aircraft reached the outer range of the 60NM Terminal Primary Approach Radar facility located just to the south of Kota Bharu airport on the north eastern coast of the Malaysian Peninsula (Malaysian Government, 2018). With the exception of a period of just over 90 seconds when the aircraft passed within close proximity of the radar antenna, referred to as the 'cone of silence' (Skolnik, 1962), the aircraft was continuously tracked by the Kota Bharu PSR on a southwesterly heading until it reached that facility's 60NM range limit at 17:44:52Z, approximately halfway across the Malaysian Peninsula, close to the waypoint TARIP on airway B219.

Prior to the loss of contact while the aircraft passed close to the radar antenna location, the track appears to make a turn to the right in the order of 20-30 degrees, however Ianello (2015) suggests that this is the effect of the slant range being projected directly to the plane. This is plausible, as the projection of the slant range to the horizontal distance from the radar head requires knowledge of the altitude, which was not available to the PSR. In principle, under the assumption of a constant heading and altitude in the vicinity of the transition, the degree of displacement across multiple radar measurements in the vicinity of the radar antenna could be used to make inferences regarding the altitude and heading during the transition of the Kota Bharu airspace.

The radar data for this phase of flight available in the public domain comes from a variety of sources, as does information regarding the location of the radar facilities used for the collection of the data and regarding the type of radar used. There are some inconsistencies across the different sources in terms of the periods during which the aircraft of interest is reported to have been tracked by primary radar and in terms of the completeness of the data. For example, the Safety Investigation Report (Malaysian Government, 2018) includes both textual and graphical descriptions of the civil radar data, where the text refers to intermittent primary radar contacts between 17:30:37Z and 17:52:35Z for which it is stated that the data was captured by the 60NM Terminal Primary Approach Radar located at Kota Bharu airport, as "confirmed by the DCA [Department of Civil Aviation] and its radar maintenance contractor" (p.7). However, Ianello (2015) notes that the attribution of radar returns after 17:44:52Z to Kota Bharu is likely to be incorrect. Indeed, a plot of the tracks from that facility, provided by the Malaysian Government (2018) shows a loss of contact shortly after 17:43Z, which would in fact be more consistent with the registered 60NM range of that facility. The later contacts at 17:47Z and 17:51Z are up to twice that registered range and, while it is theoretically possible for targets to be detected at twice the free space detection range under tropospheric ducting, super-refraction or multipath conditions (O'Donnell, 2010; Skolnik, 1962), it is also possible – and arguably more plausible - that these sections were recorded by the primary approach radar located at RMAS Butterfield, a 50NM military radar which also provides terminal approach radar service for the civil airport on Penang (DCA, 2008), for which those segments are in range.

Data obtained, reportedly from a source in Malaysia, and released into the public domain by Ianello (2017) appears to confirm this. From this source, the final contact with the Kota Bharu approach radar is recorded at 17:44:24Z at a (slant) range of 61.6NM, broadly consistent with the registered range of the 60NM Kota Bharu approach radar, followed by contact with the Butterworth Approach Radar, established just over two minutes later at 17:46:34Z. The first loss of contact from the Butterworth radar at 17:52Z and 15.2NM range corresponds approximately to the 17:52Z loss of primary civil radar contact reported by the Malaysian Government (2018). However, the data from Ianello (2017) shows that radar contact was re-established by the Butterworth radar at 17:54:54 (30.6NM) and tracked almost continuously until 18:00:51Z, to 73NM range. This section of data is entirely absent from the civil radar data and charts presented in the Malaysian Government (2018) report, however this could be explained by the fact that, although it is a source of data for civil aviation terminal operations in the vicinity of Penang Airport (DCA, 2008), strictly speaking it is from a military source and may have been excluded for that purpose, although it should be noted that the section of that report pertaining to military data does not include this entire section of radar data either.

General Lateral Flight Path Until 1822Z

Despite the fragmented and inconsistent nature of the available data, the general lateral flight path for the first 1 hour and 40 minutes of Flight 370, from takeoff at 16:42Z to the last primary radar record at 18:22Z, is reasonably well known and there is general consensus within the existing literature on the overall *lateral* path, based on civil and military PSR after 17:21Z, with the addition of SSR and ACARS prior to 17:21Z. Although there is some debate about whether small heading and track variations are due to variation in the track of the aircraft or due to measurement noise in the radar observations (Ianello, 2018), there is general agreement on the lateral flight profile, with notable exceptions such as Smithson (2016), who argues that the aircraft in fact turned not to the left but to the right, headed back to Kuala Lumpur and then continued on that heading until fuel exhaustion. In this alternative scenario, the radar returns assumed to be from the MH370 aircraft are in fact from another aircraft, however an explanation for the absence of PSR contact with the aircraft of interest on the proposed alternative route back across the Malaysian Peninsular in the direction of Kuala Lumpur, as opposed to Penang, is not elucidated.

Broadly, the available radar data indicates a lateral path as illustrated in the figure below, departing Kuala Lumpur airport (WMKK) at 16:42Z, briefly following the Pibos Alpha Standard Instrument Departure (SID) procedure until cleared direct to waypoint IGARI. Upon reaching IGARI, the aircraft very briefly proceeded as per the flight plan toward waypoint BITOD before executing the sharp left-hand turn toward the Kota Bharu airport (WMKC), passing to the north of that airfield, crossing back over the Malaysian

Peninsular toward Penang Island. Passing just to the south of Penang airport (WMKP), the aircraft turned right, passing over Pulau Perak (a small island in the Malacca Strait) toward waypoint VAMPI, then passing waypoint MEKAR, with a final primary radar contact point at 18:22Z approximately 10NM past MEKAR on, or close to, airway N571 (Malaysian Government, 2018; ATSB, 2017; SK999, 2018).

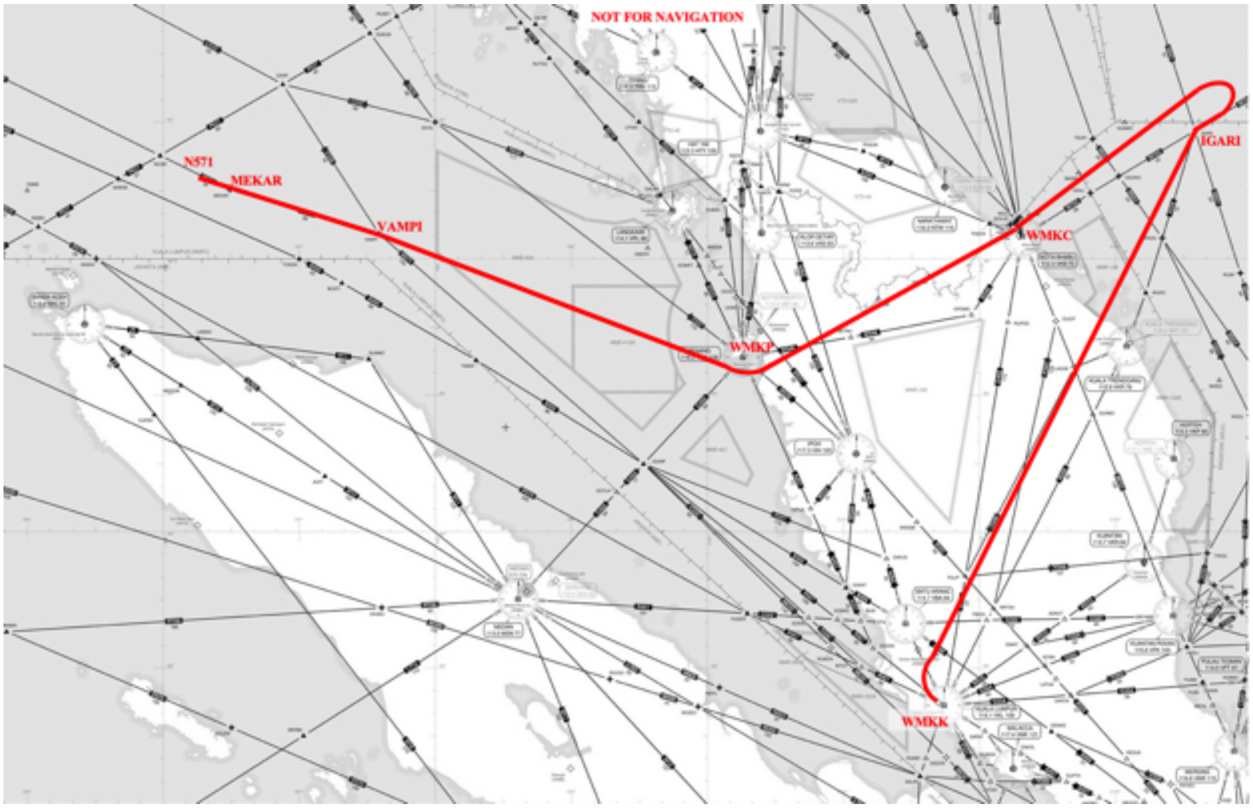

Figure 2. General Lateral Flight Path 1642Z–1822Z (Background SkyVector, 2018)

Vertical Trajectory and Velocity Profile 1721-1822Z

Although the general lateral profile is broadly well known, albeit with small variations, there is much greater ambiguity and uncertainly in determination of both the vertical profile of the aircraft after the loss of SSR and the velocity profile.

Ianello (2015) suggests that the uncertainty in the measured data precludes the determination of the velocity state over periods corresponding to segments of the order of several minutes in length, instead electing to estimate an assumed constant velocity over a period of approximately one hour by the method of Euler numerical integration. Using this approach, Ianello (2015) finds a constant velocity and constant altitude solution for the period of flight under primary radar surveillance, Mach 0.84 and FL340 respectively, although only if a time offset of 35 seconds is assumed for some of the radar records reported in Malaysian Government (2015). Based on these assumptions, Ianello (2015) concludes that fuel consumption estimates predicated on the assumption of long-range cruise speeds and typical cruising altitudes are probably correct.

If time synchronization errors of more than 30 seconds are present in the radar data during the period 17:22-18:22Z, this would have implications for the assumed trajectory. Alternatively, the 30-35 second offset might be explained by aircraft velocity changes during the period, which in this case would imply a reduction in velocity followed by an increase, in both cases relative to the assumed M0.84 constant velocity in Ianello's (2015) estimate. SK999 (2018) compares the difference between locations at a given time provided by the civil radar and the corresponding time for that location given by the output of the Kalman filter estimate performed by Davey et. al. (2015) on the military radar data, noting that the five second discontinuity observed at the transition of the Kota Bharu radar vicinity is removed if the aircraft is assumed to be at 41,000 feet, or if the aircraft was accelerating as it passed the Kota Bharu vicinity, then subsequently decelerated. Neither of these observations is consistent with a constant-altitude, constant-velocity solution (Ianello, 2015).

This uncertainly of the velocity profile during the phase of flight while under intermittent primary radar surveillance has not been well resolved; smoothing of the data provides an estimate but may not precisely reflect the either the actual trajectory or the actual fuel consumption of the aircraft during this time, which in turn affects the initial conditions for the phase of flight from 18:22Z onwards and the subsequent feasible range.

The vertical profile of the flight during this phase also remains highly uncertain. As shown in Figure 3, the reported altitudes based on primary radar records are widely dispersed, including altitudes and vertical maneuvers which are physically impossible for the aircraft in question (Malaysian Government, 2018).

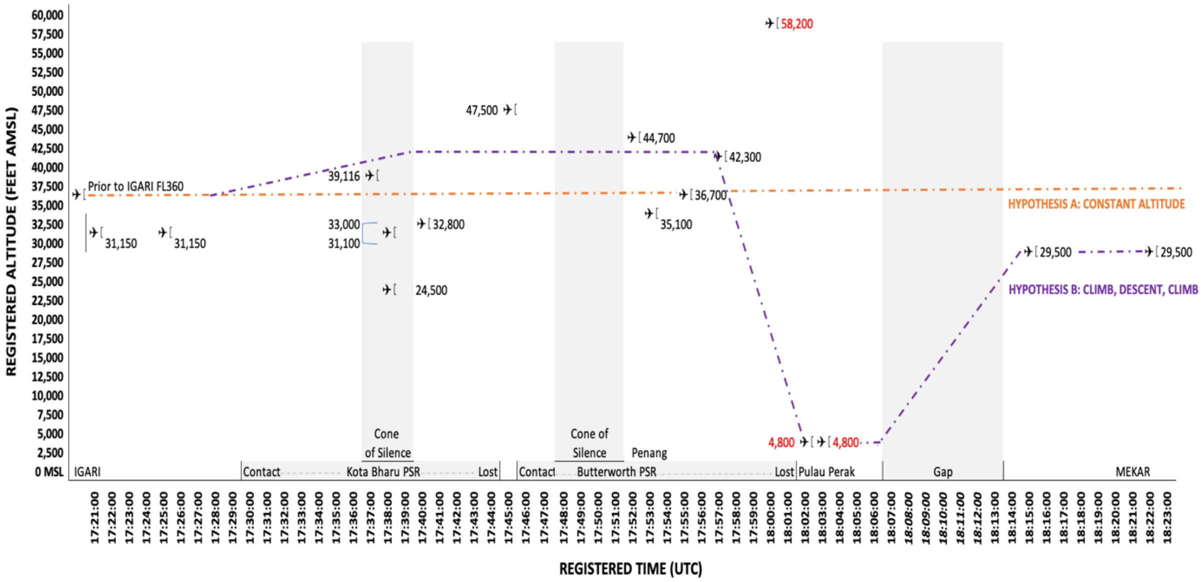

Figure 3. Primary Surveillance Radar Registered Altitude 17:22-1822Z (Malaysian Government 2014, 2018)

The wide dispersion of these primary radar derived altitudes leads to a large number of potential vertical trajectories which are possible during this period of approximately one hour of the flight, which are reduced to two fundamental hypotheses in Figure 3. Perhaps the simplest hypothesis, labelled A in the figure, is that the aircraft continued at an altitude similar to that which it was known to have attained prior to the loss of communications, namely a pressure altitude of FL360. In this case, the wide dispersion of measurements is attributable to the altitude measurement uncertainty in the primary radar systems used;

indeed, the mean of the observations is 32,700 feet geometric altitude, with a sample standard deviation of 13,275 feet. As previously noted, Ianello (2015) finds a constant-altitude constant-velocity solution at 34,000ft and Mach 0.84, but only if a 35 second time synchronization error is accepted to exist within the data, across the different radar sources used. Godfrey (2018) finds a solution at 36,000ft during the Kota Bharu transition, which includes an acceleration from 460kts to 530kts during this time, but which also requires multiple time synchronization adjustments of 10 seconds in total.

An alternate hypothesis, labelled B in the figure, is that the aircraft initiated a climb to above 40,000ft within the first few minutes after turning back past waypoint IGARI, reaching such an altitude just prior to transit of the Kota Bharu radar ‘cone of silence’. Exner (2018) posits that the aircraft crossed this region at a geometric altitude of 43,500ft, corresponding to a pressure altitude of around 41,000ft for the conditions on the night in question, pointing out that such an altitude resolves unrealistically high implied velocities if lower altitudes are assumed, also addressing the time discontinuity issue seen in Ianello (2015). SK999 (2018) notes that time discontinuities between the Kota Bharu radar and military radar records in the vicinity of Kota Bharu range from -28 seconds to zero seconds depending on the assumed altitude of transition, where the zero second solution is found at 41,000ft. Gilbert (2018) challenges the practicalities of flight at that altitude and also points out that such an altitude disregards the radar derived altitudes observed during the transition of the Kota Bharu vicinity, which are in the range of 31,100 to 39,116ft, although an explanation for the time discontinuities is not addressed.

Under hypothesis B, after the aircraft is assumed to have climbed to perhaps its ceiling at that stage of the flight, after a period of 20-30 minutes it descends rapidly prior to passing the island of Pulau Perak at 4,800ft as reported by the radar reports (Malaysian Government, 2018), then subsequently climbs back to the recorded altitude at 18:15Z and 18:22Z, namely 29,500ft (Malaysian Government, 2018). The Royal Malaysian Police Report (RMP, 2014) mentions an eyewitness on this island which, given that the aircraft would either have been passing by at cruising altitude at around 3am local time on a well-used airway or would have been passing at low altitude, may make more sense in the latter case, assuming that the eyewitness account is accurate. Pulau Perak is reported to be an uninhabited island except for a small military garrison (Wise, 2017).

Any path consistent with either hypothesis must be viable given the recorded time at various distances from the radar facility and the aircraft limitations. Also pertinent to the assessment of the likelihood of either scenario is radar data which was shown to relatives of those on board the aircraft at the Lido Hotel in Beijing on March 21, 2014, which was photographed by attendees at the meeting including the press (Photo China, 2014). The radar tracks in that image exhibit dense returns initially at approximately 50NM from Penang, then become increasingly sparse until contact is lost in an area marked on the original presentation slide with a white circle, the rightmost shaded area in Figure 3. Radar contact was subsequently re-established in the vicinity of the VAMPI waypoint, with intermittent returns until approximately 10NM past waypoint MEKAR at 18:22Z, the final PSR contact. It should be noted that this data in its entirely has not been included in any of the factual information reports made by the Malaysian Government (2014;2015;2016;2017;2018), although sections of it are consistent with textual reports in those reports, for example the loss of PSR contact at 18:22Z and the period of reported contact in the minutes prior to that.

Others have suggested that all or part of these recorded radar returns may not relate to the MH370 flight but to one or more other flights in the vicinity at that time (Gunson, 2017).

Assuming that the returns do relate to the flight of interest, and keeping in mind that the final PSR return at 18:22Z is broadly consistent with the location of the 1st BTO arc three minutes later at 18:25Z, two explanations have been put forward for why radar contact is lost during the period indicated by the white circle in the image presented at the Lido hotel; either the aircraft descended out of radar contact in the vicinity of Pulau Perak (i..e consistent with hypothesis B), for example Ianello (2015) states, “Some believe this indicates the unidentified aircraft was descending at these times” (p.5) but also noting that this contradicts the near constant-velocity, constant-altitude (M0.84, FL340) solution of Ianello (2015).

Alternatively, it has been suggested that anomalous propagation of the radar energy, specifically tropospheric ducting, together with multipath effects may be contributing factors to the anomalous positions and gaps in the data during this period, and that radiosonde data from launch sites collocated with the radars of interest exhibit temperature inversions (Thompson, 2017; BarryC, 2017). Indeed, these environmental conditions may have been conducive to super-refraction or tropospheric ducting, both in the case of the Kota Bharu radar and the Western Hill radar, although gaps in the data would more generally indicate sub-refraction, of which the conditions reported may not have been indicative (Skolnik, 1962). Multipath is also a possibility, especially for the Western Hill radar with a line of sight over open water, although the sustained outage of several minutes after that time may be more difficult to explain due to multipath if the aircraft had remained at higher altitude, given the changing geometry over that time period. Such conditions could also serve to explain the wild variations in registered altitude, particularly if returns from both distant and proximal radar facilities are reported at similar times. For example, the physically impossible climb to 58,200 feet followed by a physically impossible descent to 4,800 feet in less than two minutes as indicated in the reported radar data could be explained if the 58,200ft return was recorded by a facility on the west coast of the Malaysian Peninsular operating at the absolute limits of its range under non-standard tropospheric conditions, while the 4,800 ft return was recorded from a much closer facility on Penang. Knowledge of the sources for the observations could help resolve such questions. The report of two radar returns at 4,800 ft registered altitude may also be significant, as outlier observations are less likely to exactly repeat themselves, however it is also possible that the second observation in this particular sequence is a result of the PSR coasting from the first observation.

In principle, knowledge of the geometry, observed environmental conditions, and radar characteristics for this specific case could be combined to assess the likelihood of any of these phenomena, i.e. super-refraction, sub-refraction and multipath having occurred at the times and locations where it has been suggested they may have occurred, although such analysis is absent from the extant literature for this case. Given that the two explanations for these anomalies and outages would lead to materially different conclusions about the likely fuel state of the aircraft at the time of the last primary radar return, and also have a bearing on assessment of the presence or absence of human control of the aircraft at this point in time, such analysis could serve to isolate one or other of these possible causes.

L-Band Aeronautical Satellite Communications

The potential for artificial satellites to provide global communications was known from the mid-twentieth century. For example, Clarke (1945) noted that, from the known physical relationship between the orbital velocity and the orbital period of an artificial satellite, an orbit existed for which the apparent position of the satellite as viewed from earth would remain constant, due to the orbital period being coincident with the earth's rotational period; a Clarke orbit, also referred to as a geosynchronous equatorial orbit (GEO) or geostationary orbit, the latter term being an entirely relative one, as the orbital velocity is in fact in excess of 3 km/sec or approximately 6,900 miles per hour. Clarke (1945) proposed this orbit as one from which 'extra-terrestrial relays' (p.1) could be used to facilitate global communications, with three such relays spaced at 60 degrees of longitude being sufficient to achieve global coverage. He also calculated the required transmission power to receive a given field strength on earth, the periods during which the spacecraft would be in eclipse during different times of the year, and several parameters of the required launch vehicle - all remarkably forward-thinking insights at the time.

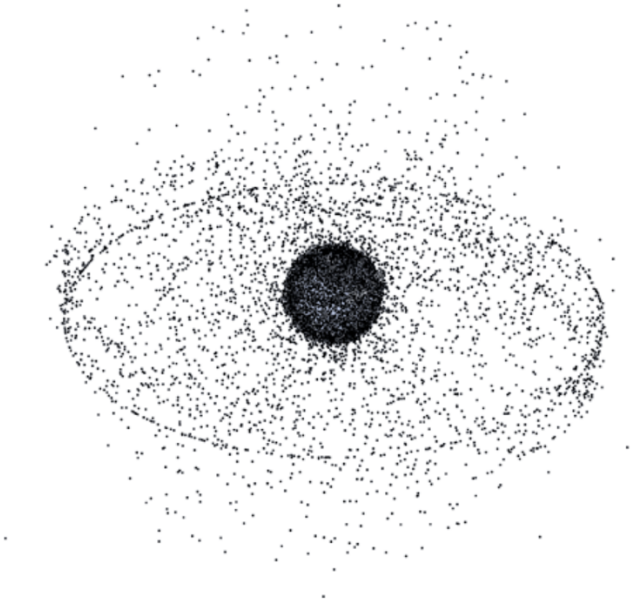

Figure 4. Image of objects in Earth orbit, showing belt of objects in geosynchronous orbit. (NASA, 2009). Public Domain.

The first satellite launched into such a geosynchronous equatorial orbit came 18 years after Clarke's exposition, with the launch of Syncom III in 1963, the spacecraft which, coincidentally, was used for the first ever demonstration of air-to-ground satellite telephony communications from a commercial (PanAm) flight in 1965 (Bertzins, Ryan & Smith, 2015). Since that time, the geosynchronous equatorial orbit has become densely populated, as can be seen from the dense belt in Figure 4.

In 1976, the Inter-Governmental Maritime Consultative Organisation, the predecessor to the International Maritime Organisation (IMO), adopted the Convention and Operating Agreement on the International Maritime Satellite Organisation, (INMARSAT), which became effective in 1979 (Bertzins, Ryan & Smith, 2015). Although formed as an intergovernmental organization to provide maritime communications, initially by operation of existing geostationary assets and later through commissioning of its own constellations, Inmarsat became involved during the 1980's in the work of the ICAO Special Committee on Future Air Navigation Systems (FANS), which led to the establishment of aeronautical satellite services for safety and operational purposes during the 1990's (Bertzins, Ryan & Smith, 2015).

These services, operating in the L-band, provide satellite telephony services, together with data communications via the Aviation Communications, Addressing and Reporting System (ACARS) service, including the carriage of Automatic Dependent Surveillance - Contract (ADS-C) and Controller-Pilot Data Link Communications (CPDLC) data traffic which together provide continuity of position reporting and two-way communications once the aircraft is out of range of terrestrial radar surveillance and VHF communications, primarily when operating on oceanic routes or over remote land areas (ICAO, 2013). ACARS is routinely used for real-time data communications for airline operational purposes (its original function) and for condition and health monitoring reports used by airlines, airframe and engine OEMs, and others.

As was the case with the aircraft used for the MH370 flight, these L-band services may also be used to provide in-flight entertainment and communications (IFEC) via services offered in the passenger cabin of the aircraft, although as a general trend these L-band IFEC services are gradually being replaced by higher capacity K-band systems.

MH370 L-Band Satellite Communications

The 777-200ER aircraft registered as 9M-MRO and assigned to flight MH370 was equipped with an L-band aeronautical mobile satellite services (MSS) communications system which provided satellite voice, ACARS data and IFC data via the Inmarsat *Classic Aero* service.

The Aircraft Earth Station (AES) equipment in the specific configuration of the 9M-MRO aircraft, comprises of a Satellite Data Unit (SDU), an RF Unit (RFU), one or more High Power Amplifiers (HPA), connected via coaxial cables to a High Power Relay (HPR), three Diplexer Low Noise Amplifiers (DLNAs) serving three antennas; a Low Gain Antenna (LGA) mounted on the top of the fuselage and two conformal High Gain Antenna (HGA) side-mounted arrays mounted on the port and starboard sides of the fuselage over the #3 exit doors immediately aft the wing, nominally at 45 degrees to the horizontal, each controlled by an independent Beam Steering Unit (BSU) (Malaysian Government, 2018; Westfeldt & Konrad, 1992; Ball Aerospace, 2017; ARINC, 1994).

In the modern implementation of Clarke's concept, the communications link consists of a forward link from the Inmarsat Ground Earth Station or GES using a C-band feeder uplink, received by the communications payload on board the Inmarsat-3 Flight 1 spacecraft in this case, amplified and retransmitted on the L-band downlink on either a global or regional beam, to be received at the AES antenna.

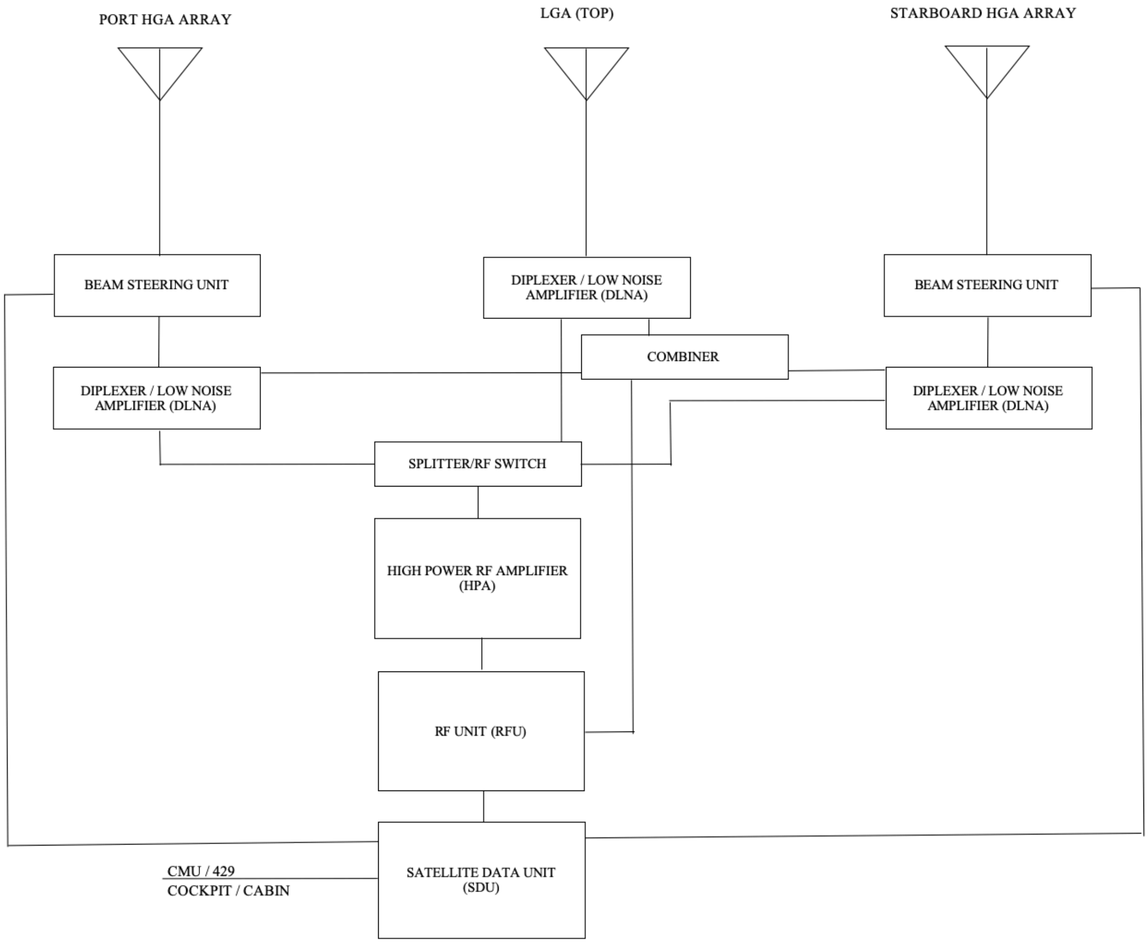

Figure 5: Indicative 9M-MRO AES Configuration (Adapted from ARINC, 1994; Westfeldt & Konrad, 1992)

In the return link, the AES transmits using assigned channels in the L-band, received at the satellite's L-band antenna via the satellite's L-band reflector in either the global or regional beams, amplified and retransmitted on the C-band downlink to be received at the GES antenna element via a large reflector. The communications chain after the GES antenna subsequently amplifies, down-converts and then processes the signal in a number of ways.

For both the forward and return link, the GES connects via the Inmarsat network to the global telecommunications network and PSTN, facilitating both telephony and data communications to and from end-points globally.

The MH370 AES was operating normally until the last ACARS transmission at 17:07:29Z (Malaysian Government, 2018), routinely sent after reaching cruising altitude. Due to the lack of data communications for one hour after this final ACARS transmission, the Inmarsat network transmitted a log on/log off request to the AES from the Perth GES at 18:07Z, a normal automated procedure to avoid the allocation of resources to a terminal which is no longer active but which did not log off the network. The AES terminal did not respond to this signaling request from the GES, suggesting that it was either powered down (suddenly, as it did not correctly log off the network) or was otherwise unable to communicate with the network. It is quite possible that the AES became inoperative at the same time as the loss of SSR capability, however this cannot be established with any certainty, as the terminal did not log off the network at that time.

However, at 18:25Z and just over one hour after the initial loss of communications, the AES resumed operation, logging back on to the network and communicating via the Perth Ground Earth Station in the form of link information data units (LIDUs) consisting of network management and signaling exchanges, periodically for several hours until the final transmission received at 00:19Z on March 8th, 2014, seven hours and thirty-seven minutes after departure from Kuala Lumpur. Many of these exchanges consist of a single line of data so far as the return link direction is concerned.

Burst Timing Offset

The satellite network log files contain a *Burst Timing Offset*, or BTO, measurement for messages received at the GES from the AES via the satellite, which can be considered as a form of pseudo-range measurement (Hoffmann-Wellenhoff, Lichtenegger & Collins, 1992), being a range-related observable with a constant or very slowly changing bias. The BTO observations can be related to the range R_{SC-AES} between the aircraft and the spacecraft at the point of time *t* at which it was observed, through the functional relation (Ashton et al., 2014):

$$R_{SC-AES} = \frac{c.(BTO_t - \beta)}{2} - R_{SC-GES} \ ,$$

where the second range, R_{SC-GES} from GES to spacecraft, is known to high precision from tracking, telemetry and command (TT&C) measurements (Roddy, 1989), c is the propagation velocity of the electromagnetic wave, and the bias β can be estimated by making use of BTO measurements recorded when the position of the aircraft, and thus the range R_{SC-AES}, was known (Ashton et al., 2014).

With this technique, Ashton et al. (2014) derived seven location arcs from BTO measurements made periodically after the loss of radar primary contact, starting with the 1st arc at 18:25Z (March 7, 2014) and ending with the 7th arc at 00:19Z on March 8, 2014. Although the 7th arc is thousands of miles long, not all points along it are feasible from an aircraft performance and endurance standpoint. By combining knowledge of the approximate time of fuel exhaustion (assumed to be after 00:11Z and prior to 00:19Z), with the last received fuel-on-board report, together with knowledge of the aircraft performance characteristics, it is possible to bound the region of the 7th arc within which feasible trajectories exist which would have resulted in fuel exhaustion at that time and on that arc.

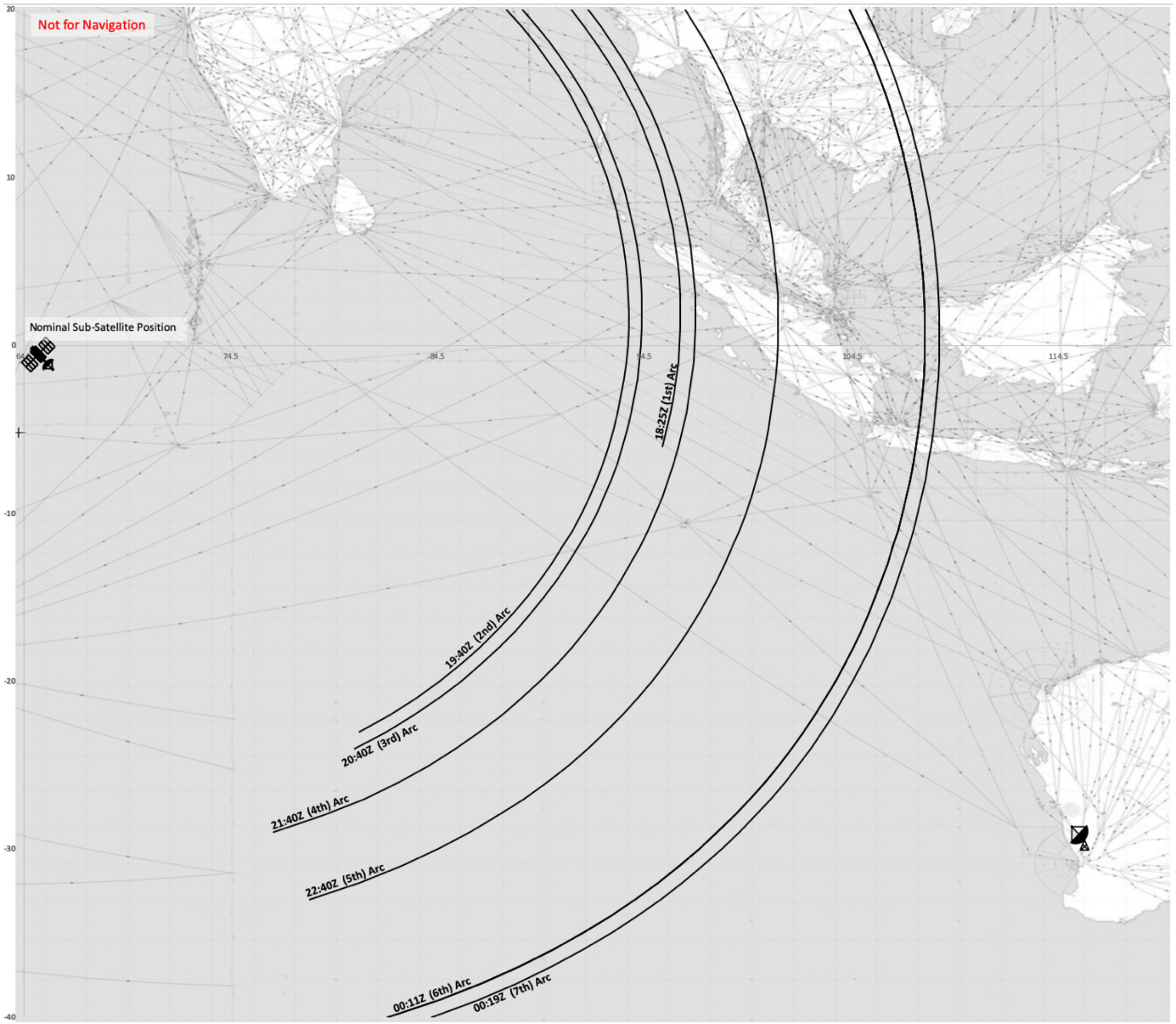

Figure 6. Arcs defined from Burst Timing Offset (BTO) measurements 18:25Z to 00:19Z (Background Skyvector, 2018)

An appendix to the Safety Investigation Report (Malaysian Government, 2018) provides a report from Boeing which indicates feasible trajectories which terminate along the 7th arc at between approximately 22S and 40S, at altitudes of between FL150 and FL400, with corresponding true airspeeds of between 333kts and 469kts. Pleter, Constantinescu and Jakab (2015) find plausible trajectories terminating on the arc between approximately 25S and 40S, with a preference for the more southerly location. The northerly bound may however be north of 22S; Marchand, Gasser, Delarche and Garot (2018) demonstrate a trajectory which reaches fuel exhaustion on the 7th arc at 12S. In their model, a deliberate actor is exploiting knowledge of the FIR boundaries and radar coverage in the region to avoid detection. The Boeing estimated trajectories at this latitude (12S) fall short of the 6th arc and are about 100 miles short of the 7th arc at the time of fuel exhaustion, however this difference can be explained by the fact that these trajectories are flown at constant low altitudes from the first arc, for example FL030 or FL150, with turns only allowed at the point of crossing of each arc, whereas in the case of Marchand, Gasser, Delarche and Garot (2018) the initial altitude is FL328, with a series of descents and corresponding reductions in speed over ground, such that the two independent simulations are not entirely contradictory in regard to the plausibility of a end of flight location occurring on the 7th arc at such a high latitude.

When using only BTO data and aircraft performance data and prior to incorporating Burst Frequency Offset (BFO) data, Ashton et al. (2014, p.8) estimate a trajectory assuming high altitude and high velocity which terminates between around 35S and 40S on the 7th arc (as with the other BTO-only cases, there is also an equivalent northerly track terminating over Asia due to the north-south ambiguity present in the BTO arcs).

Constraining the solution to that which would be seen if the aircraft were flown at the maximum range cruise (MRC) performance and constraining to altitudes between 25,000ft and 40,000ft, ATSB (2014) found solutions conforming to the BTO observations and aircraft performance parameters which terminated between approximately 30S and 37S, depending also on the assumed time of the turn south.

In summary, when using only the time of fuel exhaustion, the constraints to the BTO arc locations together with an aircraft performance model, termination of the flight at any point along the 7th arc between approximately 12S and 40S is possible, as are paths which terminate in the northern hemisphere, in the absence of any additional information which can reliably narrow these bounds further, or resolve the north-south ambiguity on the arc.

Burst Frequency Offset

As initially described and developed by Ashton et al. (2014), the recorded frequency offset on the return link for each AES transmission received at the GES via the 3F1 satellite can be used to make inferences about aircraft position, heading and velocity, by making use of the known physical relationships between the position and dynamics of the aircraft and spacecraft, the known GES position, and the induced Doppler effect at a given frequency due to both aircraft and spacecraft position and dynamics. As with the BTO, there are biases in the BFO observables originating from the AES, satellite, and GES, which must all be compensated for. The observed BFO is described by the following functional relationship to those parameters and biases (Ashton et al., 2014):

$$BFO = \Delta F_{up} + \Delta F_{down} + \delta f_{comp} + \delta f_{sat} + \delta f_{AFC} + \delta f_{bias}$$

Where the first two terms are the motion-induced Doppler effects on the uplink and downlink carriers, followed by the effect of Doppler pre-compensation in the aircraft MSS terminal prior to transmission, the effect of frequency translation on board the spacecraft, the effect of Automatic Frequency Control compensation at the ground earth station, and the bias, assumed to be fixed.

As the position and dynamics of the aircraft are unknown, the general technique is to simulate trial positions, velocities and headings, while using known spacecraft position and velocity vectors obtained from the Tracking, Telemetry and Command functions (TT&C), in order to find aircraft trajectories which are both feasible based on aircraft performance factors and which would best fit the observed frequency offsets at the points in time when they were observed, in addition to fitting the known arcs of position obtained from the BTO measurements at the right points in time (Ashton et al., 2014).

In contrast to a satellite navigation system where the induced Doppler frequency shift on the received signal is an observable of interest (Wells, 1974), velocity induced Doppler effects on satellite communications systems are generally considered undesirable due to the nuisance effects they can generate. Accordingly, these effects are reduced in the return link by pre-compensation of the uplink Doppler effect within the AES terminal prior to transmission, as well as by post-processing of the downlink Doppler effect at the GES through Automatic Frequency Control or AFC. The raw observables in the data log are affected by both of these compensation measures, however if the pre-compensation algorithm is known, then the numerical simulation can model for this variable, while the AFC measures were recorded by Inmarsat and thus can be removed from the raw data (Ashton et al., 2014).

In the case of the specific terminal with which the 9M-MRO was equipped, the in-flight Doppler pre-compensation, in one mode of operation, makes use of inputs from the aircraft avionics to determine the relative location and motion of the aircraft with respect to the satellite with which it is communicating but does so assuming the spacecraft is located at a fixed, perfectly geosynchronous, orbital station. If this stationary assumption were in fact the case, the BFO observations would likely contain no useful information about the aircraft velocity or heading due to the perfectly successful pre-compensation. In fact, this is not the case; the 3F1 spacecraft at the time of the flight in 2014 exhibited significant motion, particularly in the north-south direction, due to operation in a propellant-efficient inclined orbit.

Thus, the observed BFO, pre-compensated with a slight miscalculation under the assumption described above, contains a residual error: specifically, the difference between the induced Doppler effect on the uplink as assumed by the pre-compensation algorithm and its parameters in the AES terminal, and the actual induced Doppler effect on the uplink as a result of the actual aircraft-spacecraft relative position and velocity. It is this residual effect which ultimately forms the observable of interest in the BFO measurements, once the other factors in the functional model as shown in the expression above have been estimated.

By incorporating the BFO data, Ashton et al. (2014) demonstrate that computed trajectories which terminate in the southern hemisphere fit the observed data much better than do those which travel north after the loss of primary radar, which effectively resolves the north-south ambiguity inherent in the estimates which use only use BTO and aircraft performance data. Davis et al. (2015) concur with this result, reporting that the northerly route exceeds the measured noise in the BFO data by more than ten standard deviations.

Ashton et al. (2014) also report the simulation of a large number of potential trajectories at ground speeds from 375 to 500 kts, from which many candidate trajectories fit the data within the estimated bounds of error, and present one such trajectory, terminating on the 7th arc at approximately 35S, as that which best fits the observed data when a constant speed over ground and near-constant track over ground are assumed.

Davey et al. (2015) also report the results of a large number of simulated trajectories implemented in a Markov Chain Monte Carlo particle filter, resampled at the observation points based on statistical importance and thus producing a posterior probability density function estimate, where the highest probability density occurs in the vicinity of 38S on the

7th arc but extends several hundred kilometers along the arc and tens of kilometers perpendicular to it.

BTO and BFO Biases and Stochastics

BTO Bias. Both the BTO and BFO observables contain biases, and spatial estimators based on the BTO and BFO measurements are highly sensitive to changes in these biases. For example, all the studies selected for the meta-analysis are distributed along or in the vicinity of the 7th arc, which itself depends on the BTO bias. A 10 microsecond change in the BTO bias translates to a ~3km difference in the satellite-aircraft range estimate. ATSB (2014) provides data on the stochastics of the BTO measurements, which are noted to be quantized at 20μs, concluding that the BTO noise is distinctly non-Gaussian and that the 99th percentile of the test data was bounded by 53μs, propagating into a +/- 10km horizontal line of position error (~+/- 6NM). An error propagation analysis is shown in the Appendix.

Ashton et al (2014) estimated a mean bias of -495,679 μsec from n=17 observations on the ground at KLIA and from the table of data values provided, the standard deviation can be estimated as 32 μsec. (Noting that this standard deviation applies to a non-Gaussian distribution). Davey et al (2015) estimate an R1200 channel bias of -495,679 μsec from a larger sample which includes data from flight MH371 earlier on March 7, 2014; standard deviations of the residuals over 20 flights are estimated as 29 μsec for the R-1200 channel, where the residuals are described as approximately Gaussian and 62 μsec for the R-600 channel, noting that the BTO bias changes over time but is generally stable over the timescale of a typical flight duration.

BFO Bias. Regarding the Burst Frequency Offset bias, the ATSB (2014) reported the results of a sensitivity analysis which concluded that a 1Hz change in the fixed BFO bias propagated to approximately a 100km change in estimated location along the arc. Ashton et al (2014) estimated a fixed bias of 150Hz for the MH370 flight, while Davey et al (2015) studied the variation of the BFO bias over 20 flights and found that the BFO bias changes between flights and during the duration of a flight, where significant excursions which can peak at 20-30Hz are observed in the residuals, often ephemeral in nature with duration measured in the order of minutes or tens of minutes, as opposed to hours or days. With statistical outliers removed but including these transients, Davey et al (2015) estimated the standard deviation of the residuals to be 4Hz (although a 7 Hz value was used in estimation), with a mean close to zero, and where the tails of the distribution deviate from a Gaussian pdf.

The transient bias component of the residuals can be treated in at least two different ways; one being to incorporate it within the overall noise estimation and the other to treat the underlying noise $\epsilon_{\delta f_{bias}}$ (i.e. in the absence of the transient effect) as a distinct from the ephemeral bias $\delta f_{bias(transient_t)}$ at time t. That is:

$$\delta f_{bias} = \delta f_{bias(fixed)} + \delta f_{bias(transient_t)} + \epsilon_{\delta f_{bias}}.$$

Estimates of the underlying noise in the residuals $\epsilon_{\delta f_{bias}}$ performed on shorter periods of data where the ephemeral bias is zero naturally tend to yield lower variance than, for example, the 4Hz estimated above. The practical significance of the difference between these two approaches relates to estimation problems making use of the data after the 18:25Z restart. Many of the hourly transmissions after that time consist of a single response on the return link to a GES-initiated request on the forward link. With a sample of n=1 for a BFO observation on the return link at any given observation point, no way has been yet found to determine whether or not the transient bias is present at that moment. If the transient $\delta f_{bias(transient_t)}$ could be estimated from an independent model, or could be determined to equal zero at that time, the higher precision reflected in the underlying noise allows for better estimation of the track of the aircraft at that time, while incorporation of the transient in the noise increases the uncertainty in such estimates.

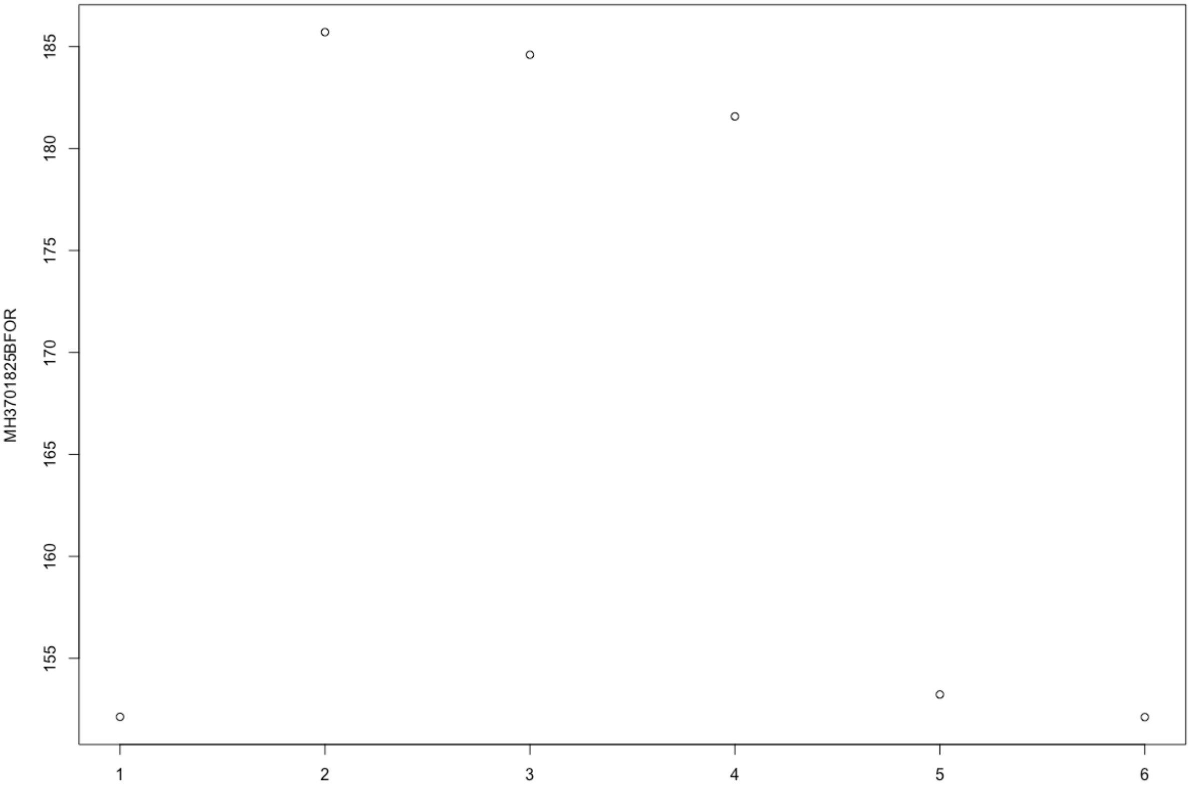

Figure 7. 18:25Z Restart R600 Channel BFO (1st observation) and R1200 Channel (subsequent observations), where a rapidly declining transient bias can be seen to affect the R1200 Channel (2nd-4th observations).

There is evidence for at least two different causes of the transient BFO bias. As reported by Holland (2018), the BFO measurements during the 18:25Z re-start appear to be exhibiting a transient effect which is believed to be due to instabilities in the AES terminal's oven-controlled crystal oscillator (OCXO) output prior to reaching normal operating temperature. This is apparent in Figure 7, where a bias of almost 30Hz can be observed in a series of six observations earlier in the sequence, which subsequently declines (a 273Hz outlier has been removed from this sequence).

After this 18:25-18:28Z log-on sequence, all of the hourly log-on/log-off responses from the AES terminal between 1941Z and 0011Z were transmitted on the R1200-0-36ED channel, which is known from the 18:25Z log-on sequence to be susceptible to the ephemeral bias. Under the assumption that the transient in that case is solely due to OCXO effects, this is not of concern, at least not until the restart prior to the 00:19Z log-on sequence. However, these ephemeral biases can be observed elsewhere in the data where OCXO instability associated with a restart is not necessarily the cause.

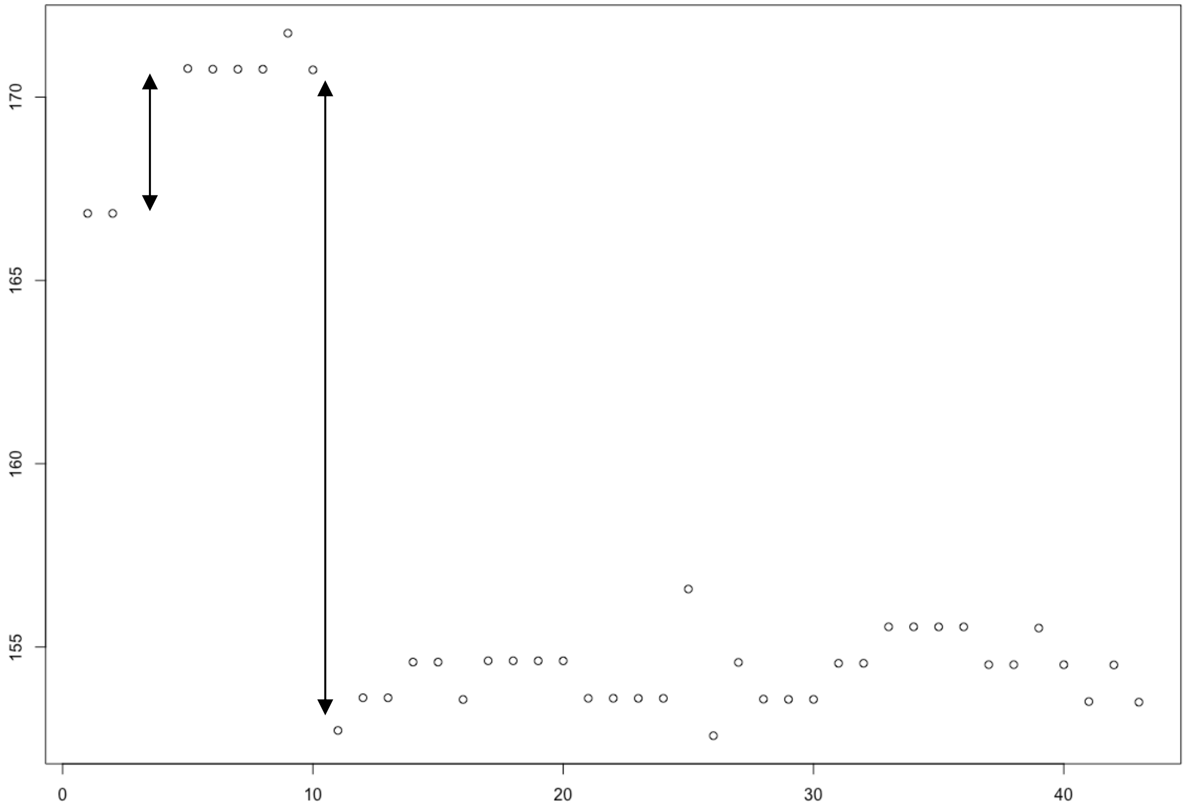

Figure 8. 16:00Z R600-36F8 (1st 2 observations) and R1200-36D3 with transient bias initially present (2nd-6th observations).

For example, the R-1200 data observed at approximately 16:00Z while the MH370 flight was static at gate C1 at KLIA exhibits a transient bias as shown in Figure 8. Although this was a log-on sequence, the AES was in fact switching between the POR and IOR satellites and had been communicating almost continuously with the POR satellite for 17 minutes (15:42-15:59Z) prior to the IOR log-on; with only one second elapsed between the POR and IOR transmissions, a restart and associated OCXO instability being the cause of the ephemeral bias at this time is not likely. The first two observations in the sequence are on an R-600 channel, and the first, small arrow in the chart shows the offset between that channel and the R-1200 sequence of 6 observations which follow.

Previous studies have indicated that the BFO bias has channel dependent effects; Exner (2017) reports variation between -3.56 and +4.18 Hz across seven different channel units and types, while SK999 (2016) measures variation between -4 and +16 Hz across eleven different channels, therefore estimation specific to the channel of interest is necessary (in this case the R1200-0-36ED channel used for most of the transmissions which define the BTO arcs, and where the difference in the chart above to the R-600 channel is approximately 4.1Hz).

The second, longer arrow in Figure 8 indicates the magnitude of the transient bias on the R-1200 channel, of approximately 17Hz, which in this case appears to have rapidly decayed to zero in the nine second gap from 16:00:23Z to 16:00:32Z which elapsed between the biased group of six observations at the top of the chart and the start of the (unbiased) sequence which followed.

A notable difference between the 16:00Z case above, where the transient bias appears to be affecting both the R-600 and R-1200 channels at this time, and the 18:25Z log-on sequence is that, on visual inspection, in the latter case the transient bias does not appear to affect the R-600 channel. This difference in characteristic may support the hypothesis that there are potentially different causes for the transient bias, although if the 18:25Z bias was due to instability in the OCXO while the 16:00Z was not, we might intuitively expect the converse of what is actually observed here.

Davey et al (2015) also observe an ephemeral bias of ~20Hz several hours into a flight from Mumbai to Kuala Lumpur in the 9M-MRO aircraft, which when the time of occurrence of the transient is overlaid on the approximate route of flight as shown in the chart below, appears to occur in the same approximate vicinity as the 18:25Z re-start, viz. around the northern tip of Sumatra.

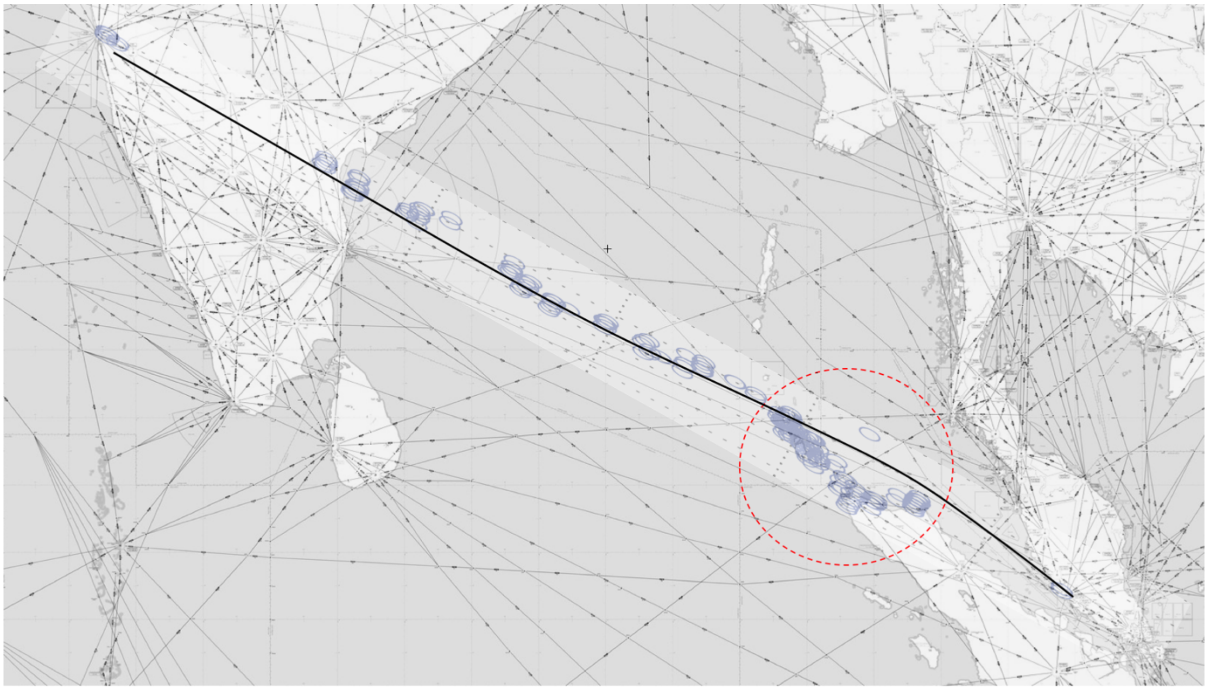

Figure 9. Kuala Lumpur to Amsterdam route with approximate location of transient BFO bias excursion overlaid (Adapted from Davey et al, 2015, Background Skyvector, 2018).

Davey et. al. (2015) also note that the transient has a ‘geographic dependency’ (p.28), thus it is not entirely clear whether there are two independent causes of the transient, namely one due to OCXO warm-up and another of unknown cause, which by coincidence occurred in the same approximate geographic vicinity, or whether these transients were caused by the same effect.

The treatment of the biases during the startup sequences and subsequent inferences made upon them has an important impact on the width of the defined search zones. In the case of both the 18:25Z and 00:19Z restarts, the first transmission was made via an R600 channel (R600-0-36E1 in the first case and R600-0-36F8 in the latter case), followed by transmissions on an R1200 channel (R1200-0-36ED and R1200-0-36F6 respectively), where only a single transmission was made in the latter case, for a total of two transmissions during the 00:19Z sequence (one on the R600 and one on the R1200 channel). Holland (2018) discards the R600-0-36E1 observation during the 18:25Z restart on the assertion that it is unreliable due to a non-zero bit error rate (BER), an unusually low C/No and what is stated to be an unusually low received power level, while for the 00:19Z data a range of 17Hz to 136Hz is subtracted from the raw R600-0-36F8 BFO observation of 182Hz, to account for the effect on that channel of a postulated warm-up drift in the terminal's oven controlled crystal oscillator (OCXO), and assuming that the postulated effect is present in the R600 observation, leading to a conclusion of a rate of descent of between 3,900 and 14,800 feet per minute.

This conclusion, in combination with simulations of the descent profile under the assumption of no human intervention, led to a narrowing of the search distance orthogonally to the 7th arc to 25NM, at one point in time to 12.5NM, an area which also includes an allowance for the uncertainty in the location of the arc itself, due to the noise in the BTO measurements.

Further analysis of the R600 channel observations and associated testing of some of these assumptions is addressed in RQ1(b) of the present study.

Received Power Observations and AES Antenna Gain Characteristics

The Inmarsat network log files which provide the BTO and BFO observations also contain the recorded received signal power at the GES in decibel milliwatts (dBm) and the combined received carrier-to-noise density ratio or C/No (combined in the sense that it is the combination of the uplink AES-SC C/No and the downlink SC-GES C/No). These received power levels and carrier-to-noise ratios are a function of a number of variables including the transmitted power from the AES, the gain of the AES antenna in the direction of the satellite, the aircraft-spacecraft and spacecraft-GES distances, the frequencies being used, the gain and G/T of the satellite, the satellite amplification characteristics, the gain and G/T of the GES antenna being used, amplification and processing in the GES receive chain, atmospheric losses, interference effects, and other noise and loss parameters (Roddy, 1989).

In theory, these parameters can be estimated in a physical model, however there may be little opportunity in the MH370 case to model the link in such a way as to provide any useful information about location, heading or orientation of the aircraft; even a large distance between different potential locations of the aircraft is a very small percentage of the total path length of the return signal, such that the sensitivity of the path loss to significant changes position is very small and likely undetectable within the underlying noise in the link.

The performance of phased array antennas across the relevant field of view and in normal operating attitudes is generally very good, creating little opportunity for detection of heading or orientation, perhaps with the exception of one characteristic of the specific antenna used on the 9M-MRO aircraft, which is explored in further detail below.

It is worth noting that the satellite communications link can be interrupted by (highly) unusual attitudes. To illustrate this point with the extreme case, an aircraft which is inverted may lose the satellite communications link completely (BEA, 2011), while one in a highly unusual attitude may see significant degradation of the link as measured by the received power and C/No under certain circumstances (BEA, 2011). It has been suggested (Ulich, 2018) that the absence of an IFE log on at 00:21Z could be due not to fuel exhaustion of the APU at that time, but to the aircraft entering such an attitude.

Of particular note in regard to the 9M-MRO aircraft is the specific type of AES antenna configuration (Malaysian Government, 2018; Westfeldt & Konrad, 1992; Ball Aerospace, 2017). Although the dominant design (Anderson & Tushman, 1990) for aeronautical satellite high gain antennas has proven to be the single, top mounted configuration, alternative designs are in service on both commercial and military aircraft (Ball Aerospace, 2017).

The 9M-MRO aircraft was equipped with the less common configuration of a pair of side-mounted high gain conformal phased array antennas, with one mounted on each side of the airframe above the #3 exit door at approximately 45 degrees to the horizontal, combined with a single, top-mounted low gain antenna. The AES system can switch between the LGA and either of the HGA elements and, as evidenced from the decoded LIDU information, frequently did so during the 24-hour period of the satellite communications data file, however it exclusively used the HGA antenna after takeoff of flight MH370 at 16:42Z.

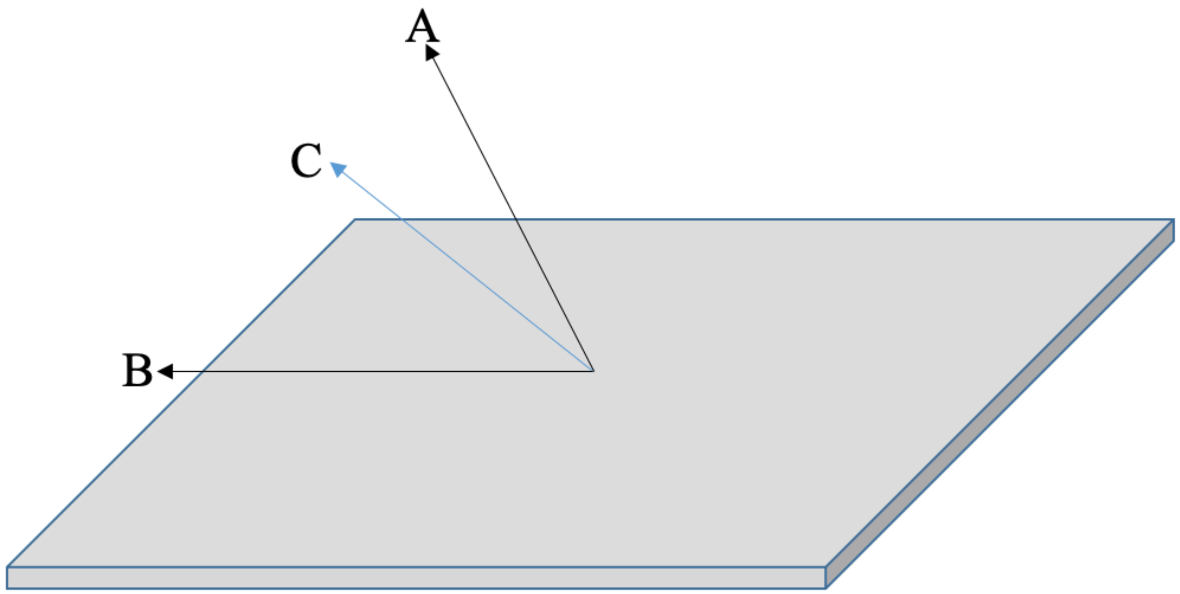

Figure 10. Conceptual illustration of a phased array antenna mounted at an angle to the horizontal.

In the side-mounted configuration, the gain pattern of the antenna when viewed in aircraft coordinates – i.e. with the north-south axis aligned along the longitudinal or roll axis of the aircraft and the other orthogonal axes aligned with the aircraft pitch and yaw axes – exhibits significant variation, especially toward the nose and tail of the aircraft. With reference to Figure 10, the gain performance of the antenna is at a peak when the line of sight to the satellite is orthogonal to the horizontal plane of the antenna, toward the point marked A. The beam can be steered electronically down a point where it is almost aligned with that plane, an example is shown toward the point marked B, however the gain performance is reduced. The beam can be steered in both dimensions to any arbitrary point in the hemisphere, for example to the point marked C, for which the gain can be estimated with reference to results measured in a test environment.

As a result of this variation, the 25.5dBW EIRP contours (assuming an HPA output of 16dBW, losses of 2.7dB and gain of just over 12dB on that contour) do not cover the entire hemisphere as viewed in aircraft coordinates (Westfeldt & Konrad, 1992). Considering a 360 degree sphere centered at the centroid of the airframe, of which Figure 11 shows the upper hemisphere viewed from above, this HGA configuration achieves a gain of 12 dBic or greater at the horizon between the directions of approximately 55 to 120 degrees and 235 to 300 degrees in aircraft co-ordinates; i.e. over less than half of all possible directions at the horizon – however the percentage of the total area of the hemisphere of coverage at 12dBic or greater is more than half.

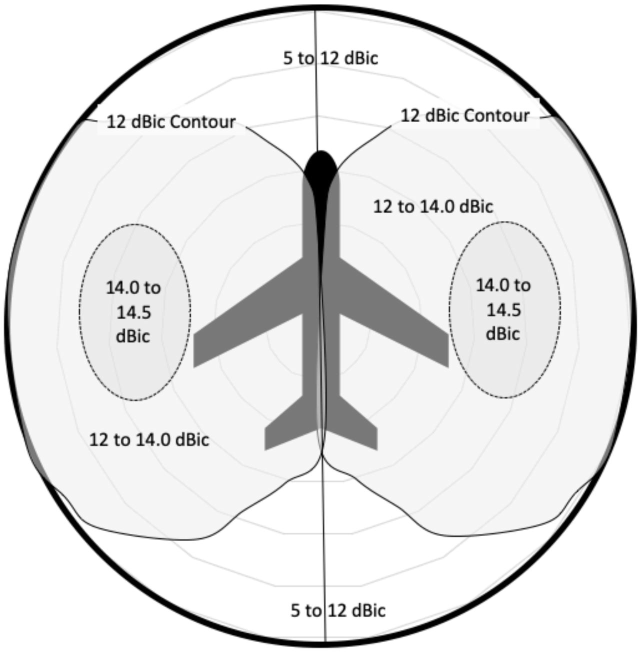

Figure 11: Indicative side-mounted predictable antenna gain variation (5 to 14.5 dBic) as a function of azimuth and elevation in aircraft coordinates.

The ARINC 741 standard (ARINC, 1988) requires the antenna to achieve a minimum of 12 dB gain over at least 75% of the area of a defined hemisphere, to which standard this antenna conforms.

With reference to the peak gain pattern of the electronically steered beam, over a 180 degree scan the peak gain pattern varies from 14.5dB in the boresight of the main lobe of the beam, as would be seen if the satellite were at 90 degrees horizontally to the longitudinal axis of the aircraft and at an elevation of 45 degrees to the horizon, assuming straight-and-level flight, to 5dB when the beam is steered to the 90 degree extremes (Westfeldt & Konrad, 1992, Fig. 8).

The latter case (5dB) would be seen, for example, if the satellite were at 90 degrees horizontally to the aircraft longitudinal axis, close to the earth's horizon, while at the same time the aircraft was banking at around 40 degrees, or if the aircraft heading was within approximately 20 degrees of the direction to the satellite (or from it in the case of the reverse direction) and the elevation angle of the satellite was close to the earth's horizon, or if it was above the horizon and the aircraft has a significant positive pitch angle (or negative pitch angle in the reverse case).

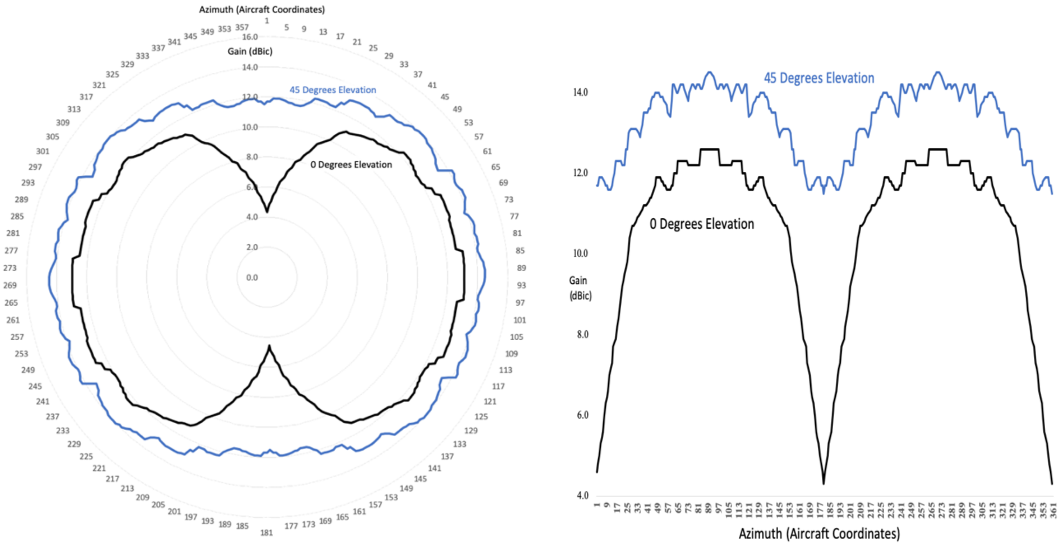

Figure 12. Gain variation from 5 to 14.5 dBic as a function of azimuth in aircraft coordinates, shown at zero degrees elevation (black lines) and 45 degrees elevation (blue lines)

Between these extremes, predictable variations in EIRP due to changes in gain from 10 to14.5 dBic would be expected to occur in less extreme attitudes and orientations, which raises the question of whether these known peak gain variations could be isolated from other sources of variation in the observed received power levels in order to make coarse inferences about aircraft heading or attitude, particularly at some critical junctures of the flight, a question which is further explored within RQ-2 of this study.

Geospatial Estimates of Impact Location and Search Areas

The ATSB (2014) initially defined three underwater search areas of successively greater area, (a) a priority area between 27.4S and 32.1S along the 7th arc, with an orthogonal distance from the arc of +30NM and -20NM, where the positive sign indicates a greater distance from the sub-satellite position, (b) a medium area, 24.4S to 34.7S on the 7th arc, +60/-30NM orthogonally, and (c) a wide are of 16.4S to 39S on the 7th arc, +/- 100NM orthogonally. These regions cover 60,450km^2, 240,000km^2 and 1,120,000km^2 respectively. Later in 2014, Ashton et al. (2014) offered a point solution at 34.7S, 93.0E (on the 7th arc), which corresponds to the southerly extent of the medium area as defined in ATSB (2014), and noting a significant uncertainty in the estimate.

The Independent Group (Anderson et al., 2014) raised a number of questions relating to the results contained in ATSB (2014) and subsequently the group proposed a most probable end point on the 7th arc at 37.71S, 88.75E (Anderson et al. 2014), while Spinor (2014) estimated 38.65S 88.29E. Pleter, Constantinescu and Jakab (2015) identified trajectories terminating on the arc between approximately 25S and 40S, with a preference for the more southerly location where a rectangular search area is proposed, aligned with the 7th arc between approximately 37S and 40S. Yap (2015) finds a constant azimuth track which corresponds to the minimum root mean square (RMS) error of the BFO measurement, terminating on the 7th arc at 37.5S, 89E, however noting that the sensitivity of the BFO residuals to changes in track and position on the arc is such that the uncertainty around the solution extends three degrees of longitude up and down the 7th arc, to between 34.5S and 40.5S. Ulich (2014) found a solution for a 2,200km^2 search area in the vicinity of 40.24S, 83.53E, while GlobusMax (2015) proposed a solution at 40.174S 84.695E based on a waypoint hypothesis.

The ATSB (2015) defined a p=0.90 search area extending from approximately 36S to 39.5S along the 7th arc, with distances orthogonal to the arc of +/- 20NM as a highest priority and +/- 40NM as a secondary priority. This revised area was partially covered by the wide area defined in ATSB (2014), while the previously defined priority area and medium area are entirely outside of these updated priority area definitions, representing a major shift in the priority search area. The ATSB (2017) reports that the underwater search covered an area of 75,000km^2 between 32.8S and 39.5S along the 7th arc by the end of November, 2015, with a further 45,000km^2 between 36.1S and 39.5S searched from then until the end of the ATSB-led search in January, 2017, chosen to cover the probability density function derived by Davey et al. (2015), reported to be at the p=0.85-0.90 level. The inclusion of drift model analysis performed on discovered debris was incorporated into the search area definition but did not change the geospatial parameters substantially (Davey et al., 2015).

A first principles review was conducted by the ATSB (2016) which expressed a high degree of confidence in the previously defined search area, and also noted that the confidence level of detection within the searched area was p=0.95; that is, a probability of detecting the ocean floor debris if it was covered within the survey area. It was also noted that the CSIRO drift analysis, combined with the most advanced analysis of the satellite communications data at that time, identified a high probability area between 32.5S and 36S along the 7th arc and, based on analysis of the possible descent profile after fuel exhaustion, the orthogonal distance from the arc for the remaining search area was reduced to 25NM east and west of the arc. This essentially moved the remaining search area entirely north of, and thus outside of, the p=0.90 region identified in ATSB (2015), partially overlapping the medium search area identified in ATSB (2014) but still remaining entirely south of the primary area in ATSB (2014).

Ianello and Godfrey (2016) propose a flight path which ends at 26.9S on the 7th arc, which assumed flight toward a waypoint at McMurdo station in Antarctica (which as the authors note, may not have been in the database available to the Flight Management System on this particular aircraft). Ianello and Guillaume (2016) assess the terminal location of 26.9S 100.6E alongside flight path data recovered from a crew member's personal flight simulator (Malaysian Government, 2018). Workman (2017), finds that the region of 26S on the 7th arc is an indicated terminus, using a geometric algebra approach.

SK999 (2016) finds solutions ending between 21.9S and 37.4S on the 7th arc, noting that the BFO residuals are lowest in the 30S-34S region. Ianello (2017) finds a BFO best fit at 34S, within a range of 29.3S-38.5S and also identifies a range of great circle paths which would pass the 7th arc between 22S and 40S, noting the relationship between one which intersects the arc at 28.3S and potential debris identified in aerial photography taken during the air search (Ianello, 2017). Godfrey (2017) find solutions between 29S and 31S on the 7th arc using a drift model for the debris, with a point solution at the mid-point of 30S. Chillit (2017) estimates a terminus at 24.598S 101.646E, while Gilbert (2017) finds two solutions for the end point, 30.72S 97.67E and 33.64S 94.36E, with a preference for the latter and defining a 15,750km^2 search area within a 50km vicinity of these locations.

At the southerly extreme, Smithson (2016) proposes end points in the vicinity of 44-46S, 89-90E, although noting that the trajectories used fit neither the observed BTO data nor the available radar data. At the northerly extreme, Marchand, Gasser, Delarche and Garot (2018) demonstrate a trajectory which does fit the initial radar data and BTO measurements, reaching fuel exhaustion on the 7th arc at 12S; in their model, a deliberate actor is exploiting knowledge of the FIR boundaries and radar coverage in the region to avoid detection. Kristensen (2018) finds two solutions, one in the vicinity of 13S and the other near 35S. Nederland (2017) also assumes maneuvers relating to Indonesian radar coverage and airspace, finding a terminus on the 7th arc at 31.1S 97.2E.

Ulich (2018) finds a 7th arc crossing point at 31.6S based on a 181.2 degree constant magnetic track assumption and provides a summary of nine other independent estimates using satellite data and aircraft performance data, ranging from 11.8S to 39S, although presenting a case that locations north of 25N are not likely (Ulich, 2018). Conversely, Ianello (2018) finds a solution north of 25S, at 21.97S 103.57E which conforms to aircraft performance and satellite observational data. GlobusMax (2018) estimates residual probabilities for the aircraft location incorporating the areas searched up until January 2018 together with drift analysis, satellite communications data and aircraft performance data. The residual areas are located between 18S and 40S, with peaks at 30S (p=0.34), 33S-36S (p=0.31), and lower probability estimates for the area between 18S-25S (p=0.14), 26S-29S (p=0.03) and at 40S (p=0.03).

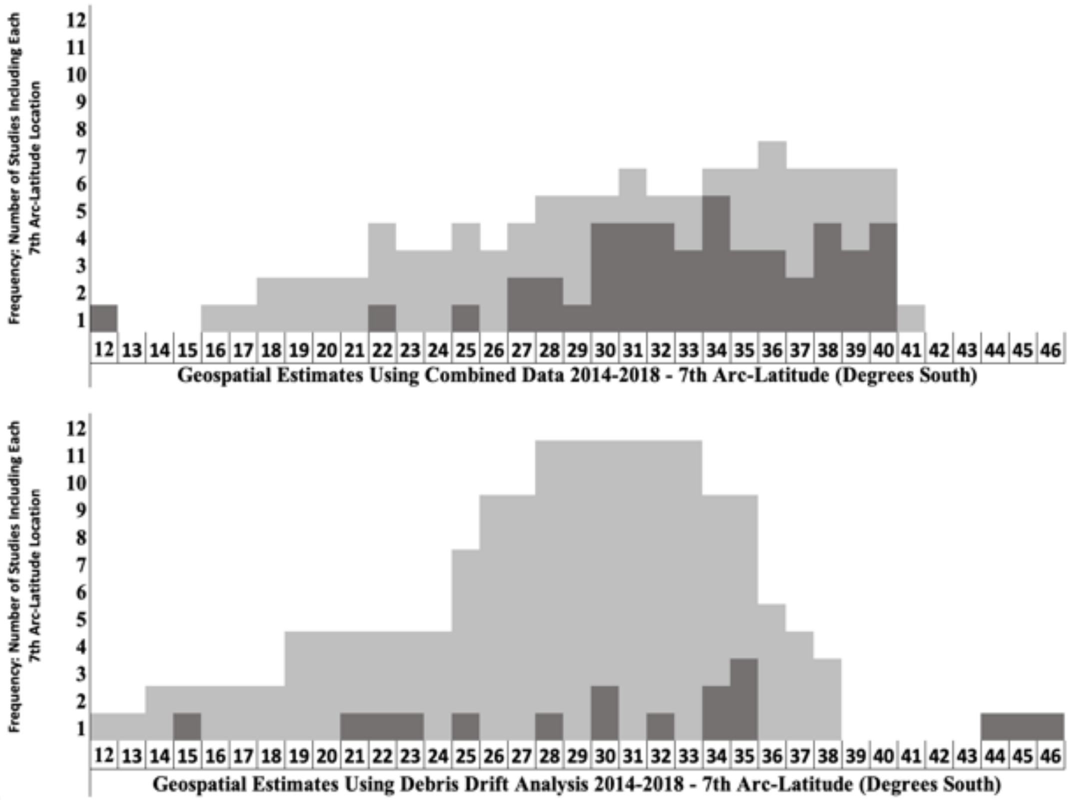

Figure 13. Estimates on 7th arc, combined (upper panel) & drift analysis (lower panel).

In summary, there is a very broad distribution of geospatial estimates along the 7th arc, ranging from 12S to 46S, a distance of well over 2,000 nautical miles. Figure 13 shows the distribution of estimates along the arc, where the frequency counts the number of studies which include each degree of 7th arc-latitude and the darker shading represents areas of higher confidence expressed in any given study. The upper panel includes studies which make use of multiple sources of data, including the satellite communications measurements, aircraft performance models, primary radar data, and in some cases drift analysis, referred to in the figures as combined estimates. The lower panel includes studies which primarily or solely use ocean drift analysis on debris, either that located on shores far to the west of the 7th arc, or on potential objects of interest identified in satellite imagery or aerial photography, referred to in the figures as drift analysis. It can be seen that the distribution of drift estimates is displaced slightly to the north of the combined estimates. Ulich (2018n) provides a summary of ten studies which include geospatial estimates of the source location of debris based on ocean drift modeling and analysis, which range from 12S to 38S in the vicinity of the 7th arc (Pattiaratchi & Wijeratne, 2016; Rydberg, 2015; Daniel, 2016; Jansen et al., 2016; Durgadoo et al., 2016; Trinanes et al., 2016; Griffin, Oke & Jones, 2016, Godfrey, 2017; Nesterov, 2017; Godfrey, 2018; Griffin & Oke, 2017;2018). In addition, Miron, Beron-Vera, Olascoaga and Koltai (2019) estimate an origin of 25S on the 7th arc and a 95% region of 17S-33S.

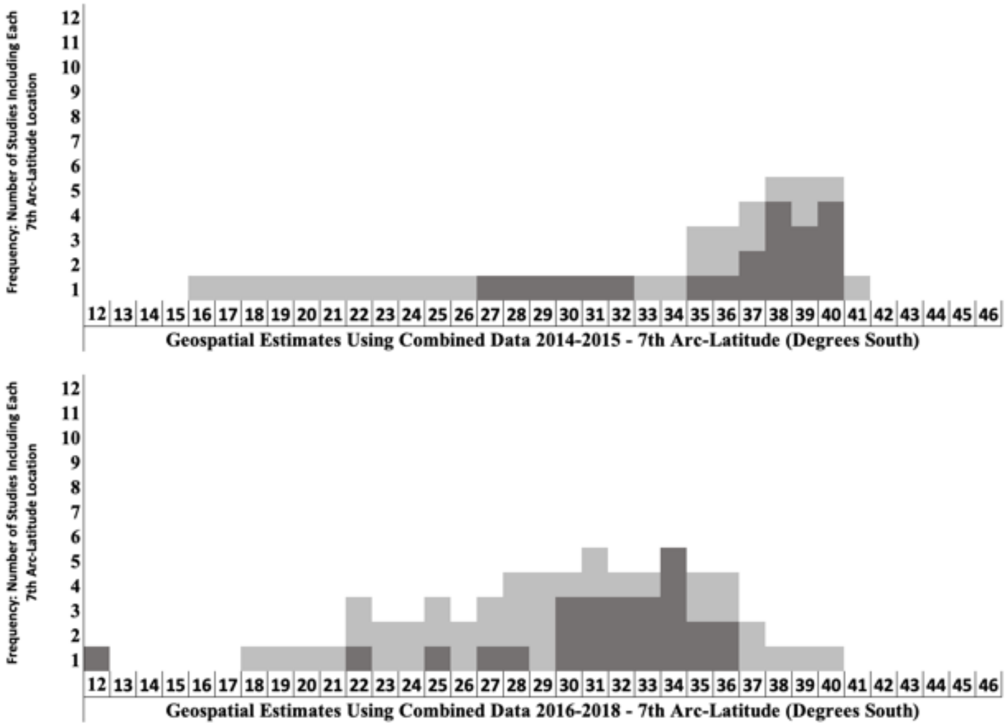

Figure 14: Combined estimates on 7th Arc, 2014-2015 (upper), 2016-2018 (lower).

There is also an apparent shift in the combined estimates over time, as can be observed in Figure 14, which splits combined estimates published during the period 2014-2015 in the upper panel from those published in 2016-2018 in the lower panel, where the density of estimates appears to move north along the arc in the latter period. New information, including the availability of drift analysis on debris discovered during 2015, refined analysis of the available satellite communications and aircraft performance data, and the unsuccessful search results in the more southerly region, may all have contributed to this apparent shift. Further analysis of this broad distribution is the subject of research question RQ-1 for this study.

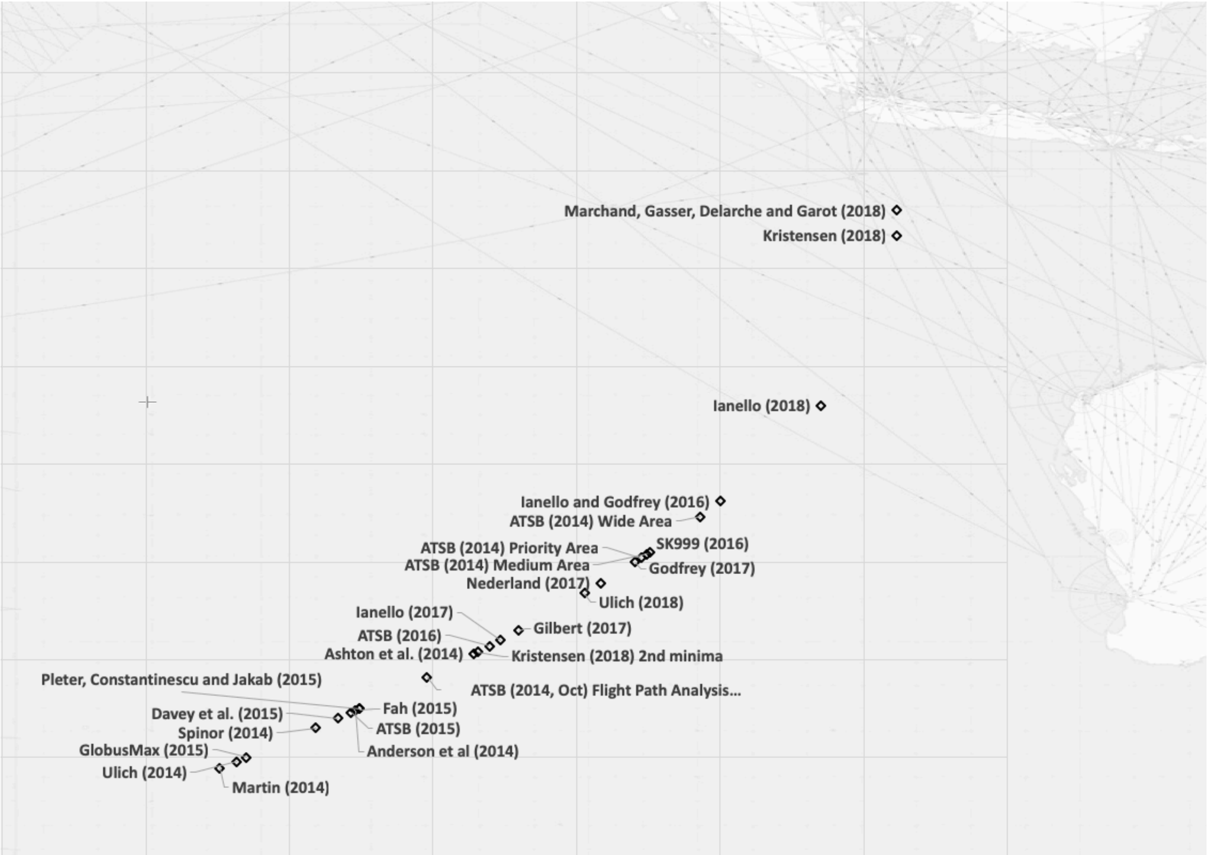

Figure 15: Indicative geographical context for selected estimates on the 7th Arc, 2014-2018 (Background image Skyvector, 2018).

Key Assumptions in Geospatial Estimates

The definition of the search areas during the period 2015-2017 was largely informed by the work of Davey et al. (2015), in which the Mach number for the aircraft was constrained to the range M0.73-M0.84 and the end of flight scenario was assumed to be one of no human intervention or control of the flight. The former assumption, in common with the assumed range of fuel states at the time of the final radar return at 18:22Z, affects the area of the 7th arc where the resulting probability density function will select end points, while the latter assumption significantly affects the orthogonal dimensions of the search area relative to the 7th arc; 25NM versus 100NM.

If either or both of these assumptions were incorrect, this could be one explanation as to why the aircraft remains were not located in the high probability search area informed by the posterior probability density derived by Davey et al. (2015). It should be noted, however, that there are other factors which could explain this, for example if the wreckage was located in this high probability area but was not detected by the search, or if other, more implicit assumptions proved to be incorrect.

For example, the bias terms defined in both the BTO and BFO functional models were estimated during the time on the ground, however the MSS airborne terminal rebooted twice during the flight and prior to the 7th arc; if the bias terms had changed, then the BTO and BFO calculations would contain an unknown bias. Or, as another example, the validation flights used in Davey et al. (2015) were all contained within the northern hemisphere, while much of the flight of interest was south of the equator. While there is no immediate reason to suspect a difference between the two, it was found in the case of the automatic frequency compensation in the Perth GES that the software was not designed to receive a negative latitude, which resulted in an unexpected result (Ashton et al., 2015); any other unknown hemisphere-related error would not be detected in validation which does not contain flights south of the equator.

Similarly to the phase of flight during partial primary radar contact (17:21Z-18:22Z), there are a large number of potential vertical profiles and velocity profiles for the aircraft during the period from the 1st and 7th BTO arcs (18:25Z-00:19Z), which can be simplified to three scenarios: (a) an approximately constant altitude terminated by a very steep descent after fuel exhaustion, (b) a series of step climbs followed by a managed descent, consistent with normal flight, and (c) a staged descent in anticipation of fuel exhaustion.

The scenario (a) appears to have been the working assumption of the ATSB (2017), where it is assumed that the flight during this period had the characteristics of a hypoxic flight and therefore there is no human control during the cruise portion of this period, nor during the descent, which would have become inevitable at the point of fuel exhaustion. The rapid final descent profile assumption is supported by the results of Holland (2018), where a solution is presented which isolates key components of the final BFO measurements at 00:19Z, namely that component due to the instability of the MSS terminal's Oven Controlled Crystal Oscillator (OCXO) during the warm-up phase immediately after a power cycle of the terminal, and that component due to the descent of the aircraft, in this case found to indicate an abnormally high rate of descent, notwithstanding the inherent ambiguity in a descent versus a turn in the case of the BFO measurements.

The other alternatives (b) and (c) could only be viable if there was human control of the flight during the period 18:22Z to 00:19Z, however the extant literature offers no clear, compelling evidence or reason to accept (a) and entirely reject (b) and (c).

Another way to look at this is as an assessment of scenarios as presented in Figure 16, where the physiological states of either having reasonable capacity or being incapacitated are applied either to all passengers on board, or to all except a small minority.

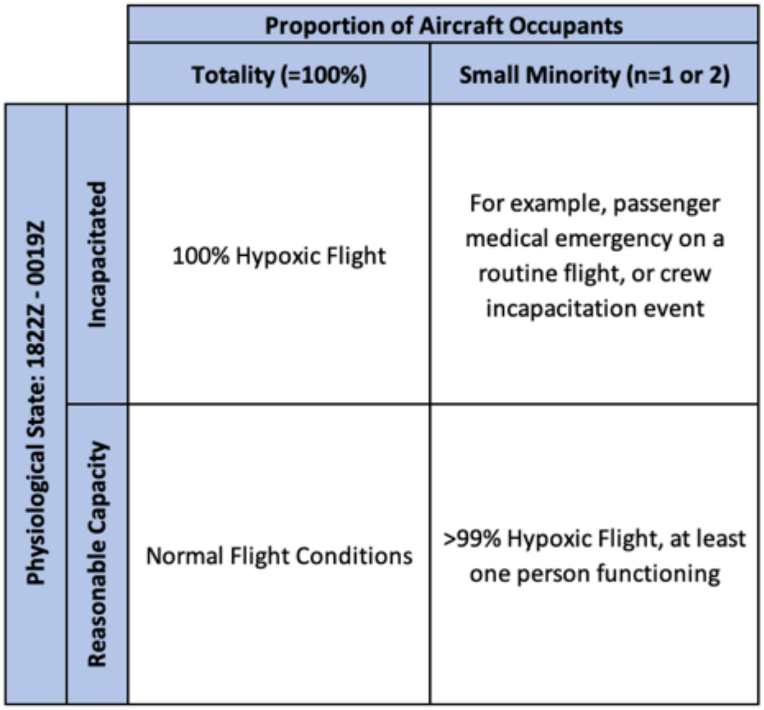

		Proportion of Aircraft Occupants	
		Totality (=100%)	Small Minority (n=1 or 2)
Physiological State: 1822Z - 0019Z	Incapacitated	100% Hypoxic Flight	For example, passenger medical emergency on a routine flight, or crew incapacitation event
	Reasonable Capacity	Normal Flight Conditions	>99% Hypoxic Flight, at least one person functioning

Figure 16. Scenarios for physiological state.

By far the majority of all routine flights operate in the lower left-hand quadrant, where all occupants of the aircraft have reasonable capacity. The next most common occurrence is the upper right-hand quadrant, where a small minority (e.g. 1) of the occupants are incapacitated, most commonly due to an in-flight passenger medical emergency, which occurs on around one in 600 flights (Bellamy, 2015), or much more rarely, an in-flight crew member incapacitation.

There is certainly precedent for the upper left-hand quadrant, where hypoxia and subsequent incapacitation have overcome 100% of the occupants including all crew members, after which flights have continued until fuel exhaustion. Such a scenario has been one working assumption in the MH370 case, an assumption which has an important bearing on both the range of plausible trajectories of the flight after the loss of primary radar contact and on the end of flight trajectory after total fuel exhaustion, which in turn affects the dimensions of the search area orthogonal to the 7th BTO arc.

The unsuccessful underwater search over a vast area of the Southern Indian Ocean raises the question of whether the flight terminated elsewhere on the 7th arc, i.e. entirely outside of the searched area, or if the confined orthogonal dimensions of the search based on the absence of human control at that time served to over-constrain the search area (or both). This gives cause to reconsider the plausibility of the lower right-hand quadrant as a possibility and the question of whether or not it can be categorically excluded as an alternative hypothesis, based on the available evidence.

There is little to no precedent in air transport history for the lower right-hand quadrant, which makes the scenario more difficult to qualify, although that in itself is insufficient grounds upon which to reject it entirely. The plausibility of the scenario described by the lower right-hand quadrant rests somewhat on the question of survivability of such an event for a very small minority of the occupants, assuming access to a sufficient supply of oxygen under pressure, including survival of the physiological effects of prolonged exposure to decompression at high altitude (Auten, Kuhne, Walker & Porter, 2010) and exposure to extremely low temperatures for a sustained period (Tikuisis, 1995).

In this regard, nothing was found in the extant literature in terms of survivability of a decompression event at high altitude and exposure to the prevailing temperature at the time, altitude and location of the initial departure from the flight plan in the vicinity of waypoint IGARI (~ -41 to -42 C) for an hour or more in light clothing, which would provide evidence to exclude it as one of the plausible scenarios. For example, Tikuisis (1995) estimates the survival time at -40C when wearing two layers of 1mm thick clothing to be 5.6 hours. It should be noted that there is no direct evidence for decompression of the aircraft, it is a working hypothesis relevant to both the upper left-hand and lower right-hand quadrants. Although it is beyond the scope of this study to further investigate the plausibility of these scenarios, it is noted that the studies selected for the meta-analysis incorporate diversity of the assumptions in this regard; while many assume no human control after the loss of primary radar contact, others explicitly assume that the manual control observed in the initial turn from the flight plan continues for the duration of the flight.

It should also be noted that examination of a recovered flaperon from the aircraft concluded that it was likely in a retracted position when sheared from its mountings, which is taken as evidence of configuration of the aircraft other than that recommended for ditching (ATSB, 2016). On the other hand, there is a broad continuum between the extremes of a completely uncontrolled descent from cruising altitude at one end and a perfectly executed ocean ditching at the other; indication that the latter extreme did not occur is not necessarily evidence that the former extreme did, the reality could plausibly be somewhere between the two. The nature of a surface debris field would also be expected to be related to the nature of the final descent and the energy of the ocean surface impact. Chen et al (2015) study five modes of water entry from a gliding entry at one extreme to a -90 degree pitch angle nose dive at the other, concluding that the latter is the most likely in part due to the absence of detection of the substantial surface debris field which might be expected for some of the other scenarios. However, García-Garrido, Mancho, Wiggins and Mendoza (2015) point out that the discovery of the flaperon may be cause to change that conclusion. Using a Lagrangian descriptors dynamical systems approach, they suggest that local structures in the ocean surface currents along the 7th arc may have resulted in debris locations outside of the intensive air and surface search areas conducted shortly after the initial loss of the aircraft. Potential debris fields have also been identified in satellite imagery taken in the vicinity, of which perhaps the most salient is that provided by the French government from the PLEIADES 1A satellite. Minchin, Mueller, Lewis, Byrne and Tran (2017) conclude that 70 objects in the images taken over an area ~34-35S 90-91E are likely of non-natural origin, although none of the objects could be positively identified as being from the accident (or any) aircraft. Griffin (2017), considering local currents in the area, suggests that 35.6S 92.8E would be the likely source of such debris if it were in fact from the MH370 aircraft.

Fuel Flow

Flight MH370 departed with a known amount of fuel on board and the 17:07Z ACARS data includes a fuel mass report. Under the assumption that the 00:19Z AES log-on was the result of an automated APU start due to fuel exhaustion in the supply to the last operating main engine, the fuel flow integral $\int_{16:27Z}^{00:15Z} FF\,dt$ is known to reasonable precision, where the time of fuel exhaustion is estimated as 00:15Z +/- 4 minutes. While the integral is known reasonably well, the extent of fuel flow variation during the flight is unknown after 17:21Z and a large number of solutions exist. Some of the meta-analysis studies include fuel flow as a parameter or condition in the model, while others do not. These studies show that fuel flow solutions exist for the most northerly and most southerly estimates, therefore fuel flow alone cannot resolve the ambiguity of these different end zones, but nonetheless is an important parameter. Fuel flow uncertainty exists during both the period after 18:25Z and during the primary radar phase of the flight, where the difference between a constant altitude profile and one with a climb, descent and climb could equate to a difference of 45 minutes or more of normal cruising time, or a substantial difference in range for a fixed flight time.

CHAPTER III

METHODOLGY

The underlying conceptual and theoretical framework for this study is that of General Systems Theory (von Bertalanffy, 1968;1972; Lin, 1999), where the case is considered in the conceptual context of a supra-system (Mele, Pels and Polese, 2010) consisting of two interacting sub-systems: that of the physical system and that of the human system, as illustrated in the figure below.

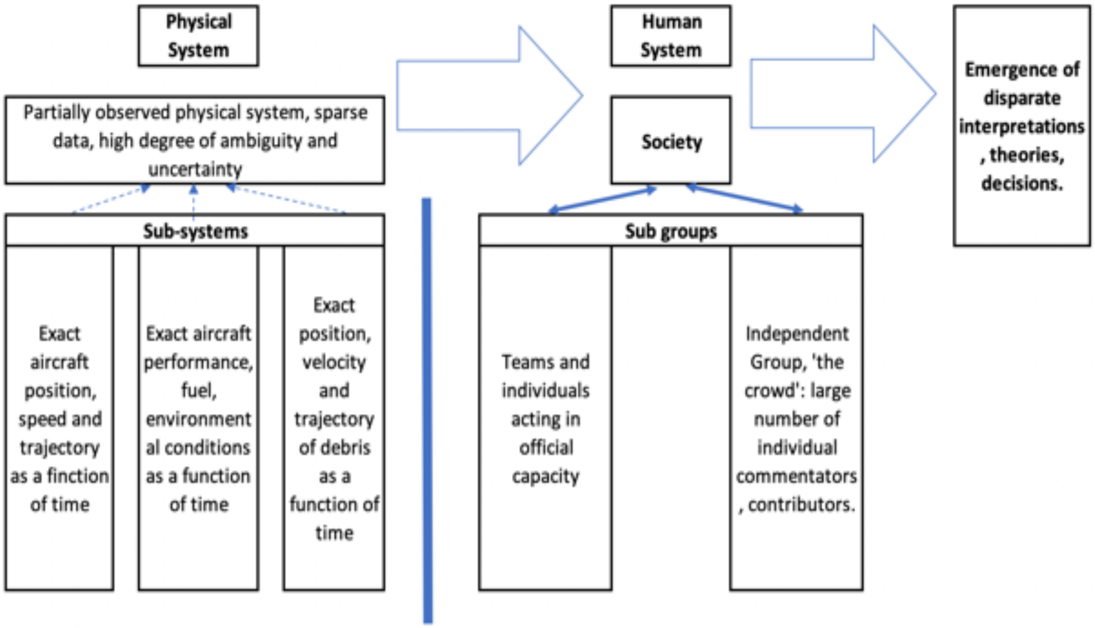

Figure 17. MH370 Case Supra-System

The physical system consists of the aspects of the case which are governed by the laws of physics, including all spatio-temporal variables relating to the aircraft, spacecraft, satellite ground system, and the oceanic area of interest, including their relevant and respective system dynamics. Quantitative information relating to the physical system has been gained by means of measurements and observations of various parameters together with their concomitant uncertainty, bounded by known performance characteristics based on prior knowledge and analysis.

The human system interacts with the physical system; this is where evaluation and inference are made based on the available information and its analysis, where assumptions are made and where opinions are formed, and where decisions are made based on the combination of the available information, outputs from the physical system, expert opinion, and consensus forming.

From an epistemological perspective, this is consistent with a post-positivist approach (Cook, 1985), assuming that an external reality or truth exists in the physical system, however recognizing that the interpretation of data from the physical system takes place in the human system. From a positivist viewpoint, it is for example in this study assumed that a true physical trajectory for the aircraft exists, consisting of a continuous-time actual state vector for the duration of the flight, an exact end of flight trajectory from the top of descent, to a specific point in space and time where impact with the ocean occurred, followed by a sub-surface descent trajectory from the ocean surface to the ocean floor and concluding with a true set of coordinates which exist for the actual location of components of the aircraft, including the flight recorders. This final location of the flight recorders $\widehat{\theta_F}$ consists of a latitude, longitude and depth: $\widehat{\theta_F} = \{\widehat{\lambda_F}, \ \widehat{\phi_F}, \ \widehat{d_F}\}$, where $\widehat{\theta_F}$ is related to the point (latitude, longitude and geometric height) of crossing the 7th BTO arc, $\widehat{\theta_7} = \{\widehat{\lambda_7}, \ \widehat{\phi_7}, \ \widehat{h_7}\}$, by the integral of the rate of change of latitude, longitude and height over the period from the time of crossing the 7th arc (0019Z) to the (unknown) time of impact with the ocean floor:

$$\widehat{\theta_F} = \widehat{\theta_7} + [\mathit{\Delta}\lambda\ \mathit{\Delta}\phi\ \mathit{\Delta}h]_{0019Z}^{t_{OSI}} + [\mathit{\Delta}\lambda\ \mathit{\Delta}\phi\ \mathit{\Delta}h]_{t_{OSI}}^{t_{OFI}}$$

The values of these true states are unknown at the time of writing, however they are the external truth which is assumed to exist, which is assumed to be deterministic despite the presence of high uncertainty in the partially observed variables, and which spatial models used in the case are ultimately attempting to model and estimate.

In consideration of the human sub-system, the interpretation of pieces of information gained from the physical system which are ambiguous, incomplete or partially observed and lacking the overdetermined condition normally required to provide high reliability in spatial estimates, can be seen as a constructivist activity where choices of assumptions and formulation of a view of the likely outcomes takes place based on the construction of potential realities based on human judgements about the data, events, and their interpretation.

Thus, the human sub-system is a potential contributor to heterogeneity in the derived geospatial estimates from the studies included in the meta-analysis, just as is the statistical uncertainty surrounding the measurements made in the physical model.

Adherence to Principles of Ethical Conduct / IRB Compliance

All normal and generally accepted principles of ethical conduct in research were adhered to in the course of this study. The research proposal was approved by the Institutional Review Board (IRB) of the Oklahoma State University, under application number ED-19-6, as non-human subjects research. The study employed quantitative methods, using data available in the public domain and did not incorporate human subjects research. No commercial funding or commercial interests were involved with the study.

Research Questions

Table 3

Studies Selected for Meta-Analysis

		7th Arc-Latitude Range	
	Author(s)	Lower Bound (Degrees South)	Upper Bound (Degrees South)
	Satellite Communications Sub-Group of Studies		
1	ATSB (2014) Wide Area	16.4	39.0
2	ATSB (2014) Priority Area	27.4	32.1
3	ATSB (2014) Medium Area	24.4	34.7
4	ATSB (2014, Oct) Flight Path Analysis Update	33.5	38.3
5	Ashton et al. (2014)	34.7	34.7
6	Anderson et al (2014)	37.5	37.7
7	Spinor (2014)	38.5	38.5
8	Ulich (2014)	40.2	40.2
9	Martin (2014)	40.6	40.6
10	Pleter, Constantinescu and Jakab (2015)	38.2	39.9
11	Fah (2015)	34.5	40.5
12	Davey et al. (2015)	34.0	40.0
13	GlobusMax (2015)	40.0	40.0
14	ATSB (2015)	36.0	39.3
15	ATSB (2016)	32.5	36.0
16	Ianello and Godfrey (2016)	26.9	26.9
17	SK999 (2016)	22.0	37.0
18	Ianello (2017)	28.0	39.0
19	Godfrey (2017)	29.0	31.0
20	Nederland (2017)	31.0	31.0
21	Gilbert (2017)	31.0	34.0
22	Marchand, Gasser, Delarche and Garot (2018)	12.0	12.0
23	Ulich (2018)	31.6	31.6
24	Ianello (2018)	22.0	22.0
25	Kristensen (2018)	13.3	13.3
26	Kristensen (2018) 2nd minima	34.6	34.6
	Ocean Drift Sub-Group of Studies		
27	Pattiaratchi & Wijeratne (2016)	28	33
28	Rydberg (2015)	12	38
29	Daniel (2016)	25	35
30	Jansen et al. (2016)	28	35
31	Durgadoo et al. (2016)	14	33
32	Trinanes et al. (2016)	26	38
33	Griffin, Oke & Jones (2016)	26	38
34	Godfrey (2017)	19	37
35	Nesterov (2018)	25	35
36	Godfrey (2018)	19	35
37	Griffin & Oke (2018)	25	36
38	Miron et al (2019)	17	33

RQ-1. Meta-Analysis

For the studies identified in Table 5, which provide geospatial estimates of the MH370 trajectory and/or end of flight vicinity:

(a): Is the observed variation in estimated probable impact location for MH370 across these studies due to random variation within the range of uncertainty of the observed data and propagated error, or do the studies exhibit statistical heterogeneity?

(b): To which factors are the arc-latitude estimates most sensitive?

RQ-2. The Spatial Characteristics of Antennas

Can the spatial characteristics of antennas be used to reduce the uncertainty in the estimates?

RQ-3. Effect of GADSS on Future Occurrences

In the absence of an adopted probable cause for the loss of MH370, what is an estimate of the probability of an oceanic hull loss with high spatial uncertainty (>5NM LKP) as a function of time, during the period 2020 to 2030?

Research Hypotheses

Research Question 1, sub-questions (a) and (b)

H-1(a): *For the satellite communications and ocean drift sub-groups:*

$H_{1a\text{-}0}$: There is no statistically significant heterogeneity across the studies.

$H_{1a\text{-}A}$: There is statistically significant heterogeneity across the studies.

H-1(b): *For each regression coefficient (predictor) or set of coefficients:*

$H_{1b\text{-}1\text{-}0}$: The regression coefficient (predictor) is not significantly different to zero (zero slope).

H_{1b-1-A}: The regression coefficient (predictor) is significantly different to zero (zero slope).

For each BFO bias tested for statistical significance in difference across time and across channels:

H_{1b-2-0}: There is no significant different in the bias over time or across channels.

H_{1b-2-A}: There is a significant different in the bias over time or across channels.

Research Question 2

H-2 H_{2-0}: There is no significant difference in the sum of squared residuals for a linear model estimated using BFO data and a fixed gain model and that estimated using both BFO data and the peak gain variation model for the AES antenna.

H_{2-A}: A statistically significant difference is found in the sum of squared residuals for a linear model estimated using BFO data and a fixed gain model and that estimated using both BFO data and the peak gain variation model for the AES antenna

Research Question 3

H-3 H_{3-0}: No statistically significant reduction in the estimated probability of an oceanic hull loss with high spatial uncertainty is forecast during the period 2020-2030 as a result of the GADSS measures.

$H_{3\text{-}A}$: A statistically significant reduction in the estimated probability of an oceanic hull loss with high spatial uncertainty is forecast during the period 2020-2030 as a result of the GADSS measures.

Research Design

The research was conducted as a quantitative analysis of historical data for RQ-1 & 2 and as a forecast and quantitative analysis of simulated future data for RQ-3. The fundamental research design for RQ-1(a) was that of a statistical test for heterogeneity. For RQ-1(b) the research design is that of meta-analysis, specifically meta-regression, sensitivity analysis, and statistical testing for significance on a number of relevant hypotheses. For RQ-2 the quantitative design is that of linear regression, probability density function estimation and subsequent statistical testing for significance. For RQ-3 the research design is that of Monte Carlo simulation based on a Poisson probability mass function and randomized variables.

Data Sources and Selection

All data used in this research is in the public domain. The sources of data used in the quantitative analysis of historical data for RQ-1 and RQ-2 consist of that contained in the studies selected for meta-analysis, published data recorded by the Inmarsat network on the day of the MH370 flight, published data from the measurement of the gain pattern of the HGA antenna, published technical narrative relating to the Inmarsat I3 satellite and ground stations, and environmental data such as wind direction, velocity, and static air temperature at locations and times of interest for the study.

For RQ-3 the sources of data include published data on air transport accidents, published data on global flight hours and oceanic flight hours, and a long-term air transport fleet forecast.

Meta-Analysis Data

The selection criteria for studies to be included in the meta-analysis for this study are that they (a) include an estimate of the end of flight location for the specific MH370 flight, either as a geographical position or as a point of crossing the 7th BTO, making use of the satellite communications measurements, either BTO, BFO or both, or (b) include a geographical position or area in which debris from the MH370 flight is estimated by ocean drift analysis to have originated, either including at least one item of debris positively identified as being from the MH370 aircraft, or using a debris field which plausibly could have contained such an item, (c) in aggregate provided a representative sample of the overall geographical distribution of spatial locations along the 7th arc and broad methodological diversity, and (d) contained sufficient information to extract the variables of interest for the meta regression.

Of forty-two formally and informally published studies initially identified for potential inclusion in the meta-analysis, the twenty-six selected for the satellite communications sub-group and twelve selected for the ocean drift subgroup represent those for which the criteria above were met, while the remaining four studies did not contain sufficient information to meet the specific criteria identified for this particular study, although they each contain important analysis and other useful information.

For each study included in the meta-analysis, $k_{1,\ldots,}k_n$, the estimated parameter $\emptyset_7$ is the arc-latitude at which the aircraft is estimated in that study to have crossed the 7th arc, or for which debris is estimated to have originated in the vicinity of the 7th arc.

A subset of ten of the twenty-six studies selected for the meta-analysis in the satellite communications sub-group included sufficient data to determine five states of the aircraft at the times of crossing each of the BTO arcs as estimated by each researcher, namely the estimated aircraft latitude, longitude, altitude, ground track azimuth and ground track velocity, which facilitated further analysis on this subset as described for RQ-2 later in this chapter.

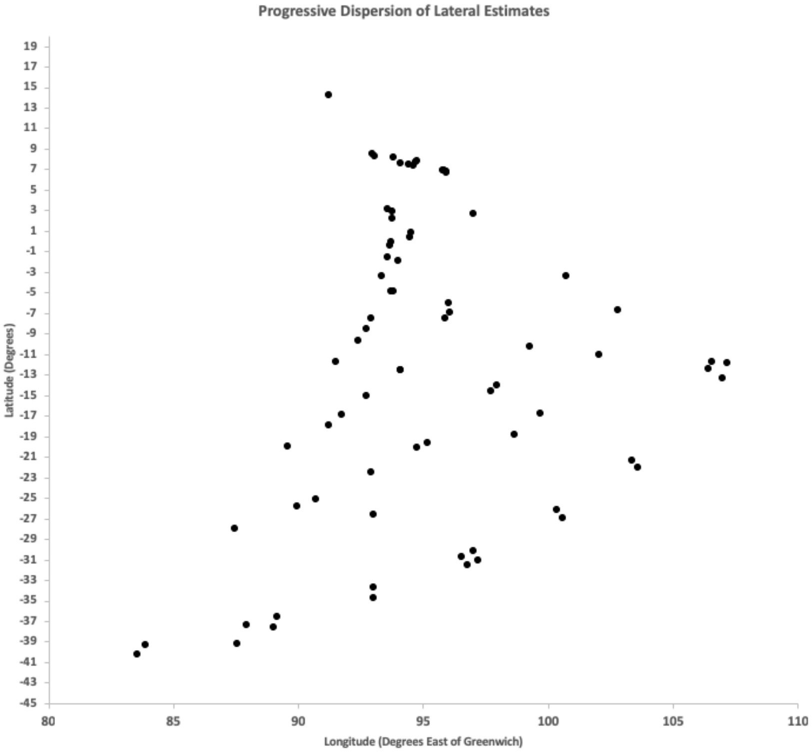

Figure 18. Progressive dispersion of lateral estimates for the subset of 10 of 26 studies in sub-group 1 for which detailed trajectory information was available.

Figure 18 shows the progressive geospatial diffusion of this subset as the flight progresses, while Table 4 shows the states at the time of the single AES log-on/log-off acknowledgement transmission at 00:10:59.928Z via the IOR-R1200-0-36ED channel, i.e. at the point of crossing the 6th BTO arc.

Table 4

Estimated aircraft state at 0011Z, crossing the 6th BTO arc, for the subset of 10 of 26 studies

Author(s)	Estimated End Point *(ordered from North to South)*	6th Arc Latitude	6th Arc Longitude (East)	6th Arc Altitude (ft)	Ground Track Azimuth (True)	Ground Track Velocity (kts)	Reported BFO Calculated (252Hz Observed)
Marchand et al (2018)	12S	-11.674	106.561	5000	0	300	246
Kristensen (2018)	13.3S	-12.440	106.420		147	430	
Ianello (2018)	22S	-21.373	103.336	32000	144.7	354	(-11.85 residual)
Ianello and Godfrey (2016)	26.9S	-26.083	100.360	35000	167.2	484	(+10.87 residual)
Nederland (2017)	31S	-30.164	97.015	28871	170.6	427	248.2
Ulich (2018)	32S	-30.741	96.524	34255	174.8	395	249.3
Ashton et al (2014)	34.7S	-33.700	93.000		180	448	252
Fah (2015)	36.6S	-36.599	89.155	35105	186.7	425	252.3
Pleter et al (2015)	Sol#20 39.2S	-37.340	87.920	41000	188	476	
Ulich (2014)	40.2	-39.258	83.893	15000	193.1	449	258.6

Inmarsat Network Log File

In addition to the data extracted from the studies selected for meta-analysis, the quantitative data includes the log file recorded by the Inmarsat ground network prior to and during the incident flight, which consists of over 7,000 data records during the period of just over 24 hours from midnight UTC on March 7, 2014 to the final AES transmission just after midnight UTC on March 8. This data is in the public domain; fragments of the log file were included in Ashton et al (2014) and in May 2014 a redacted file was released by the Malaysian Government (2014), who in turn had received them from the communications service providers to Malaysian Airlines. In 2017, an unredacted version of the file, which spans an approximately 24 hour period to include the aircraft's previous flight from Beijing to Kuala Lumpur (MH371) as well as the complete incident flight (MH370), was released by the Malaysian Government to one of the relatives of a passenger on MH370 without restriction on further release, who in turn released it to a member of the MH370 Independent

Group, who in turn released it into the public domain (Ianello, 2017; Huffington Post, 2017). The availability of this data has enabled independent researchers to conduct their own analysis and provides opportunities for validation and replication of previous results, including in the context of the present study.

Conversion of Hexadecimal Data and Decoding of LIDUs.

In addition to the ASCII text characters in the log file, from which data such as time, transmission channel, and the observed BTO, BFO, received power and C/No values can be immediately extracted, the log file also contains hexadecimal data which includes the contents of ACARS messages and Link Interface Data Unit (LIDU) network signaling messages which in some cases contain information about the antenna being used by the AES, the transmitted EIRP level, or changes in the AES EIRP level as commanded by the GES (ICAO, 2007). The hexadecimal ACARS data were converted to text, while the SIDUs were decoded with reference to ICAO (2007) and ICAO (1999). For the MH371 flight and MH370 flight up until the final 17:07Z ACARS transmission, the ACARS data provides, inter alia, observations of aircraft position, velocity, heading and environmental parameters such as wind direction, velocity and static air temperature, all at approximately five-minute intervals, which are grouped and transmitted in blocks approximately every thirty minutes.

Sampled AES Antenna Gain Pattern and Peak Gain Variation

To facilitate investigation of RQ-2 of this study, the measured peak gain variation is illustrated in Figure 19, produced from data reported by Westfeldt & Konrad (1992) and digitized at a resolution of 1 degree of θ angle (in antenna coordinates) and 0.2 dB of amplitude. Data provided in Westfeldt & Konrad (1992) shows that the peak gain variation is approximately rotationally symmetrical across 360 degrees of $\emptyset$ angle (in antenna coordinates), based on which the digitized data were replicated at 1 degree ∅ angle increments, to produce a peak gain variation model for 0-360 degrees of ∅ angle and 0-90 degrees of θ angle, in antenna coordinates.

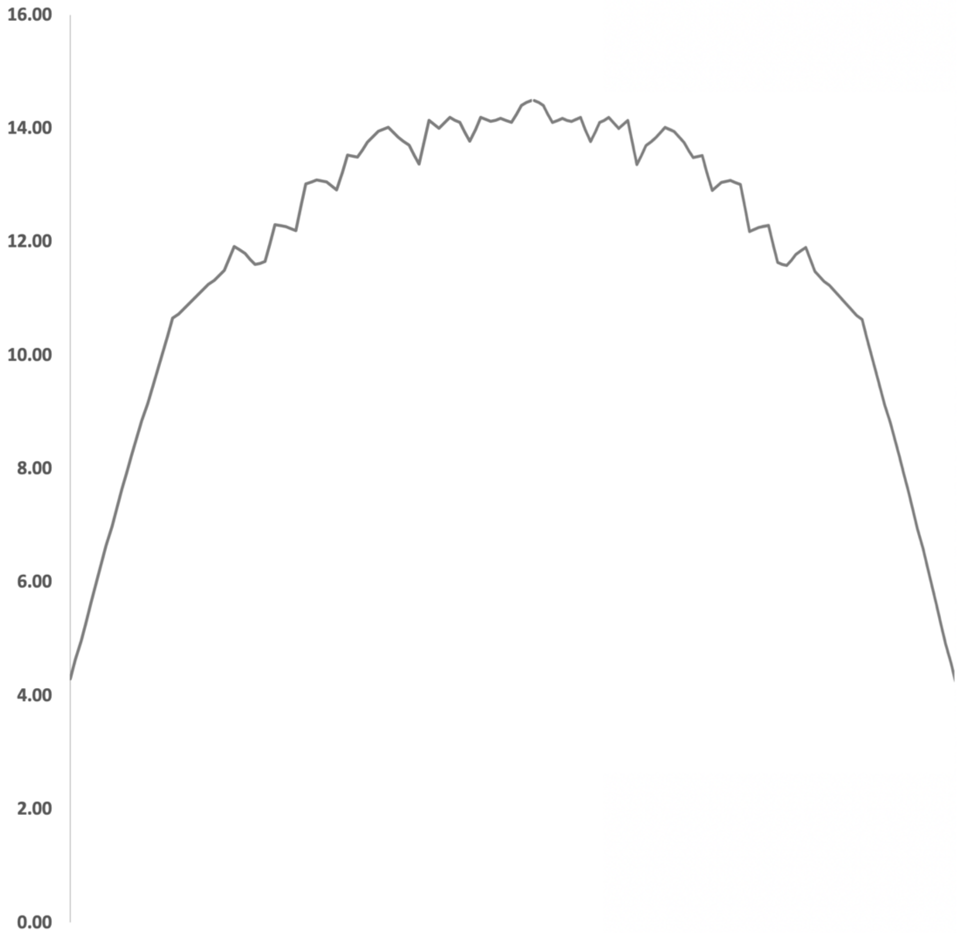

Figure 19. Peak Gain Variation as a Function of θ angle. Adapted from Westfeldt and Konrad (1992)

In order to use the data for inferences regarding aircraft heading, the data were transformed into aircraft coordinates for the port and starboard HGA antenna elements, by means of a rotation in 3D space of the peak gain variation model in antenna coordinates around the long axis of the antenna in the antenna plane, and assuming the nominal 45-degree orientation of the antenna plane to the aircraft's X-Y plane (i.e. the plane formed by the lateral and longitudinal, or roll and pitch, axes of the aircraft).

After rotation, this yielded a pair of matrices, one each for the port and starboard apertures, for which the gain could be extracted for any coordinate pair, defined by a clockwise bearing from the positive longitudinal axis (i.e. nose) of the aircraft and an elevation angle from the aforementioned X-Y plane. For any given aircraft position and time, the 'look' angles to the satellite can be calculated, as an azimuth from true north and an elevation angle to the local geodetic horizon. These look angles can in turn be translated into aircraft coordinates for any given aircraft heading, and assuming level flight for the elevation angle. The a priori standard deviation for G_{AES} values thus extracted was estimated as 0.5dBi (note that this is the estimated digitization error for the gain model, not the standard deviation of the observed data, which was separately estimated as described later in this chapter).

Environmental Parameters

Where wind direction, velocity and temperature were available from the decoded ACARS data, those values were used in the analysis for RQ-1(b) and RQ-2. Where ACARS data were not available, environmental parameters were extracted from Beccario (2018), available at 3-hour intervals for the date of the flight, and typically extracted at the 250 hPa level.

Historical Data: Hull Losses, Oceanic Flight Hours, Air Transport Fleet Forecast.

The total number of air transport category hull loss accidents occurring in oceanic airspace (more than 12 miles or 20km in offshore waters, excludes near-shore accidents) was compiled from the Flight Safety Foundation Aviation Safety Network database (Flight Safety Foundation, 2018).

The Aviation Safety Network database reports n=438 aircraft accidents between 1930 and 2018 in the offshore (>12 miles) regions of the Atlantic, Pacific and Indian Oceans, the

Mediterranean Sea, Antarctica and the North Pole region, or where the location of the loss is unknown. Of these, the subset of n=20 losses between 1980 and 2016 was selected for the study, consisting of commercial air transport (passenger and cargo) aircraft in the air transport category of 19 seats or greater or MTOW in excess of 19,000 lbs and excluding government use aircraft, business and general aviation aircraft, accidents which did not result in complete hull loss, and all incidents prior to 1980.

It is noted that (a) approximately half of the losses in water of transport category aircraft in the 20-year period between 1996-2016 occurred within 12 miles of shore, and thus are not included in this sample and (b) a small number of incidents during the 1980-2016 period which were recorded as occurring over international waters and which resulted in a safe landing without fatalities but where the aircraft was subsequently declared as a hull loss. In both cases, these incidents are not included in the sample, as the scope of interest for this specific study is the rate of hull losses in oceanic regions outside of terrestrial radar surveillance coverage, where the risk of a loss with high spatial uncertainty is high. For other purposes, the probabilities including near-shore losses can be estimated as approximately double those presented herein for offshore losses.

Historical global flight hours data between 1980 and 2018 was obtained from historical reports given in Boeing (2018) and Boeing (2010). The percentage of global flight hours operated in oceanic FIRs was estimated from long-term CANSO reported data (CANSO 2011, 2018).

Baseline data for the long-term air transport fleet forecast used for RQ-3 was extracted from the Boeing Commercial Market Outlook 2018-2038, Boeing (2018) and based on the compound long-term fleet growth estimates provided therein.

Selection of Variables

Significant spatial variation in the estimated 7th arc latitude position is exhibited across the studies in this sub-group. An initial review of these meta-analysis studies revealed differences in assumptions about factors such as when the aircraft turned to the south, how many major turns were executed after that major turn south, and whether the aircraft was flown at an approximately constant altitude and velocity, or whether significant changes occurred in those parameters during the phase of flight after 18:22Z. These initial observations informed the selection of variables as regression coefficients as described in more detail below, with the overall intent of identifying predictor variables which may serve to at least partially explain the very broad spatial dispersion of estimates which are ultimately derived from the same primary data.

The variables identified as potential candidates for the meta regression are shown in Table 5 consisting of (a) the upper bound and lower bound for the 7th arc-latitude location for the study, (b) a stated point location estimate within the range if given, otherwise the mid-point between the upper and lower bounds, (c) the maximum time after 1822Z at which the study assumed the turn south had occurred, (d) the altitude variation present in the constituent trajectories used to derive the upper and lower bounds estimate, (e) the variation in ground track velocity present in the constituent trajectories used to derive the upper and lower bounds estimate and (f) the maximum cumulative change in the true track of the aircraft present in the constituent trajectories used to derive the upper and lower bounds estimate, measured from the assumed track of 296 degrees (true) at the time of the final primary radar contact at 1822Z.

A subtle but significant distinction is drawn between the altitude and velocity range present in the constituent trajectories used for the location estimates, and the altitude and velocity ranges from which those constituent trajectories may have initially been selected. That is, a number of studies selected trajectories from an initially wide range of altitude and velocity possibilities, however the trajectories actually selected to produce the location estimate are a selection from that initial range, for example with a fixed altitude and/or velocity selected from the initial range of possibilities. For the purposes of meta regression and investigation of the sensitivity of the arc-latitude estimates to variation in these parameters, it is the variation of altitude and velocity present in the trajectories actually selected and used for the spatial estimate which is of interest (i.e. the constituent trajectories), as opposed to the range of altitude and velocity possibilities from which those trajectories were originally selected.

Accordingly, a value of zero for the altitude or ground track velocity in Table 5 indicates that the selected trajectories used to derive the location estimate assume a constant altitude, or constant ground track velocity, even if that constituent trajectory was initially selected from a broad range of possibilities.

In some cases, the location estimate is derived from parameter estimation for a physical model which does not explicitly model the aircraft trajectory, however the heading and velocity are estimated after the fact from the derived parameters, in these cases, those heading and velocity estimates are usually fixed values. Presence of non-zero values for altitude and velocity changes in the table indicates that the trajectories used to derive the location estimate exhibit significant changes in altitude, velocity, or both. In some cases this is a single trajectory where altitude or velocity variation is present, in other cases a range estimate is derived from a sample of selected trajectories, where the variation in altitude or velocity is observed between trajectories within that selected sample, and where each of the constituent trajectories may consist of fixed values.

Table 5

Meta-analysis studies with reported and imputed variables identified as potential candidates for meta-regression.

	Author(s)	Lower Bound (Degrees South)	Upper Bound (Degrees South)	Imputed Mean (Degrees South)	Imputed Standard Deviation	Maximum Time of Turn After 1822Z (Mins)	Altitude Variation of Constituent Trajectories (ft)	Variation in Ground Track Velocity of Constituent Trajectories (kts)	Maximum Cumulative True Track Change from 296T @ 1822Z in Constituent Trajectories (Degrees)
1	ATSB (2014) Wide Area	16.4	39	27.7	5.8	90	25000	200	200
2	ATSB (2014) Priority Area	27.4	32.1	29.8	1.2	90	15000	0	165
3	ATSB (2014) Medium Area	24.4	34.7	29.6	2.6	90	22000	150	165
4	ATSB (2014, Oct) Flight Path Anal	33.5	38.3	35.9	1.9	18	10000	63	150
5	Ashton et al. (2014)	34.7	34.7	34.7	0.5	20	0	16	121
6	Anderson et al (2014)	37.5	37.7	37.6	0.5	17	0	20	114
7	Spinor (2014)	38.5	38.5	38.5	0.5	119	0	0	120
8	Ulich (2014)	40.2	40.2	40.2	0.1	6	36	36	97
9	Martin (2014)	40.55	40.55	40.55	0.5	3	0	0	103
10	Pleter, Constantinescu and Jakab (2	38.2	39.9	37.5	0.7	17	3000	39	115
11	Fah (2015)	34.5	40.5	37.5	1.5	20	0	77	109
12	Davey et al. (2015)	34	40	38	1.5	17	18000	65	125
13	GlobusMax (2015)	40	40	40	0.5	-1	5000	0	109
14	ATSB (2015)	36	39.3	37.7	1	6	18000	65	125
15	ATSB (2016)	32.5	36	34.3	0.9	6	18000	0	127
16	Ianello and Godfrey (2016)	26.9	26.9	26.9	0.5	114	15000	0	133
17	SK999 (2016)	22	37	29.5	3.8	16	20000	140	132
18	Ianello (2017)	28	39	34	2.8	119	0	0	138
19	Godfrey (2017)	29	31	30	0.5	114	0	0	126
20	Nederland (2017)	31	31	31.1	0.5	28	12139	73	152
21	Gilbert (2017)	31	34	33.5	0.8	98	0	0	150
22	Marchand, Gasser, Delarche and Ga	12	12	12	0.5	21	30000	218	161
23	Ulich (2018)	31.6	31.6	31.6	0.5	17	500	68	132
24	Ianello (2018)	22	22	22	0.5	110	0	135	155
25	Kristensen (2018)	13.3	13.3	13.3	0.8	119	0	1	210
26	Kristensen (2018) 2nd minima	34.6	34.6	34.6	0.8	119	0	1	120

The maximum cumulative change in ground track azimuth indicates the sum of degrees of turns from the initially assumed true track of 296 degrees on N571 between waypoints MEKAR and NILAM. For some studies, the selected trajectories turn approximately south after 18:22Z and remain on a similar heading until fuel exhaustion, in which case the cumulative track change is in the order of 296-180, ~116 degrees, plus potentially some small changes related to wind correction angles due to wind direction and velocity changes during the flight (and depending on the autopilot mode assumed), spatial variation in magnetic declination, or small random deviations from a generally consistent direction generated in the sampling process for a given study.

Other studies assume multiple significant turns after 18:22Z, in which case the cumulative track change is the sum of those turns. More than one of the studies incorporate local maneuvers, for example holding patterns or significant turns associated with aborted approach procedures into their selected trajectories after 18:22Z.

Where studies included such maneuvers with substantial turns in a locality, in some cases turns of 360 degrees or more, only the difference in direction of flight between the entry and exit of the local maneuver are included in the cumulative sum of true track changes, as it is that difference which affects the direction of the trajectory on a timeframe consistent with the time interval between BTO and BFO observations, outside of the local maneuver.

Treatment of Missing Data

All of the studies selected for the meta-analysis include either a range estimate for position on or near the 7th arc, or a point estimate. Most of the studies do not explicitly include a mean or standard deviation for the location estimate. The mean data are imputed as follows: for range estimates, the mid-point along the arc is taken as the imputed mean, except where a given study identifies specific preference point within the range estimate, in which case that point is taken as the mean. For point estimates, the imputed mean equals the point estimate.

For the imputed standard deviation, a missing precision technique (Schwarzer, Carpenter & Rücker, 2015) was used. Where a range is quoted for θ_k as opposed to a point estimate, the range was taken to represent a 0.95 confidence or $2\sigma_{\emptyset_{7k}}$ unless the study explicitly stated otherwise, thus deriving an implied standard deviation and variance for study k. In the case of a single point estimate, the 0.95 confidence interval is assumed to equal one degree of arc-latitude, unless the study explicitly states otherwise. In cases where a stated preference point within the identified range was not equal to the mid-point, the imputed skewness was also calculated. The underlying distributions are assumed to be Gaussian for the purposes of imputation.

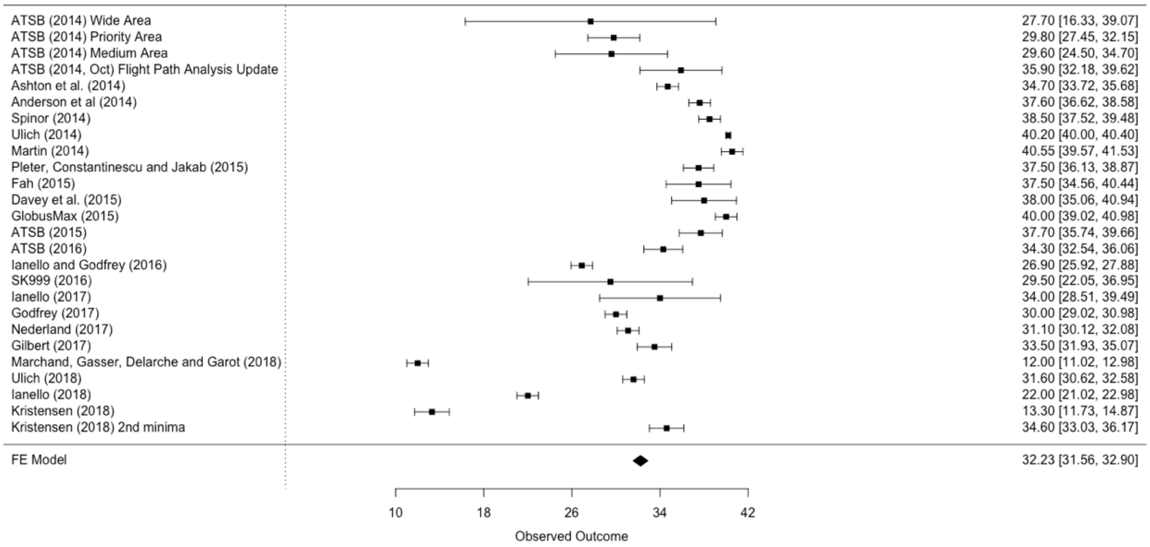

Figure 20. Imputed mean and 0.95 confidence intervals for selected meta-analysis studies.

Statistical and Computational Methodology

Statistical Tools

Statistical testing and meta-regression analyses were performed using the R software v.3.4.4 and RStudio interface v1.1.442 (R Core Team, 2018; RStudio Team, 2016) and R ‘metaphor’ user library (Viechtbauer, 2017), running on an Apple iMac Pro, 8-core Intel Xeon W CPU, 64GB RAM. Other computations were performed in Microsoft Excel for Mac v16.22 with the Analysis ToolPak.

Research Question 1(a) Hypothesis H1a-1 (Test for Statistical Heterogeneity of Studies)

Prior to the meta-regression, the spatial estimates from the studies selected for the meta-analysis in sub-groups 1 and 2 were separately tested for statistical heterogeneity using both an unweighted fixed effects and weighted random effects model. The use of both weighted and unweighted estimators reflects the fact that the weights are calculated as the reciprocal of imputed variances, which in this case may or may not reliably indicate the precision of the estimates contained within the selected studies due to the imputation. Under both the unweighted fixed effects and weighted random effects model, the data were tested at an α = 0.05 level of significance using Cochran’s Q statistic (Cochran, 1954):

$$Q = \sum_{k=1}^{k} w_k \left\{ \overline{\emptyset}_{7k} - \frac{\sum_{k=1}^{k} w_k \overline{\emptyset}_{7k}}{\sum_{k=1}^{k} w_k} \right\}^2 ,$$

with 25 degrees of freedom. Under the weighted random effects model, the τ^2, I^2 and H^2 statistics were also calculated. Under the null hypothesis of no heterogeneity, the Q statistic follows a χ^2 distribution, therefore the test for heterogeneity for was performed using a p-value estimated from the χ^2 distribution, with k-1 degrees of freedom, which was tested at a p=0.95 level of significance. Meta-regression was only performed on any sub-group which was found to be statistically heterogenous at this level of significance or greater.

Research Question 1(b) Hypothesis H1b-1 (Meta-Regression)

A linear mixed-effects meta-regression (Schwarzer, Carpenter & Rücker, 2015) of the form $\overline{\emptyset}_{7k} = \emptyset + \beta_n a_n + \mu_k + \sigma_k \varepsilon_k$ was performed on the data from the 26 studies on sub-group 2, where $\overline{\emptyset}_7$ is the estimate of arc-latitude crossing the 7th BTO arc considered here as the dependent variable, $\emptyset$ is an intercept, and the regression coefficients, β_n, represent the sensitivity of $\overline{\emptyset}_7$ with respect to each parameter a_n included in the regression from the candidate predictors: t_{TS} the assumed time of the turn south after 18:25Z, V_{Range} the range of ground track velocities for the constituent trajectories, A_{Range} the range of altitudes for the constituent trajectories, C_{TTrack} the cumulative change in true track in the constituent trajectories, measured from the 296 degrees track assumed at 18:25Z. The independent error terms μ, ε represent the effects of between study and within study variance, respectively.

Assumptions of Linear Regression. To make inferences from a linear regression model, the assumptions (Sheather, 2009) are that (a) the predictors are linearly related to the dependent variable in the form given in the previous paragraph, (b) the regression residuals or errors are normally distributed, with zero mean and a constant common variance, and (c) the errors are statistically independent. The linear relationship assumption was tested by inspection of scatterplots between the dependent variable and each of the candidate predictors, by calculation of the correlation coefficients between the same, and by estimation of the linear regression with each of the candidate predictors in isolation as the sole predictor. For the combined regression (with multiple predictors selected), in addition to the test of significance for the intercept and coefficient estimates, the distribution of the residuals was tested for normality using the Anderson-Darling test at an α=0.05 level of significance, along with inspection of both a histogram and a normal Q-Q plot of the residuals. The mean and variance of the residual distribution was estimated and a t-test performed on the mean for significance of the difference to the assumed mean of zero.

Linear Regression Hypothesis Test. For each regression, the r^2, τ^2, I^2 and H^2 statistics were calculated, and for each regression the hypothesis:

$H_{1b\text{-}1\text{-}0}$: The regression coefficient (predictor) is not significantly different to zero (zero slope).

$H_{1b\text{-}1\text{-}A}$: The regression coefficient (predictor) is significantly different to zero (non-zero slope).

was tested for each coefficient or set of coefficients using both the Wald-type χ^2 test (Viechtbauer, 2017) and the F-test (Snedecor, 1934), performed on the significance of the r^2 value for each predictor, at an α = 0.05 level of significance.

The intent of this approach is to estimate the sensitivity of $\emptyset_{7k}$ to certain parameters which have not been directly observed in the available data and which may be introduced into the selected studies either under assumption or as a result of inference. It is of interest in this study to estimate the significance of the systematic effect these assumptions and inferences may have on the estimates $\emptyset_{7k}$ and the extent to which they may explain heterogeneity in the data. It is also of interest to assess the question of the extent to which the statistical uncertainty in these specific parameters can be quantified from the available data. For each regression, the variance of the predictors and the residual heterogeneity were also estimated.

It is expected that the magnitude and statistical significance of the estimated β coefficients, together with the estimate of Cochran's Q for the data, will address the question of whether there are systematic differences or biases which can be identified across these studies; if Q suggests heterogeneity to a high level of significance and the regression model estimates significant β coefficient values with a significant r^2 value, then this may be indicative of systematic effects due to different assumptions and inferences used across the studies in the meta-analysis. From the Systems Theory perspective, this would be indicative of the interaction between the physical system and the human system, where assumptions are made in the latter which can affect the interpretation of partially observed signals and measurements from the former.

Research Question 1(b) Hypothesis $H_{1b\text{-}2}$ (Stationarity and Stochastics of Biases)

The BFO biases were not suitable for inclusion in the meta-regression as predictor variables due to the lack of diversity of assumptions about them across the studies, i.e. the studies generally assumed the same bias values. Of the subset of ten studies selected for the meta-analysis for which detailed trajectory information was available, four studies explicitly stated the BFO bias value used in the calculations, while the bias used for three more of the studies could be inferred; in two cases the residual between the observed and calculated BFO value was explicitly reported, which provides sufficient information to calculate the BFO bias used, while the third study referred to other studies which had been followed in respect of the BFO bias used, where the bias value was explicitly stated in those primary sources referred to. For this sample of n=7, the mean BFO bias value used was 150.1 Hz with a sample standard deviation of 0.36Hz; essentially the same bias.

Given the sensitivity of location to the BFO bias, and given the potential for the bias to change when the AES is restarted, particular attention was paid in this study to analysis of the bias for the R-1200-0-36ED channel, being that used for the sole transmission in the case of the 2nd through 6th BTO arcs and for six of the transmissions in the 1825Z log-on sequence of transmissions.

The BFO bias was tested for (a) significance in difference between the MH371 and MH370 flights, i.e. before and after a shutdown and restart, (b) significance in difference of the R-1200-0-36ED channel compared to other R-channels, (c) significance in difference for the MH370 flight before and after the 18:25Z restart, and (d) sensitivity to a slight change in return link transmission frequency within the 1645-1655MHz range.

The procedure used for the BFO bias analysis was to first estimate the bias statistics across multiple channels the available data from the MH371 and MH370 flights, then to estimate the bias for the R-1200-0-36ED channel in isolation, and to perform a series of statistical tests on the differences between these estimates.

Multiple Channel BFO Bias Estimation and Testing. The BFO bias was estimated using four groups of measurements: 75 data points recorded while 9M-MRO was on the ground in Beijing (Flight MH371), 661 data points recorded while 9M-MRO was in cruise flight (MH371), 77 data points recorded while the aircraft was at Kuala Lumpur International Airport Gate C1, and 132 measurements made during the initial cruise phase of Flight MH370 prior to the first in-flight shutdown, a total sample of n=945 measurements. For each group, the mean, sample standard deviation, and standard deviation of the mean were estimated. To assess differences between different channels, the mean, sample standard deviation and standard deviation of the mean were also estimated individually for the R600, R1200 and T1200 channels.

The aircraft position prior to departure from Beijing Capital Airport was estimated as 40.0596N, 116.6143E, Elevation 115’ MSL, corresponding to an ECEF XYZ position of -2183.890931, 4358.415334, 4071.772793. This position is in the vicinity of Terminal 3 as used by Malaysian Airlines at Beijing Capital Airport. The decoded ACARS data shows a reported ‘OFF’ time of 01:34:16Z, therefore data recorded between 01:07:42Z and 01:28:05Z was used for the on-ground period at PEK, with the assumption that the aircraft was either motionless or moving with low velocity (taxi speed) during that period; a ground track velocity and azimuth of zero was used for the calculations.

Preliminary investigation identified larger BFO observed – calculated residuals during periods when the aircraft was under significant acceleration and/or was climbing or descending. For this reason, such periods were excluded from the BFO bias calculation, while periods during which the aircraft was in steady-state normal cruise were included, rather than relying solely on the ground portion, in order to assess the stochastics during normal flight conditions. It has also been suggested by Holland (2017) that the AES Doppler pre-compensation algorithm may operate in a closed-loop mode when on the ground, therefore it is desirable to include data recorded when the aircraft was in open-loop mode, taking a position, heading and velocity input from the aircraft avionics. Multiple satellite communications bursts recorded during cruise flight between 03:29:06.417Z and 06:49:43.407Z were included in the calculation (n=661 individual records). Headings and velocities for the in-flight records at 5-minute intervals were extracted from the decoded ACARS data; ground track velocities and directions were calculated by making use of the wind direction and velocity data contained in the ACARS reports, at the same 5-minute interval.

To test for differences between the estimated means between channels, between phases of flight, and between the two different flights MH371 and MH370 (between which the AES user terminal may have been shut down and restarted), a t-test for difference between sample means was performed on a number of combinations of interest. As substantial variation was observed in the sample standard deviation estimates across the different subgroups, therefore Welch's unequal variances t-test was selected, with the tests performed at a level of $\alpha = 0.05$.

R-1200-0-36ED Channel BFO Bias. For the R-1200-0-36ED channel in isolation, the available data consists of n=33 observed BFO values from the MH371 flight and n=37 observed values from the MH370 flight, of which the last 5 were the 2nd through 6th arc transmissions, preceded by 6 transmissions on this channel during the 1825Z log-on sequence. Of the 33 MH371 recorded observations, 17 were recorded while the aircraft was either departing from Beijing or on approach to Kuala Lumpur and were excluded from this analysis due to the unreliability of the models used when the aircraft is under significant acceleration, deceleration, or has significant vertical speed.

The remaining 16 records were recorded in cruise flight in four transmission bursts spread over approximately three hours, on the flight's approximately SSW (~198 degree) track, at positions between 24N 114E and 5N 105E. For these n=16 observations, the decoded ACARS data provides the required aircraft state vector elements and environmental parameters such as wind direction, velocity and static air temperature necessary to estimate the BFO bias using the calculated true track azimuth and ground track velocity, at 5-minute intervals.

The 5-minute interval ACARS reports do not exactly coincide with the time of transmission, except in the case of the 04:03:55-04:04:09 burst spanned a 04:04:01 report, <+/- 8 seconds. The other three bursts occurred within 56 seconds, 38 seconds, and 1 minute 56 seconds of an ACARS reported position, respectively. In all cases, the ACARS reported position, velocity and heading were used along with the environmental data to propagate the aircraft state in order to estimate the state at the exact time of transmission, enabling the bias to be estimated for each observation. The mean bias, sample standard deviation and standard deviation of the mean bias for this MH371 cruise phase of flight were thus estimated.

The n=26 MH370 R-1200-0-36ED observations recorded prior to the 1825Z restart consist of two measurements recorded on the ground at 16:29:49-16:29:52, occurring two minutes after the ATC transcript recorded the ground controller's approval of the flight's request to push back from gate C1 and start the engines, 1 minute 38 seconds after the ACARS 'out' report, assumed to coincide with brake release, and 37 seconds after the ACARS reported APU start and operations report commenced. Therefore, it is inferred that these two transmissions were made during the engine start procedure, after push back but prior to taxi, and thus the aircraft was static.

Sixteen subsequent observations were recorded during the takeoff and climb phase of flight while the aircraft was under significant acceleration, deceleration and vertical speed, thus were excluded from this analysis for the same reason as above for the MH371 flight. The remaining 8 measurements were recorded in cruise flight, starting 6 seconds after MH370's final ACARS position report at 17:06:43 and ending 1 minute and 5 seconds after that final report. The propagation of the aircraft state vector, use of environmental parameters from the ACARS report and estimation of the BFO bias parameter and associated statistics was calculated as described above for the MH371 cruise flight data.

The useable sample of n=16 from MH371 and n=10 from MH370 prior to the 1825 restart was used to test the hypothesis of zero difference in the mean BFO bias value between the two flights of the same aircraft on the same channel, where a shut down and restart of the AES user terminal between the two flights could potentially change the BFO bias value. Due to the small sample size, Student's t test was used, using a pooled (i.e. equal) variance assumption and a level of significance $\alpha = 0.05$. The equal variance assumption reflects an assumption that the underlying noise in the BFO data is the same across the two flights, however the mean value may change; the latter being the question of interest for this particular test. Formally, the hypotheses tested were: Ho = no difference in the mean BFO bias value between the two flights; Ha = a statistically significant difference in the mean BFO bias value exists between the two flights.

18:25Z Restart. It is possible that a shutdown in flight during the period from sometime between 1722Z and 1807Z, to the AES restart just prior to 1825Z resulted in another significant change in the bias. To re-estimate the bias after the restart using the 13 measurements recorded during the 1825:27 – 1828:15 log-on sequence, the BFO bias was estimated assuming that the position was 3 minutes down route of the last reported primary air defense radar position at approximately 10 NMi past waypoint MEKAR on airway N571. At an assumed Mach number of 0.82 and a ground track aligned with N571 (296 degrees true), the estimated position of the aircraft during the 1828Z log-on sequence is in the vicinity of the waypoint NILAM, or 6.75N 96.0E. A two-sided t-test was performed separately for the R- and T-Channel estimates based on the 1825-1828Z data from the log-on sequence, against the R- and T-Channel estimates from the combined MH370 ground and 1707 cruise flight observations, respectively. A pooled variance was used; the assumption being that when a change occurs in the bias due to a restart of the user terminal, the underlying noise in the data is consistent over the short time period concerned, it is a change in the mean value of the bias which is of interest for this test. A level of significance $\alpha = 0.05$ was used for the tests. This possibility was tested using the R1200-0-36ED data from the 1825 log-on sequence, as well as for the T1200-0-36D7 data from the same sequence.

R600 Channel Biases and Power Biases. The BFO biases for the R600-0-36E1 and R600-0-36F8 channels used during the 18:25Z and 00:19Z restart sequences are of interest for testing of assumptions in prior work relating to their reliability and susceptibility to transient biases postulated to be caused by transient instability of the AES terminal's OCXO during a restart. The normally observed difference in received power between these R600 channels and certain R1200 channels is also of interest to the study in testing of assumptions about the validity of the data.

For the R600-0-36E1 channel (18:25Z sequence), sufficient data existed in the MH371 dataset to estimate the BFO and received power offsets to the R1200-0-36ED channel directly. The combined mean and combined standard deviation of the BFO difference were estimated from four transmission sequences between 01:37Z and 07:29Z, containing n=38 samples in total where the two channels were used for transmissions spaced within between 6 and 26 seconds of one another and where the mean value of the BFO was assumed to be stationary over such a short time period. The received power difference was estimated using the same data and technique, with the exception of the 07:29Z sequence, where the terminal was switching between the LGA and HGA, coupled with changes in the reported initial EIRP, such that the total sample in this case was n=24.

A two-sample t-test was subsequently performed on the difference in BFO observations between these two channels during the 18:25Z sequence, where the null hypothesis Ho is that the difference in mean between observed R1200 channel BFO values and the R600 channel BFO value plus the known difference to the R1200 channel, is zero. The previously estimated population standard deviation for the BFO of 4Hz was used in the test, conducted at a 0.05 level of significance. Due to the presence of a large but rapidly decaying transient bias in the R1200-0-36ED BFO data during this sequence, the last two values in the sequence were used in the test, where the bias appears to be at a minimum (although may not have entirely decayed to zero). The difference in received power was tested in the same manner, using a previously estimated population standard deviation of 1.6dBm.

For estimation of the fixed BFO bias and power offset for the R600-0-36F8 channel used at the beginning of the 00:19Z restart sequence a two-step procedure using intermediate channels was used to estimate the bias from the previously estimated R1200-0-36ED due to the absence of proximal transmissions in the available data to facilitate direct estimation. In the first step, the BFO biases and power offsets were estimated on three intermediate channels (R1200-0-36D3, R1200-0-36F2 and R1200-0-36D8) for which proximal transmissions were available to both the R1200-0-36ED and R600-0-36F8 channels. In the second step, the R600-0-36F8 bias and power offset was estimated from those of the intermediate channels. For the estimation of the R1200-0-36ED to intermediate channel bias differences, six transmission sequences between 04:03Z and 17:07Z were used, containing a total of n=224 individual observations and for the intermediate channel biases to the R600-0-36F8 bias, three transmission sequences between 01:21Z and 16:00Z were used, containing a total of n=32 individual observations. Due to the insufficient degrees of freedom in the comparison of a difference of two observations during the 00:19Z sequence (the only two available) precluding the use of a t-test, a z-score was calculated where the samples were assumed to be drawn from a population for which the population standard deviation has previously been estimated as 4Hz. The linear combination of the two samples in calculating the observed difference results in an increase in the noise, and where the resulting standard deviation is estimated from the Gaussian error propagation law as 5.7 Hz. Thus, the difference between the two samples is considered to be drawn from a population with mean of zero and standard deviation of 5.7 Hz. A z-score was calculated accordingly and the null hypothesis that the observed difference is significantly different to zero was tested at a 0.05 level of significance. The observed power difference during the 00:19Z sequence was tested in the same manner, using a previously estimated population standard deviation of 1.6dBm for the observables, and 2.3dBm for the calculated difference by error propagation.

Research Question 2 Hypothesis H2 (Sensitivity Analysis and Inclusion of AES Antenna Peak Gain Variation Model)

The purpose of this sub-question is to investigate whether or not the inclusion of the AES antenna gain variation data can serve to reduce the uncertainly in the derived geospatial estimates. The hypothesis test was performed on the results of two linear regression models, one using BFO data combined with a fixed AES antenna gain (12 dBic) model and the other using the BFO data combined with a variable gain model. Sensitivity analysis for the BFO data only and the combined BFO and antenna gain (fixed and variable models) was conducted for all R1200-0-36ED channel observations made during the MH371 and MH370 flights, sampled along arcs of approximately 20 degrees of latitude for each arc, in one degree increments, and across 360 degrees of true heading at each arc-latitude sample point. Probability density functions for the BFO-only data and the combined BFO and antenna gain data were numerically estimated at the same sample points, across the same increments of location and heading.

Estimation of the probability density functions first required estimation of the observed – calculated residuals, $\upsilon_{BFO\propto_{\phi}}$ & $\upsilon_{RxP\propto_{\phi}}$, for the BFO and received power data –

that is, the difference between the observed BFO and received power values and those calculated from a physical functional model as described further below – which were systematically sampled at one degree increments of true heading from 0-359 degrees, across a broad range of arc-latitudes at each observation epoch. The observation epochs used consist of the R1200-0-36ED channel transmissions made during both the MH371 Beijing-Kuala Lumpur and MH370 flights, distributed in time from 01:38Z on March 7, 2014 to 00:11Z on March 8, 2014.

In addition, the $\upsilon_{BFO\propto_{\phi}}$ & $\upsilon_{RxP\propto_{\phi}}$ residuals were systematically sampled using data from the 18:38Z and 23:14Z telephony attempts, to allow for probability density function estimation at those times. For observation epochs where the aircraft position, heading and velocity are known – for example from the ACARS reports –the pdf was systematically sampled at the known arc-latitude +/- 10 degrees of arc-latitude in one-degree increments. For observations where the aircraft state vector is unknown, that is after 18:22Z, the 0-360 degree heading systematic sampling was performed at the arc-latitudes from the subset of meta-analysis group 1 for which detailed trajectory data could be extracted. This selection of arc-latitude samples serves two purposes: one being to sample the arc-latitudes over the full range of diverse estimates across the meta-analysis studies, and the other being to enable the pdf for each trajectory from those studies to be evaluated at each measurement epoch.

The above yielded approximately 100,000 systematic samples for each of the BFO-only and BFO plus AES gain variation model observed – calculated residuals, $\upsilon_{BFO\propto_{\phi}}$ & $\upsilon_{RxP\propto_{\phi}}$, sampled across 15 observation epochs, each at 0-360 degrees of heading at each of 6-10 arc-latitude locations, generating a systematic sample and sensitivity analysis typically spread over approximately 2,000km of the BTO arc at each observation epoch, i.e.

seeking to replicate the spatial uncertainty toward the end of the MH370 flight. A subset of these estimates was also resampled at different Mach numbers across a feasible range of values, in order to estimate the sensitivity of location and heading to changes in velocity.

BFO Physical Functional Model. The functional model from which the observed – calculated BFO residuals $v_{BFO\propto_{\phi}}$ were calculated is given by:

$$v_{BFO\propto_{\phi}(t)} = BFO_{Obs(t)} - \left[\left(\Delta f_{up} + \Delta f_{down} + \delta f_{Sat} + \delta f_{AFC}\right) - \delta f_{AESPrecomp}\right]_{t},$$

where:

$$\Delta f = \frac{f}{c} \cdot \frac{(\Delta X_{SC-AC}.\Delta\dot{X}_{SC-AC})+(\Delta Y_{SC-AC}.\Delta\dot{Y}_{SC-AC})+ (\Delta Z_{SC-AC}.\Delta\dot{Z}_{SC-AC})}{R_{AES-SC}}$$

and $\Delta X_{SC-AC}, \Delta Y_{SC-AC}, \Delta Z_{SC-AC}, \Delta\dot{X}_{SC-AC}, \Delta\dot{Y}_{SC-AC}, \Delta\dot{Z}_{SC-AC}$ are the differences in X,Y,Z ECEF coordinates between the spacecraft and aircraft positions at the time of observation, and the difference in their time derivatives, respectively. Implementation of this model was after that of Yap (2015), where the values for δf_{Sat} , δf_{AFC} are interpolated from proprietary data given in Ashton et al (2014).

$\delta f_{AESPrecomp}$ was calculated as per Δf_{up} but using only the sampled ground track velocity and ground track azimuth of the aircraft, i.e. ignoring aircraft acceleration and vertical speed, while also assuming a fixed spacecraft X,Y,Z ECEF coordinate of $[18153.04, 38058.64, 0]_{\mathrm{km}}$, with time derivates of zero with respect to an observer on earth.

Because the sensitivity analysis was performed using a true heading as an input, which is the appropriate direction angle for the antenna gain calculations but where the BFO calculation requires the true track, the latter was estimated from the former by solving for the wind correction angle at each sampled point. The ground track velocities were also estimated from the selected Mach number for each sampled heading and position by estimation of true airspeed from the available static air temperature at altitude and subsequent application of the relative wind component in the direction of sampled true heading.

BFO Stochastic Estimation. Prior studies have extensively investigated the statistical characteristics of the BFO observable; in particular Davey et al (2015) estimated a 4Hz standard deviation from a much larger sample than is available for the present study. From the data available for this study, the standard deviation when including the time varying bias component in the noise estimation was estimated from a sample of n=934 υ_{BFO} residuals for data observed during flights MH371 and MH370 from 01:55Z to 17:07Z, at approximately 3.4Hz, with little difference in the underlying noise estimates when the R-600, R-1200 and T-1200 channels were sequentially included or excluded from the calculation. Based on the significantly larger sample size for the Davey et al (2015) estimate, a value of 4Hz was used in estimation of the likelihood function for the BFO-only and combined BFO and received power probability density function estimation.

Received Power Physical Functional Model. The functional model (in decibels) from which the observed – calculated received power residuals υ_{PRx}were calculated is given by:

$$\upsilon_{RxP\propto_{\phi}} = PRx_{Obs(t)} - [EIRP_{AES} - FSL_{UP} + G_{SCTotal} - FSL_{DOWN} + G_{GESTotal} - L],$$

where the RF power received at the ground earth station is the radiated power from the AES antenna, minus the path loss in free space to the satellite, plus the total gain achieved in the satellite amplification and retransmission, minus the path loss from the satellite to the earth station, plus the total gain achieved at the earth station prior to measurement of the received power level, minus a set of other power losses throughout the chain, and where:

$$EIRP_{AES} = P_{HPA} - L_{Cable} + G_{AESAnt_{\propto_{\phi}}}$$

$$FSL_{dB} = 10.Log_{10}.\left[\frac{\lambda}{4.\Pi.R_{TX-RX}}\right]^{2}$$

$$G_{SCTotal} = G_{SCAnt_{LOStoAC}} + G_{SCTxpdrAmp} + G_{SCAnt_{TX\,LOStoGES}}$$

$$G_{GESTotal} = G_{GESRXAnt} + G_{GESAmpTotal}.$$

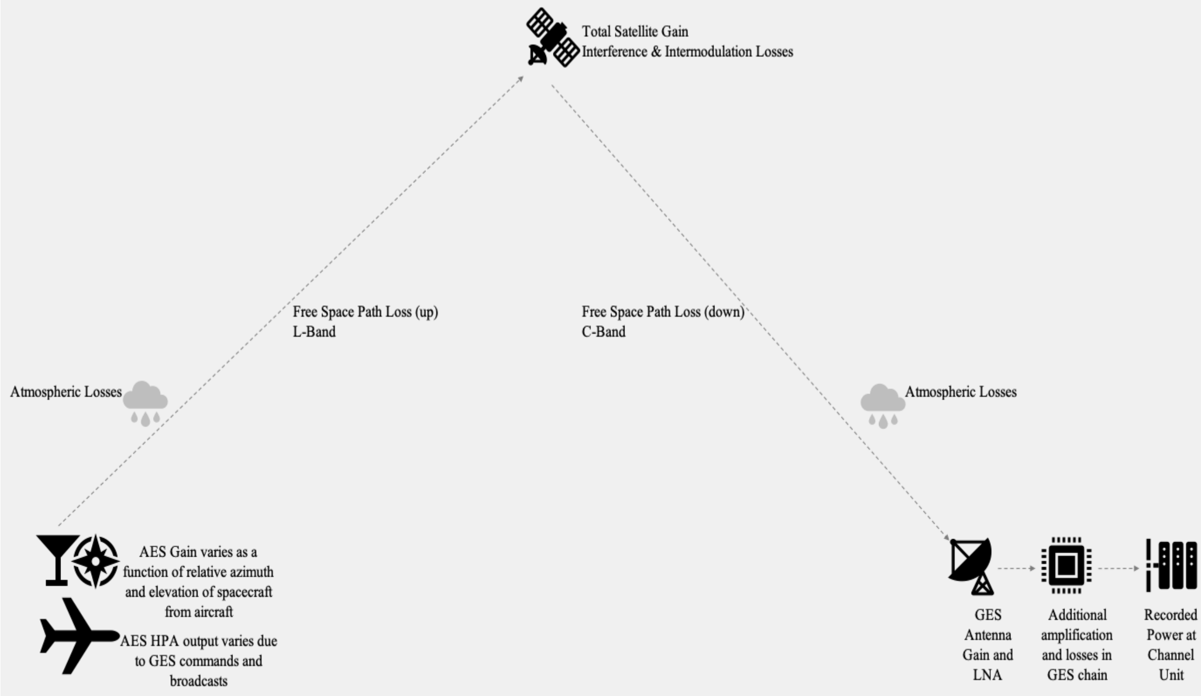

Figure 21. Conceptual return link communications chain from AES to GES channel unit.

In the estimation of the Effective Isotropic Radiated Power (EIRP) for the AES in the return link, $\mathrm{EIRP}_{\mathrm{AES}}$, at any given time, the $G_{AESAnt_{\propto_{\phi}}}$ term represents the AES antenna gain in the specific direction of the spacecraft from the aircraft, for a given aircraft location and true heading. For each sampled location, the ‘look’ angles to the satellite were calculated, as an azimuth from true north and an elevation angle from the local geodetic horizon to the spacecraft, which were then rotated into aircraft coordinates for each sampled aircraft (true) heading and assuming level flight. The value of $G_{AESAnt_{\alpha\emptyset}}$ was then selected from the port and starboard antenna gain matrices described earlier in this chapter, for each sampled heading and location.

The L_{Cable} term represents the power loss in the cable between the HPA and antenna, for which a value of -2.68dB was used, following Westfeldt and Konrad (1992). The $\mathrm{P}_{\mathrm{HPA}}$ term represents the commanded power output of the High Power Amplifier, or HPA, at the time of transmission, which can vary for example due to requests from the Inmarsat network. Requested EIRP levels reported in the Inmarsat log file and in some cases decoded from the LIDU data were used to derive the $\mathrm{P}_{\mathrm{HPA}}$ estimates, and where the relationship between the commanded HPA output and the commanded EIRP was assumed to incorporate the known cable loss and a nominal AES antenna gain values of -2.68 dB and +12 dBi, respectively.

The Free Space Path Losses FSL_{UP} and FSL_{DOWN} were estimated using a transmission wavelength λ of 0.18206m for the L-band return earth-to-space uplink and 0.08328m for the C-band return space-to-earth downlink. Path lengths R_{TX-RX} for a given transmission epoch were calculated from the distance between the sampled aircraft location and instantaneous spacecraft position at that time, and from that instantaneous spacecraft position to the fixed GES XYZ position of $[-2368.841, 4881.08, -3342.092]_{\mathrm{km}}$ in Perth, Western Australia. The total gain achieved by the spacecraft element of the link includes the gain of the L-band receiving antenna in the direction of the aircraft, plus on-board amplification, and the gain of the C-band downlink antenna in the direction of the Perth GES. For very similar satellites in the I-3 constellation, Inmarsat (2007) states that the peak receive gain for the L-band global return link is 18.5 dBi at the nadir, with contours given for the -2dB and -2.5dB locations on earth. Estimation of the expected satellite antenna gain on the L-band return uplink for each sampled aircraft location was achieved by interpolation of these values using a quadratic function relating the elevation look angle from the aircraft to the spacecraft used at a given sample point to the estimated spacecraft receive gain in the global beam. For the MH371 and

MH370 flights these estimated typically ranged between 16.5 to 17.5 dBi for the R1200 channel in the global beam.

Return link transmissions on the 21000 channel during the telephony attempts were found from the decoded LIDU data to have been received using a regional beam, for which the additional G_{SCAnt} over the global beam due to beamforming, was not found in the public domain, nor was a reliable method identified to estimate it from the data, therefore the $v_{RxP\propto_{\phi}}$ received power residuals estimated for the telephony attempts are assumed to be biased by unknown amount. However, the relative magnitude of the residuals may still have utility in the pdf estimation.

After reception at the L-band antenna on the global beam, the maximum satellite transponder gain for the return link is stated by Inmarsat (2007) as 127dB, the peak transmission gain of the SC C-band horn is ~20dBi, and GES antennas with peak receive gains of between 49.2 and 52.9 dBi are described, for which the sum of approximately +200dB was used for the initial calculations, although it is noted that the transponder gain can be dynamically controlled by the GES, which (among other causes) would cause unmodeled systematic variations in the $v_{RxP\propto_{\phi}}$ residuals over time.

The preceding methodology provides for an estimate from the aircraft HPA up to the point of reception at the GES antenna element. The recorded, i.e. observed, received power values $PRx_{Obs(t)}$ are assumed to be measured at the Intermediate Frequency (IF) input to the channel unit in use for the specific received signal, such that total effect, $G_{GESAmpTotal}$, of the stages of amplification before and after down-conversion which may occur between the GES antenna element and the channel unit IF input must also be estimated. In addition, various losses, L_{Other}, throughout the entire communications chain must be accounted for, including atmospheric losses, cable losses in the spacecraft and GES, the effects of interference, intermodulation noise and so on.

Rather than attempting to include all of these effects in the functional model, the $G_{GESAmpTotal}$ and sum of fixed losses which remain approximately constant over the duration of the flight was estimated empirically from n=3,239 observations from 01:36Z to 17:07Z on March 7, 2014 (as being in the order of approximately +100 dB, with channel dependent variations), by first estimating the $v_{RxP\propto_{\phi}}$ residuals using the model as previously described, then finding a value of $G_{GESAmpTotal} + L_{Other}$ which minimized the sum of the squares of the residuals. The remaining aforementioned effects which are not included in the physical model and which are not assumed to be constant for the duration of the flight were treated as noise and thus included in the stochastic estimates for the received power observable, i.e. σ_{Prx}.

Received Power Stochastic Estimation. Statistical analysis of the $v_{RxP\propto_{\phi}}$ residuals was carried out with two key intentions; one being to determine whether or not the effect of the peak gain variation in the AES antenna was both present and detectable, the other being to characterize the distribution of the residuals for subsequent probability density function estimation.

Although the peak gain variation is known to exist in the antenna, it may not necessarily exist in the data. For example, in principle it would be possible for the AES to compensate for this effect when commanding the HPA power output, given knowledge of the aircraft-spacecraft relative geometry and a table of values for the gain as a function of relative position. In this scenario, although the antenna gain variation would still exist, dynamic compensation of the HPA output would render the effective gain as a fixed value (for example 12dBic). In the alternative scenario, the gain would exhibit significant variation (typically in the range of 10 to 14.5 dBi but potentially in the range of 5 to 14.5 dBi depending on elevation angle and heading), as a predictable function of apparent direction and elevation angle of the spacecraft for a given aircraft position and heading.

Thus, the presence of the gain variation effect in the EIRP must be tested for. Secondarily, even if the peak gain variation is indeed present, it is also necessary to test for whether or not it is detectable within the overall noise inherent in the received power at the end of a ~75,000km return path length and in the presence of signal fading effects.

In order to test for the presence and detectability, or not, of the postulated gain variation, the two alternative physical models (fixed effective gain and variation in gain) were used in two alternative (nested) linear least squares regression models, lm_1 and lm_2:

$$lm_1 \colon P_{RXObserved(t)} = \beta_0 + P_{RXCalc12dBi} + \varepsilon$$

$$lm_2 \colon P_{RXObserved(t)} = \beta_0 + P_{RXCalc12dBi} + \Delta G_{\alpha\emptyset t} + \varepsilon,$$

where is $P_{RXCalc12dBi}$ is the sum of all power terms from the previously described physical functional model, assuming a fixed effective AES gain of 12dBic, and β_0, ε represent the regression intercept and the noise terms, respectively. In the second model the additional $\Delta G_{\alpha\emptyset t}$ term represents the difference between the assumed fixed gain value and the gain calculated from the peak gain variation model for the specific apparent direction of the satellite at the time of observation, making use of the previously described matrix of gain values as a function of relative horizontal direction and elevation angle, as derived from the peak gain variations of the antenna reported by Westfeldt and Konrad (1993). In this formulation, $\Delta G_{\alpha\emptyset t}$ can be considered as a correction term to the fixed gain value under the assumption that $\Delta G_{\alpha\emptyset t}$ exists. The models lm_1 and lm_2 are considered nested, as lm_1 is a special case of lm_2 where $\Delta G_{\alpha\emptyset t}$ is equal to zero. To test the assumptions of linear regression, the linear relationship was assessed via inspection of scatterplots for lm_1 and lm_2, the correlation coefficient between the two independent variables was calculated, and the regression residuals were assessed for normality.

The linear regressions lm_1 and lm_2 were estimated with a data set of n=937 individual observed received power values across multiple R600, R1200 and T1200 channels and channel units recorded during flights MH371 and MH370 from 01:55Z to 17:07Z, both in flight and on the ground, for which the heading of the aircraft at the time of observation necessary for the $\Delta G_{\alpha\emptyset t}$ parameter estimation was either known or could be estimated with a high degree of confidence.

If the postulated gain variation is absent from the data or entirely undetectable, then the addition of significant power variation in the calculated P_{rx} value in the lm_2 model would be expected to increase the sum of the squares of the $\upsilon_{RxP\propto_\phi}$ observed – calculated residuals, due to the inclusion in the estimation model of an effect which is not in fact present in the data. Conversely, if the postulated gain variation is present and detectable in the observed received power data, then the use of a fixed value in the P_{rx} calculations for lm_1 would be expected to yield a higher sum of squares of the residuals than lm_2 for any data set which included sufficient changes in aircraft direction and the apparent elevation angle of the satellite for gain variation to occur, due to the presence of significant received power variations in the observed data which are included in the calculated P_{rx} estimates in the physical functional model in lm_2 but not in lm_1.

Accordingly, the test performed was an ANOVA F-test on the sum of squares of the residuals for the regressions lm_1 and lm_2, where lm_1 is the restricted model and the formal hypothesis is whether or not the $\Delta G_{\alpha\emptyset t}$ coefficient in lm_2 is equal to zero:

H_0: $\Delta G_{\alpha\emptyset t}\ \text{coefficient} = 0$

H_A: $\Delta G_{\alpha\emptyset t}\ \text{coefficient} \neq 0$

The F-test was conducted at an $\propto=0.05$ level of significance, with H_0 accepted unless the computed F value exceeded the critical value at 934 degrees of freedom.

The RQ-2 hypotheses were tested using this result, with $H_{2\text{-}0}$ accepted if the $\Delta G_{\alpha\emptyset t}$ coefficient was found not to be significantly different to zero, and rejected otherwise:

H-2 $H_{2\text{-}0}$: There is no significant difference in the sum of squared residuals for a linear model estimated using BFO data and a fixed gain model and that estimated using both BFO data and the peak gain variation model for the AES antenna.

$H_{2\text{-}A}$: A statistically significant difference is found in the sum of squared residuals for a linear model estimated using BFO data and a fixed gain model and that estimated using both BFO data and the peak gain variation model for the AES antenna.

Other analysis included inspection of the r^2 value for the regression coefficients in both models, stepwise calculation of the coefficients, Akaike information criterion, and testing of the least-squares residuals for normality, linear correlation and equality of variance across the two models. The regressions were also recalculated and the statistical tests repeated for a fixed gain value of 13.1dBi as opposed to 12dBi, where 13.1dBi is the sum of 12dBi plus the (non-zero) mean of the n=962 residuals when lm_1 is calculated using the

12dBi fixed value, i.e. 13.1dBi is the fixed value for which the mean value of the residuals is zero, under the lm_1 model assumptions.

To characterize the distribution of the residuals for subsequent probability density function estimation, the standard deviation of the received power residuals was estimated from the same n=937 samples, as $\sigma_{PRx} = 1.6$ dBm.

Probability Density Function Estimation and Analysis

For the R1200-36ED observation epochs during the MH371 and MH370 fights at 04:04Z, 06:11Z, 06:48Z, 07:07Z, 17:06Z (prior to loss of normal communications) and for each of the six BTO arcs from 18:25Z to 00:11Z, plus the two telephony attempts at 18:40Z and 23:14Z observations, the conditional probability density functions were estimated from the data by numerical sampling, first using the BFO residual data in isolation and then using both the BFO and received power data. The 00:19Z 7th arc was not used in these calculations for two reasons, one being the fact that the R1200-0-36ED channel for which bias and stochastic data has been estimated for this study was not used in that observation and the other being that the functional models used are not reliable when the aircraft has a significant vertical velocity or is under significant acceleration or deceleration.

The data set used was the ~100,000 systematically sampled $\upsilon_{BFO\propto_{\phi}}$ & $\upsilon_{RxP\propto_{\phi}}$ residuals, being the observed BFO and received power values minus those estimated from the physical model, sampled across multiple observation epochs, locations, headings and velocities, as previously described.

In both cases, the probability density of interest is the conditional probability of the sampled true heading $\propto$ at location (arc-latitude) ϕ and ground track velocity V, given the observed $\upsilon_{BFO\propto_{\phi V}}$ residual in the first iteration, and given both the $\upsilon_{BFO\propto_{\phi V}}$ & $\upsilon_{RxP\propto_{\phi V}}$

residuals in the second iteration. If the functional models used to derive the residuals are reasonably representative of the underlying physical processes and the stochastic estimation is reasonably representative of the underlying noise, the expected value of the residuals at the exact true location and heading of the aircraft would be close to zero in both cases, within the inherent noise level of the data. From the previous section, the probability density for the BFO and received power residuals given any sampled heading, location and velocity was estimated by:

$$\rho\left(v_{BFO\ \phi\propto V}\middle|\propto_{\phi V}\right) = \left[\frac{1}{\left(2.\Pi.\sigma_{BFO}^{2}\right)^{\frac{1}{2}}}.e^{-\frac{\left(v_{BFO\ \phi,\propto}-0\right)^{2}}{2.\sigma_{BFO}^{2}}}\right] \tag{1}$$

$$\rho\left(v_{PRx\ \phi\propto V}\middle|\propto_{\phi V}\right) = \left[\frac{1}{\left(2.\Pi.\sigma_{PRx}^{2}\right)^{\frac{1}{2}}}.e^{-\frac{\left(v_{PRx\ \phi,\propto}-0\right)^{2}}{2.\sigma_{PRx}^{2}}}\right] \tag{2}$$

and the joint probability density of a combined observation of BFO and power residuals by:

$$\rho\left(v_{BFO\theta_{\phi,\propto}}, v_{PRx\theta_{\phi,\propto}}\middle|\propto_{\phi V}\right) = \left[\frac{1}{\left(2.\Pi.\sigma_{BFO}^{2}\right)^{\frac{1}{2}}}.e^{-\frac{\left(v_{BFO\theta_{\phi,\propto}}-0\right)^{2}}{2.\sigma_{BFO}^{2}}}\right].\left[\frac{1}{\left(2.\Pi.\sigma_{PRx}^{2}\right)^{\frac{1}{2}}}.e^{-\frac{\left(v_{PRx\theta_{\phi,\propto}}-0\right)^{2}}{2.\sigma_{PRx}^{2}}}\right] \tag{3}$$

or, equivalently, by the joint or bivariate Gaussian density:

$$\rho_{\left(v_{BFO\propto_{\phi}},\ v_{RxP\propto_{\phi}}|\propto_{\phi V}\right)} = \frac{1}{2.\pi.\sigma_{v_{BFO}}.\sigma_{v_{Prx}}}.e^{-\frac{{v_{BFO\propto_{\phi}}}^{2}}{2\sigma_{BFO}^{2}}-\frac{{v_{RxP\propto_{\phi}}}^{2}}{2\sigma_{Prx}^{2}}}. \tag{4}$$

Given these estimated densities, together with the observations and the systematically sampled points, the conditional probability density for a sampled true heading $\propto$ at location (arc-latitude) ϕ and ground track velocity V, given the BFO residual for that heading, location and velocity, was estimated both by using the Gaussian probability density functions above in isolation and by the application of Bayes' Theorem, with the Gaussian density functions providing the likelihood estimation:

$$P\ \left(\propto_{\phi V} \mid \upsilon_{BFO\ {\phi \propto V}}\right) = \frac{P\left(\upsilon_{BFO\ {\phi\propto V}} \mid \propto_{\phi V}\right).P\left(\propto_{\phi V}\right)}{P(\ \upsilon_{BFO\ {\phi\propto V}})} \tag{5}$$

where the prior $P\left(\propto_{\phi V}\right)$ was estimated as 1 / [$360.n_{\phi}$], where $n_{\phi}$is the number of arc-latitudes over which the systematic samples were taken, where at each arc-latitude the true heading was sampled over 1 to 360 degrees in one-degree increments, such that the prior values were equiprobable for any selected sample but sum to 1 over the feasible range evaluated, i.e. all possible headings in 1-degree increments over an arc ~2000km long for each observation.

The joint posterior probability densities were estimated with two different priors: once with the same uniform prior as above, and again with the posterior pdf from the BFO-only estimation above serving as the prior for the joint estimation from:

$$P\ \left(\propto_{\phi V} \mid \upsilon_{BFO\ {\phi\propto V}}\ , \upsilon_{PRx\ {\phi\propto V}}\right) = \frac{P\left(\upsilon_{BFO\ {\phi\propto V}} \mid \propto_{\phi V}\right).P\left(\upsilon_{Prx\ {\phi\propto V}} \mid \propto_{\phi V}\right).P\left(\propto_{\phi V}\right)}{P(\ \upsilon_{BFO\ {\phi\propto V}}\ , \upsilon_{Prx\ {\phi\propto V}})}. \tag{6}$$

and where $\upsilon_{BFO\ {\phi\propto V}}\ , \upsilon_{PRx\ {\phi\propto V}}$ are assumed to be conditionally independent, based on the different underlying physical processes for Doppler shift and power variation.

At each systematically sampled arc-latitude location for the observation times with known aircraft state (04:04Z, 06:11Z, 06:48Z, 17:07Z from ACARS and 18:28Z with a propagated state from the last primary surveillance radar estimate), two numerically sampled conditional density estimates were made: one using the residuals for the BFO and fixed (12dBi) gain model and the other using the BFO residuals and the variable gain model. In both cases, the bivariate Gaussian density function described above was used to estimate the conditional probability density of the residuals given the sampled heading and location, $\rho_{\left(\upsilon_{BFO\propto_{\phi}},\ \upsilon_{RxP\propto_{\phi}} \mid \propto_{\phi V}\right)}$, with a zero mean and standard deviation of 4Hz for the BFO data and 1.6 dBm for the received power data.

As the sampled density functions were found to be generally bimodal or multimodal in nature and the distribution could not be treated as approximately Gaussian, a non-parametric Kolmolgorov-Smirnov test was used to compare the BFO/fixed gain and BFO/variable gain density estimated. For each of the sample locations, a two-sample Kolmolgorov-Smirnov test was conducted on the n=360 degrees numerical samples of the conditional density function, where the BFO and fixed gain estimates were compared to the BFO and variable gain estimates, in a one-tailed test where the null hypothesis is that the two distributions from which the numerical samples were drawn from the same underlying cumulative density function and the alternative hypothesis being that the cumulative distribution function from which the BFO and fixed gain model data was drawn is larger than that for the BFO and variable gain model; the reasoning being that the latter would be smaller if the inclusion of the variable gain model serves to reduce the spatial uncertainty. It is possible that the variable gain model increases the uncertainty, in which case Ho would be accepted; the tests above were also evaluated under the alternative hypothesis that the BFO and fixed gain model data was drawn from a smaller cdf than that for the BFO and variable gain model.

Another mode of comparison of the estimated density functions for the BFO/fixed gain model data and the BFO/variable gain model concerns the differences in peaks of bimodal or multimodal density functions. The reasoning in this case is that the BFO-only model tends to produce multiple peaks of equal or near equal probability density, while the inclusion of the variable gain model in some cases serves to change the relative probabilities of the two peaks, especially when the two peaks occur on headings for which the difference in gain is significant. In fact, this is precisely the potential utility of inclusion of the received power model in combination with the BFO model, i.e. a reduction in the number of possible solutions based on the reduced likelihood of both the BFO and the received power residuals having a near-zero value at the same location and heading.

To compare these differences, Hartigan's dip test (Hartigan & Hartigan, 1985) was performed on the multimodal estimated probability density functions for the observation epochs with known aircraft state, in order to assess whether or not the inclusion of the variable gain model served to decrease (or increase) the degree of multimodality in the estimated probability density functions when compared across all systematic samples for each given observation epoch.

Given that the BTO arcs from 18:25Z to 00:11Z, plus the two telephony attempts at 18:40Z and 23:14Z observations were sampled at arc-latitudes corresponding to those estimated in the subset of meta-analysis studies for which detailed trajectory information was available, the probability densities for each such trajectory were compared at the 00:11Z arc and compared on the sum of estimated probability densities from the 2nd to 6th arcs for each of the trajectories.

Sensitivity analysis and probability density function estimation was also carried out for the R600 channel observations during the 18:25Z and 00:19Z restart sequences. In the case of the 18:25Z observation, the sensitivity analysis and pdf were sampled at 6.75N on the 1st BTO arc, at Mach 0.82 and FL350. No heading was assumed; the sensitivity analysis was performed across 360 degrees of heading at 1-degree intervals and the results subsequently compared with the postulated 296(T) heading on or parallel to N571 to assess the validity of the R600 observation based on this assumption.

For the 00:19Z R600 channel observation, the sensitivity analysis was conducted at eight sample locations along the 7th BTO arc, between 12S to 40S, each across 360 degrees of heading. Under the assumption that the 00:19Z transmission sequence was caused by a restart following fuel exhaustion to both engines and a subsequent (assumed automatic) APU start, it is reasonable to assume that the aircraft was descending. Based on this assumption, the sensitivity analysis was first estimated by systematically sampling the BFO residuals along the 7th arc at 10 arc-latitudes between 12S and 40S (corresponding to estimated 7th-arc crossing positions from the meta-analysis subset), each over 360 degrees of heading, and assuming zero vertical speed (i.e. level flight) and a Mach number of 0.78. The vertical speed was then estimated by finding the required vertical speed at each sample location to align the minima of the sampled BFO residual sinusoid with the zero-value axis. This method was tested for observations with known non-zero vertical speed at 01:38Z, 16:42Z and 16:55Z and was found, when compared to the known vertical speed from the ACARS data, to approximate the correct vertical speed within the overall range of error in the observables.

Research Question 3 Hypothesis $H_{3\text{-}1}$

For RQ-3, the methodological steps were to (a) estimate a baseline historical probability from historical air transport hull loss data during phases of flight over water, (b) estimate a baseline forecast distribution for the period 2020-2030, without implementation of new GADSS measures, making use of Monte Carlo simulation, (c) estimate forecast distributions for the period 2020-2030 including implementation of new GADSS measures under both mandatory-only and mandatory plus voluntary adoption scenarios, also making use of Monte Carlo simulation, and (d) statistical testing of the thus derived distributions for significance in difference. The forecast distribution of interest for RQ-3 is that of the probability of an oceanic hull loss accident in international waters with high spatial uncertainty (>5NMi LKP), estimated with and without the GADSS implementation.

The baseline probability was estimated as a probability of occurrence per oceanic flight hour, for hull loss accidents occurring in oceanic waters as least 12 miles offshore. Although it is known that the long-term accident rate has a higher correlation to the number of flights than to the number of flight hours (Boeing, 2017), the use of flight hours reflects the format of the available data on oceanic versus continental flight hours (CANSO 2010; 2011; 2012; 2013; 2014; 2015; 2016; 2017).

The twenty air transport category hull loss accidents occurring in oceanic airspace (more than 12 miles or 20km in offshore waters) compiled from the Flight Safety Foundation Aviation Safety Network database (Flight Safety Foundation, 2018) provided a baseline historical dataset between 1980 and 2016, which was summarized by year and by decade. An exponential function of the form:

$$R_{HullLoss} = a.\, e^{b.n_{Dec}} \qquad (7)$$

was estimated, where $R_{HullLoss}$ is the hull loss rate per million oceanic flight hours, a is an empirically estimated constant and n_{Dec} is the number of decades since 1980, with the 1980's as decade 1, the period 2010-2019 is decade 4 and where the $a.\, e^{b.n_{Dec}}$ term adjusts for an approximately exponentially decaying long-term rate per million flight hours, estimated on a ten-year basis. The discrete probability of x oceanic hull loss events in any given year during decade n_{Dec} was then estimated for any given year from the Poisson probability mass function:

$$P(x_{Yr}) = e^{-\mu_{Yr}}.\, \frac{{\mu_{Yr}}^{x_{Yr}}}{x_{Yr}!} \qquad (8)$$

And where

$$\mu_{Yr} = R_{HullLoss} . \sum Oceanic\ Flight\ Hrs\ in\ Yr \quad (9)$$

The Poisson distributed probabilities of x=0,1,2,3 or more oceanic hull loss incidents were estimated on an annual basis for the period 2020-2030, under the assumption that the estimated annual oceanic flight hours will grow at a compound rate of 3.7% per annum during the period, estimated from the prior ten years of data. The $a. e^{b.n_{Dec}}$ term was evaluated at a value of n=4 in 2020 and n=5 in 2030, with -0.1 increments for the intervening years, extending the long term trend of a reduction of this value of approximately -1 every decade, as a result of more modern aircraft, enhanced crew training and safety initiatives, etc. This future rate is in itself a forecast with inherent uncertainty; it is possible that the rate could exhibit asymptotic behavior in the next decade, or that it will continue to decay exponentially as it has since 1980; stepping the value in -0.1 increments approximately takes a line between these two possibilities.

For the baseline scenario forecast, a mean and variance for the cumulative number of hull loss incidents during the period 2020-2029 was estimated by Monte Carlo simulation, where for each year and for each iteration, a random number generator was used to randomly select from one of the four Poisson distributed probabilities of x=0,1,2,3+ proportional to their probability.

This produces an oceanic hull loss forecast distribution, from which the distribution of such events with high spatial uncertainty was derived by application of two other random variables: (a) the success rate of the current generation of installed ELTs and their UWBs, taken as p=0.50 from prior studies (e.g. NASA, 2015; ATSB,2013), and (b) the probability of total communications failure, including ADS-B, VHF and satellite communications, for more than 2 minutes before impact, estimated as p=0.75 based on the incidents in the prior ten years. The selection of 2 minutes in the latter case is based on the requirement to localize the aircraft to within 5NM (BEA, 2011) close to the time of impact to avoid an incident with high spatial uncertainty.

Although the GADSS normal tracking requirements are now in effect, and despite having other positive effects, they are not considered in this study to change the probability of an oceanic loss with high spatial uncertainty due to the distance which can be traveled in 15 minutes; Air France 447 was in fact reporting its position every 10 mins (BEA, 2011) prior to the loss of the aircraft and subsequent long recovery process. The last report in the Air France 447 case occurred approximately 5 minutes before the end of flight and, while a large volume of ACARS traffic was generated by automated condition and health monitoring logic due to a large number of unusual conditions and exceeded tolerances, transmitted via satellite communications including during the descent, none of those transmissions included a position (Schuster-Bruce, 2014). The probability of an oceanic hull loss accident with high spatial uncertainty is taken to be one where both the ELT/UWB *and* loss of communications occur, being the product of the two probabilities, considered for this simulation to be independent. The logic in this case being that when both conditions occur the spatial uncertainty is high, while if either the ELT/UWB functions as required or continuity of communications is maintained to within 2 minutes of impact, one of those conditions is expected to reduce the spatial uncertainty significantly.

For the alternative (GADSS) forecast, the Monte Carlo simulation replicated that as described for the baseline scenario above, with modification to the fleet equipage forecast based on ICAO Annex 6 amendments becoming applicable during the forecast period, and to the random variables used, as described below. For the fleet forecast, new deliveries after 1/1/2021 are modelled to include equipage compliant with the GADSS autonomous distress tracking requirements. Deliveries of new types of aircraft for which the type certificate application is submitted after 1/1/2021 are modelled to include the GADSS flight data recovery requirements for a forecast first delivery date, typically 4-8 years after first application, depending on whether the new type certificate is for an entirely new type or for a new variant; a value of 6 years was used for the simulation. Two new hypothetical types were forecast, with a production rate of 200 per year for each type each, growing by 3.5% per year.

The random variables used in the alternative (GADSS) Monte Carlo simulation modified the forecast success rate of 0.50 for the ELT used for the baseline forecast to 0.85 for newly equipped aircraft, which includes flight data streaming, ELT-DTs or ADFRs and the probability of total communications failure was modified from 0.75 to 0.15, to allow for the improvements implemented in autonomous distress tracking measures, while the non-zero modified value reflects the existence of sudden impact scenarios where these measures would be ineffective. Space-based ADS-B is not factored into the model as an autonomous distress tracking capability, as total communications failure includes loss of transponder function, after which neither SSR nor space-based ADS-B are effective. Flight data streaming via satellite communications is included in the model in so far as new ADT or FDR compliant solutions incorporate that capability.

The selection of p=0.85 reflects that fact that the GADSS measures improve upon the current situation but cannot be realistically modelled to assume an absolute certainty of success. The effectiveness of ADT triggers and equipment has yet to be demonstrated, while

ADFR experience on military types has produced mixed results, and no substantial baseline currently exists for ELT-DT reliability in actual emergency situations. Furthermore, even if the equipment itself were 100% reliable, there are a set of circumstances where these measures may still prove to be ineffective. For example, a mid-air collision or explosion at altitude is likely to provide insufficient time for any triggering mechanism to work and in any case may still lead to high spatial uncertainty even if the ADFR and/or ELT-DT are present and operative, while continuous streaming of flight data (without triggering) could provide information up until to point of lost communication, likely to be very close to the time of incidence in these scenarios.

The selection of p=0.85 for the simulation reflects an expectation that the performance will improve substantially over the current generation of equipment, however also reflecting the sum of the effects above, i.e. the uncertainty about actual performance in practice and the finite probability of events other than loss of control in flight.

The additional random variable included in the second simulation is that of voluntary adoption of GADSS ADT and FDR measures in cases where it is non-mandated. This could happen in a number of ways; for example, new aircraft delivered in the 2020's for which the type certificate was issued prior to 1/1/21 could feasibly be equipped with the new ADT or FDR capabilities, or both, either as an option or as standard, even though there is no regulatory requirement to mandate their installation on those aircraft.

Furthermore, aircraft operators may elect to retrofit existing aircraft with such capabilities, depending on the priorities for the operator, the potential additional benefit of the retrofit (for example making operational use of streamed data), the age and remaining service life of the aircraft, and so on. This was modelled as a random variable of between 0.10 and 0.70 for new deliveries after 2021 and between 0.05 and 0.50 for the existing fleet.

To test the RQ-3 hypotheses:

H-3 $H_{3\text{-}0}$: No statistically significant reduction in the estimated probability of an oceanic hull loss with high spatial uncertainty is forecast during the period 2020-2030 as a result of the GADSS measures.

$H_{3\text{-}A}$: A statistically significant reduction in the estimated probability of an oceanic hull loss with high spatial uncertainty is forecast during the period 2020-2030 as a result of the GADSS measures.

a test for significance in the difference between the Poisson rates estimated from the Monte Carlo simulations described above was conducted using the r Poisson test, a binomial test conditioned on the event counts, at an α=0.05 level of significance.

CHAPTER IV

FINDINGS

The obtained results based on the methodological approaches described in the previous chapter are set out in the sections below. First, for RQ-1(a), the results of the tests for statistical heterogeneity performed on the ocean drift and satellite communications sub-groups are presented, followed by, for RQ-1(b), the results of the meta-regressions performed on the satellite communications sub-group. No regression was performed on the ocean drift sub-group as it was found to be statistically homogenous. Also for RQ-1(b), the results of statistical tests performed on the BFO bias for difference in the mean value on the same channel between the MH371 and MH370 flights and between the MH370 flight before and after the 18:25Z restart are presented, together with analysis of the between channel differences and estimation of the post 18:25Z bias value.

For RQ-2, the results of the linear regressions performed using a BFO plus fixed AES antenna gain power model and that using a BFO plus variable gain model are presented, together with statistical analysis on the results. The systematic sampling results are also presented, in the form of sensitivity analysis charts and estimated probability density functions, for which the Kolmolgorov-Smirnov and Hartigan's dip test results are presented. Finally, for RQ-3, the results of the Monte Carlo simulations and subsequent statistical testing are presented.

RQ-1. Meta-Analysis, RQ-1(a)

For the studies identified in Tables 1 and 2, which provide geospatial estimates of the MH370 trajectory and/or end of flight vicinity: (a): Is the observed variation in estimated probable impact location for MH370 across these studies likely due to random variation within the range of uncertainty of the observed data and propagated error, or do the studies exhibit statistical heterogeneity?

H-1(a): *For the satellite communications and ocean drift sub-groups:*

$H_{1a\text{-}0}$: There is no statistically significant heterogeneity across the studies.

$H_{1a\text{-}A}$: There is statistically significant heterogeneity across the studies

Satellite Communications Sub-Group. The Q-test for statistical heterogeneity of the satellite communications sub-group with 25 degrees of freedom resulted in a Q value of 6368.5 for both the unweighted fixed effects model and weighted random effects model, for which the p-value in both cases is <0.0001. The forest plots for each of the fixed and random effects models are shown in Figure 22 and Figure *23*.

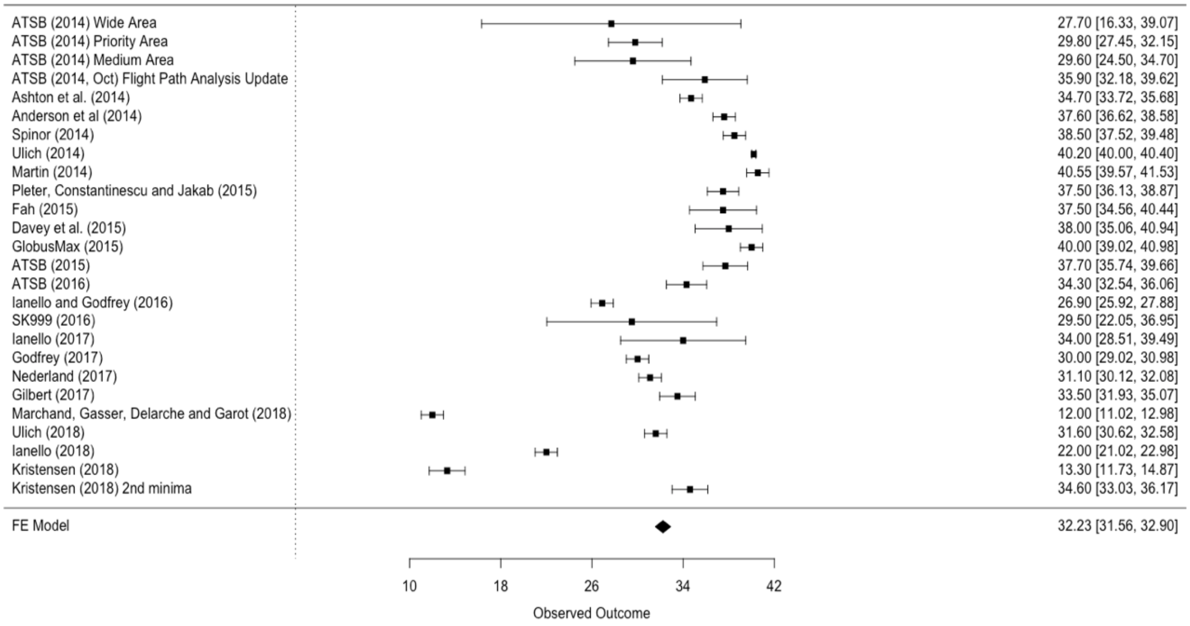

Figure 22. Fixed Effects Unweighted Forest Plot, Satellite Communications Sub-Group

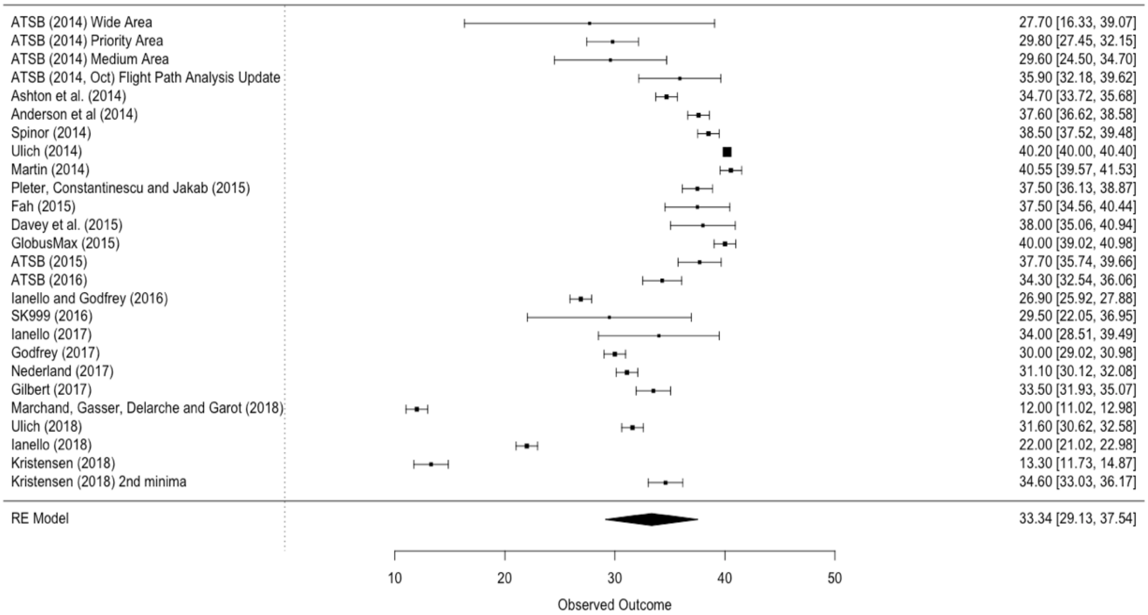

Figure 23. Random Effects Weighted Forest Plot, Satellite Communications Sub-Group

As the studies are listed in approximate order of publication in the forest plots, a broad trend during the period 2014-2018 can be observed, where an initially wide estimate centered around 28S was followed by a sequential trend of the estimates toward the south, with the study results concentrating in the 35-40S region from late 2014 through 2015. From the beginning of 2016, the general trend can be seen to be to the north of that region, together with an increasing spatial dispersion of the estimates during the 2017-2018 period.

Under both models, the data were found from the Q-test to be statistically heterogenous at a level of significance greater than 0.9999, under the assumptions previously described for the imputation of the first and second moments of the sample distributions for each study. Therefore, the null hypothesis H_{1a-0} was rejected in the case of the satellite communications sub-group.

Ocean Drift Sub-Group. The Q-test for statistical heterogeneity of the ocean drift sub-group with 11 degrees of freedom resulted in a Q value of 6.55 for both the unweighted fixed effects model and weighted random effects model, for which the p-value in both cases is 0.83. The mean of the imputed mean locations is 30.2S. The forest plot for the fixed effects unweighted model is shown in Figure 24.

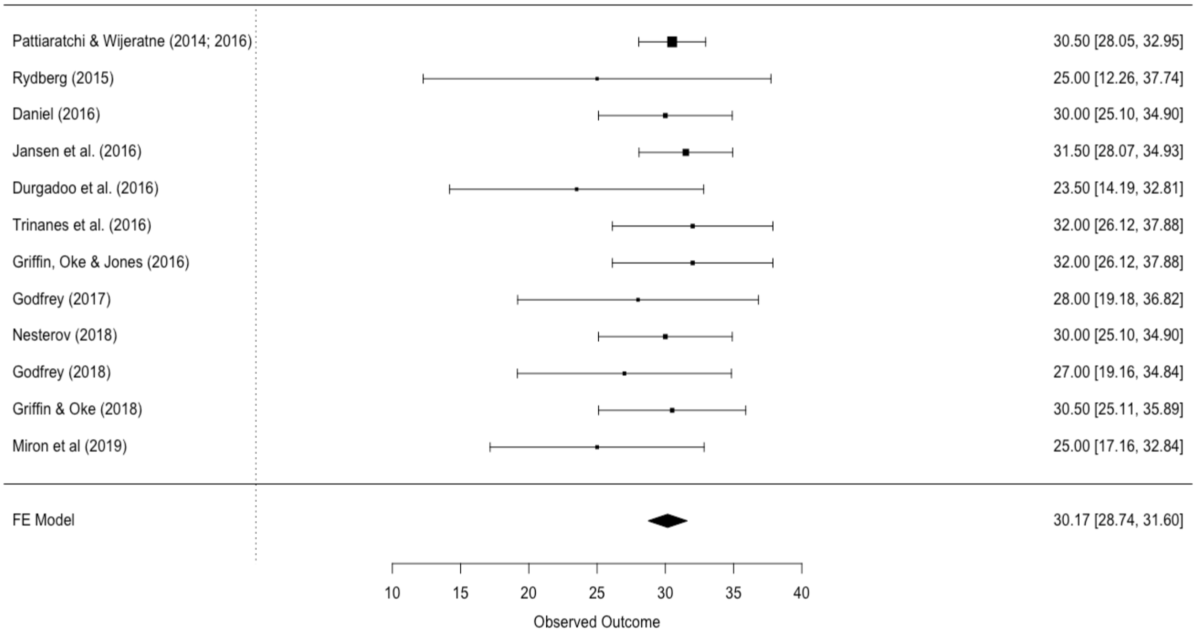

Figure 24. Fixed Effects Unweighted Forest Plot, Ocean Drift Sub-Group

The studies in the forest plot are listed in the approximate order of publication during the period 2014-2018 and it can be observed that the range estimates have been reasonably consistently centered in the vicinity of 30S, with the spread of the range around that vicinity being the main distinguishing characteristics of the different studies, most of which is concentrated in the 25S-35S range, although extending many degrees or more beyond that in some cases.

Under both models, the data were found from the Q-test to be statistically homogenous at the tested level of significance of α=0.05, under the assumptions previously described for the imputation of the first and second moments of the sample distributions for each study. Therefore, the null hypothesis H_{1a-0} was accepted in the case of the ocean drift sub-group.

RQ-1. Meta-Analysis, RQ-1(b) H-1b-1.

Assumptions of Linear Regression. The scatterplots between the dependent variable (the arc-latitude estimate) and each of the candidate predictors are shown in Figure 25. The negative linear trend visible for the Cumulative True Track Changes predictor (upper left panel) is supported by the regression result for that covariate in isolation (r^2 and p-values of 0.71 and <0.0001 respectively) and by the correlation coefficient of -0.67; this is also the case for the Variation in Ground Track Velocity of Constituent Trajectories (upper right hand panel) predictor, although both on visual inspection and in the single predictor regression result (r^2 =0.29, p-value= 0.0016) the relationship can be seen to be weaker, especially toward the lower latitude estimates. The correlation coefficient in this case is -0.46.

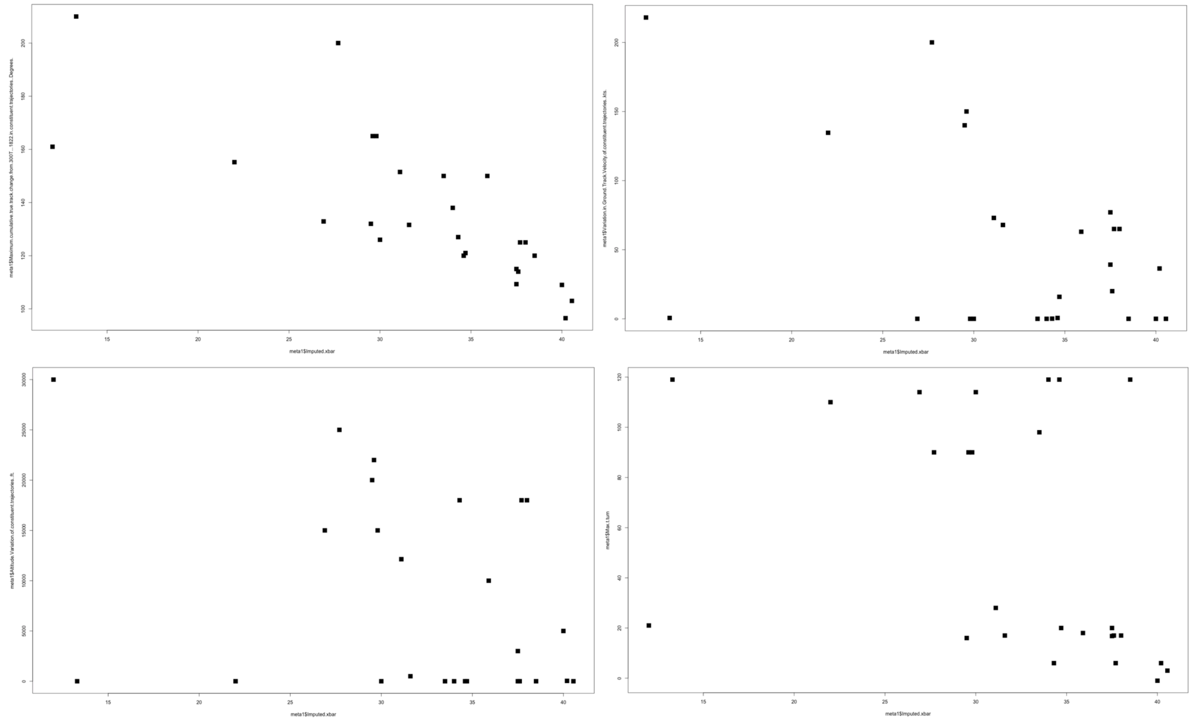

Figure 25. Scatterplots of candidate predictors versus arc-latitude estimates: cumulative turns (upper left panel), velocity variation (upper right), altitude variation (lower left) and time of turn south (lower right).

For the Maximum Time to Turn South (lower left panel) and Variation in Altitude of Constituent Trajectories (lower right), a clear linear relationship is not readily apparent on visual inspection, while the correlation coefficients are the lowest of the four (-0.35 and -0.41 respectively). Furthermore, the altitude variation and velocity variation candidate predictors were found to be correlated with one another (correlation coefficient = 0.66). Based on the weaker linear relationship and in order to avoid the introduction of multicollinearity into the regression by inclusion of both the altitude and velocity predictors, the time to turn and altitude variation candidate predictors were excluded from the combined regression.

The histogram and normal Q-Q plot of the residuals from the combined regression are shown in Figure 26, for which the mean is calculated as 1.59 with a standard deviation of 5.1. Although some deviation from normality can be observed, particularly in the positive tail due to one influential point, a two-tailed t-test for significance of the difference of the estimated mean to the assumed value of zero yielded a t statistic of 1.59 and a p-value of 0.12, such that the null hypothesis of zero mean was not rejected at an α=0.05 level of significance.

The large positive residual is generated by study number 1 in the meta-analysis, namely the initial ATSB (2014) wide area search definition; at 3.4 standard deviations it is rather improbable in a Gaussian distribution, however it was not considered to be sufficiently improbable to justify rejection as a true outlier to the distribution. Additionally, the Anderson-Darling test for normality was performed on the regression residuals including this value and the null hypothesis of normality was accepted at an α=0.05 level of significance.

The presence of this larger but feasible within the estimated distribution was not taken as evidence for non-constant variance, nor was the variance concluded to increase or decrease significantly across the sample based on inspection of the residual plots, hence the linear regression assumption of constant variance is considered to be met.

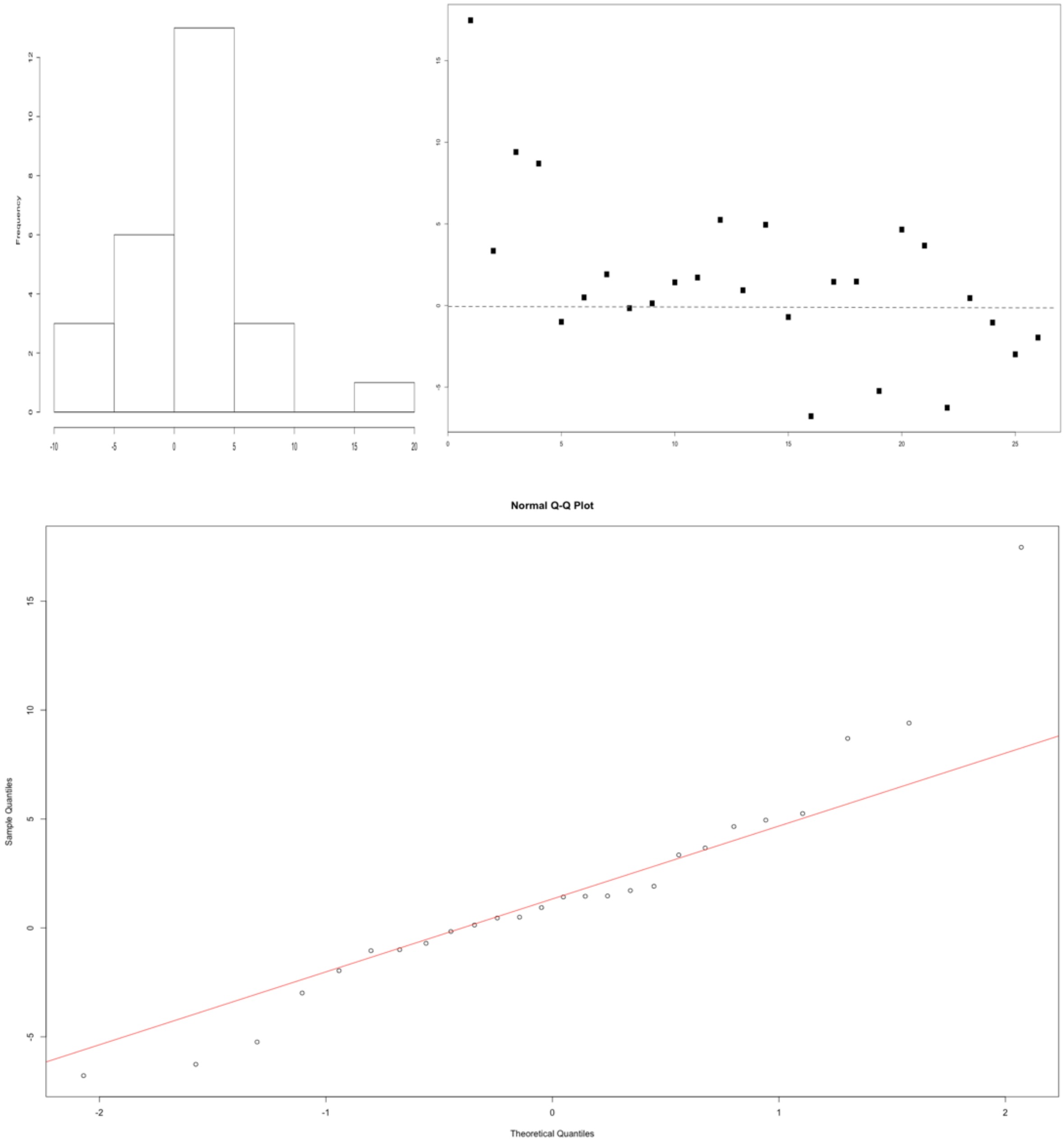

Figure 26. Regression Residuals: Histogram (upper left panel), Scatterplot (upper left) and Normal Q-Q Plot (lower)

Hypothesis Testing. For the studies identified in Tables 1 and 2, which provide geospatial estimates of the MH370 trajectory and/or end of flight vicinity:

(b): To which factors are the arc-latitude estimates most sensitive?

H-1(b): *For each regression coefficient (predictor) or set of coefficients:*

$H_{1b\text{-}1\text{-}0}$: The regression coefficient (predictor) is not significantly different to zero (zero slope).

$H_{1b\text{-}1\text{-}A}$: The regression coefficient (predictor) is significantly different to zero (zero slope).

Given the stronger apparent linear relationship between the dependent variable and the independent variables of Cumulative True Track Changes and the Variation in Ground Track Velocity of Constituent Trajectories, and the relatively low correlation between those two variables (0.2), the meta-regression was estimated with those two predictors, while the sensitivity of the arc-latitude estimates to the constituent altitude changes and the time of turn south is considered to be relatively low.

Table 6

Meta-Regression Results with 2 Coefficients

		95% CI		
Variable	Coefficient b_i	LL	UL	p-value
Constant	63.6210	52.2211	75.0221	<0.0001
Maximum Cumulative Track Change from 296(T)	-0.225	-0.3100	-0.1406	<0.0001
Variation in Ground Track Velocity of Constituent Trajectories	-0.0417	-0.0719	-0.0011	0.007
R^2	0.78			
QM Test of Moderators (df=2)	53.97			<0.0001
QE Test for Residual Heterogeneity (df=21)	658.4			<0.0001

The results for the combined meta-regression including the two predictors noted above are presented in Table 6. In the combined regression, the p-value for the non-zero test of the predictor was less than the tested α=0.05 level of significance in the case of both the cumulative true track changes and variation in ground track velocity predictors, therefore for the combined regression the null hypothesis $H_{1b\text{-}1\text{-}0}$: was accepted in both cases (maximum time to turn south and variation in altitude of constituent trajectories) and rejected for the former two (cumulative true track changes and variation in ground track velocity).

The regression r^2 value of 78% indicates that the predictors explain a substantial amount, but clearly not all, of the heterogeneity; also evidenced by the very low p-value (<0.0001) for the (Cochran's Q) test for residual heterogeneity, thus there are almost certainly additional factors contributing to the observed variation which are not included in the model.

Of the predictors tested and under the assumptions previously described, the arc-latitude estimates in the satellite communications sub-group of the selected meta-analysis studies were found to be most sensitive to the cumulative track changes of the constituent trajectories used in the estimation, followed by the constituent range of ground track velocities, for which the null hypothesis $H_{1b\text{-}1\text{-}0}$ is rejected in both the case of regression in isolation and in combination. Due to the marginal result for regression in isolation in both cases, the null hypothesis $H_{1b\text{-}1\text{-}0}$ is found to be accepted in the case of the maximum time to turn south and variation in altitude of constituent trajectories. Of all four predictors selected to assess the sensitivity of the arc-latitude estimates against, the cumulative track changes predictor is the most significant result. Hence, *sensing of direction* at each of the BTO arc crossing points is of particular interest in distinguishing between different potential trajectories and possible end points, which serves as additional motivation for RQ-2 of the present study.

RQ-1. Meta-Analysis, RQ-1(b) H-1b-2.

For each bias used in estimation, across time and across channels:

$H_{1b\text{-}2\text{-}0}$: There is no significant different in the bias over time or across channels.

$H_{1b\text{-}2\text{-}A}$: There is a significant different in the bias over time or across channels.

The BFO bias was tested for (a) significance in difference between the MH371 and MH370 flights, i.e. before and after a shutdown and restart, (b) significance in difference of the R-1200-0-36ED channel compared to other R-channels, (c) significance in difference for the MH370 flight before and after the 18:25Z restart, and (d) sensitivity to a slight change in return link transmission frequency within the 1645-1655MHz range.

The two-sample t-test result for the difference in mean BFO bias on the R1200-0-36ED channel between the MH371 (Mean bias = 171.36) and MH370 (Mean bias = 150.8) flights generated a t statistic of 42.4 evaluated at 23 degrees of freedom, with a p-value of $<2.2 \times 10^{-16}$. Thus, the difference in means is found to have changed significantly between the two flights when tested at an α=0.05 level of significance and therefore the null hypothesis $H_{1b\text{-}2\text{-}0}$ is rejected, with the new bias estimated as 150.8 Hz when using only the MH370 cruise data (17:07Z transmission).

The two-sample t-test for a difference in the mean BFO bias on the R1200-0-36ED during the MH370 flight, before (Mean Bias = 150.8) and after (Mean Bias = 152.1) the in-flight restart at 18:25Z using the last two observed values in the R1200-0-36ED sequence (due to a decaying time varying bias in the earlier observations during that sequence) generated a t statistic of -2.18 evaluated at 10 degrees of freedom and a p-value of 0.054 when using both of the final two observations in the sequence. When tested on the final and penultimate observations in the sequence in isolation, both evaluated at 9 degrees of freedom, the resulting t statistics and p-values were -1.093 and a p-value of 0.30, and -2.0/0.07, respectively.

In all three cases, the difference in means for the estimated BFO bias during the MH370 flight data before and after the 18:25Z restart is not found to have changed significantly when tested at an α=0.05 level of significance, therefore the null hypothesis H_{1b-2-0} is accepted and thus it is inferred that the MH370 R1200-0-36ED BFO remained at a value of approximately 150Hz during the subsequent observations, at least until the 6th BTO arc prior to the second in-flight restart at approximately 00:15Z.

A more precise value of 150.4Hz was estimated by four different methods as illustrated in the figure below:

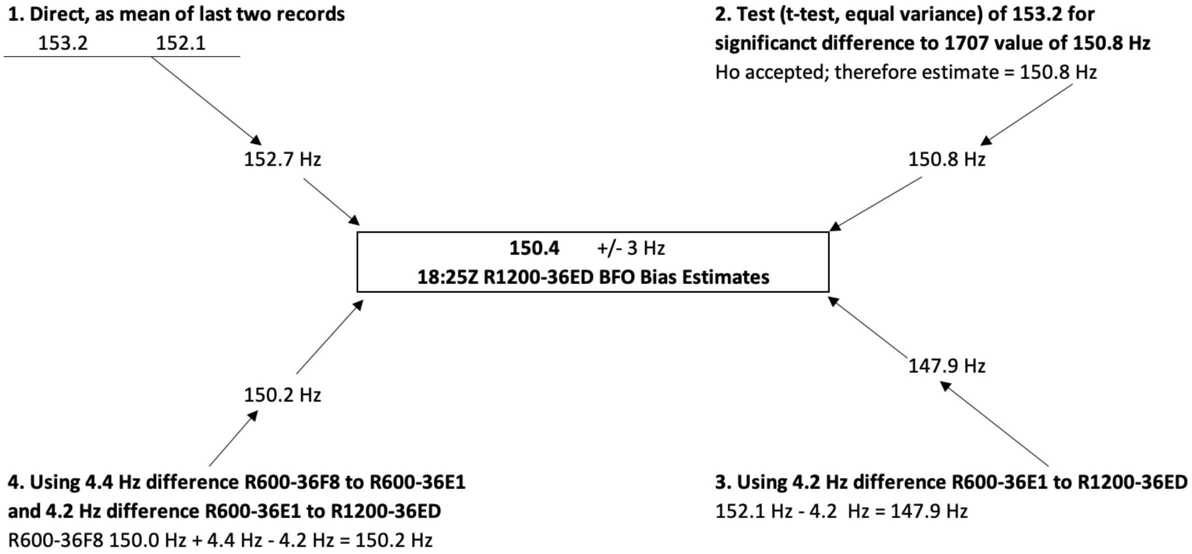

Figure 27. Estimate of R1200-0-36ED Channel BFO Bias at 18:28Z

First, the channel BFO bias was estimated directly by taking the mean of the last two records of the R1200-36ED transmissions in the 1825Z sequence. Only the last two observations were used for the 1825Z sequence due to the presence of the large but rapidly decaying additional transient bias in the R1200-36ED data at the start of the sequence (although the bias may not have decayed entirely by the end of the sequence). Second, the t-test described above provides another estimate, as not being found to be significantly different to the 150.8Hz estimated from the 17:07Z MH370 cruise data. The third and fourth estimates take advantage of the fact that the first channel used in the 18:25Z restart sequence is the R600-36E1 channel, which does not appear to be affected by the same large 30Hz transient bias as the R1200 channel. From data recorded in the earlier MH371 flight, the difference between the two channels is -4.2 Hz, then applied to the R600-36E1 channel to derive the third estimate. The fourth estimate takes a similar approach, but applying a previously observed +4.4Hz difference between the R600-36F8 and R600-36E1 channels, both used on the MH370 flight, applied to the R600-36F8 BFO bias estimated prior to the shutdown when the aircraft position was known, with the -4.2 Hz R600-36F8 to R1200-36ED difference then applied. The fact that this last estimate is within 0.2 Hz of the mean value is taken as evidence that the R600-36E1 channel may not have been affected by the same ~30Hz transient bias as the R1200-0-36ED channel during the 18:25Z restart sequence.

As shown in the graphic, the unweighted mean of the four estimates is 150.4 Hz, which agrees within 0.32 Hz with the mean of the reported and inferred BFO bias values used in the studies selected for the meta-analysis where such data were available (μ = 150.08 Hz, n=7, σ=0.35Hz) and agrees with the original estimate of Ashton et al (2014) to within 0.4 Hz. Therefore, the 150.1Hz value was taken as the best estimate of the R1200-0-36ED channel based on all these estimated and, accordingly, was used as the BFO bias value for the sensitivity analysis and probability density function estimates performed for RQ1(c).

The results for the Anderson-Darling test, a modification of the Kolmogorov-Smirnov test, to assess whether or not the underlying noise in the R1200-0-36ED channel follows a Gaussian distribution (in the absence of a transient bias), are as follows: n=42 R1200-0-36ED

Channel BFO Bias residuals sampled over a 15 ½ hour period from 01:37Z to 17:07Z, A statistic = 0.56476, p-value = 0.135. A normal Q-Q plot is shown below.

The null hypothesis of the distribution being approximately Gaussian (in the absence of the transient bias) was accepted at an α=0.05 level of significance, with a p-value of 0.135 for the Anderson-Darling test. This result supports the use of statistical tests which assume a Gaussian distribution, and the use of a Gaussian probability density function in the likelihood estimation for the conditional probability density of an observed BFO residual given a sampled heading, velocity and position.

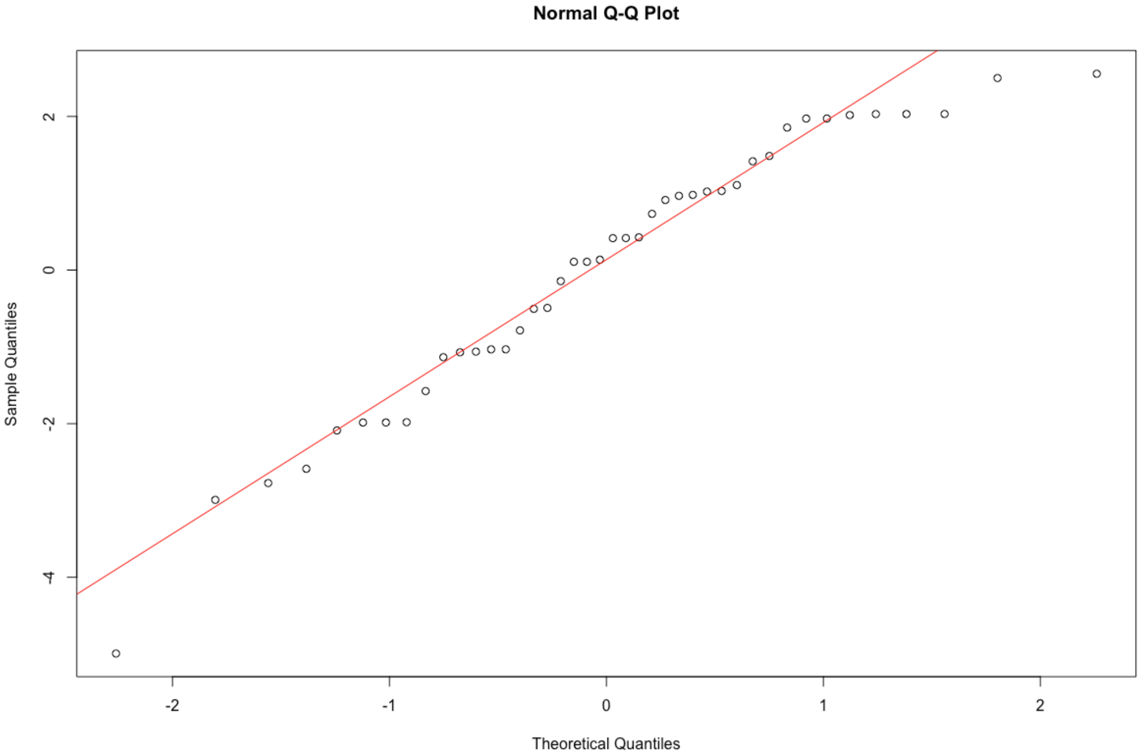

Figure 28. Q-Q Plot for n=42 R1200-0-36ED Channel BFO Bias residuals sampled over a 15 ½ hour period from 01:37Z to 17:07Z.

R600 Channel Bias Estimation. The first observation in the sequences for the 18:25Z and 00:19Z restarts were transmitted on the R600-0-36E1 and R600-0-36F8 channels, respectively, as shown in Table 7 and Table 8.

Table 7

00:19Z R600 and R1200 Channel Observations (BFO and Received Power)

Date and Time (UTC)	Transmission Channel	BFO Observed (Hz)	Received Power Observed (dBm)
8/03/2014 00:19:29.416	IOR-R600-0-36F8	182	-50.95
8/03/2014 00:19:37.443	IOR-R1200-0-36F6	-2	-53.65

Table 8

18:25Z R600 and R1200 Channel Observations (BFO and Received Power)

Date and Time (UTC)	Transmission Channel	BFO Observed (Hz)	Received Power Observed (dBm)
7/03/2014 18:25:27.421	IOR-R600-0-36E1	142	-52.34
7/03/2014 18:25:34.461	IOR-R1200-0-36ED	273	-54.59
7/03/2014 18:27:03.905	IOR-R1200-0-36ED	176	-54.15
7/03/2014 18:27:04.405	IOR-R1200-0-36ED	175	-54.7
7/03/2014 18:27:08.404	IOR-R1200-0-36ED	172	-54.86
7/03/2014 18:28:05.904	IOR-R1200-0-36ED	144	-54.54
7/03/2014 18:28:14.904	IOR-R1200-0-36ED	143	-54.47

The estimated BFO bias and received power difference between the R600-0-36E1 and R1200-0-36ED channels is to both these channels are provided below.

Table 9

Estimation of BFO and Received Power Differences R600-0-36E1, R1200-0-36ED Channels

Channel	Proximity of Observation Times (Times of Closest Transmission) UTC	n=	BFO (Hz)	BFO Sample Std. Dev.	Cross-Channel BFO Difference (Hz)	Received Power (dBm)	Received Power Sample Std. Dev.	Cross-Channel Received Power Difference (dB)
R1200-0-36ED	7/03/2014 01:37:25.923	6	214.8	1.9	4.2	-56.2	0.2	2.4
IOR-R600-0-36E1	7/03/2014 01:36:59.429	2	219.0	0.0		-53.9	0.2	
R1200-0-36ED	7/03/2014 04:03:55.416	11	232.9	0.9	3.6	-55.6	0.1	2.8
IOR-R600-0-36E1	7/03/2014 04:03:36.421	2	236.5	0.7		-52.8	0.0	
IOR-R1200-0-36ED	7/03/2014 06:48:26.462	2	226.0	0.0	6.0	-54.3	0.1	2.7
IOR-R600-0-36E1	7/03/2014 06:48:20.414	2	232.0	0.0		-51.5	0.0	
IOR-R1200-0-36ED	7/03/2014 07:29:42.433	11	177.3	1.1	4.2			
IOR-R600-0-36E1	7/03/2014 07:29:22.411	2	181.5	0.7				
Combined Mean Difference R1200-0-36ED to R600-0-36E1 Channel (BFO Bias and received power)					4.2			2.7
Combined Standard Deviation					1.4			0.2

For the t-test on the observed BFO difference between the R600-0-36E1 observation of 142 Hz (Table 8) and the mean of the last two R1200-0-36ED observations of

143.5 Hz (Table 8), based on the estimated cross-channel difference of 4.2 Hz (Table 9), the expected difference between the R600 observation of 142 Hz minus the 4.2 Hz offset (=137.8), and the R1200 mean observation of 143.5 Hz, is zero. The t statistic for the observed 5.7 Hz difference and the 5.7 Hz (coincidentally) estimated standard deviation for the computed difference of two observations each with a 4 Hz standard deviation, is calculated as 1.16, where the critical value of t for 1 degree of freedom is 12.7. Thus, the null hypothesis Ho of the observed difference not being significantly different to zero is accepted and therefore the observed difference in BFO is not found to be statistically significant. This is also taken as one point of evidence against the rejection of the R600-0-36E1 as unreliable or as a statistical outlier so far as the BFO observation is concerned.

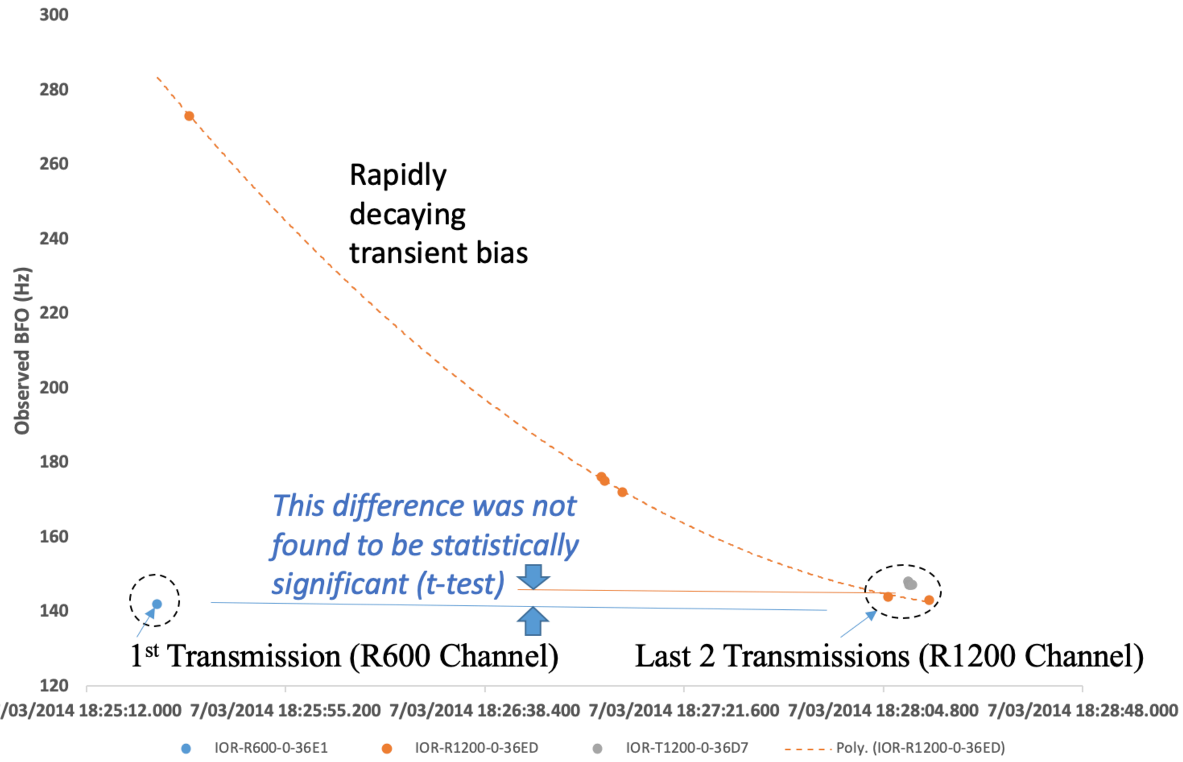

Figure 29. 18:25Z Test of BFO Bias Difference Between R600 Channel (1st Transmission) and R1200 Channel (Last 2 Transmissions)

For the t-test on the observed received power difference between the R600-0-36E1 observation of -52.34 dBm (Table 8) and the mean of n=6 R1200-0-36ED received power observations, equal to -54.55 dBm (the transient BFO bias does not affect the received power, the two being independent, thus all data can be used in this case) based on the estimated cross-channel difference of 2.7 dBm (Table 9), the expected difference between the R600 observed received power level of -52.34 dBm minus the 2.7 dBm offset (= -55.04 dBm), and the R1200 mean observation of -54.55 dBm, is zero. The t statistic for the observed 0.48 dBm difference and the 2.3 dBm estimated standard deviation for the computed difference of two observations each with a 1.6 dBm standard deviation, is calculated as 0.28, where the critical value of t for 5 degrees of freedom is 2.571.

Thus, the null hypothesis Ho of the observed difference not being significantly different to zero is accepted and therefore the observed difference in received power is not found to be statistically significant. This is also taken as evidence against the rejection of the R600-0-36E1 as unreliable or as a statistical outlier so far as the received power observation is concerned.

The C/No carrier-to-noise density observation, not shown or tested here, on inspection is likely to be significantly different to an expected value, however given the result above it is suggested that this is due to an increase in the denominator, i.e. the noise power density, as opposed to the numerator. That is, an apparent increase in the noise power somewhere in the communications chain at the time of the R600 channel transmission appears to have resulted in a much lower than normal C/No observation, however the received power observation does not appear to have been affected (nor the BFO).

For the 00:19Z R600 channel (R600-0-36F8), the estimated fixed BFO bias from the two-stage procedure described in Chapter III is 150.0Hz as shown in Table 10 and for the received power offset in Table 11.

Table 10

Estimation of R600-0-36F8 Fixed BFO Bias

Channel	R1200-0-36ED BFO Bias	Delta Bias 1 (36ED to Intermediate Channel)	Intermediate Channel Bias Estimate	Delta Bias 2 (Intermediate Channel to 36F8)	R600-0-36F8 Channel Bias Estimate
IOR-R1200-0-36ED	150.1				
IOR-R1200-0-36D3		2.8	152.9	-4.2	148.7
IOR-T1200-0-36F2		0.4	150.5	-0.5	150.0
IOR-T1200-0-36D8		3.2	153.3	-2.0	151.3
Mean Estimated R600-0-36F8 BFO Bias (Hz)					150.0

Table 11

Estimation of R600-0-36F8 to R1200-0-36ED Received Power Offset

Channel	R1200-0-36ED	Delta Prx 1 (36ED to Intermediate Channel)	Intermediate Channel Power Difference Estimate to 36ED	Delta Prx 2 (Intermediate Channel to 36F8)	R600-0-36F8 Channel Power Difference Estimate to 36ED
IOR-R1200-0-36ED	0				
IOR-R1200-0-36D3		-0.5	-0.5	4.3	3.8
IOR-T1200-0-36D7		-0.4	-0.4	3.9	3.5
IOR-T1200-0-36D8		-0.2	-0.2	3.3	3.2
Mean Estimated R600-0-36F8 Power Difference to R1200-0-36ED Channel					3.5

Table 12

Estimation of BFO and Receiver Power Offsets, R1200-0-36ED and R1200-0-36F6 Channels

Channel	Proximity of Observation Times (Times of Closest Transmission) UTC	n=	BFO (Hz)	BFO Sample Std. Dev.	Cross-Channel BFO Difference	Received Power (dBm)	Received Power Sample Std. Dev.	Cross-Channel Received Power Difference
IOR-R1200-0-36ED	7/03/2014 06:48:26.462	3	226.0	0.0	-0.8	-54.3	0.1	-0.4
IOR-R1200-0-36F6	7/03/2014 06:48:33.907	9	225.2	0.4		-54.6	0.3	
IOR-R1200-0-36ED	7/03/2014 06:10:59.909	2	234.5	0.7	-0.7	-54.5	0.1	0.3
IOR-R1200-0-36F6	7/03/2014 06:10:48.413	10	235.2	1.3		-54.7	0.1	
Combined Mean Difference R1200-0-36ED to R1200-0-36F6 Channel (BFO Bias and received power					-0.8			-0.1
Combined Standard Deviation					1.1			0.4

For the z-score test as described in Chapter III, the BFO difference between that observed on the R1200-0-36F8 channel at 00:19Z (-2 Hz, Table 7) and that observed on the R600 channel (182 Hz, Table 7) minus the 0.8 Hz offset, equates to more than 32 standard deviations, thus further testing is hardly necessary to conclude that the difference is statistically significant. Based on a p-value of <0.0001 the null hypothesis is rejected and it is concluded that the difference is statistically significant.

In the case of the received power difference between the two channels during the 00:19Z sequence, the observed received power difference is 0.9 dBm when the 3.6 dBm offset is applied to the R600 channel observation, where a z-score of 0.9/2.2=0.40 corresponds to a cumulative density of 0.655, such that the area under the normal curve within +/- 0.4 standard deviations is (0.655-0.5)*2 = 0.31, which is taken as insufficient evidence to reject the hull hypothesis that the observed difference is significantly different to zero, at a 0.05 level of significance.

RQ-2. Antenna Spatial Characteristics as a Direction Sensing Technique

For the studies identified in Tables 1 and 2, which provide geospatial estimates of the MH370 trajectory and/or end of flight vicinity:

(c): Can the spatial characteristics of antennas be used to reduce the uncertainty in the estimates?

H-2 $H_{2\text{-}0}$: There is no significant difference in the sum of squared residuals for a linear model estimated using BFO data and a fixed gain model and that estimated using both BFO data and the peak gain variation model for the AES antenna.

$H_{2\text{-}A}$: A statistically significant difference is found in the sum of squared residuals for a linear model estimated using BFO data and a fixed gain model and that estimated using both BFO data and the peak gain variation model for the AES antenna

If the antenna gain variation effect is present at all, its effects are likely to be most apparent when large differences exist between a fixed value and that predicted by the variable model. For the MH371 flight, the best examples of this occur during the earlier part of the flight, where the highest and lowest variable gain estimates occur within less than 90 minutes of one another; a heading of 236(T) at 01:55 leads to a gain estimate of 10.4dBic given the relative aircraft-spacecraft geometry at that time, while at 03:21Z a heading of 158(T) leads to a gain estimate of 14.1dBi, an increase of 3.7dB. Nine minutes later, a turn of over 60 degrees to the right resulted in an updated gain estimate of 11.7dBi; a subsequent decrease of 2.4dB. Table 13 shows the time, heading, observed received power at the GES, the number of observations, predicted AES antenna gain and, in the two right-hand columns, the difference in gain predicted from the AES antenna gain model, followed by the difference in received power as observed between the two observation epochs. It can be observed that in these cases, the observed-calculated residuals are in the order of <0.4dB in the first case where the largest change in calculated gain occurs and ~1.3dB in the second case.

Table 13

Predicted and Observed Power Differences During Major Heading Changes

Time (UTC)	Heading (True)	Observed received power level (dBm)	Number of observation samples (n)	AES antenna gain estimated from variable gain model (dBic)	Predicted difference in received power between observations due to antenna gain variation	Observed difference in received power between observations
01:55	236	-59.06	25	10.4	3.7	3.3
03:21	158	-55.75	9	14.1	-2.4	-1.1
03:29	219	-56.80	95	11.7		

For the fixed gain model, either at 12dBi or 13.1dBi, the predicted change in power due to antenna gain variation is zero, hence the residuals under that model would equal

+3.3dB and -1.05dB respectively. Thus, the variable model has a lower residual in the first case and a higher one in the second case, however the sum of the squares of the residuals (1.98 and 11.99 respectively) is lower for the variable model.

This small sample of the data is presented to illustrate these apparent effects during the MH371 flight when the predicted changes in gain, and thus in received power, are substantial. The regression results below describe the more comprehensive comparison of the fixed estimate and the variable estimate on an observation-by-observation basis over 937 received power observations made between 01:55Z and 17:07Z, including long phases of the MH371 flight where the direction of flight was generally constant and little to no gain variation was predicted, as well as periods such as the one shown above, where the changes were significant. The broad question under investigation being whether the variable model generally fits better to the observed data than the fixed model over a larger sample.

Test for Presence and Detectability of Antenna Gain Variation. As described in Chapter III, the presence and detectability of the antenna gain variation effect was evaluated by performing two nested linear regressions lm_1 and lm_2, the first assuming a fixed gain of 12dBi and the second including the application of the $\Delta G_{\alpha\emptyset t}$ term to the 12dBi constant, calculated for the appropriate true heading, geographical position for each of the n=937 individual observed received power values sampled between 01:55Z to 17:07Z, for which the heading of the aircraft at the time of observation necessary for the $\Delta G_{\alpha\emptyset t}$ parameter estimation was either known or could be estimated with a high degree of confidence.

Figure 30 shows the raw data on which the lm1 and lm2 regressions are performed, with the fixed 12dBi gain data in the upper panel and the variable gain model in the lower panel. The dependent variable, i.e. the observed received power at the GES, is plotted on the x-axis and the independent variable, in the first case the predicted received power using a fixed 12dBi gain AES antenna model and in the second case the predicted received power using the variable AES antenna gain model, is plotted on the y-axis. The blue lines indicate a perfectly linear relationship, as would be observed if the predicted values exactly matched the observed values.

It can be observed that (a) a substantial amount of unmodeled variation exists between the predicted and observed values in both cases and (b) visual inspection of the distribution of the second model data about the line may suggest a closer fit to a linear relationship than the first.

This is not entirely unexpected in this case, as the intercept estimates the mean of the received power if the predicted received power was zero, and the received power would be expected to be zero in that instance, i.e. the intercept is expected to be zero. On the other hand, the significant result for the non-zero value of the slope for the predictors supports the existence of a linear relationship, albeit a relatively weak one, between the dependent and independent variables, including for the $\Delta G_{\alpha\emptyset t}$ term.

Table 14 provides the summary regression results for lm_1 and lm_2, where the adjusted r^2 value for the lm_2 regression (0.294) can be seen to be approximately double that for the lm_1 model (0.145), indicating a relatively better performance lm_2 model in explaining the variation in received power, although the low overall absolute values of r^2 in both cases indicates that much of the variation in received power is due to factors other than the antenna gain variation and other parameters included in the physical model.

While the low p-values for the predictors in all cases indicate non-zero slope, the p-values for the intercept in both cases indicates a non-significant result. The p-value for the intercept reports the result of a null hypothesis (t-) test that the intercept is equal to zero, therefore in this case the null hypothesis that the intercept=0 is accepted.

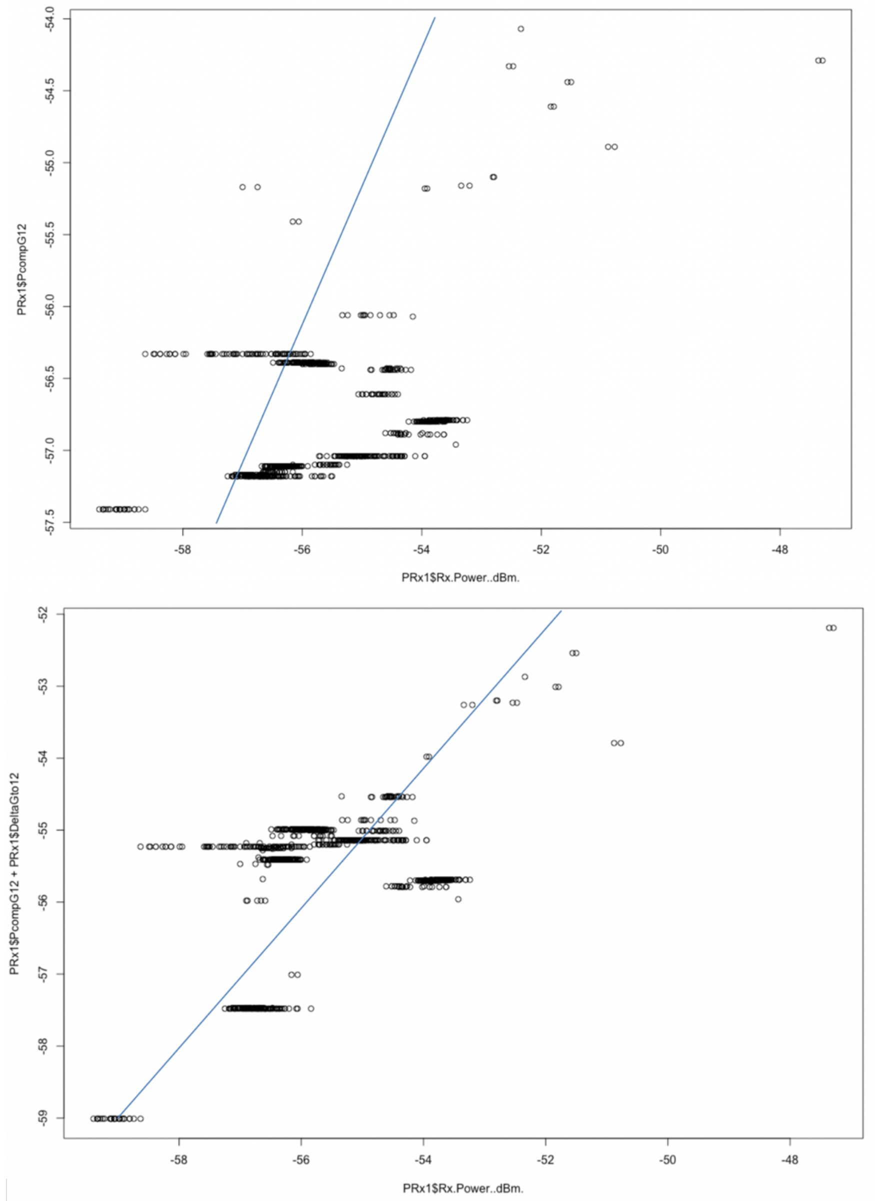

Figure 30. Dependent and Independent Variable Data for lm_1 (upper) and lm_2 (lower)

This is not entirely unexpected in this case, as the intercept estimates the mean of the received power if the predicted received power was zero, and the received power would be expected to be zero in that instance, i.e. the intercept is expected to be zero. On the other hand, the significant result for the non-zero value of the slope for the predictors supports the existence of a linear relationship, albeit a relatively weak one, between the dependent and independent variables, including for the $\Delta G_{\alpha\emptyset t}$ term.

Table 14

lm1 and lm2 Regression Results, 12dBi Fixed (Model 1) and 12dBi + ΔG *(Model 2).*

	Model 1	Model 2	
Predictor	Coefficient b_i	Coefficient b_i	SE b_i
Constant	9.25	-5.10	-1.07
Return Link Power Model with Fixed AES Gain (12dBic)	1.14***	0.90***	0.08
ΔG to 12dB from Variable Gain AES Antenna Model		0.63***	0.04
R^2	0.15	0.30	
F	160.3***	195.6***	
ΔR^2	0.15	0.15	

Note: *** p-value <0.0001

The formal hypothesis test on whether or not the $\Delta G_{\alpha\emptyset t}$ coefficient in lm_2 is equal to zero:

$$H_0: \Delta G_{\alpha\emptyset t} \text{ coefficient } = 0$$

$$H_A: \Delta G_{\alpha\emptyset t} \text{ coefficient } \neq 0.$$

was an ANOVA F-test conducted on the two regressions lm_1 and lm_2 at an $\propto$=0.05 level of significance, the result of which is shown in Table 15.

Table 15

ANOVA Results for lm1 and lm2

Source	Residual Degrees of Freedom	Residual Sum of Squares	Degrees of Freedom	Sum of Squares	F	p
Model 1	935	1456.0				
Model 2	934	1202.1	1	253.86	197.2	<0.0001

The computed F value exceeds the critical value at 934 degrees of freedom, with a p-value of $<2 \times 10^{-6}$, therefore the null hypothesis H_0 was rejected. Thus, it is inferred that the inclusion of the $\Delta G_{\alpha \emptyset t}$ term results in a better fit to the data on average across this sample than does the fixed 12dBi value, and thus that the variable gain effect is both present and detectable in the data.

Based on this result, the $H_{1c\text{-}0}$ null hypothesis is rejected:

H-2 $H_{2\text{-}0}$: There is no significant difference in the sum of squared residuals for a linear model estimated using BFO data and a fixed gain model and that estimated using both BFO data and the peak gain variation model for the AES antenna.

$H_{2\text{-}A}$: A statistically significant difference is found in the sum of squared residuals for a linear model estimated using BFO data and a fixed gain model and that estimated using both BFO data and the peak gain variation model for the AES antenna.

Table 16

Stepwise Ataike Information Criterion Test on lm2

Source	Residual Sum of Squares	Degrees of Freedom	Sum of Squares	AIC
Model 2 (no coefficients dropped)	1200.3			238.1
Model 2 (12dB fixed coefficient dropped)	1351.5	1	151.2	347.2
Model 2 (Delta G coefficient dropped) = Model 1	1455.0	1	254.6	416.3

The results of a stepwise Akaike information criterion (AIC) performed on lm_2 is shown in Table 16, where the residual sum of squares (RSS) and AIC are sequentially computed, first with both the 12dBi fixed and $\Delta G_{\alpha\emptyset t}$ terms included, then dropping the fixed term, followed by dropping the variable term.

The (RSS) residual sum of squares can be seen to be lowest when both the 12dBi and $\Delta G_{\alpha\emptyset t}$ terms are included, as is the case for the Akaike information criterion, both of which are taken as being consistent with the rejection of the null hypothesis that the $\Delta G_{\alpha\emptyset t}$ coefficient is equal to zero and supporting the hypothesis that the inclusion of the $\Delta G_{\alpha\emptyset t}$ term serves to reduce the sum of squares of the residuals, rather than increase the RSS as would be expected if the gain variation effect was not present in the observed data.

Recalculation of the regression and all tests described above, using a fixed value of 13.1dBi as opposed to 12.0dBi yielded very similar results with no change in the result of the tests or inferences thereon.

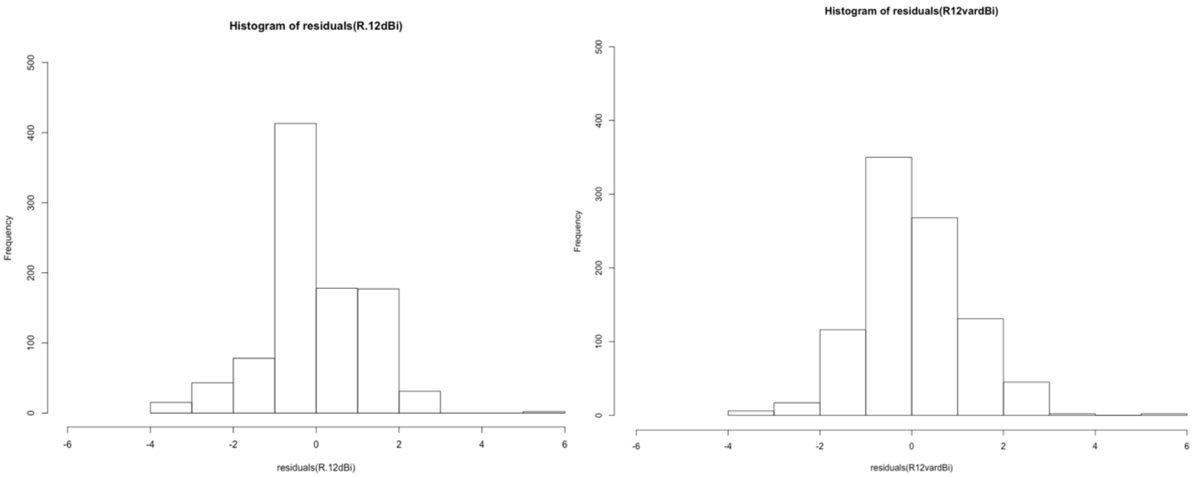

Figure 31. lm_1 and lm_2 Regression Residuals, 12dB Fixed (left) and Variable Gain (right)

Histograms of the regression residuals are shown in

Figure *31* for the fixed 12dBi model (left panel) and the variable model (right panel), where the latter can be seen to be approximately Gaussian, but with a long tail on the right-hand (i.e. positive) side of the distribution.

The lm_2 variable model residuals were tested against the null hypothesis that the distribution is Gaussian, where the null hypothesis was rejected at an α=0.05 level of significance for all four test types conducted (Shapiro-Wilk, Kolmolgorov-Smirnov, Cramer-von Mises and Anderson-Darling).

The Q-Q plot in Figure 32 suggests autocorrelation in the data and time varying biases in the residuals, likely caused by unmodeled parameters. The deviation of the data from a Gaussian distribution raises the question of validity of the ANOVA F-test above. However, results of Blanca et al (2017) show the F-test to be robust to deviations from a Gaussian distribution in 100% of cases tested, with the calculated skewness and kurtosis for the lm_2 regression residuals of 0.45 and 0.72, respectively, being well within the values for which Blanca et al (2017) found low risk of Type I error.

Taken together with the very low p-value in the test, the rejection of the null hypothesis of $\Delta G_{\alpha\emptyset t}$=0 is considered to hold. While a Gaussian probability density function is used in the likelihood estimation for the conditional probability density of an observed received power residual given a sampled heading, velocity and position, the standard deviation of that distribution is scaled by a factor of 1.5 over that estimated from the sample data, to compensate for this observed deviation and the long tails in the distribution.

Consistent with this approach, to characterize the distribution of the residuals for subsequent probability density function estimation, the mean of the received power residuals was estimated as zero from the same n=937 samples, with standard deviation σ_{vPRx} = 1.1 dBm, scaled to 1.6 dBm to approximate the observed spread in the data with a Gaussian distribution which encompasses the observed residuals at the $3\sigma_{vPRx}$ or 99.7th percentile. ($\sigma_{PRx} = 1.6 dBm$)

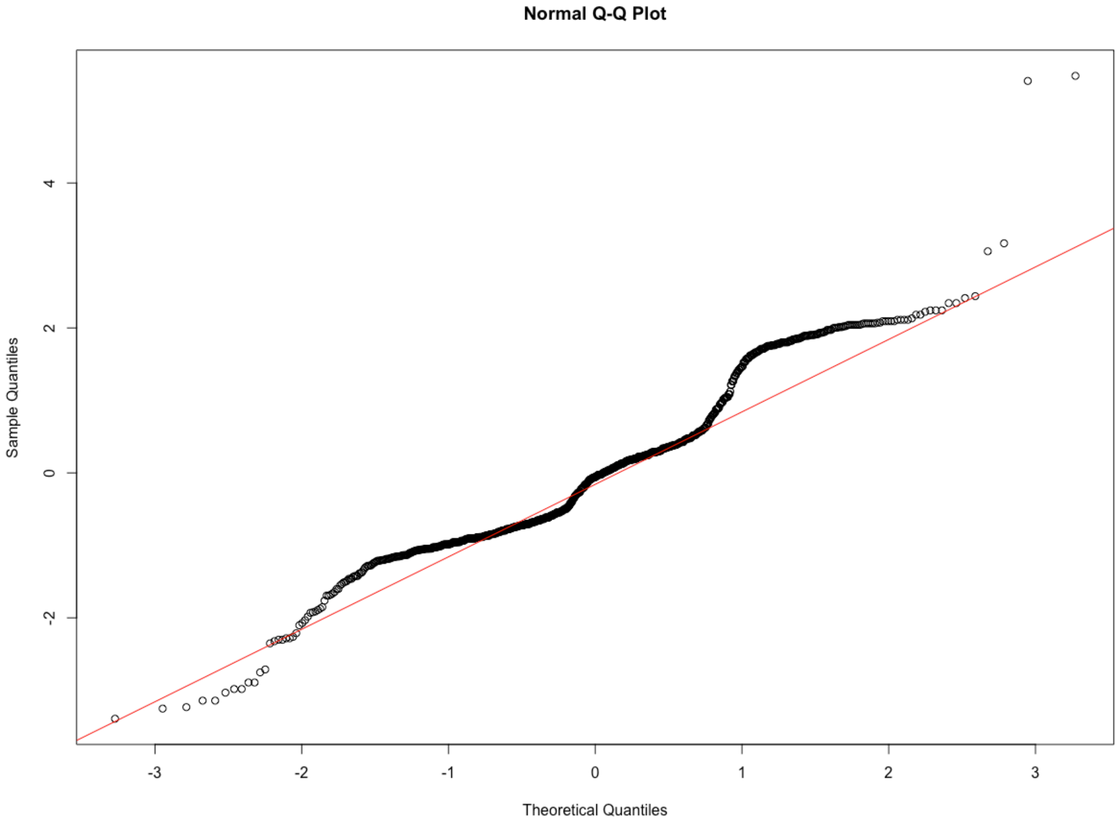

Figure 32. Gaussian Q-Q Plot, lm_2 Regression Residuals

Probability Density Function Estimation

As described in Chapter III, a set of probability density functions were estimated from the data by numerical integration, first using the BFO residual data in isolation and then using both the BFO and received power data. The data set used was the ~100,000 systematically sampled $\upsilon_{BFO\propto_{\phi}}$ & $\upsilon_{RxP\propto_{\phi}}$ residuals across multiple observation epochs, locations, headings and velocities, as previously described. The results of the systematically sampled residuals, all on the R1200-0-36ED channel are first presented, both for observations taken during the MH371/MH370 flights when the aircraft state vector was known, and for the segment of the MH370 flight for which the state vector is unknown.

These first results represent a sensitivity analysis of the BFO and received power as a function of heading, location and velocity. Following these results, the posterior probability density functions are presented, again for both for observations taken during the MH371/MH370 flights when the aircraft state vector was known, and for the segment of the MH370 flight for which the state vector is unknown, along with the formal hypothesis test on the effect of incorporating the received power data into the estimated probability density functions. Finally, the probability density estimates at the 00:11Z 6th arc and the sum of probability densities along the trajectories of the subset of meta-analysis studies for which the trajectory information is available are also presented.

The first communications burst on the R1200-0-36ED channel during the MH371 flight during cruise flight occurred between 04:04Z, with a sample of n=11 BFO and received power observations on this specific channel. An ACARS report at 04:01:01Z provides the aircraft state and environment conditions during the burst, as shown below, together with the relevant reports for the other in-cruise sample times and locations.

Table 17

Selected ACARS Reports 04:04:01Z – 17:06:43Z

Time (UTC)	Altitude (ft)	Calibrated Airspeed (kts)	Mach Number	Total Air Temperature (C)	Static Air Temperature (C)	Latitude (N)	Longitude (E)	Wind Direction	Wind Speed (Kts)	Heading (True)
040401	38100	263.6	0.833	-20.8	-51.3	24.073	113.883	259.8	94.25	193.1
060903	39997	245.3	0.812	-27.4	-55.9	9.76	107.312	84	10.75	212
061403	40000	247	0.817	-27.4	-56.1	9.206	106.95	81.9	14.13	211.7
064404	40000	247.8	0.82	-28.4	-57.3	5.765	104.805	87.5	32.88	208.4
064904	40000	248.4	0.821	-28	-57	5.193	104.452	91.8	27.88	208.8
170143	34998	278	0.819	-13.4	-43.9	4.708	102.534	69.6	17.38	26.8
170643	35004	278.4	0.821	-13.1	-43.8	5.299	102.813	70	17.13	26.7

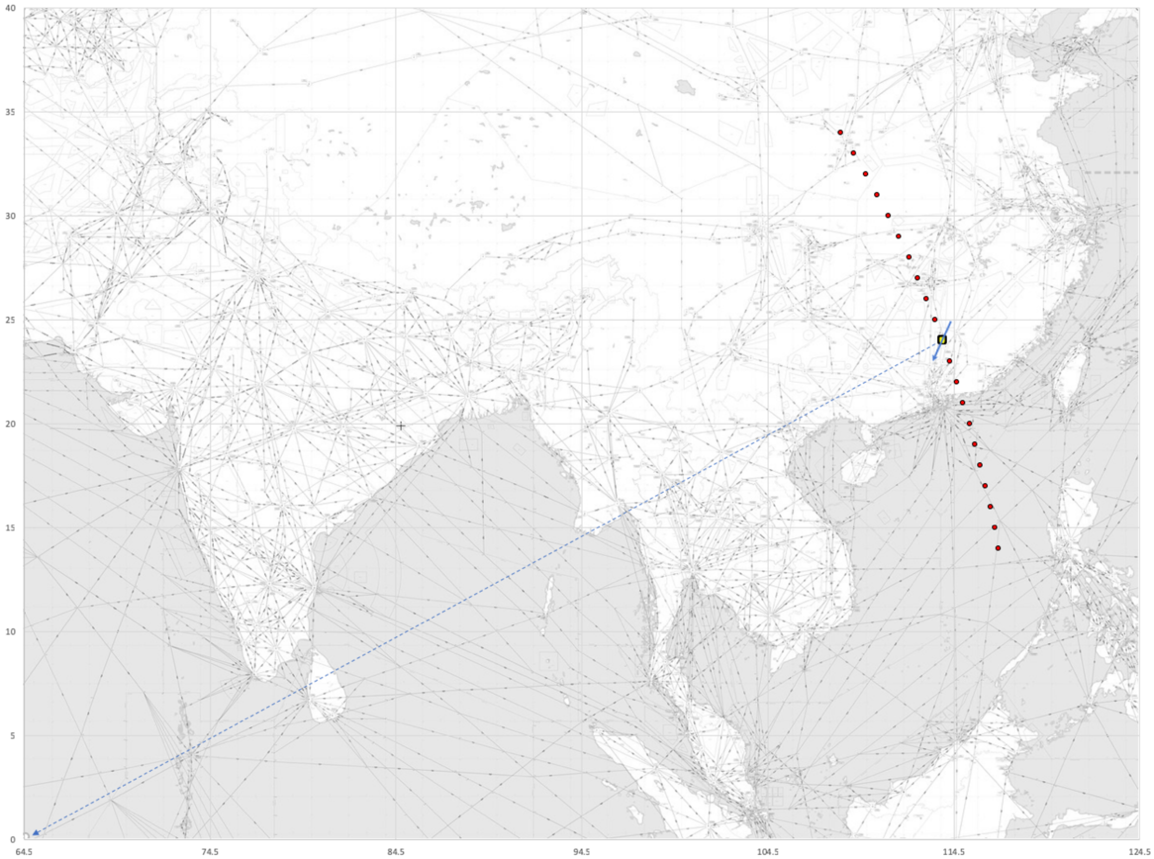

Figure 33. Geographic Context for 04:04Z Sensitivity Analysis

The chart in Figure 33 shows the location of the aircraft, together with the approximate heading and the direction of the nominal sub-satellite point. The dots along the BTO arc indicate the sampled arc-latitude locations for the 04:04Z observation time, extending between 14N and 24N in 1-degree increments, each sampled at 360 degrees of heading for both the BTO and received power residuals.

The results below were sampled using the known Mach number of 0.833 from the ACARS reports, however the sensitivity of the BFO results to changes in the velocity assumption is also shown in the charts below. For the sample at the known latitude, the known wind conditions were used to derive ground track azimuth and velocity. For the other sampled latitudes, the environmental data was sampled from external sources as described in Chapter III.

The sensitivity analysis for the BFO residuals at the 04:04Z sample points is shown in Figure 34, where each of the panels shows the result for a given arc-latitude along the 04:04Z BTO arc, from 14N to 34N. The red circle in the 24N panel indicates the known position and true heading at the time of observation.

Although the BFO residual can be seen to be close to zero at the known value of a true heading 193 degrees, it can also be seen that multiple other points of intersection with the zero-value y-axis, that is with zero-valued BFO residuals, exist across the range of latitudes sampled, up to 600NM from the known position in this example, at headings up to +/- 60 degrees from the known heading.

The general form of these systematically sampled BFO residuals can be seen to be sinusoidal in nature when sampled across 360 degrees as a given location, with the curve shifting vertically as the sample point is moved up or down the BTO arc. Although in the case of the 04:04Z observation, the trough of the sinusoid can be seen to intersect with the zero axis at the known latitude, this is not necessarily the case for other observation epochs and thus is not necessarily a reliable indicator of the true latitude.

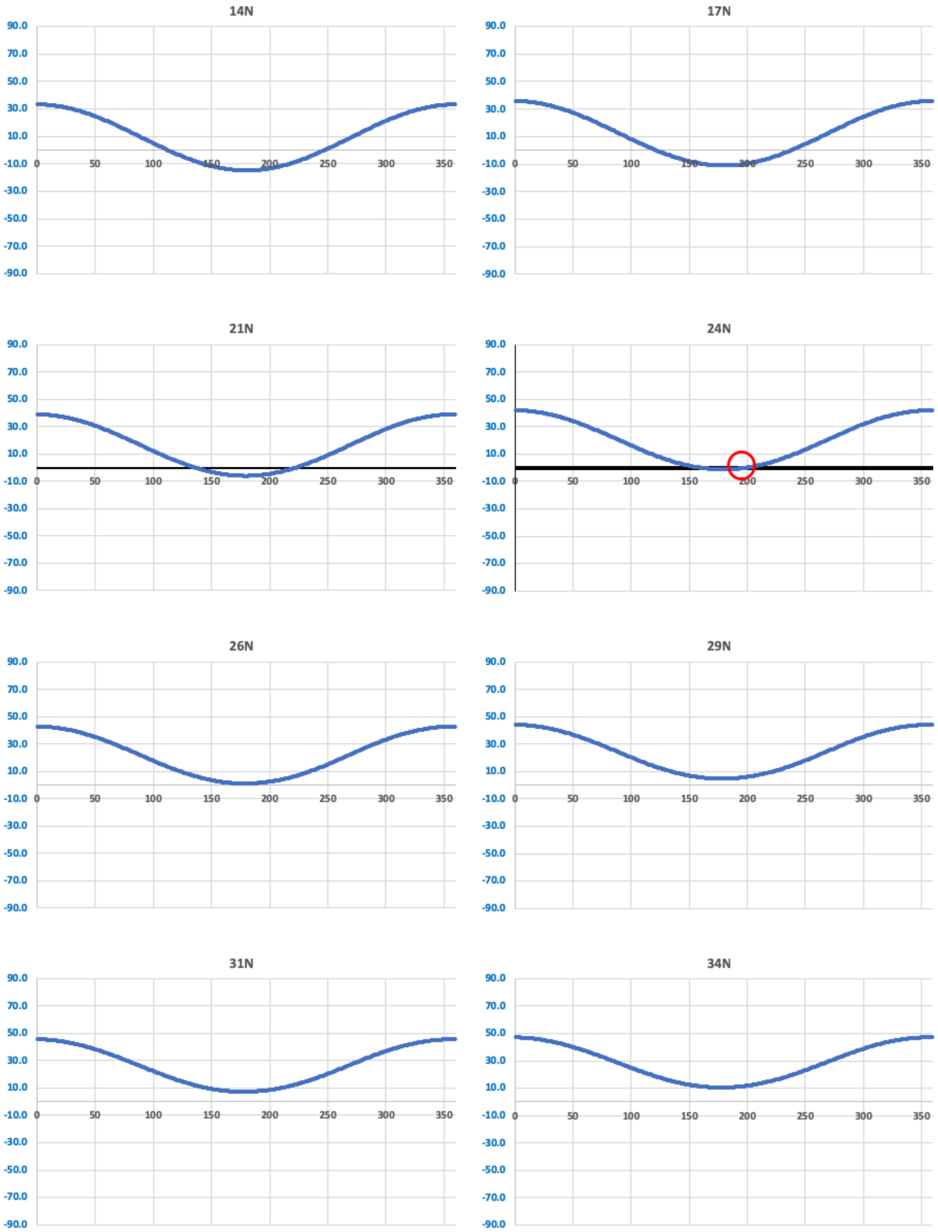

Figure 34. BFO Residuals 04:04Z Latitudes14N to 34N Heading 0-360 Degrees M0.83

In this case, i.e. at 04:04Z, the downward shift of the curve as the sample points move to the south of 24N creates multiple zero-value residual intersection points, at headings which diverge from the known value of 193 degrees, increasingly so as the sample points move south. Also in this specific example, as the sample points move north, the curve increasing shifts upwards, such that there are no zero-value residuals about ~29N. Figure 35 shows the sensitivity of the BFO residuals to changes in ground track velocity for the 04:04Z example, sampled at the known arc-latitude of 24N and at Mach numbers from 0.70 to 0.89, with the ground track velocity estimated using wind and temperature data for that location.

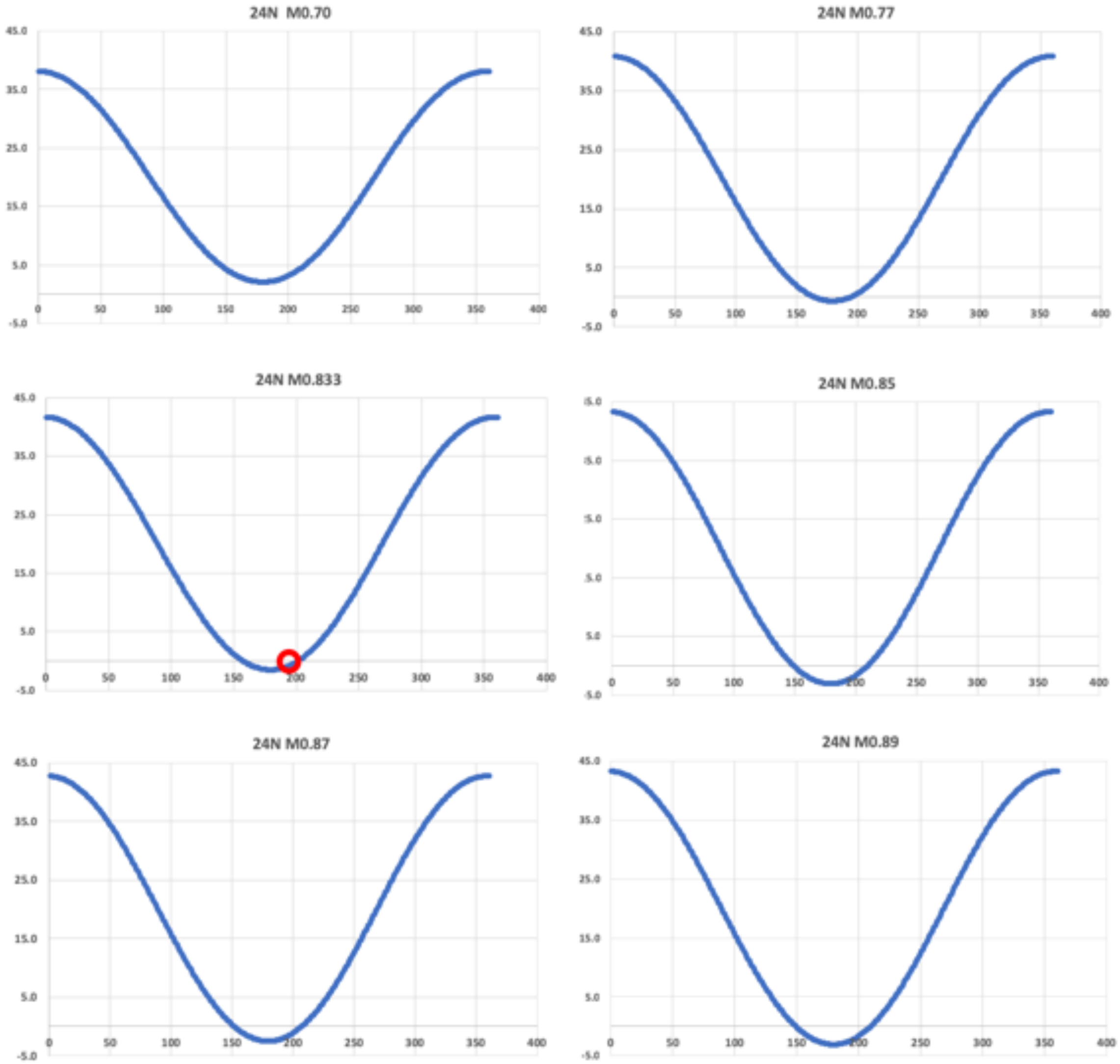

Figure 35. BFO Residuals 04:04Z Latitude 24N Heading 0-360 Degrees M0.70-0.89

Although changes in velocity can be seen to shift the curve, the maximum BFO residual at the known heading and location as a result of velocity changes is less than 1 standard deviation for the BFO distribution. The remainder of the results are shown for the known Mach number where it is known, and for a sampled value of M0.84 for the unknown segment. The charts below show the results of the combined sensitivity analysis for the BFO residuals (blue) and the received power residuals (orange), again for the 04:04Z arc.

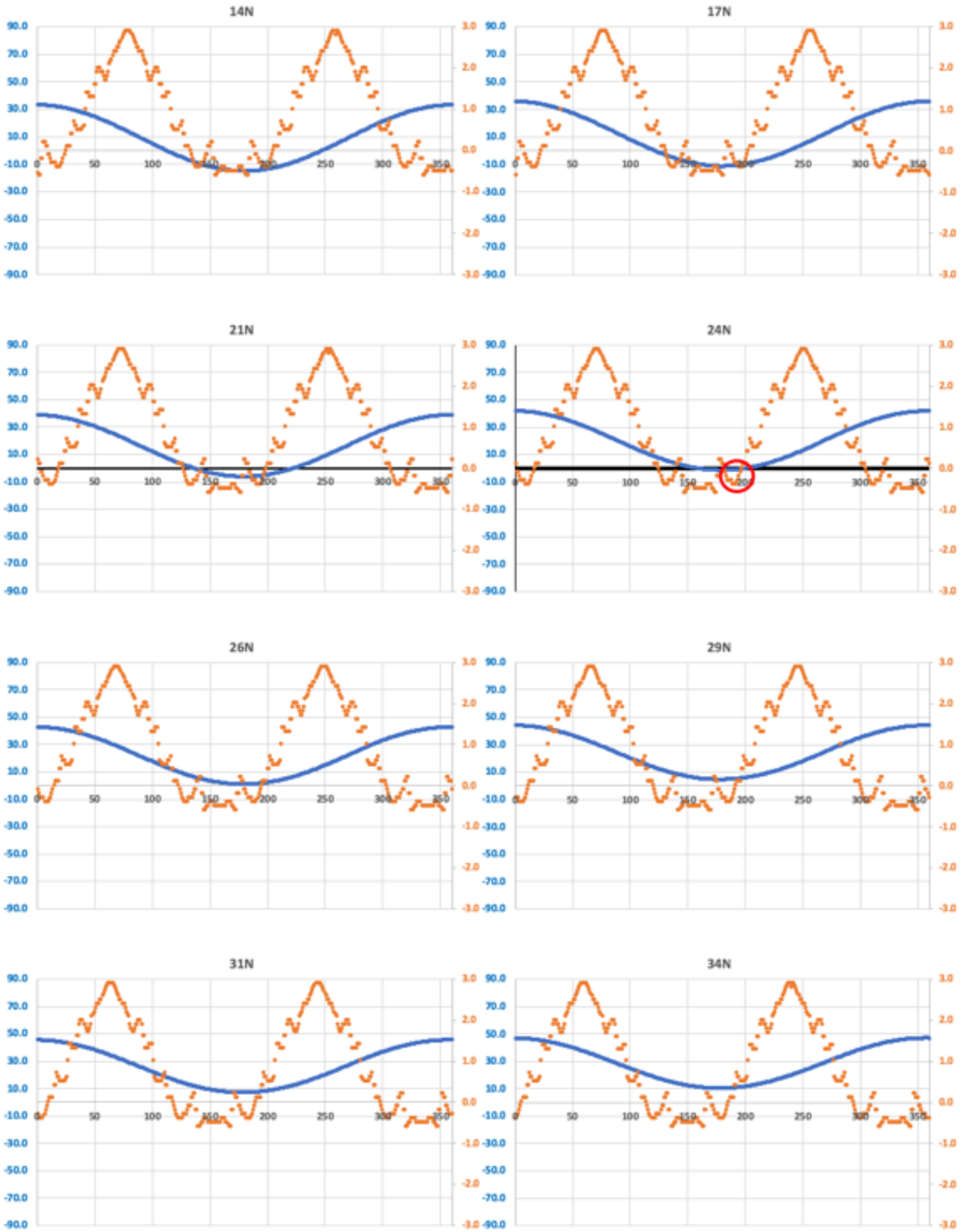
14N

17N

21N

24N

26N

29N

31N

34N

Figure 36. BFO and Received Power Residuals 04:04Z 14N to 34N 0-360 Degrees, M0.83

As with the BFO residuals, the received power residual is close to zero at the known latitude and heading (-0.3dBm in this case), also with multiple points of ambiguity (i.e. zero valued residuals) across the range of latitudes and headings sampled. However, while some of the BFO and received power ambiguity points coincide, for example those at 24N, it can be observed that others do not, for example those at 14N and 17N, where the BFO zero-value residual at a ~250 degrees heading can be seen to produce a large received power residual. This is due to the fact that a ~250 heading at those latitudes would point the aircraft toward the satellite, resulting in a significant decrease in gain which is not apparent in the data.

The combined BFO and received power residuals are presented below for the other R1200-0-36ED observation epochs for which the sensitivity analysis was computed, with the relevant positions and sampling points along the respective arcs shown in the chart below.

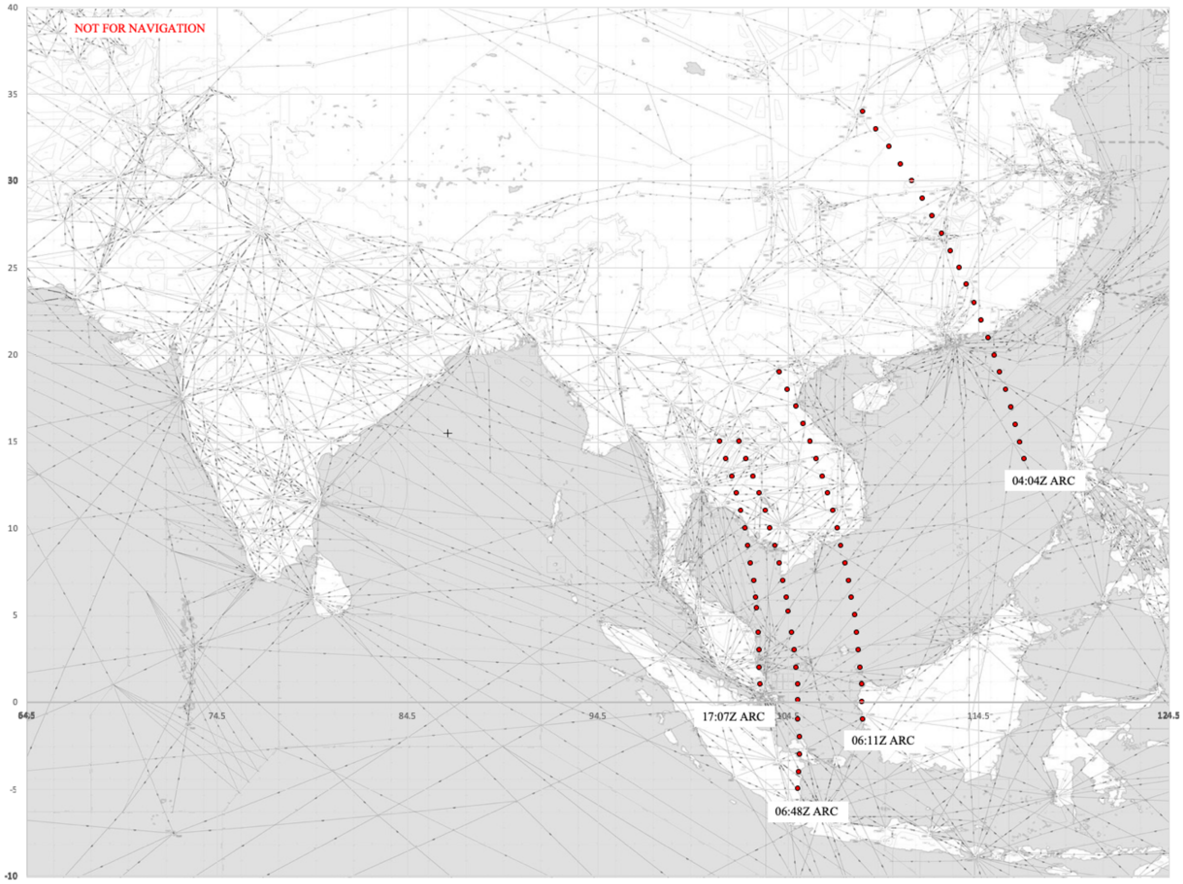

Figure 37. R1200-0-36ED Systematic Sample Locations During Cruise Flight MH371/370 04:04Z – 17:07Z (Background imagery Skyvector, 2019)

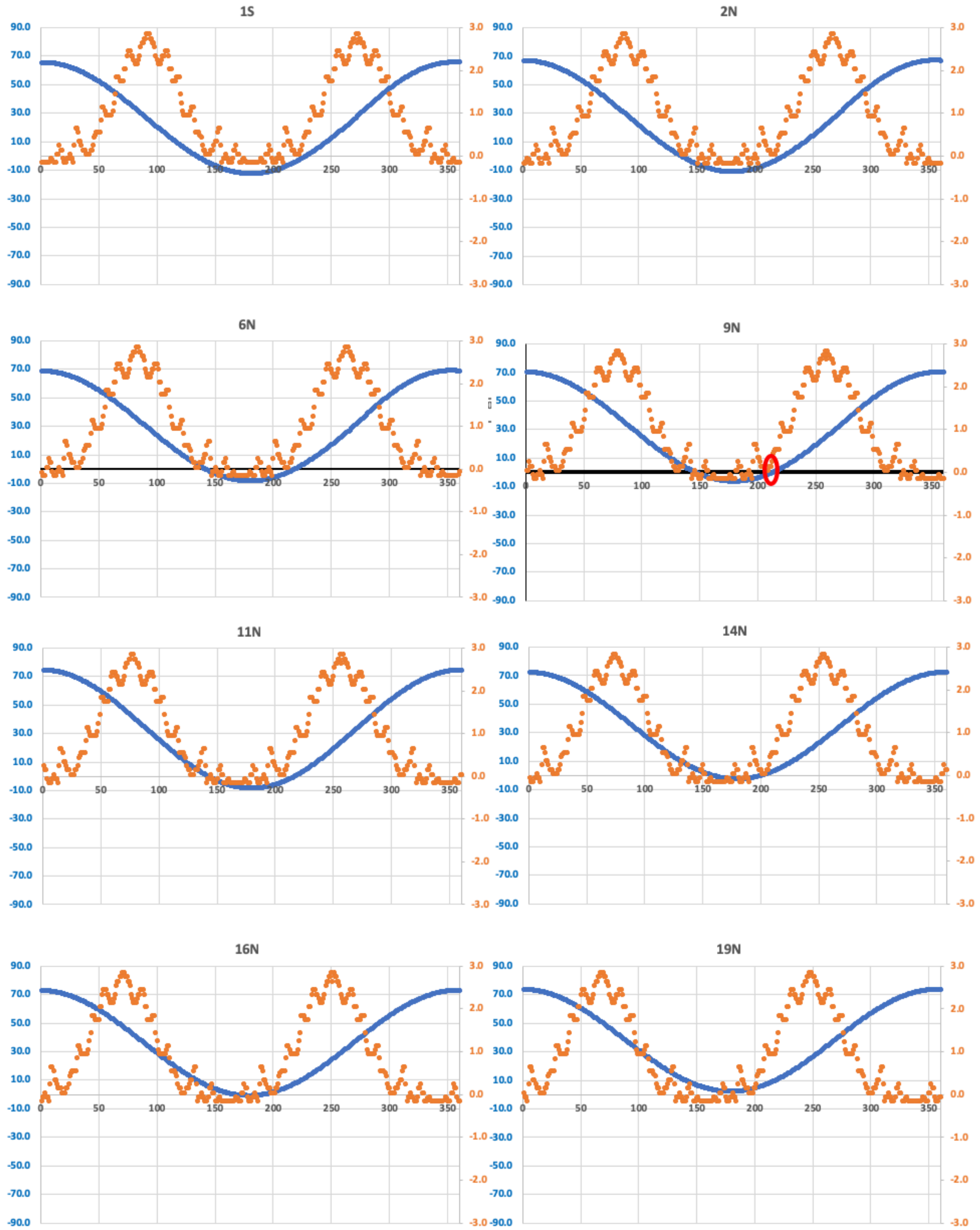

Figure 38. BFO and Received Power Residuals 06:11Z 1S to 19N 0-360 Degrees M0.82

In the 06:11Z case, it can be seen that the trough of the sinusoid for the BFO residual does not rest on the zero-value residual line at the known latitude, however a zero-axis intersection occurs at the known heading, with the received power residual also close to zero.

For both the 06:11Z (above) and 06:48Z (below) observations, the zero-value residuals for both the BFO and received power are generally coincident, thus in these cases the addition of the received power data does not serve to reduce the number of solutions.

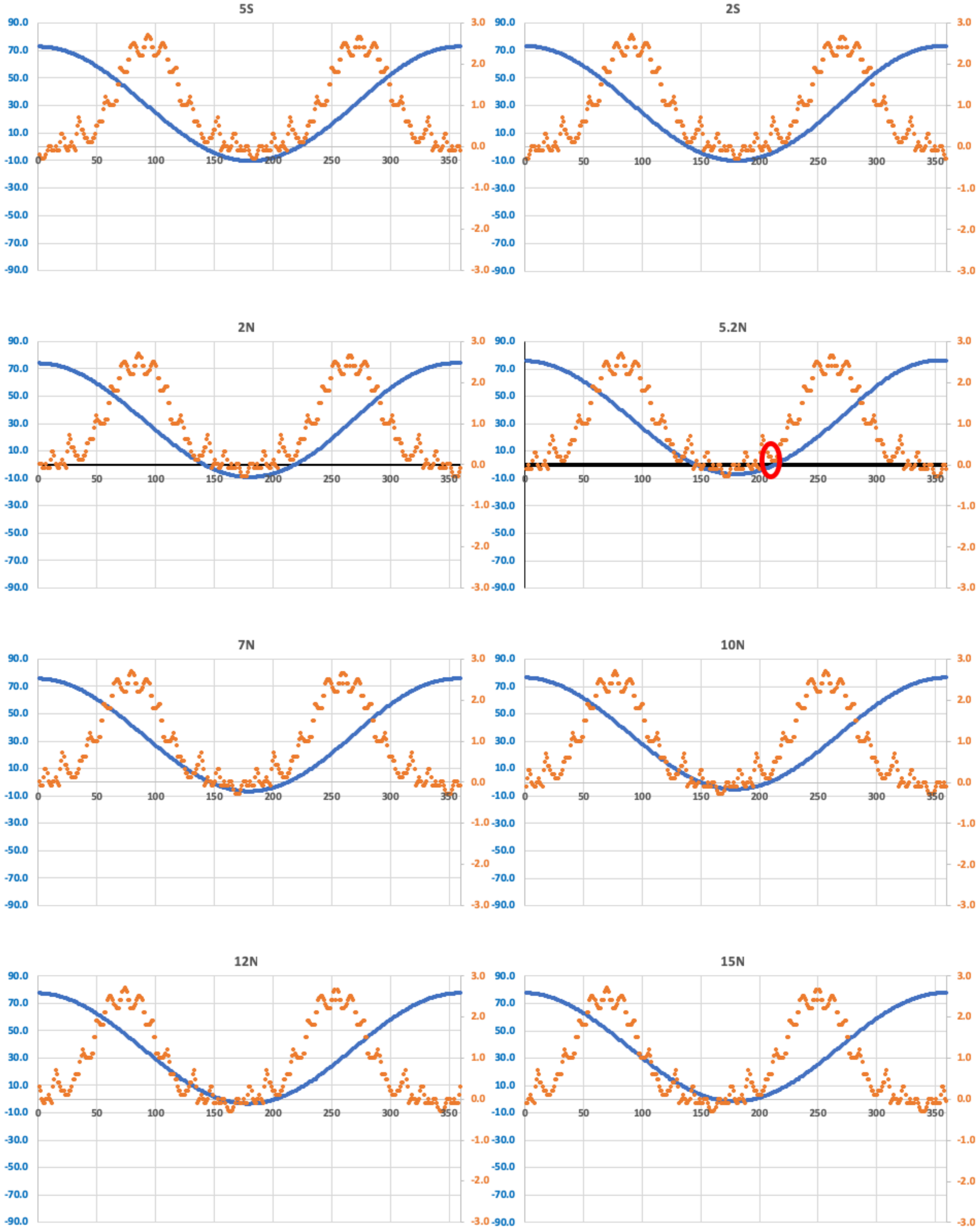

5S

2S

2N

5.2N

7N

10N

12N

15N

Figure 39. BFO and Received Power Residuals 06:48Z 5S to 15N 0-360 Degrees M0.82

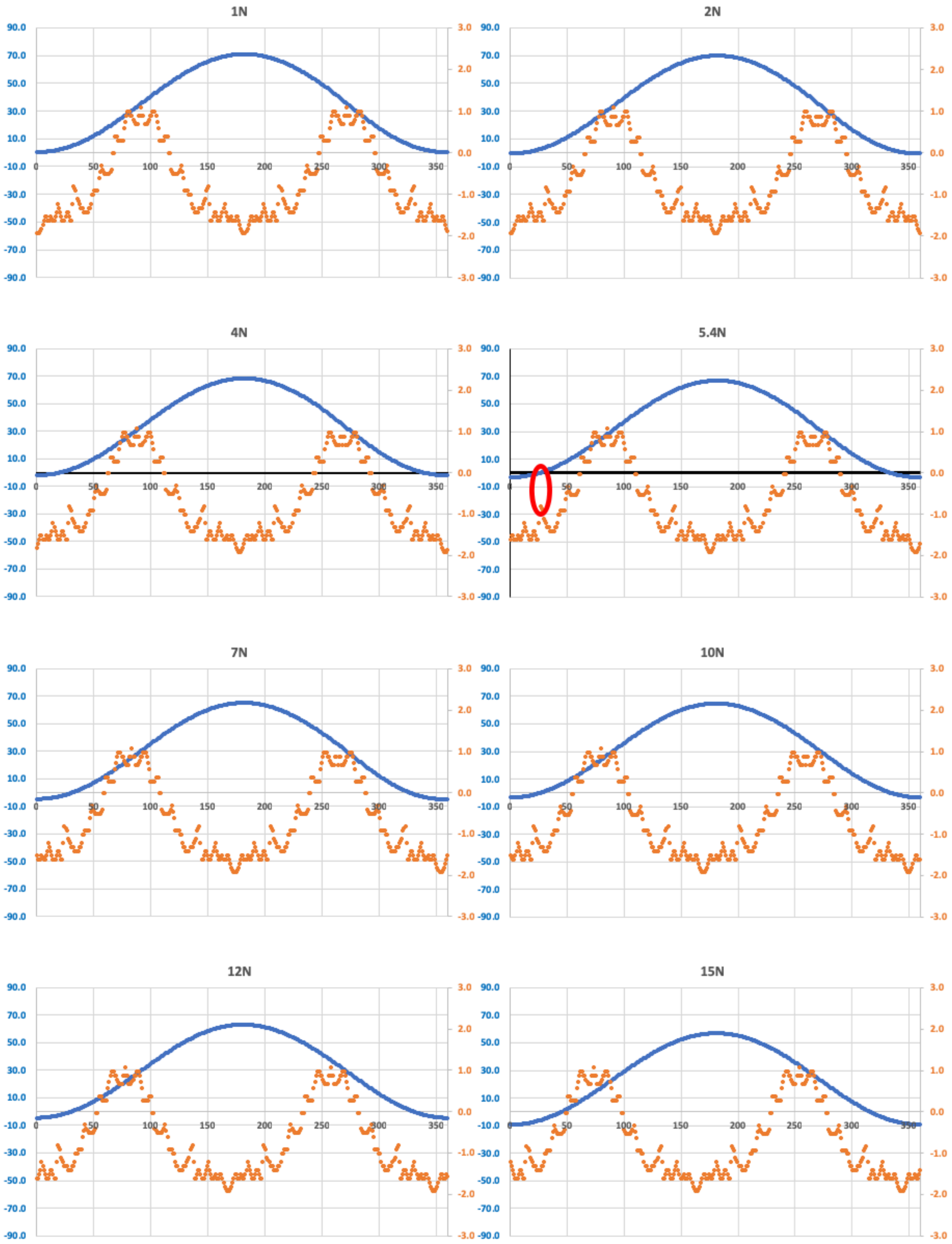

Figure 40. BFO and Received Power Residuals 17:07Z 1N to 15N 0-360 Degrees M0.82

In the 17:07Z case, the BFO line crosses the zero axis at the known heading of 027(T) at 5.4N on that arc, while the P_{rx} residual is larger at just under 1 dBm (<1 std. dev.,1.6dBm).

The table below provides a summary of the BFO and received power residuals at the known heading, location and velocity for the available R1200-0-36ED data recorded while in cruise flight. In all cases tested the BFO and P_{rx} residuals were less than 1 standard deviation from zero at the known states. However, in all cases multiple points of ambiguity exist across the wide arcs tested, typically spanning over 1,000 NM along each BTO arc, potentially presenting multiple solution points of which only one is correct. In some cases, the combination of the BFO and received power data serves to reduce the number of coincident intersection points over the BFO-only analysis, however in other cases it does not, depending on the relative geometry along a given arc.

Table 18

BFO and Received Power Residuals at Test Points with Known Aircraft State Vector

Time (UTC)	BFO Observed - Calculated Residual (Hz)	Received Power Observed - Calculated Residual (dBm)
04:04Z	-1.0	-0.3
06:11Z	0.1	0.4
06:48Z	1.6	0.2
17:07Z	-0.2	0.8
18:28Z	-0.2	0.2

Note: 18:25Z assumes a position of 6.75N on the 1st BTO arc, heading 296(T), M0.82, 153Hz BFO bias

The 18:28Z observation was tested at a hypothetical location and heading, assumed to be a position of 6.75N 96E, heading 296(T) on airway N571 at Mach 0.82. Wind effects at <3kts were negligible at this specific time and location. A 153Hz bias was used, given that this value is known from the RQ1(b) results for the observation epoch used.

Although the BFO residual shows two zero-value crossing points and thus is ambiguous in respect of heading, the combination of BFO and received power residuals strongly indicates the 296(T) heading solution as opposed to the ~60(T) alternative, demonstrating the potential utility of combining the BFO and received power residuals when the relative geometry is conducive to this kind of result. However, it should be noted that, as with the other locations tested, there exist multiple points of ambiguity at a wide range of different latitudes for this data for both the BFO and received power residuals, some of which are coincident and some of which are not.

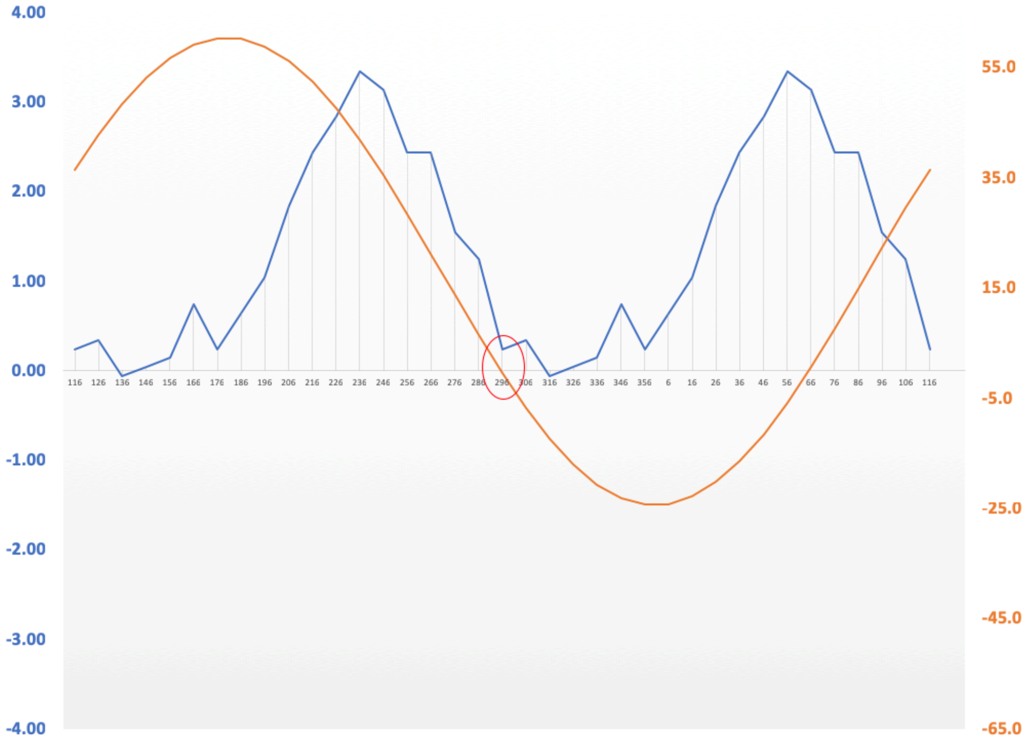

Figure 41. BFO (orange) and Received Power (blue) Sensitivity Analysis, 18:28Z Restart

Systematic Samples After 18:25Z Restart. For the 2nd (19:41Z) through 6th (00:11Z) BTO arcs and for the 23:14Z telephony attempt, the systematic sample locations were selected to coincide with the trajectory points from the subset of the satellite communications meta-analysis group for which detailed trajectory information can be extracted, with additional sample locations added in some cases to expand the length of the arc sampled. Figure 42 provides the geographical context for these systematic sampling locations.

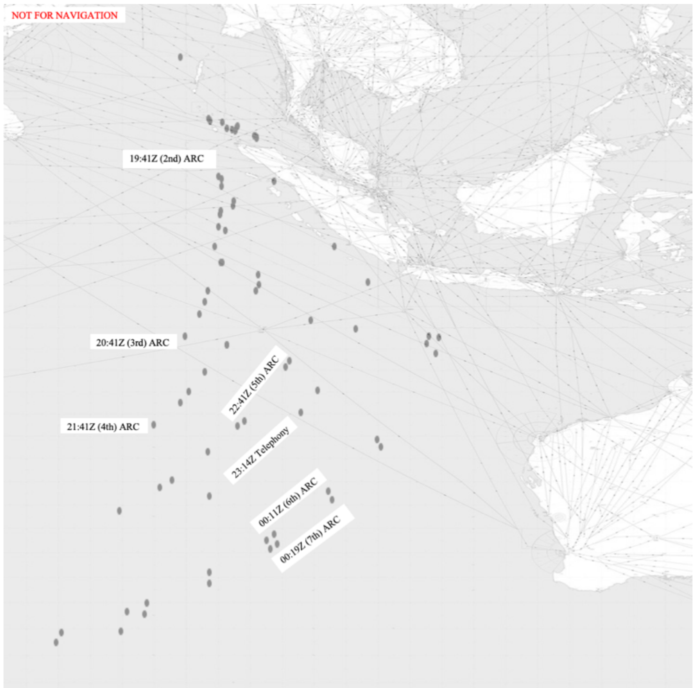

Figure 42. Geographical Context for Systematic Sampling Locations 2nd-6th Arcs.

The sensitivity analysis results for the 19:41Z (2nd) through 00:11Z (6th) arcs are presented below (Figure 43 through Figure 47). These results are sampled at a Mach number of 0.84, noting that changes in the Mach number will shift the BFO sinusoids vertically, however based on the analysis of this effect where the aircraft state is known, an error in the assumed velocity is expected to bias the BFO residual by much less than 1 standard deviation.

The (orange) received power residuals can also be seen to shift vertically between observation epochs. This is likely the result of either noise or unmodeled systematic effects. In the case of noise, these observation points consist of a single observed value (i.e. n=1) drawn from a distribution with an estimated standard deviation of 1.6 dBm. Thus, any given single sampled observation could contain an error of 2-3dB or more, which would manifest itself in the observed – calculated residual plot as a vertical shift by that amount, even if the calculated value were free of any biases. An unmodeled bias would have the same effect.

However, the relative values of the residuals, for example when comparing the received power residuals at two zero-value BFO residual points, are preserved over relatively large shifts of the curve, hence they may still provide value in discriminating between multiple BFO solutions, particularly where the difference in received power residual is significant.

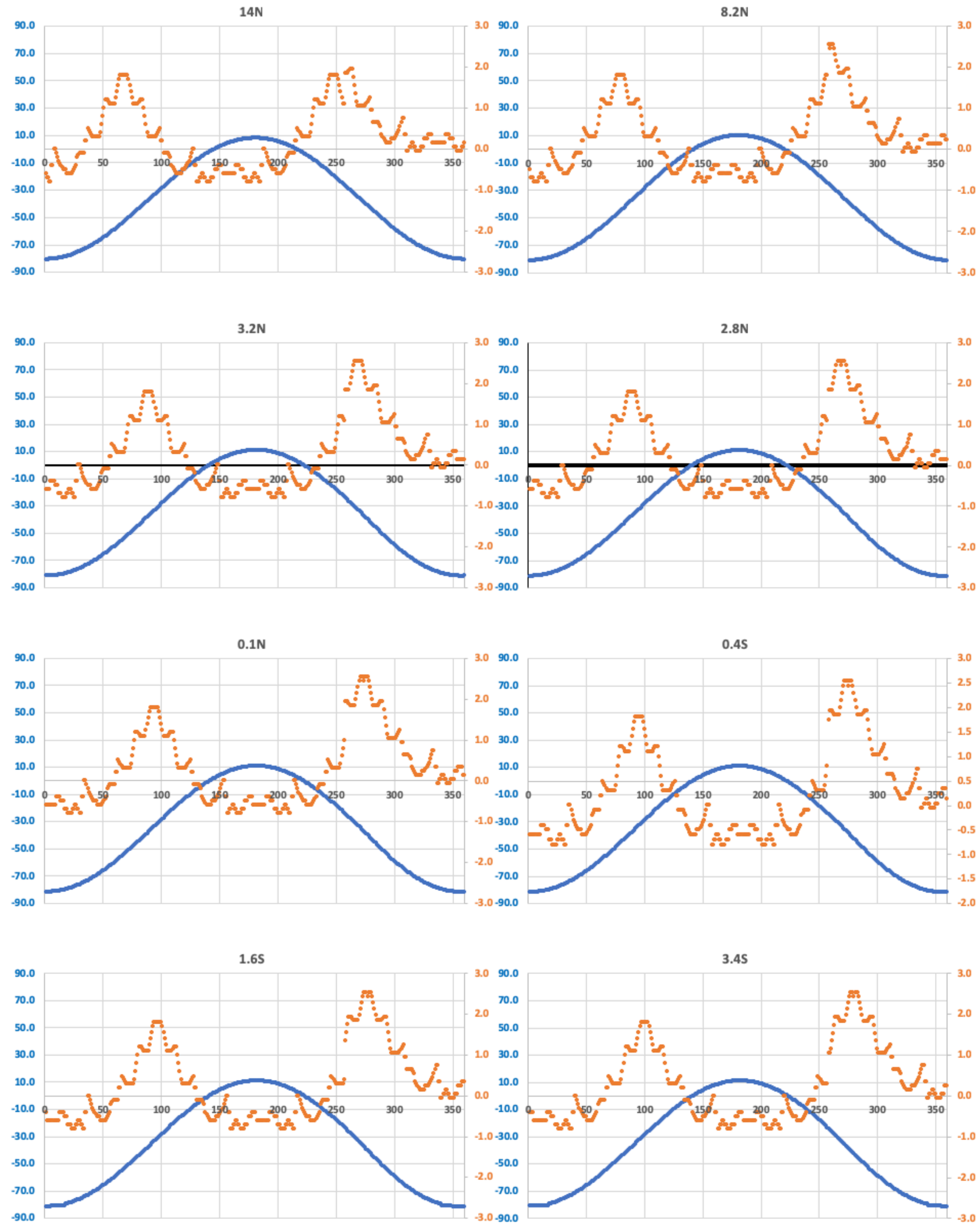

Figure 43. BFO and Received Power Residuals 19:41Z 3.4S to 14N 0-360 Degrees M0.84

In the 19:41Z case (above), the BFO and P_{rx} zero-value residuals are generally co-incident, both across headings and across sample points, offering little opportunity to discriminate. In the 20:41Z case (below), the residuals can be seen to diverge at the more northerly sample locations, and for the ~200(T) heading versus ~150(T) to the south.

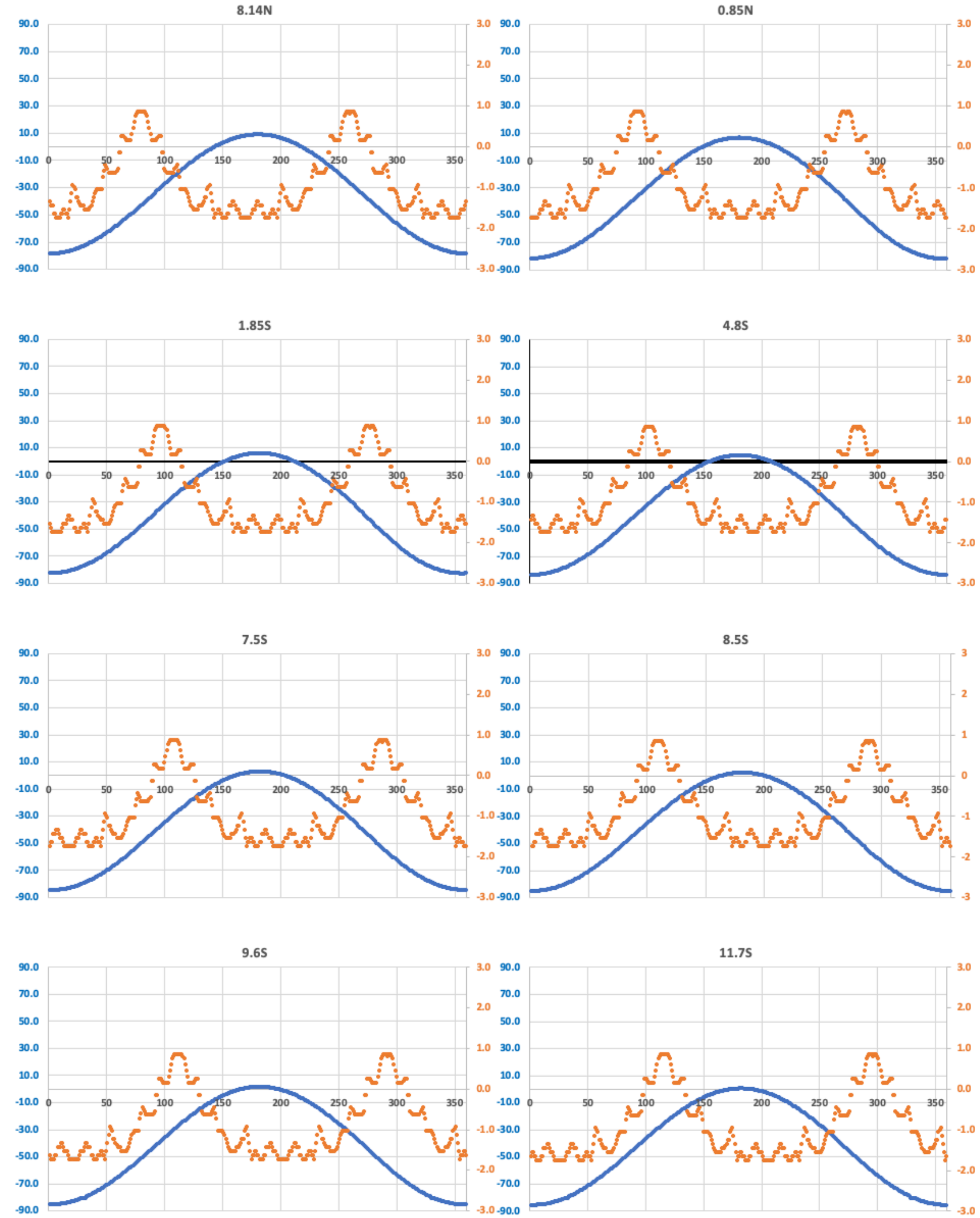

Figure 44. BFO and Received Power Residuals 20:41Z 3.4S to 14N 0-360 Degrees M0.84

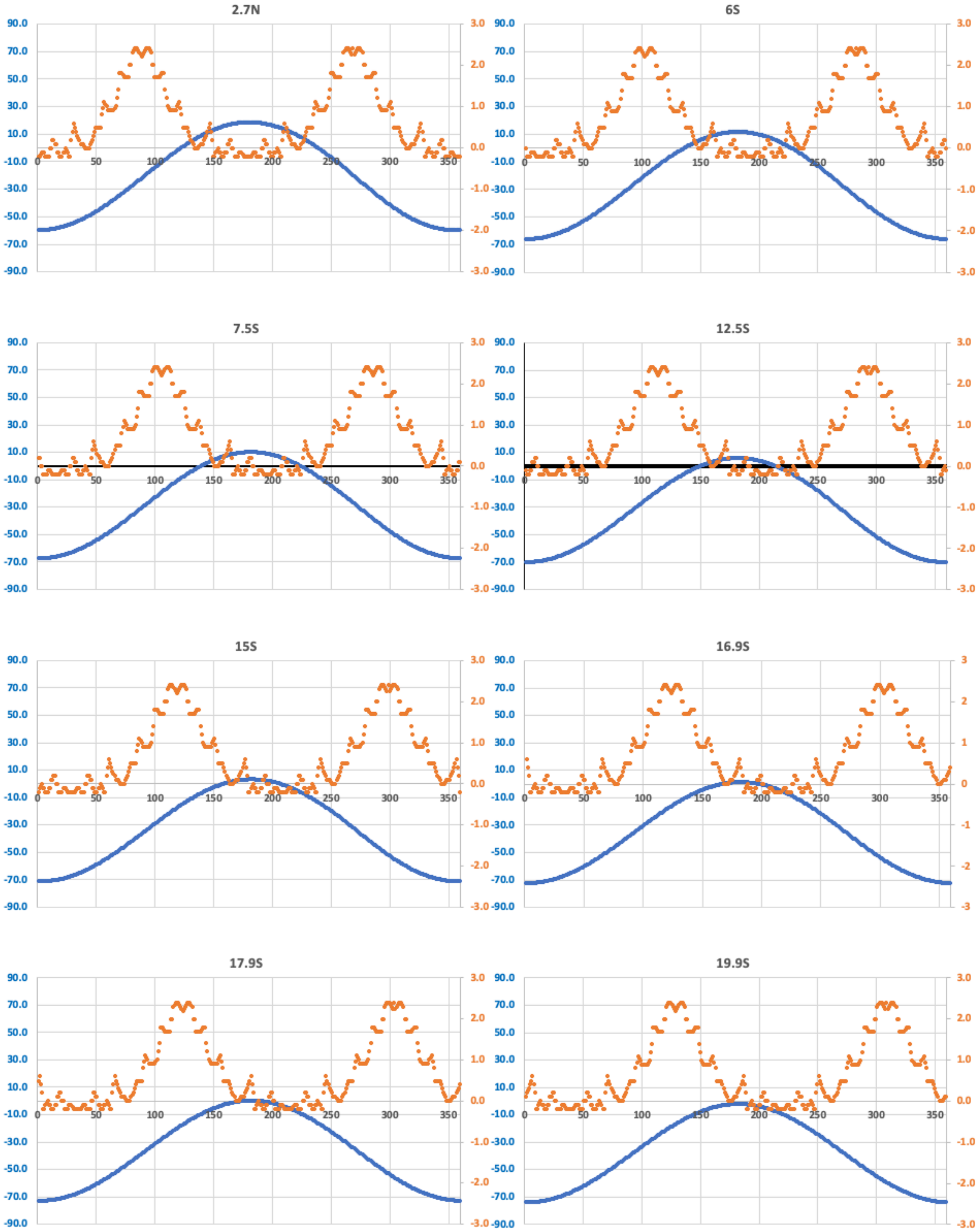

Figure 45. BFO and Received Power Residuals 21:41Z 2.7N to 20S 0-360 Degrees M0.84

In the 21:41Z case the relative geometry creates residuals which do not provide much opportunity to discriminate, with some limited opportunities, for example at the 2.7N location and for the 180-200(T) heading versus the ~150(T) heading from 15-19.9S.

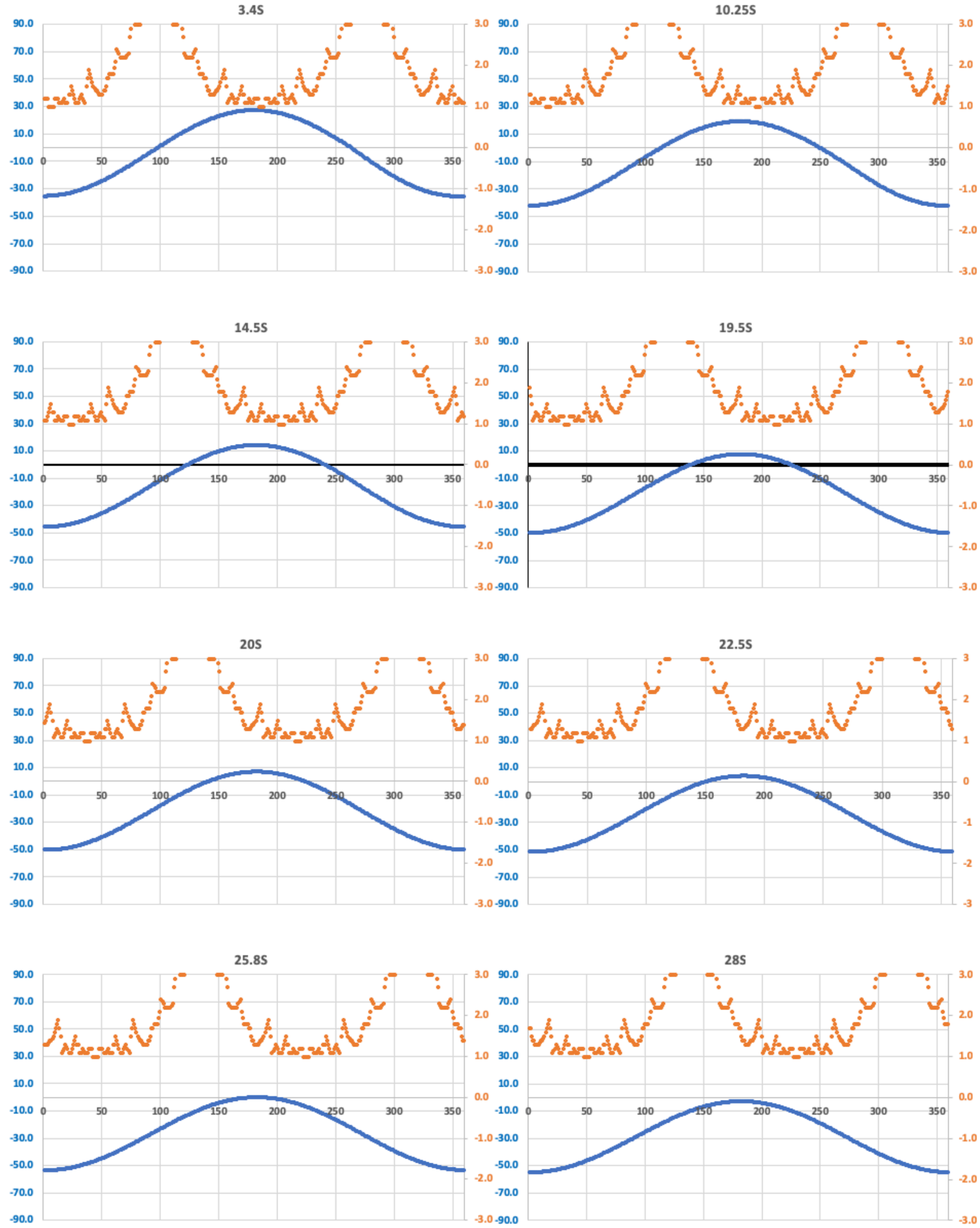

Figure 46. BFO and Received Power Residuals 22:41Z 3.4S to 28S 0-360 Degrees M0.84

Although the 22:41Z P_{rx} curve is shifted upwards in all cases, the relative value of the residuals may still provide utility. For example, the P_{rx} residuals are around 3 times greater at the BFO-indicated ~100(T) and ~270(T) headings at 3.4S or 10.25S than those for the BFO-indicated ~180(T) headings at 25.8S and 28S.

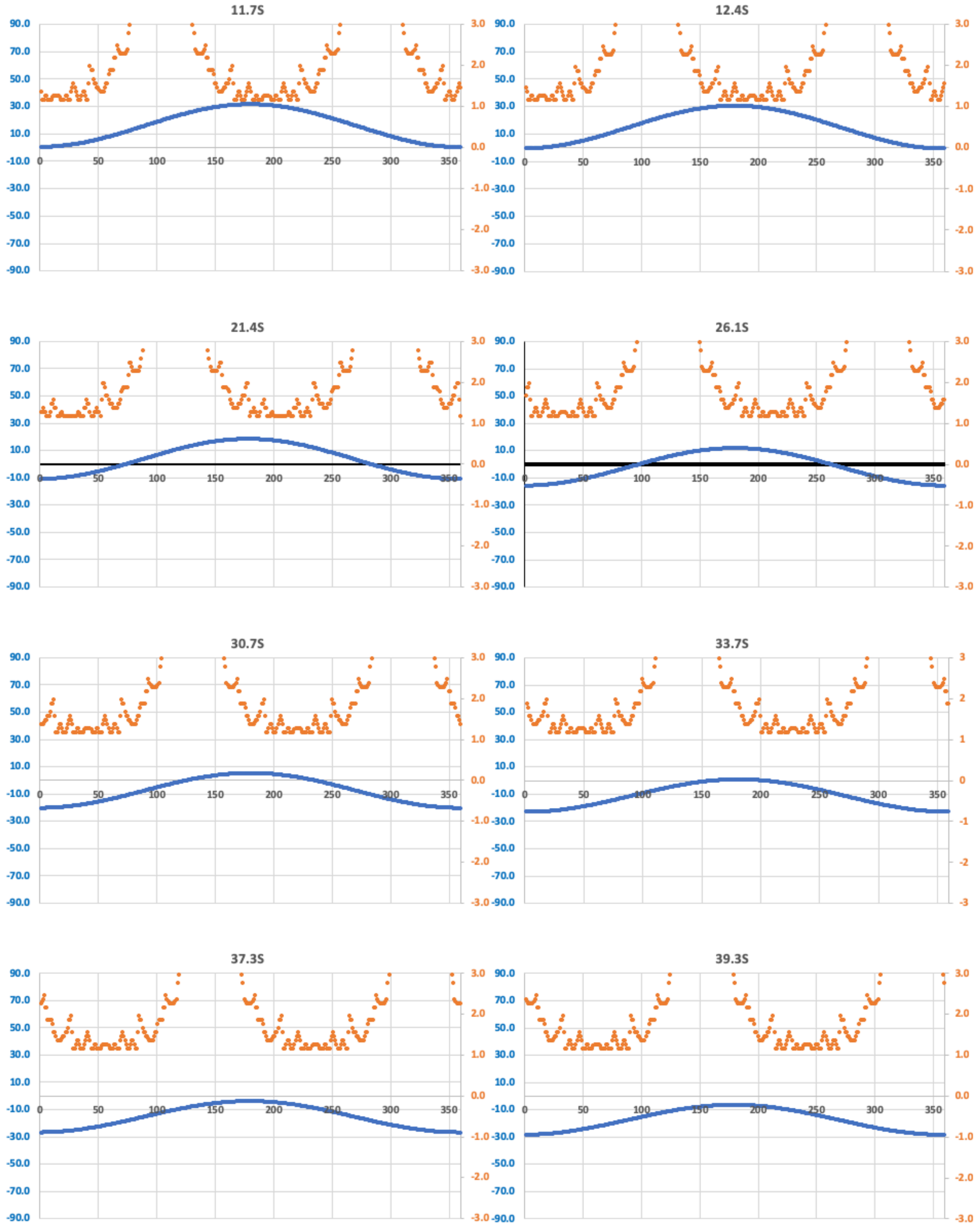

Figure 47. BFO and Received Power Residuals 00:11Z 12S to 39S 0-360 Degrees M0.84

The BFO sinusoid at for the 00:11Z observation can be seen to be relatively flat compared to the other observation times, with the trough intersecting the zero-value axis at approximately 12S and the peak intersecting it at approximately 33-34S. Due to the relative geometry, the P_{rx} residuals are almost identical for the two cases, such that inclusion of the received power data does not appear to resolve this fundamental ambiguity. However, it does serve to render some of the other potential solutions are much less likely.

Telephony Attempts (18:38Z and 23:14Z)

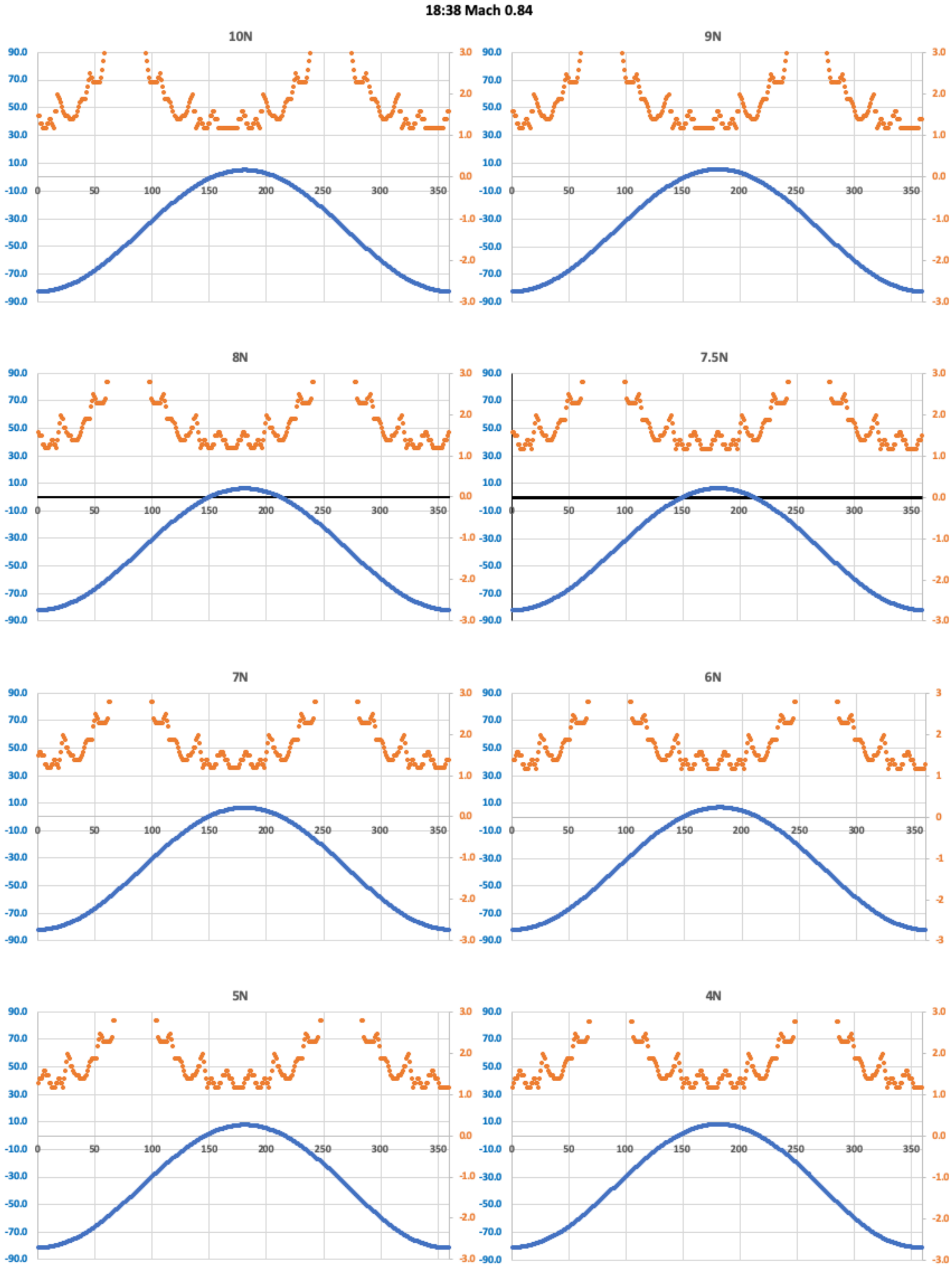

Figure 48. BFO and Received Power Residuals 18:38Z Telephony Attempt 4N to10N M0.84. (Received power uncorrected for unknown regional beam gain)

The 18:38Z (above) and 23:14Z (below) telephony attempts benefit from much larger sample sizes (n=51 and n=29 respectively) than the n=1 sample size for the BTO arcs, thus the noise can be reduced by averaging the observations during these bursts. While the P_{RX} residuals are known to be (and can be seen to be) biased due to the unknown additional gain in the regional beam, again the relative values have some utility, and where this is most apparent for the 23:14Z case, especially at the more northerly sample points (6.7S-11S), where the very large residual for the ~100(T) heading would remain relatively large compared to the other sample points even if the curve were shifted downward by 2-3dB.

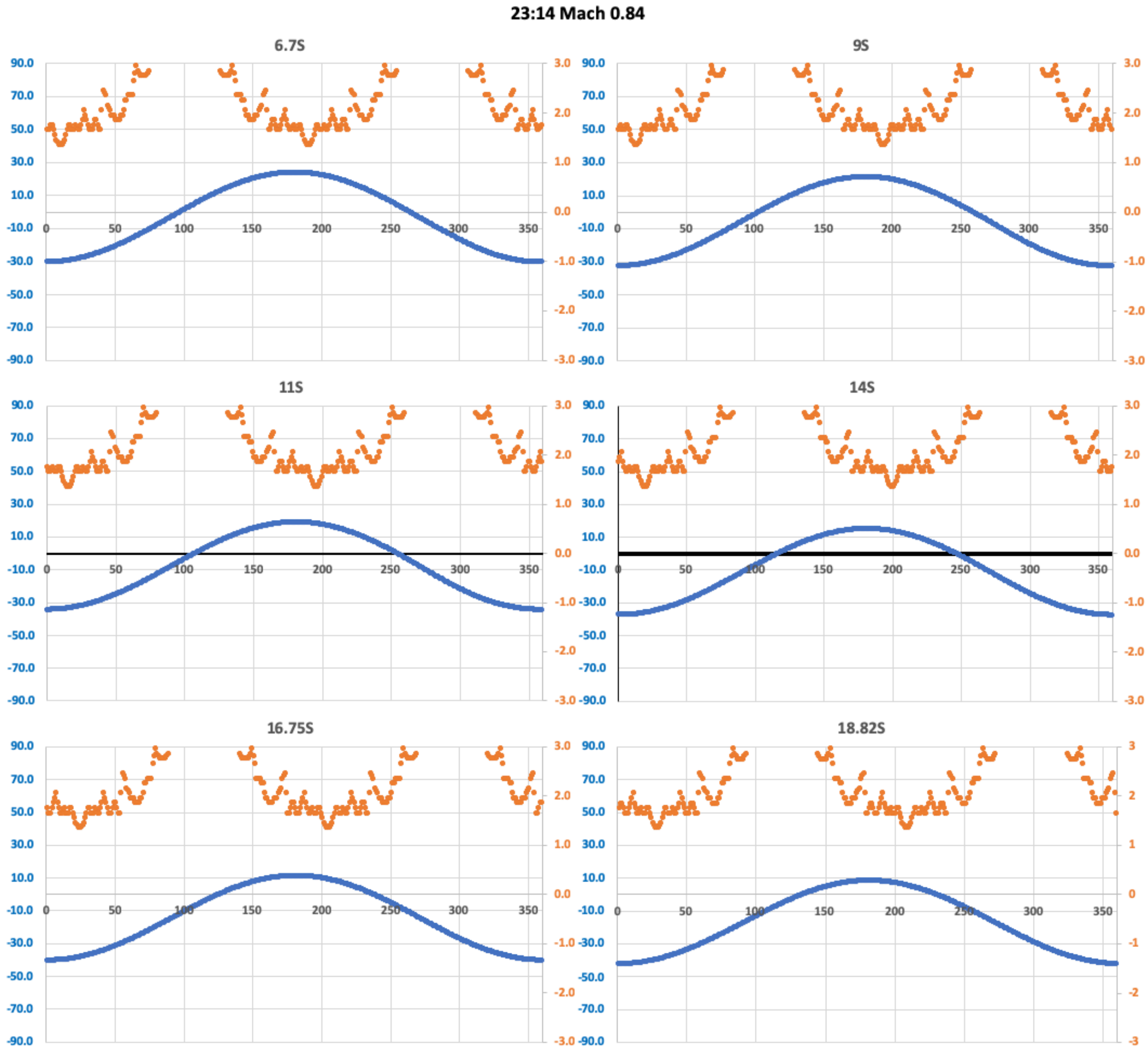

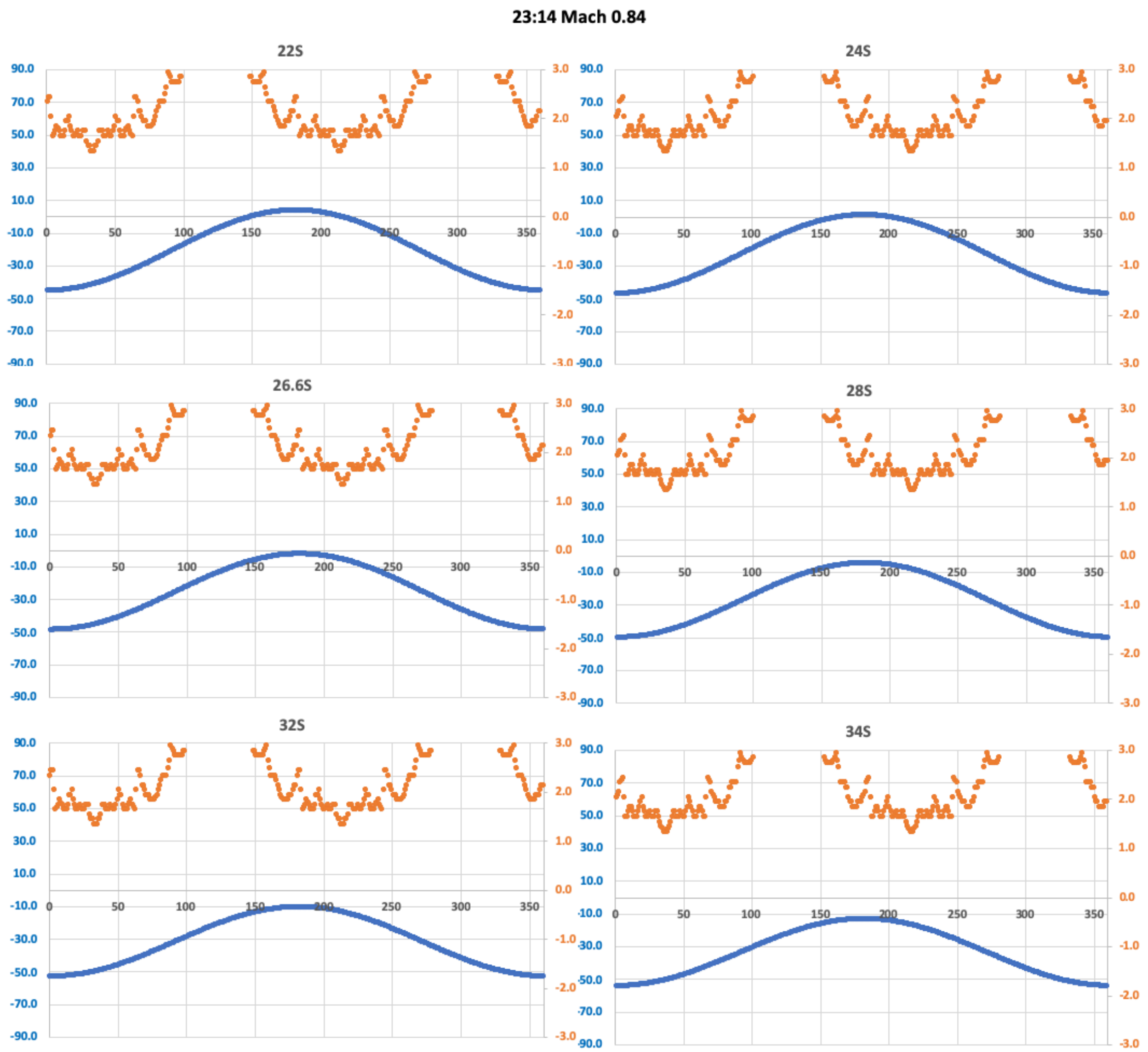

Figure 49. BFO and Received Power Residuals 23:14 Telephony Attempt 6.8S to 30S M0.84. (Received power uncorrected for unknown regional beam gain)

In summary, these sensitivity analyses show that (a) multiple solutions exist for the BFO-only residuals across headings and across the wide swath of arc-latitudes sampled for the 2nd through 6th BTO arcs and the two telephony attempts, and (b) the inclusion of the received power data provides some opportunities to discriminate between these multiple solution points, however the relative geometry does not allow for this in all cases. A salient example of this is at the 00:11Z (6th) arc, where the two solution points at ~12S and ~34S are reflections of one another around the line of sight to the satellite, yielding similar residuals.

R600 Channel Observations 18:25Z and 00:19Z. The sensitivity analysis for the single R600-0-36E1 observation at 18:25Z is shown in Figure 50, where the BFO bias used is 150.1Hz + 4.2Hz = 154.3 Hz and the received power difference relative to the calculated received power model for the R1200-0-36ED channel is +2.7dB.

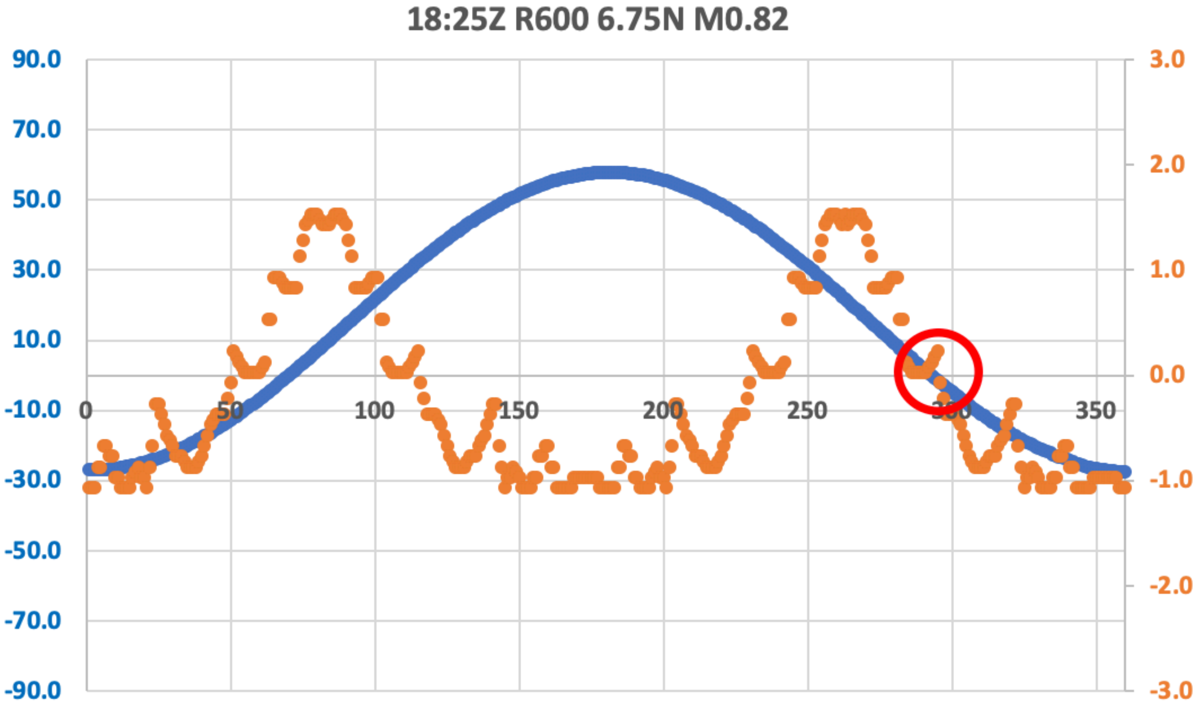

Figure 50. Sensitivity analysis for R600-0-36E1 observation at 18:25Z, sampled at 6.75N on the 1st BTO arc, Mach 0.82, FL350, across 360 degrees.

The sensitivity analysis for the observed BFO and received power shows that both curves cross the zero axis very close to a 296(T) heading at 6.75N on the 1st arc, sampled at Mach 0.82, with residuals of -0.3dBm for the power residual and -2.3 Hz for the BFO residual (0.19 and 0.625 standard deviations, respectively). The BFO residual is zero at a heading of 293(T), a 3-degree difference to the assumed heading on N571, which could also be affected by an error in the assumed Mach number, altitude, rate of climb/descent, as well as noise in the observables. However, the close match of the observed and calculated values for both the BFO and received power data at the postulated heading of 296(T) is taken as evidence against the hypothesis that the R600 channel data is unreliable for either the BFO or received power observations, or that the BFO was affected substantially by the postulated OCXO warm-up effect, as in either case the near-zero values of the independent BFO and received power residuals close to this specific heading would be very unlikely.

For the 00:19Z R600 channel data, the sensitivity analysis assuming Mach 0.78, FL300 and a zero feet-per-minute descent is shown in Figure 51. The BFO curve exhibits a sinusoidal form with a minima in the 182-184(T) range around the trough, at all arc-latitudes sampled, indicating a generally southerly direction. The residual values at the trough of the curves are shown in Table 19, together with rates of descent for which those residuals become zero at each sampled arc-latitude location, which can be seen to be in the 1400-1800 fpm range, or 980-2250 fpm at 2σ/95%. (Note that the curves could be shifted the other way to bring the peak of the curve to zero at approximately a due north heading, however this would require a climb of similar magnitude to be assumed; considered here as an unlikely scenario under the circumstances).

Table 19

Sinusoid Minima at 7th Arc Latitudes Sampled. R600 Channel.

		Sinusoid Minima		
	Arc-Latitude	HDG(T)	BFO Residual	Rate of Descent at Zero Residual (fpm)
	-11.8293	182	-32.8	1835
	-13.28	184	-33.0	1852
	-21.9842	182	-33.0	1828
	-26.9148	183	-32.4	1783
	-31.0677	184	-31.1	1707
	-31.566	184	-30.9	1696
	-34.7	184	-28.8	1573
	-37.5293	184	-27.3	1490
	-39.21	184	-26.1	1445
	-40.236	184	-26.0	1415
Mean Rate of Descent				*1662*

The sensitivity analysis was resampled based on this mean descent rate of 1,662 fpm, the results of which are displayed in Figure 52.

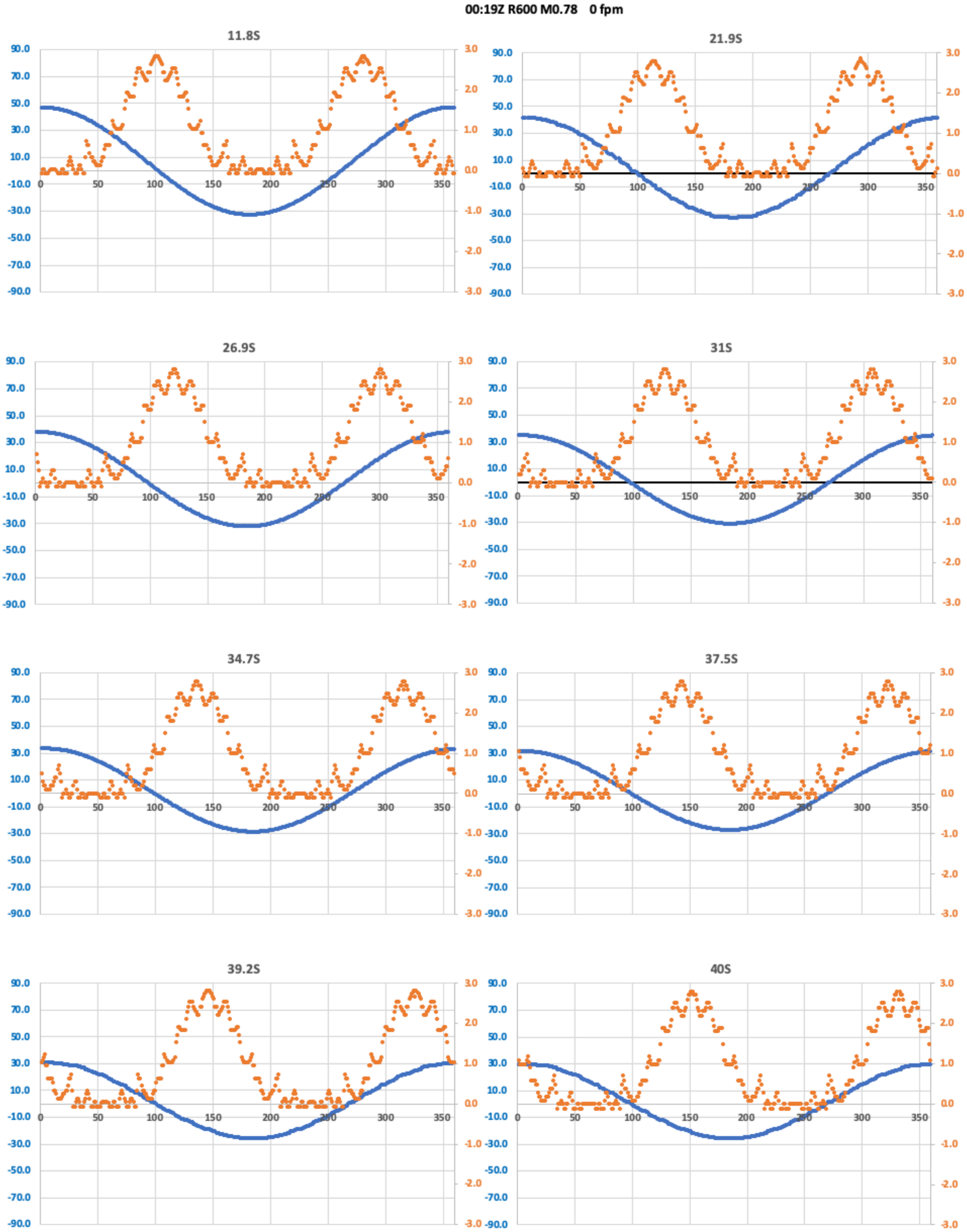

Figure 51. 00:19Z R600-0-36F8 Channel Sensitivity Analysis, Sampled at M0.78, FL300 and 0 fpm Descent.

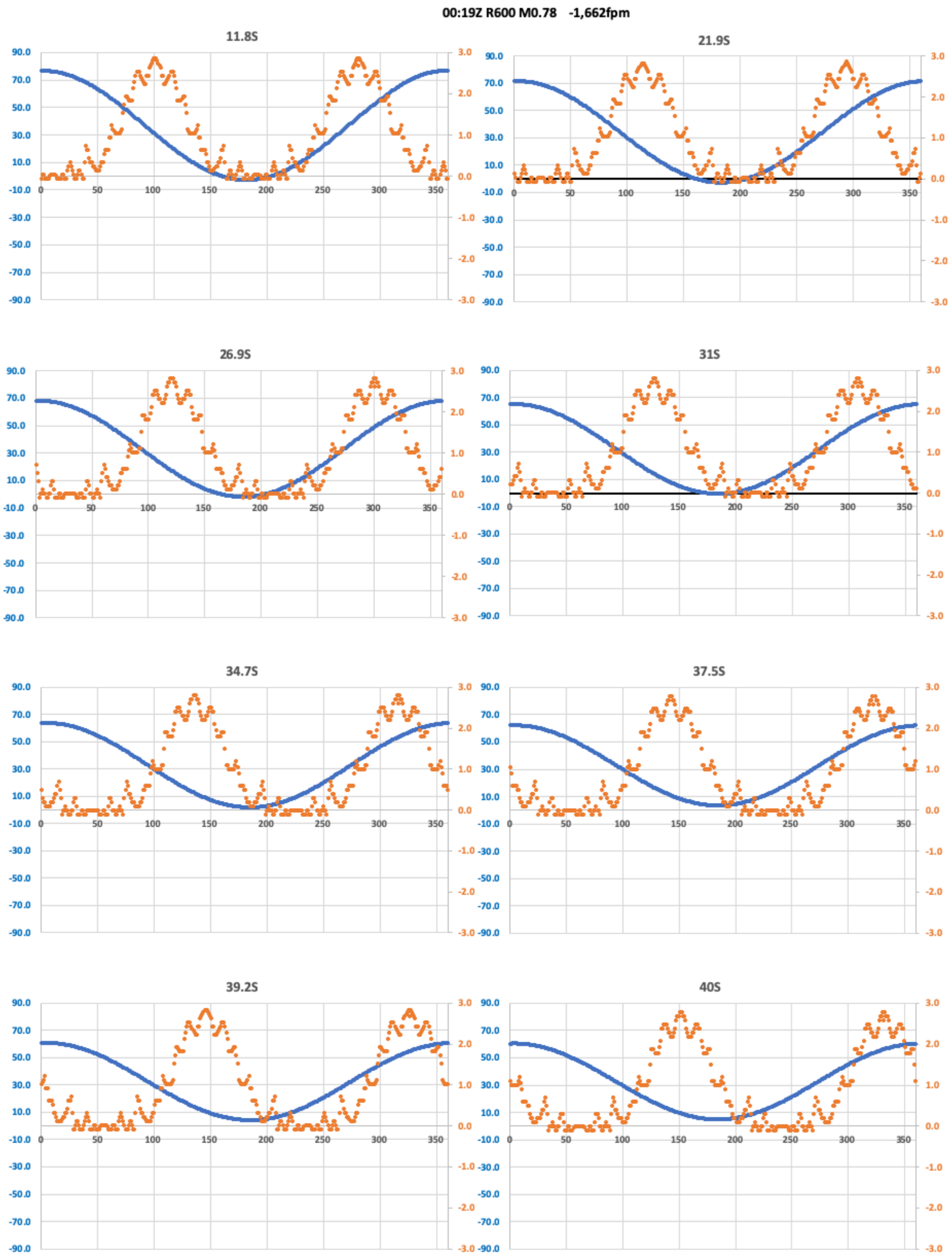

Figure 52. 00:19Z R600-0-36F8 Channel Sensitivity Analysis, Sampled at M0.78, FL300 and 1,662 fpm Descent.

Estimated Probability Density Functions

PDFs for Known States. For the 04:04Z observation, the estimated probability density functions are shown below, with BFO-only pdfs on the left-hand side and joint BFO-P_{rx} pdfs on the right. The pdfs estimated from (a) Gaussian univariate and bivariate probability density, (b) Bayes' theorem with a uniform prior and (c) Bayes' theorem with the BFO-only posterior pdf as the prior for the joint BFO-P_{rx} pdf estimation are shown in each case. The known latitude/heading combination is marked with a red circle on each pdf plot.

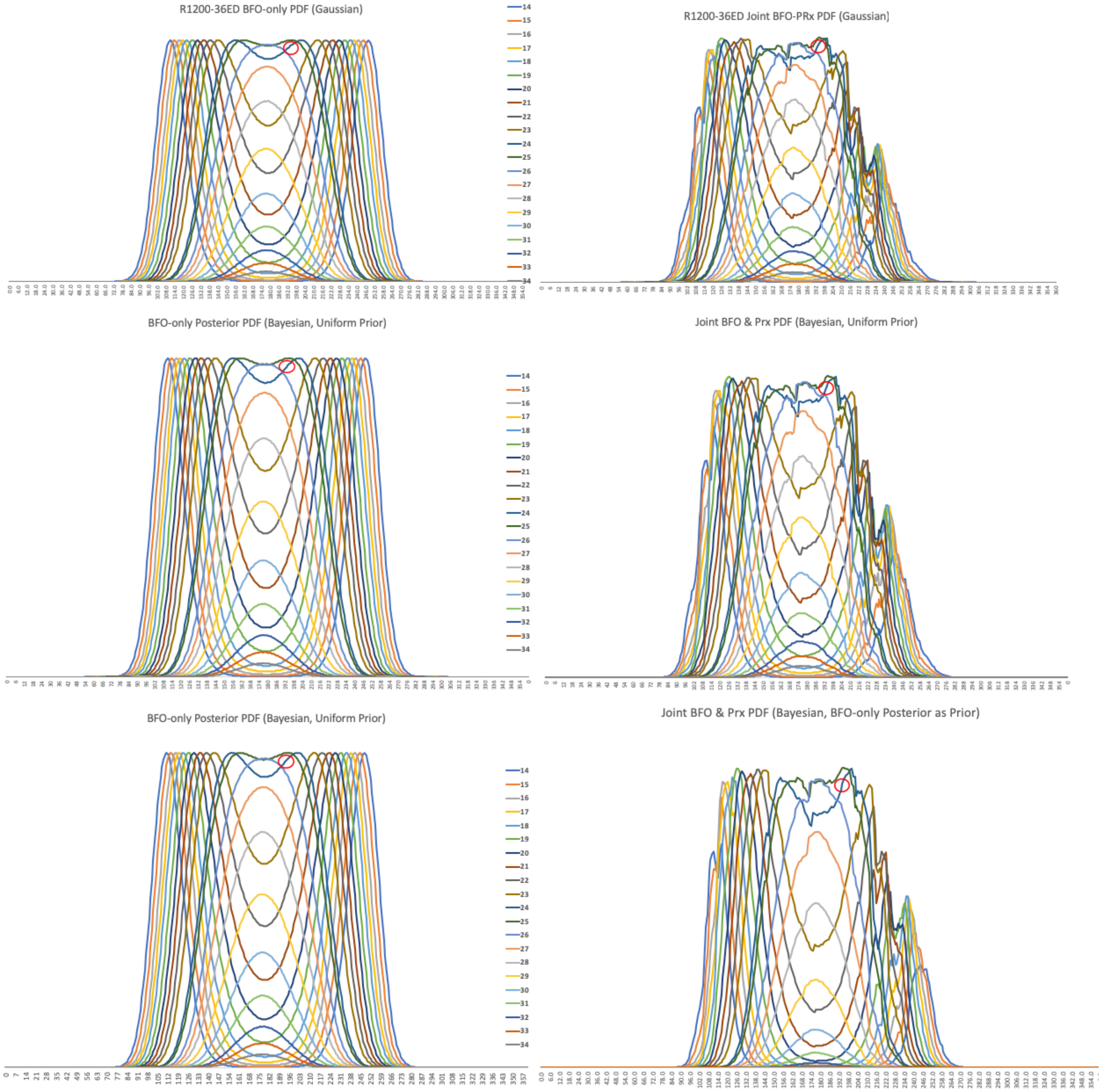

R1200-36ED BFO-only PDF (Gaussian)

R1200-36ED Joint BFO-PRx PDF (Gaussian)

BFO-only Posterior PDF (Bayesian, Uniform Prior)

Joint BFO & Prx PDF (Bayesian, Uniform Prior)

BFO-only Posterior PDF (Bayesian, Uniform Prior)

Joint BFO & Prx PDF (Bayesian, BFO-only Posterior as Prior)

Figure 53. Posterior Probability Density Functions 04:04Z R1200-0-36ED Channel

The samples across the wide range of arc-latitudes tested are overlaid to show the effect of changes in location on the estimated probability density. The general characteristic of the underlying arc-latitude samples, each sampled at 360 degrees of heading, is that of a bimodal distribution in most (but not all) cases, where two headings exhibit high probability densities at any given arc-latitude. The composite across multiple sample points for each observation epoch is highly multimodal, due to shifts in the bimodal solution with latitude.

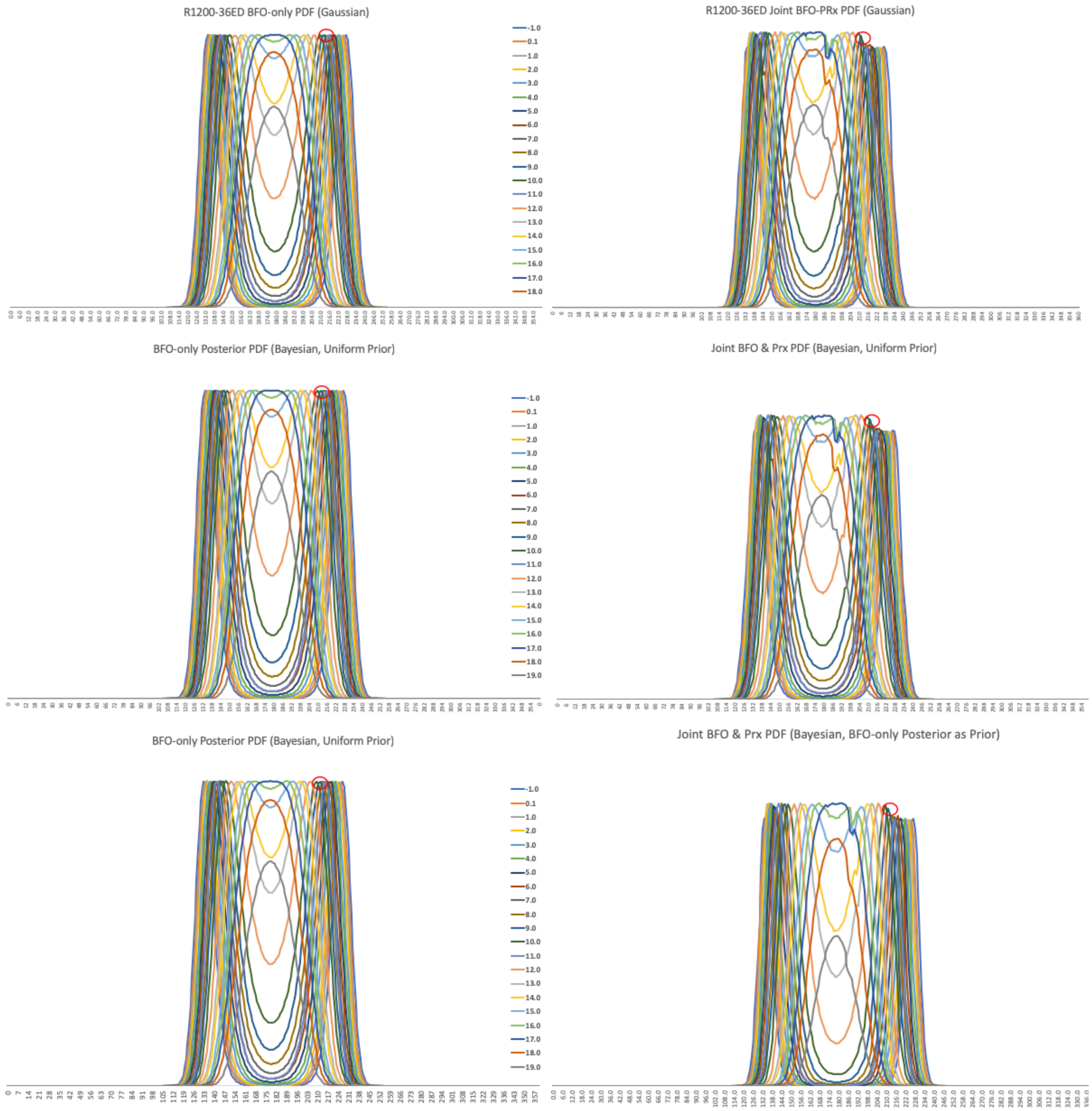
R1200-36ED BFO-only PDF (Gaussian)

R1200-36ED Joint BFO-PRx PDF (Gaussian)

BFO-only Posterior PDF (Bayesian, Uniform Prior)

Joint BFO & Prx PDF (Bayesian, Uniform Prior)

BFO-only Posterior PDF (Bayesian, Uniform Prior)

Joint BFO & Prx PDF (Bayesian, BFO-only Posterior as Prior)

Figure 54. Posterior Probability Density Functions 06:11Z R1200-0-36ED Channel

At the 04:04Z observation time (Figure 53) the inclusion of the power model can be seen to reduce the estimated probability density toward the right hand side of the pdf relative to the BFO-only pdf, that is for headings above ~205(T) across all latitudes sampled. This effect is also present in the 06:11(Z) and 06:48(Z) pdfs (Figure 54 and Figure 55, respectively) although it is much less pronounced. In all three cases, the joint pdfs remain highly multimodal across the arc-latitudes sampled.

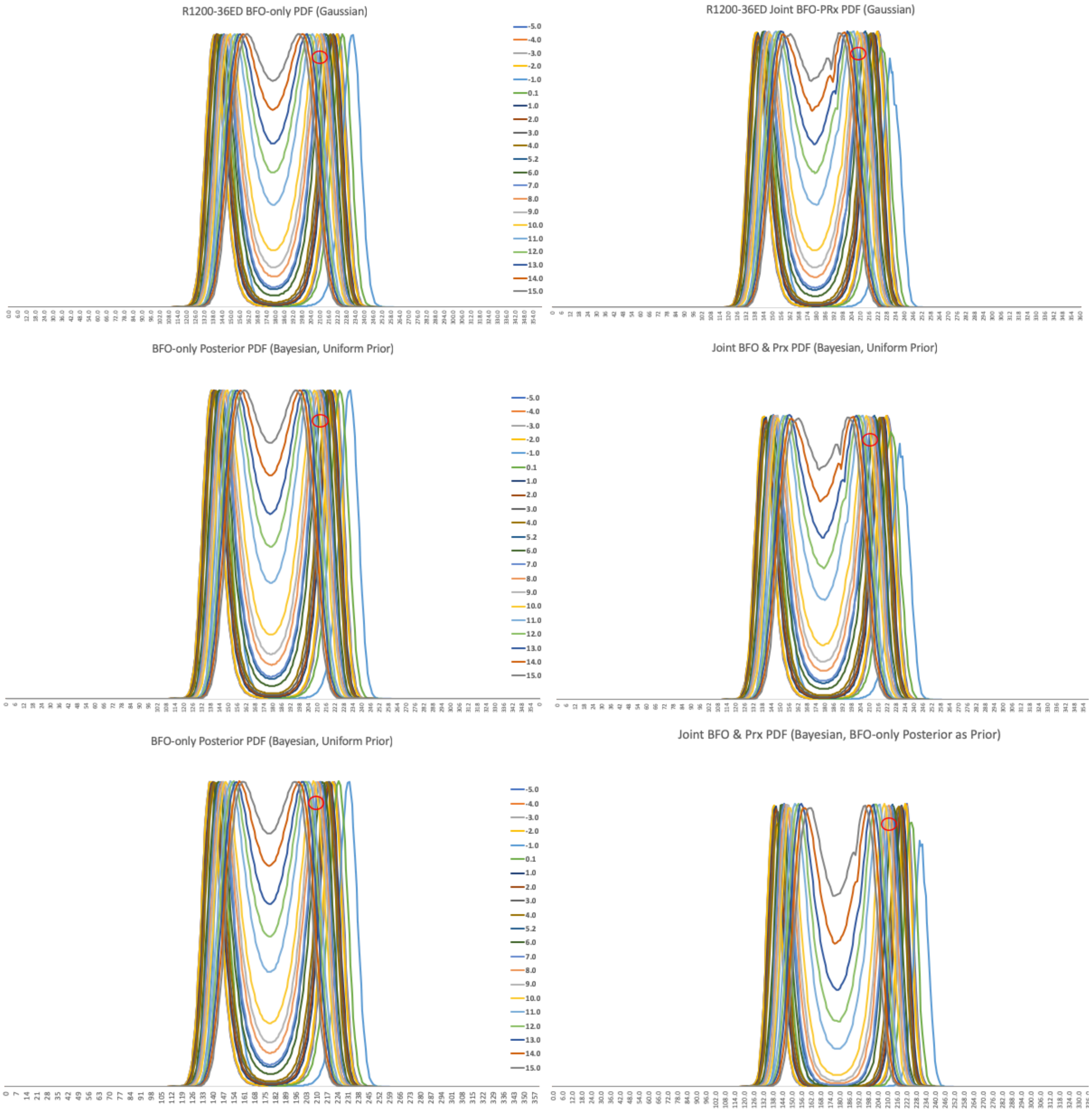

Figure 55. Posterior Probability Density Functions 06:48Z R1200-0-36ED Channel

In the 17:07Z case (Figure 56), the inclusion of the received power residual can be seen to have a more pronounced effect on the estimated pdf, and where the true state becomes one of several peaks in the pdf (highlighted with the red circle) but not in fact the highest peak; those occur at 8,9,14 and 15N on headings of 38-49(T) and 312-231(T), compared to the known state at 5.2N, heading 027(T). Hence, the inclusion of the power model serves to reduce the number of solution points compared to the BFO-only pdf, however with a slight reduction in the estimated probability density for the correct solution. Although that solution is indicated as a near-peak value, this example demonstrates that simple selection of the peak value is not a reliable indicator of the true state.

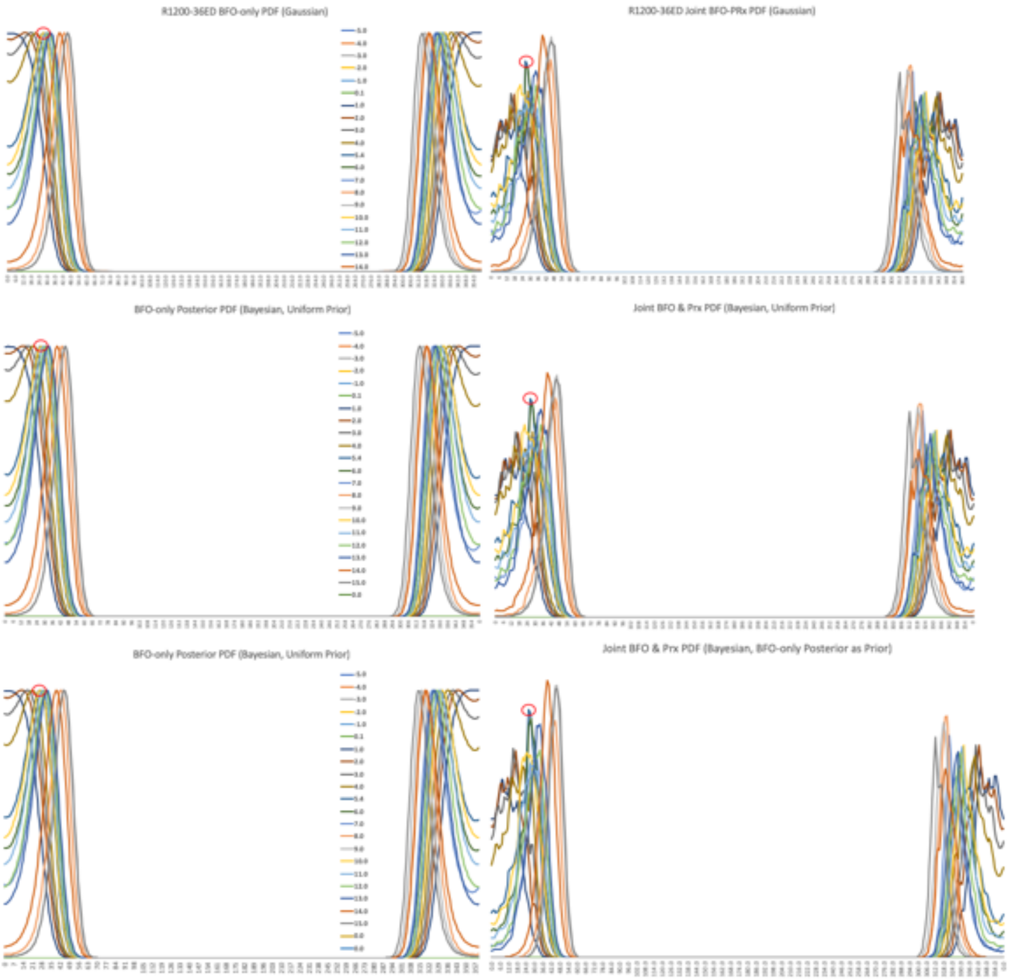

Figure 56. Posterior Probability Density Functions 17:07Z R1200-0-36ED Channel

For the estimated aircraft state at the time of the 18:28Z restart (Figure 57), the BFO-only pdf is bimodal around two headings, 66-74(T) and 285-297(T), across all arc-latitudes sampled. The inclusion of the received power model diminishes the estimated density for the first heading group relative to the second group which contains the likely state of 296(T) at 6.75N, however the false peaks are by no means entirely eliminated. Again, the true value is near-peak but is not the highest estimated density value in the joint density estmation.

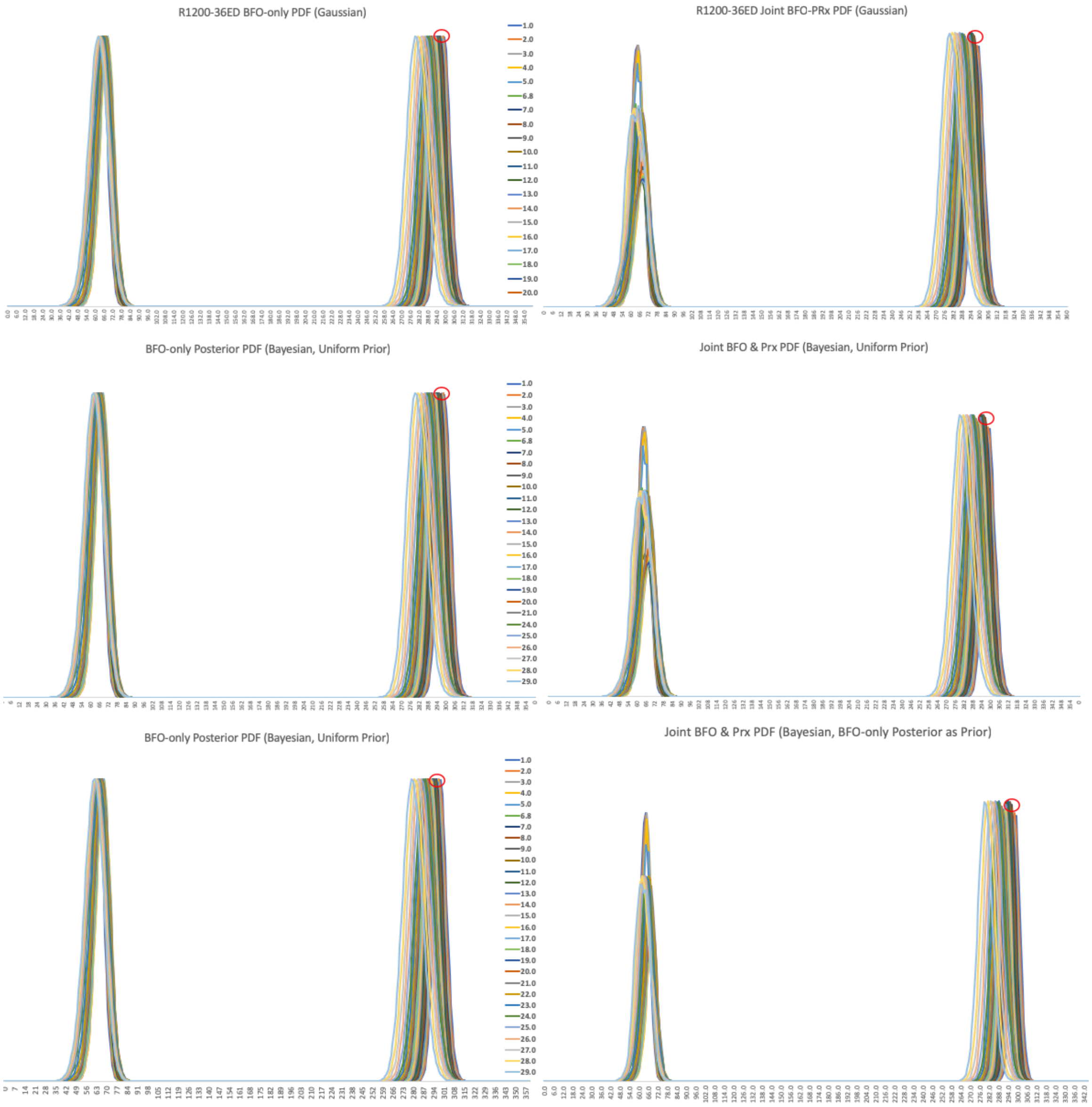
R1200-36ED BFO-only PDF (Gaussian)

R1200-36ED Joint BFO-PRx PDF (Gaussian)

BFO-only Posterior PDF (Bayesian, Uniform Prior)

Joint BFO & Prx PDF (Bayesian, Uniform Prior)

BFO-only Posterior PDF (Bayesian, Uniform Prior)

Joint BFO & Prx PDF (Bayesian, BFO-only Posterior as Prior)

Figure 57. Posterior Probability Density Functions 18:28Z R1200-0-36ED Channel

Percentiles of Probability Density Estimates at Known States.

For the known states at 04:04Z through 17:07Z, plus the assumed state at 18:28Z, the rank and percentile of the known position and heading, as calculated using all values of the estimated probability density functions for those times were found, as follows:

Table 20

Rank and Percentile of Estimated Probability Density for Known States

Time (UTC)	ϕ	λ	HDG(T)	Rank of Estimated Probability Density for Known State	Number of Systematic Samples	Percentile
04:04Z	24.06	113.88	193.1	95	7581	0.987
06:11Z	9.00	107.27	212.0	203	7581	0.973
06:48Z	5.24	104.52	208.8	213	7582	0.972
17:07Z	5.40	102.86	026.7	29	5415	0.995
18:28Z	6.75	96.0	296.0	39	10469	0.996

In all cases tested, the estimated joint probability density corresponding to the known position and heading was above the 97th percentile. In two of the cases, the exact known heading and arc-latitude was above the 0.995 percentile and in the remaining three cases, filtering on the 0.995 percentile and above yielded solutions within 1 degree of latitude and <10 degrees of heading from the known values.

Bimodality and Non-Uniqueness of Induced Error Due to Fixed Satellite Assumption.

As mentioned in Chapter II, the underlying observable of interest for the BFO is the error induced in the AES Doppler pre-compensation from using a fixed satellite assumption instead of the actual satellite position and velocity at the time of the transmission. It is this error which enables sampling of hypothetical locations and headings, by computing the BFO which would be expected at those locations and headings, using the AES pre-compensation assumptions, and then comparing that to the observed value. If the pre-compensation were perfect, or if the spacecraft were in fact in a perfect GEO orbit, this technique would not work. If the pre-compensation were not present, the solution space would be different, as the uncompensated Doppler would be known (though not necessarily unique). The results in Table 21 suggest that non-uniqueness of the induced error caused by the fixed spacecraft assumption is the cause of multiple points with a zero or near-zero residual and hence the multimodality in the estimated probability density functions.

Table 21

Repeating Induced Error Due to Fixed Satellite Assumption at Known State Observations

Sampled Latitude	HDG(T)	BFO Observed	Total Induced Doppler Hz	Induced Doppler on Uplink (dFup) Hz	Calculated Doppler Pre-compensation Value Hz	BFO Residual Observed - Calc'd	Induced Error in dFup due to Fixed SC Position & Velocity Assumption
04:04Z							
24.05	156 (Known)	234	-274	336	-337	0	1
24.05	202	234	602	-541	539	0	1
14	248	234	1236	-1175	1174	0	1
14	111	234	-965	1026	-1027	0	1
25	162	234	-163	224	-225	0	1
25	195	234	466	-405	403	0	1
06:11Z							
9	212 (Known)	234	760	-731	698	0	33
9	145	234	-349	379	-412	0	33
-1	133	234	-647	677	-710	0	33
-1	227	234	845	-815	782	0	33
17	178	234	284	-254	221	0	33
06:48Z							
5.236	210 (Known)	226	683	-665	627	-1	38
5.236	145	226	-350	368	-405	0	37
-5	138	226	-643	661	-698	0	37
-5	222	226	652	-635	598	0	37
15	160 (Tangent)	226	-13	30	-67	0	37
15	196	226	555	-537	500	0	37
17:07Z							
5.398	27 (Known)	131	-522	475	-503	0	28
5.398	332	131	303	-351	323	0	28
1	357	131	-33	-14	-14	0	28
1	1 (Tangent)	131	-15	-32	5	0	27
15	44	131	-1030	983	-1011	-1	29
15	314	131	264	-312	284	0	28
18:28Z							
6.75	296 (Estimated)	143	659	-685	669	3	17
6.75	65	143	-819	793	-809	3	16
1	64	143	-726	699	-714	4	15
1	299	143	713	-739	721	2	18
29	62	143	-964	938	-955	2	17
29	279	143	383	-410	392	2	18

The data shows, for each observation time, the known arc-latitude and heading, together with examples (drawn from many) of other zero-residual solutions found in the systematic sampling along each arc (i.e. indicating a false solution). In each case, while the total induced Doppler, and the pre-compensation values are very different, the error induced by the fixed satellite assumption is the same as that for the correct, known value. Thus, it is suggested that this observed non-uniqueness of the induced error due to the fixed satellite assumption results in the observed multimodality of the estimated pdfs.

Also identified in the table are two cases where a zero-value BFO residual occurs on a tangent to the line of sight from the aircraft to the satellite, corresponding exactly to the horizontal component of the look angle to the satellite at the sampled location, plus or minus 90 degrees. A distinguishing characteristic of these cases is that the absolute values of total Doppler, uplink Doppler and pre-compensation are lower than the other solutions along that arc, due to the fact that these values tend to a minimum on the tangent. Tangent cases are found in some of the estimated probability density functions for the unknown states.

Estimated Probability Density Functions for Unknown States (After 18:28Z)

The estimated pdfs for the observation times between 19:41Z and 00:11Z where the aircraft state is unknown are presented below, first for the BTO arcs and then for the two telephony attempts.

The 19:41Z pdf (Figure 58) is bimodal, at headings of ~140-145(T) and ~215-222(T). A due south or 180(T) heading at this time is not indicated, at least not at the sampled Mach number of 0.84. The bimodality converges to unimodality around a 183(T) (~180M) when sampled at much lower ground track velocities in the 350-400kt range (Figure 58, bottom panel), however it is noted that pronounced bimodality is present at the observation points with known aircraft state in the previous examples, where the sampled Mach number corresponds to the known value, thus either solution is plausible.

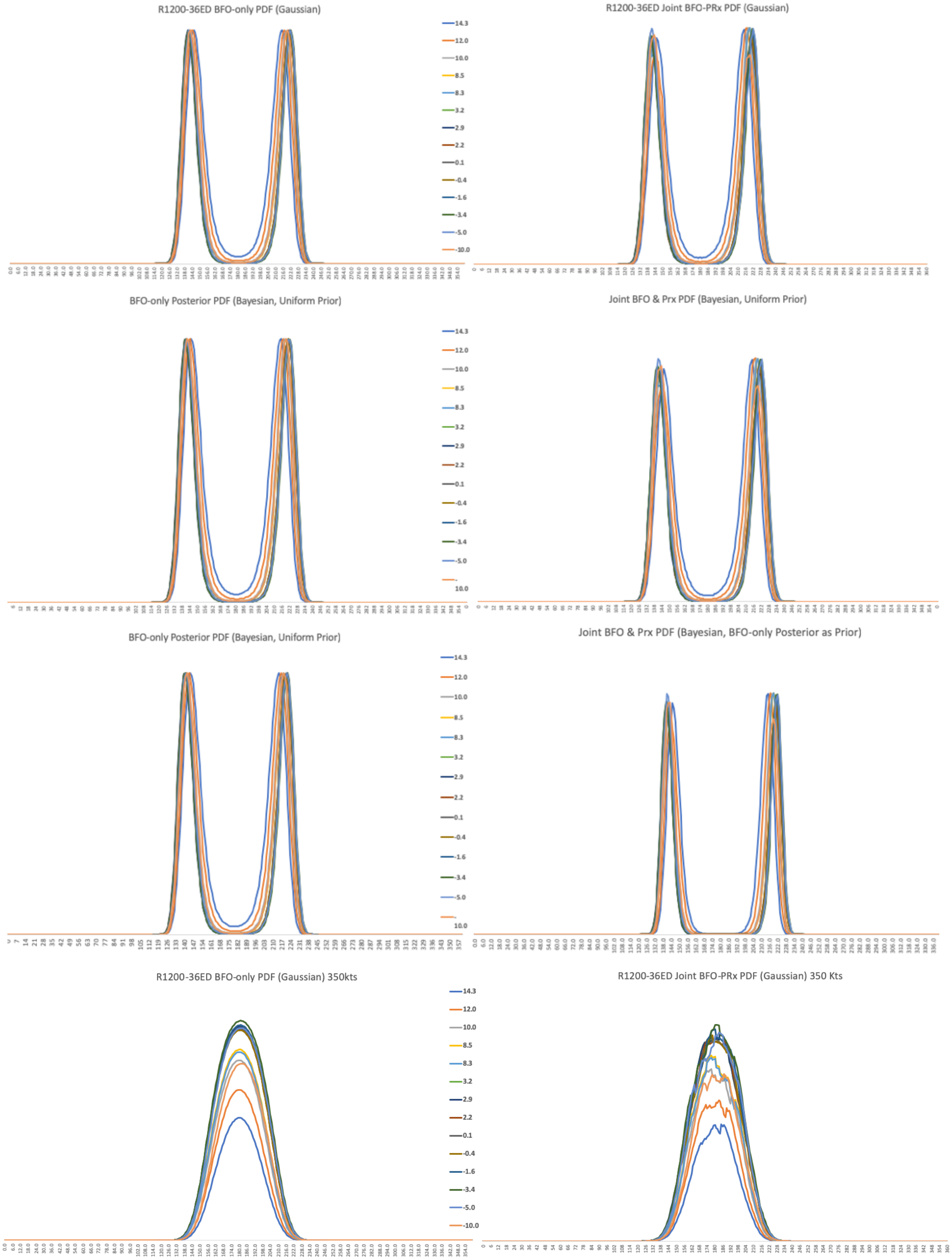
R1200-36ED BFO-only PDF (Gaussian)

R1200-36ED Joint BFO-PRx PDF (Gaussian)

BFO-only Posterior PDF (Bayesian, Uniform Prior)

Joint BFO & Prx PDF (Bayesian, Uniform Prior)

BFO-only Posterior PDF (Bayesian, Uniform Prior)

Joint BFO & Prx PDF (Bayesian, BFO-only Posterior as Prior)

R1200-36ED BFO-only PDF (Gaussian) 350kts

R1200-36ED Joint BFO-PRx PDF (Gaussian) 350 Kts

Figure 58. Posterior Probability Density Functions 19:41Z R1200-0-36ED Channel

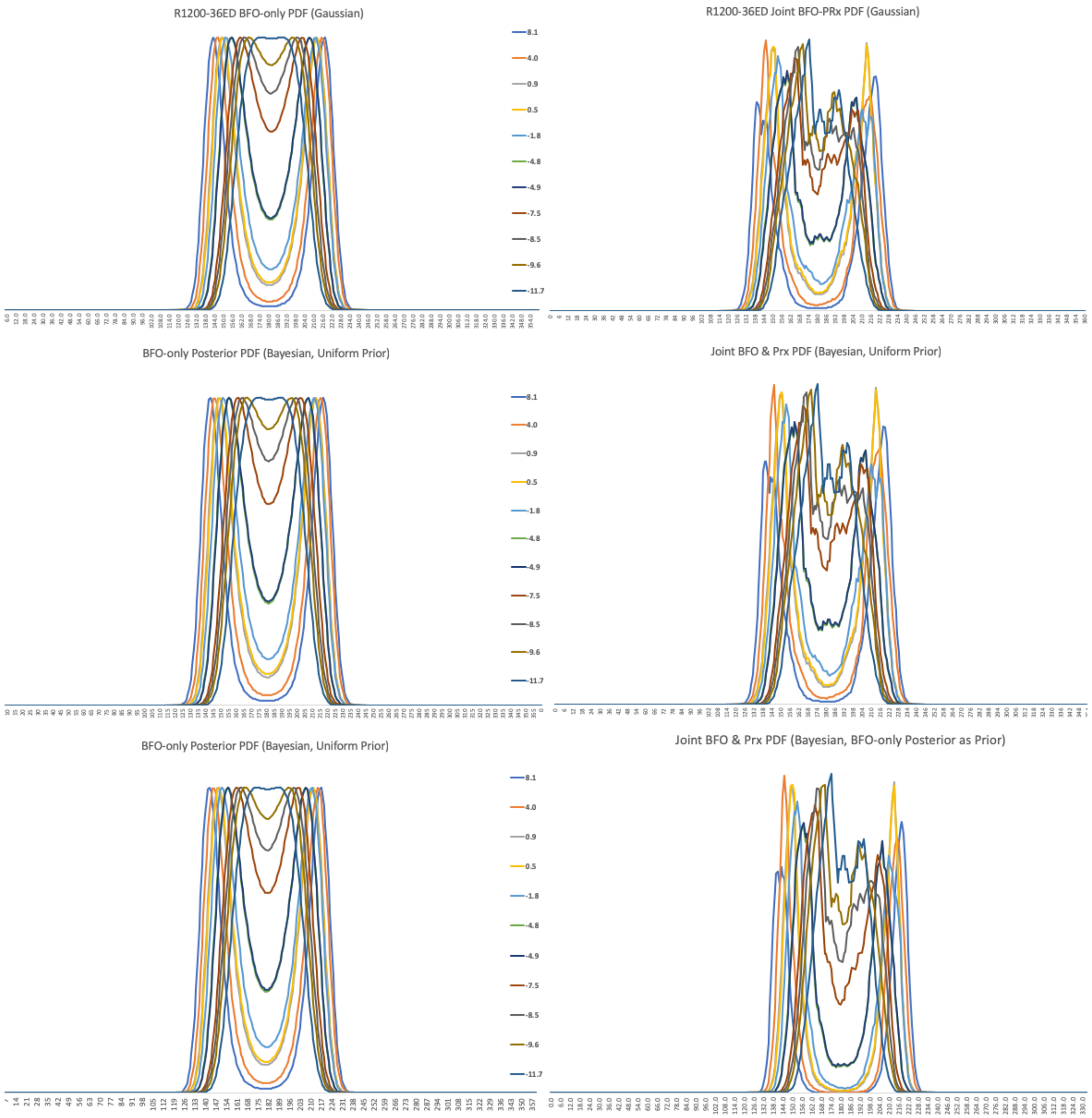
R1200-36ED BFO-only PDF (Gaussian)

R1200-36ED Joint BFO-PRx PDF (Gaussian)

BFO-only Posterior PDF (Bayesian, Uniform Prior)

Joint BFO & Prx PDF (Bayesian, Uniform Prior)

BFO-only Posterior PDF (Bayesian, Uniform Prior)

Joint BFO & Prx PDF (Bayesian, BFO-only Posterior as Prior)

Figure 59. Posterior Probability Density Functions 20:41Z R1200-0-36ED Channel

For the 20:41Z observation (Figure 59), the BFO-only solutions are diffused, with solutions between 142-168(T) and 196-216(T) across the arc-latitudes tested, plus a plateau between 174-190(T) at the 11.7S arc-latitude location, sampled at M0.84. The joint posterior pdfs exhibit peak clusters at, in order of probability density, 7.5-11.7S 164-174(T), 4N 145(T), 0.5N-0.9N at 150 and 213(T), 1.8S and 4.9S at 153-159(T) and 8.1N at 219(T). The pdfs remain bimodal when sampled across a feasible range of velocities.

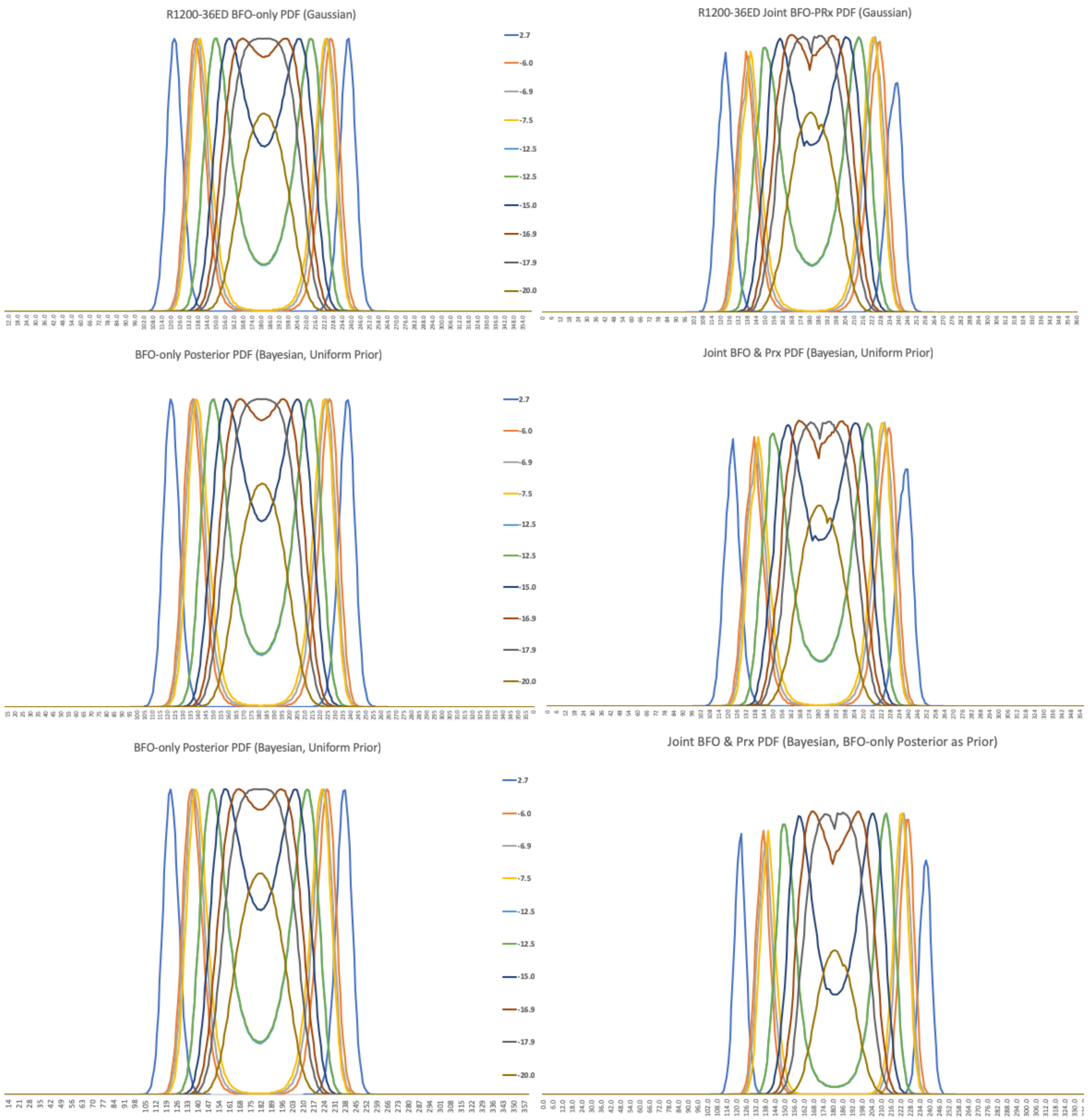
R1200-36ED BFO-only PDF (Gaussian)

R1200-36ED Joint BFO-PRx PDF (Gaussian)

BFO-only Posterior PDF (Bayesian, Uniform Prior)

Joint BFO & Prx PDF (Bayesian, Uniform Prior)

BFO-only Posterior PDF (Bayesian, Uniform Prior)

Joint BFO & Prx PDF (Bayesian, BFO-only Posterior as Prior)

Figure 60. Posterior Probability Density Functions 21:41Z R1200-0-36ED Channel

For the 21:41Z observation (Figure 60), the BFO-only solutions are diffused, with solutions between 123-238(T) across the arc-latitudes tested, sampled at M0.84 plus a plateau between 176-189(T) at the 17.9S arc-latitude location. The joint posterior pdfs exhibit probability density peaks around a 180(T) heading +/-20 degrees at 16.9S and 17.9S, followed by 6-7.5S at 223-225(T), 12.5S at 214(T), 6.9-15S at 139-162(T) and 2.7N at123(T) and 238(T). The pdfs remain bimodal when sampled across a range of feasible velocities, however the indicated latitudes move north at low velocity.

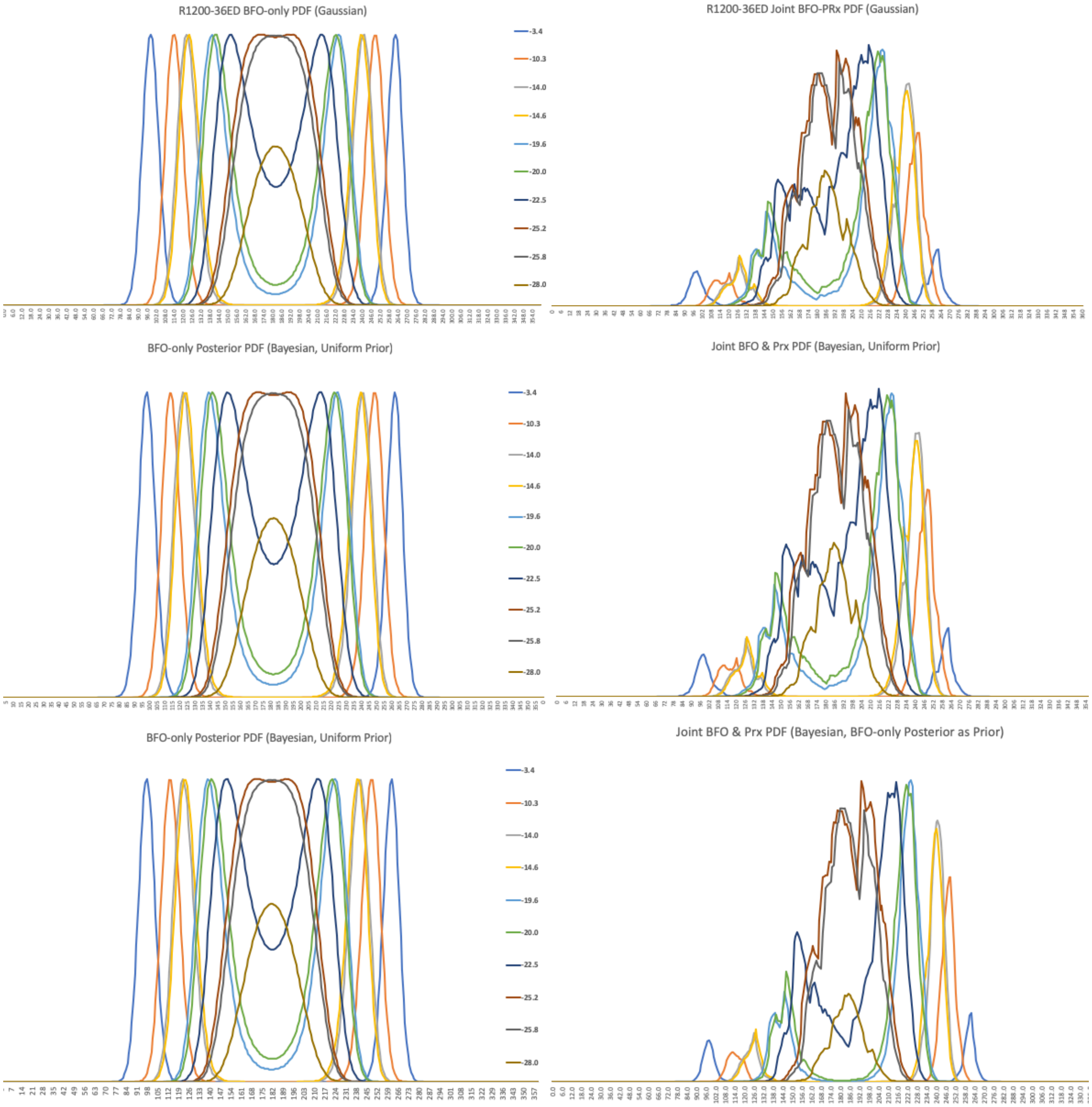

Figure 61. Posterior Probability Density Functions 22:41Z R1200-0-36ED Channel

For the 22:41Z observation (Figure 61), the BFO-only solutions range from 3.4S to 28S on headings from 98-153 and 263, with a plateau at 25-26S at 170-195(T). The joint posterior pdfs most strongly indicate the 20S to 25.8S subset of the arc-latitudes tested, with headings between 178(T) and 225(T) degrees. The peaks are at 22.5S 210-215(T), 25.2-

25.8S 193-199(T) or 180-184(T), 19.6-20S 221-224(T), 14.0-14.6S 241-243(T). The orange peak toward the right-hand side at 10S 248(T) is also a possible solution, although less likely. The pdfs remain bimodal when sampled across a broad range of feasible velocities.

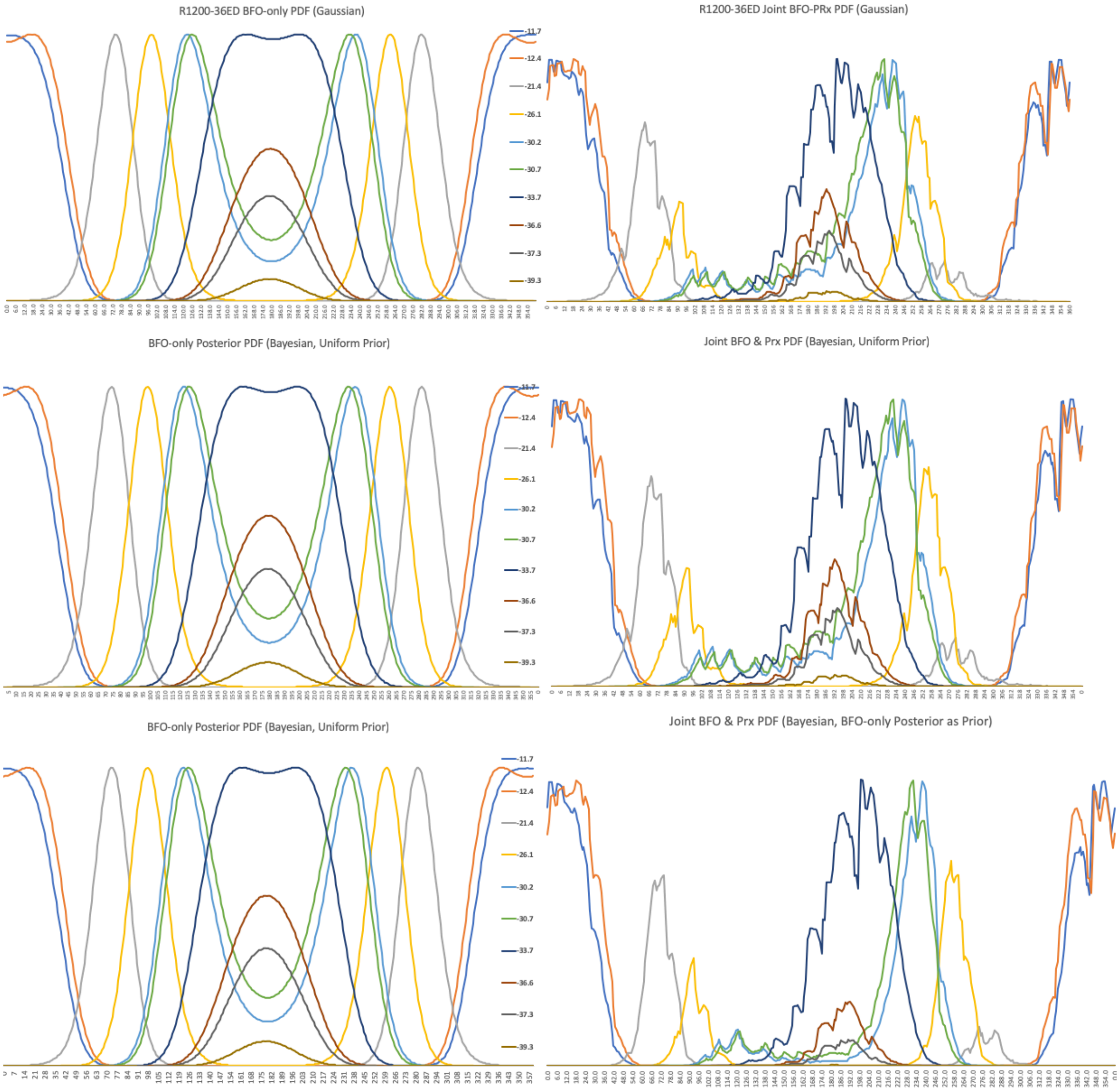
R1200-36ED BFO-only PDF (Gaussian)

R1200-36ED Joint BFO-PRx PDF (Gaussian)

BFO-only Posterior PDF (Bayesian, Uniform Prior)

Joint BFO & Prx PDF (Bayesian, Uniform Prior)

BFO-only Posterior PDF (Bayesian, Uniform Prior)

Joint BFO & Prx PDF (Bayesian, BFO-only Posterior as Prior)

Figure 62. Posterior Probability Density Functions 00:11Z R1200-0-36ED Channel

Sampled at Mach 0.84, the BFO-only solutions for the 00:11Z observation (Figure 62) are distributed broadly from 12S to 33.4S, at headings spread across the dial. The joint posterior pdfs at the 00:11Z 6th arc points tested (from the meta-analysis subset) essentially distill to two most strongly indicated solutions: one in the vicinity of 12S heading approximately true north +/- 30 degrees and the other in the vicinity of 30-34S heading approximately 216(T) +/- 30 degrees. 21.4S 068(T) and 26.1S 255(T) are also possible solutions, although less likely.

The multimodality at 00:11Z was not found to converge to unimodality when sampled from a ground track velocity of 320kts (approximately corresponding 270 KIAS, V_{LO}/V_{LE} for the type), to a ground track velocity of 520 kts (approximately corresponding to M0.89, above M_{MO} for the type).

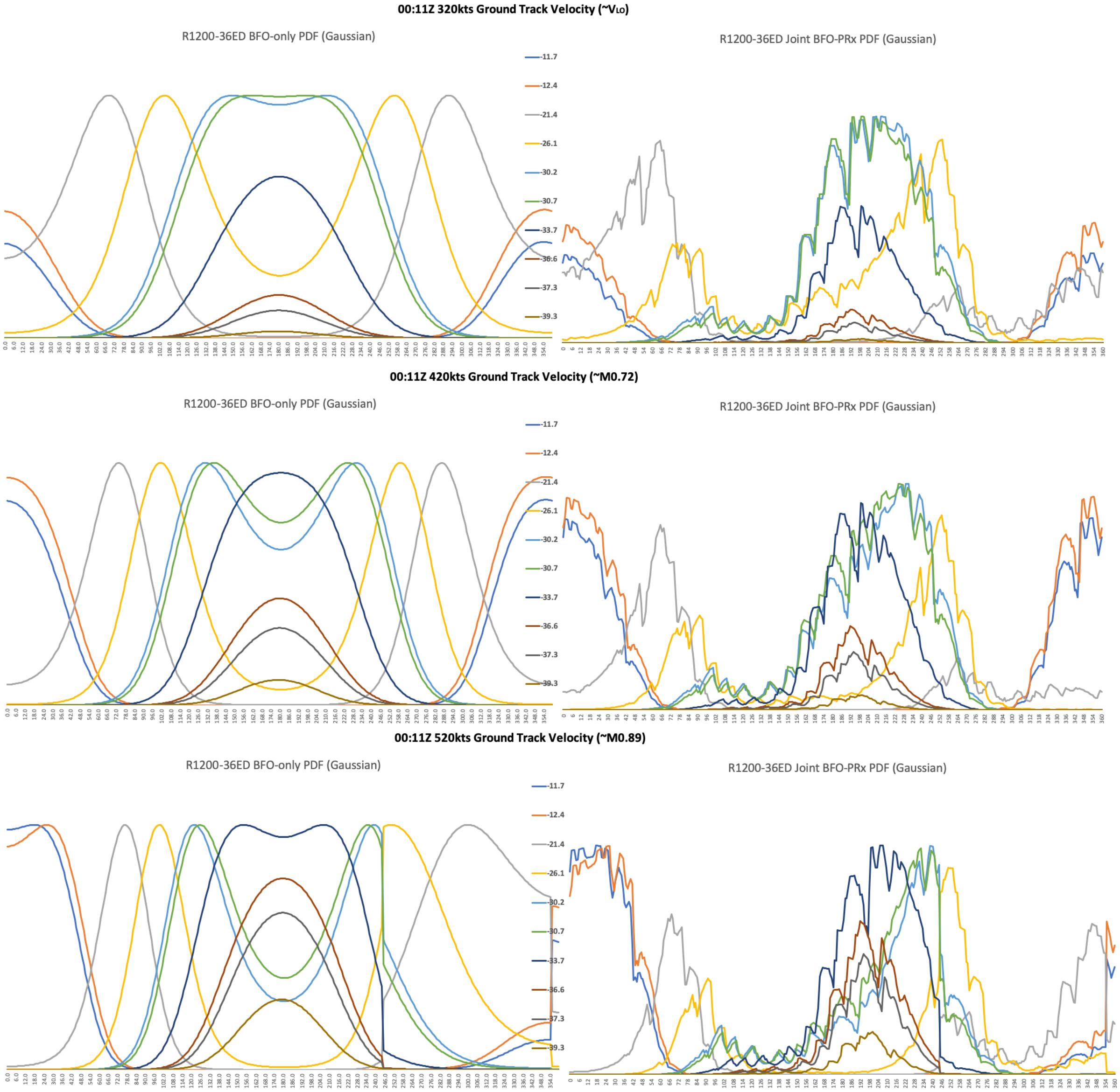

Figure 63. 00:11Z PDFs sampled at 320, 420 and 520 kts ground track velocity

As can be seen in Figure 63, the northerly solution (orange/blue) diminishes at the lower velocity, as does the 33.7S solution (dark blue, center) while the 30S (green/blue) solution is the most persistent across this range of velocities.

It is also noted that tangent solutions exist in the 00:11Z pdfs, which were observed for the known state observations as producing false solutions (however, neither is it infeasible for an aircraft to happen to be on a tangent heading, a 1/180 chance in fact, all other things being equal). For the northerly solution, the apparent azimuth to the satellite from the aircraft at 12S on the 00:11Z arc is 284 degrees (true), on a tangent to which aircraft headings of 284 +/-90 degrees, i.e. 194(T) and 014(T) would correspond, headings with are included in the peak density estimates for the 11.7S and 12.4S locations. This is also the case for the southerly solutions, although less so, for example at the sample points of 30.2S and 33.7S, the line-of-sight azimuths of 310 and 316 degrees create tangent aircraft headings at 40/200 and 46/226 respectively. While headings of 200(T) and 226(T) are not in the highest peaks at those latitudes, the estimated densities are sufficiently high to preclude the conclusion that they are not also tangent solutions.

Telephony Attempts. The pdfs for the two telephony attempts are shown below, using the globally estimated standard deviations but making use of the mean observations for those sequences of multiple transmissions, such that the standard deviation of the mean observation would be expected to reduce by a factor of one over the square root of the n=51 and n=29 data points.

For the 18:28Z telephony attempt, the BFO-only pdf is bimodal around headings of 145-152(T) and 206-216(T) when sampled at Mach 0.84, and the joint BFO-P_{rx} pdf has a higher estimated density around 145-152(T) than 206-216(T).

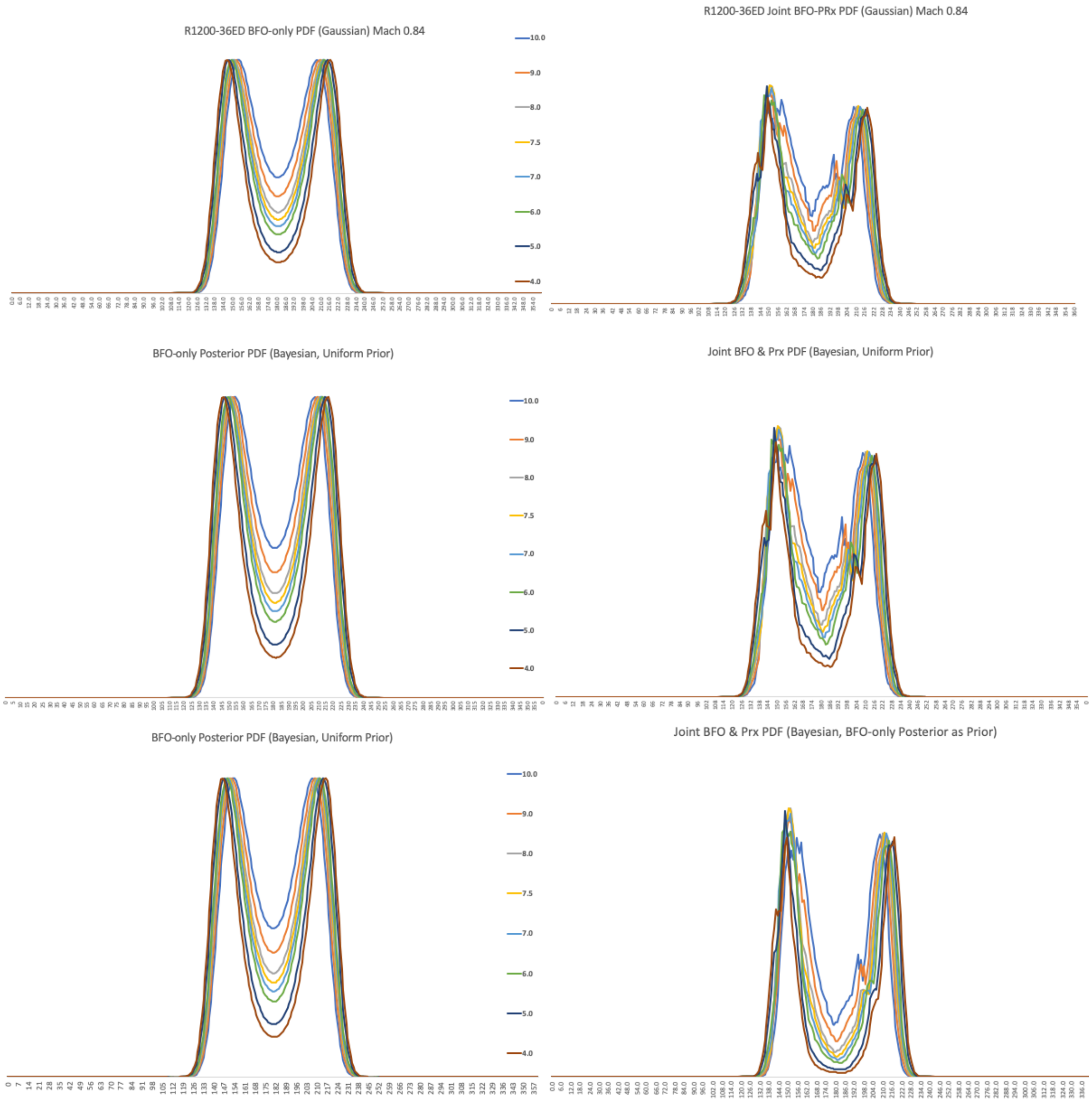

Figure 64. Posterior PDFs 18:38Z Telephony Attempt; σ_{BFO}=4.0 σ_{Prx}=1.6 Mach 0.84.

The bimodality converges to unimodality when sampled at different Mach numbers, most notably so for ground track velocities of 350-400kts, at the upper end approximately corresponding to V_{MO} (330KIAS) for the type at an altitude of 10-15,000ft. At higher velocities, the bimodality remains (Figure 65 lower panel, and where the upper three panels show the pdfs sampled at 350, 400 and 420kts and the bottom panel at 530kts). The sharp peak at 350kts indicates a heading of exactly 180(T), sampled at 4N 94.4E.

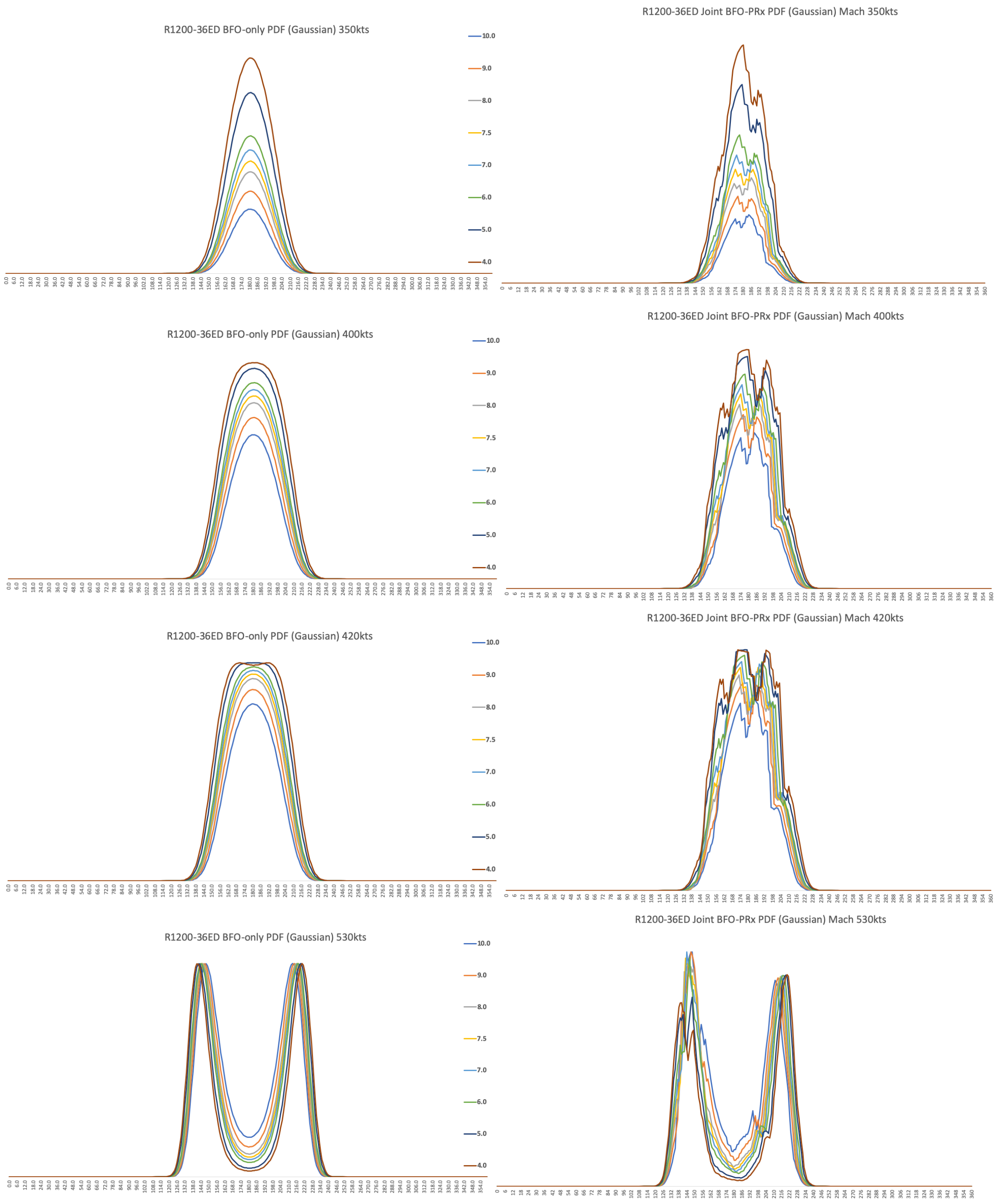

Figure 65. PDFs 18:38Z Telephony: 350, 400, 420 and 530Kts(bottom), over ground.

However, it is again noted that bimodality was found for the observation times where the aircraft state is known and when sampled at the correct, known Mach number; thus convergence to unimodality by changing the velocity does not necessarily indicate a correct solution, and therefore either the unimodal of bimodal solution is plausible. On the other hand, the ~150(T) heading which is most strongly indicated in the joint pdfs for normal cruising speeds and higher (i.e. M0.80+) is not consistent with the general direction of the track indicated by the displacement of the 19:41Z BTO arc, unless another turn was made.

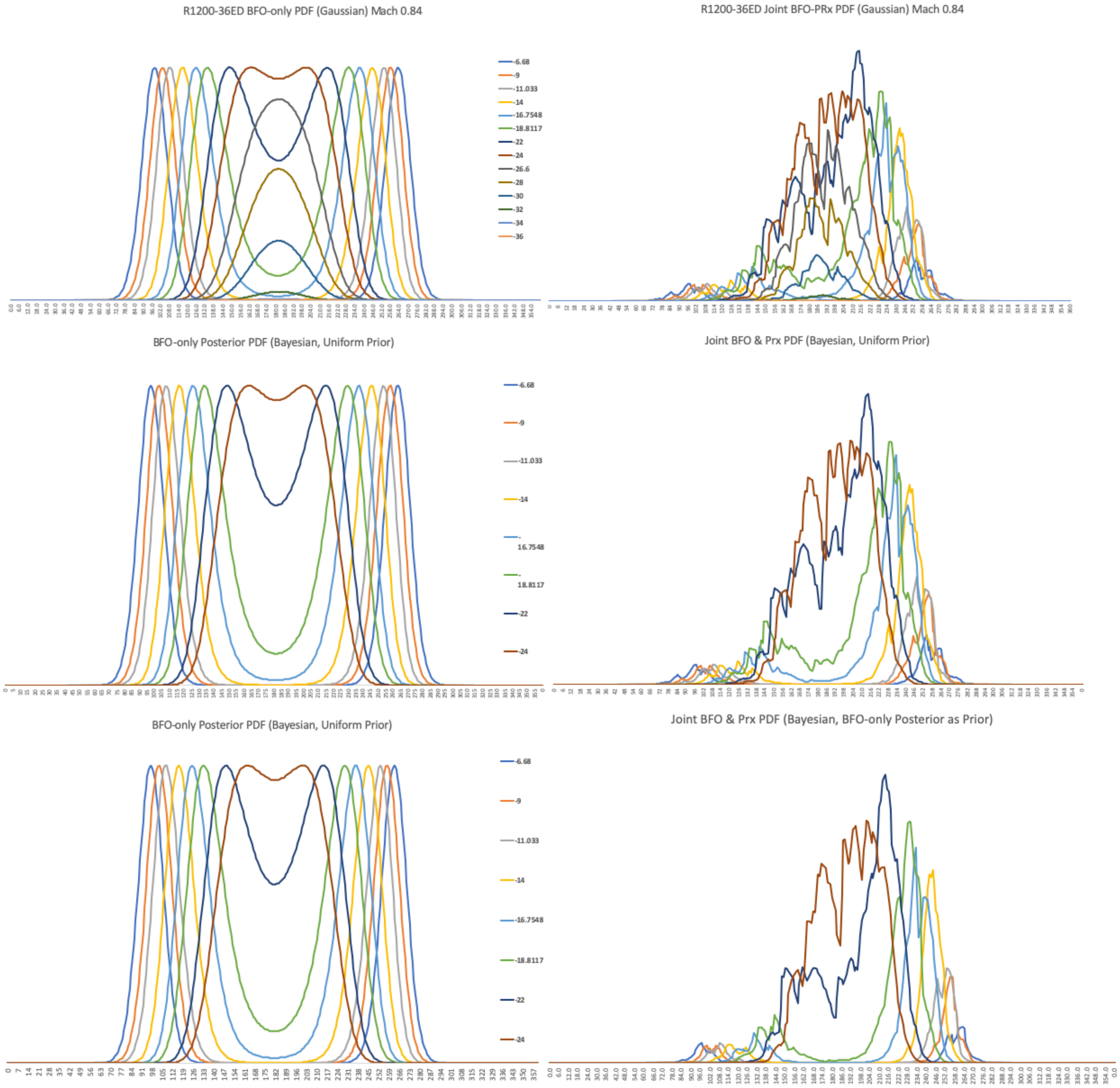

Figure 66. Posterior PDFs 23:14Z Telephony Attempt; σ_{BFO}=4 σ_{Prx}=1.6

For the 23:14Z observation set (Figure 58), the BFO-only pdfs are diffuse at Mach 0.84 across headings and sampled locations, from 098(T) to 263(T), with a plateau around 180(T) at 24S. Inclusion of the power model puts the emphasis on 22-24S at 170-215(T), followed by 14-18S at 221-242(T), while also diminishing the density estimates for the east-south-easterly headings indicated in the BFO-only pdf.

The pdfs remain bimodal when sampled across a range of feasible velocities, with 18.8S at 180(T) more strongly indicated at ~350kts over ground and 22-24S at 173-220(T) at 500kts. As a matter of pure coincidence, the time of the 23:14Z telephony attempt approximately corresponds to the time of apparent sunrise at the locations sampled.

Probability Density Functions for R600 Channel Observations at 18:25Z and 00:19Z

The pdf for the 18:25Z R600 channel observation is shown in Figure 67, where the BFO-only pdf is bimodal with peaks ~70(T) and 293(T) and where the latter is more strongly indicated in the combined BFO and received power estimation. The assumed heading of 296(T) is indicated with a red circle, about 3-degrees from the peak but above the 0.97 percentile.

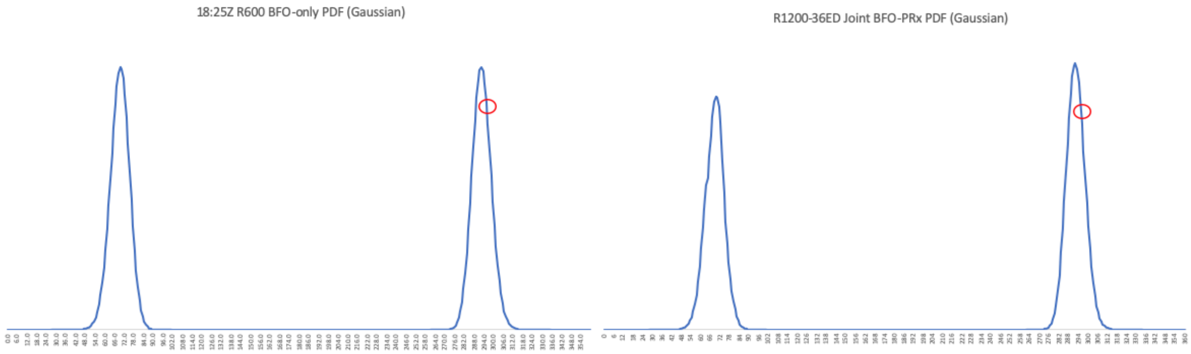

Figure 67. 18:25Z R600 Channel PDF

Figure 68 shows the estimated pdfs for both the BFO and combined BFO and received power residuals for the 00:19Z R600 observation, sampled over a wide range of 7th arc latitudes, with 0 fpm descent in the left panel and 1,662 fpm in the right. A southerly direction (~150-210T) is indicated across all of the locations sampled in the latter case.

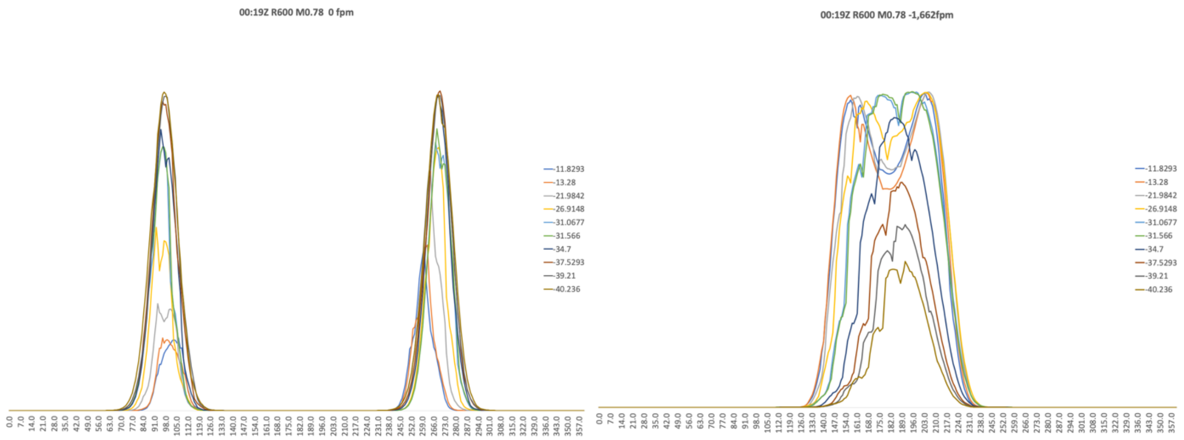

Figure 68. Probability Density Function Estimates for 00:19Z R600 Channel, 0 fpm (left), -1,662 fpm (right)

Kolmolgorov-Smirnov Test on Probability Density Functions for Known States

The non-parametric Kolmolgorov-Smirnov test results in the figures below show the p-value for 106 tests, each performed on 360 degrees of heading in 1-degree increments at an sample arc-latitude, with 106 such sample locations across the R1200-0-36ED channel observations from 04:04Z, 06:11Z, 06:48Z, 17:07Z and 18:28Z, a total systematic sample of n=38,160 location/heading samples.

In the first figure, the null hypothesis is that the two sampled probability density functions are not significantly different and the alternative hypothesis is that the combined BFO and variable gain model is significantly smaller (smaller CDF) than the BFO and fixed 12dBi gain model. In the second figure, the alternative hypothesis is that the BFO and variable gain model is significantly larger than that for the BFO and fixed 12dBi gain model (i.e. the spatial uncertainty has increased). The horizontal line shows the 0.05 p-value = α = 0.05.

It can be observed that the result of the test varies across the times and locations sampled; where H_A: BFO & 12dBi > BFO & Variable Gain (Figure 69), the null hypothesis is accepted in 51 of 106 tests (48%) and rejected in 55 of 106 tests (52%).

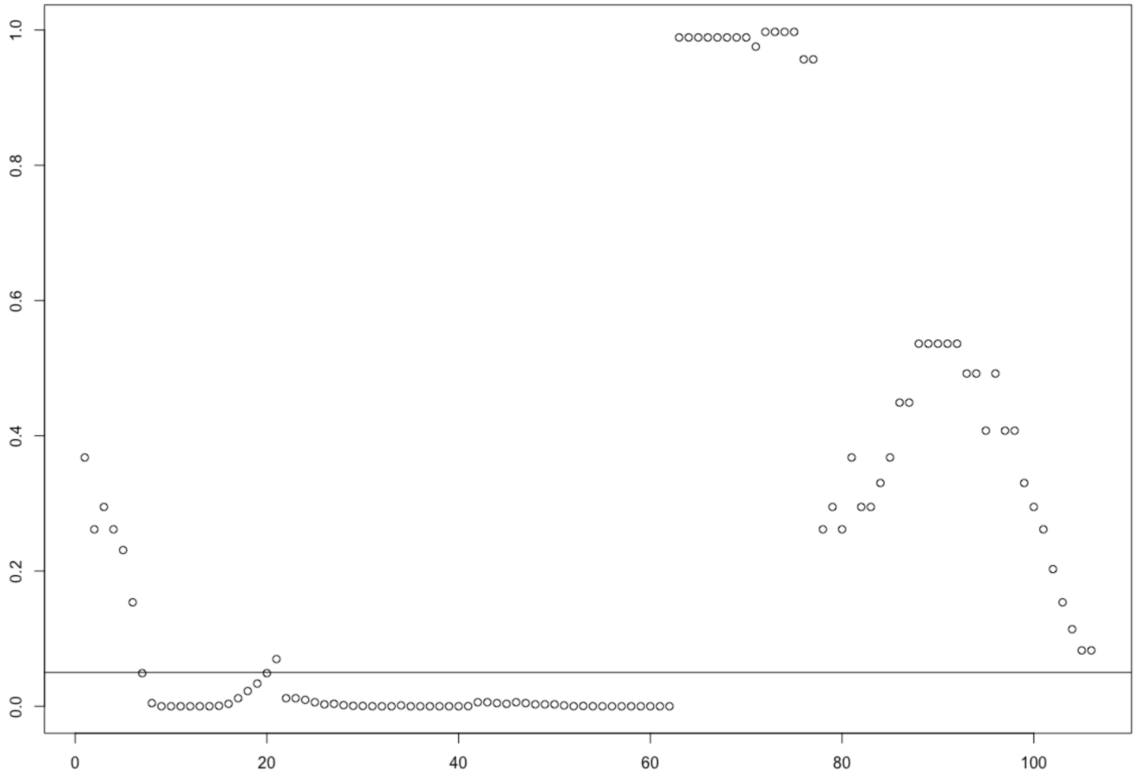

Figure 69. Kolmolgorov-Smirnov Test P-Values H_A: BFO&12dBi > BFO&Variable Gain

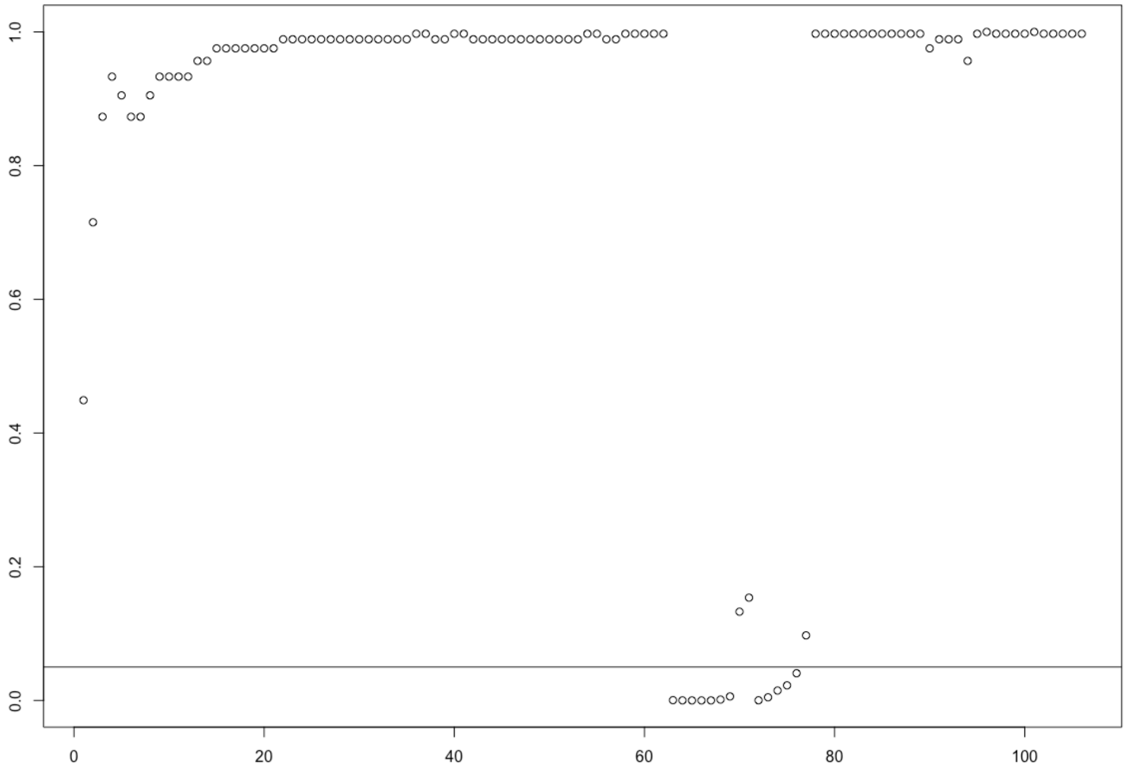

Figure 70. Kolmolgorov-Smirnov Test P-Values H_A: BFO&12dBi < BFO&Variable Gain

Where H_A: BFO & 12dBi < BFO & Variable Gain (Figure 70), the null hypothesis is accepted in 94 of 106 tests (89%) and rejected in 12 of 106 tests (11%). That is, in 52% of the tested cases the cumulative density function estimated with the variable gain model is found to be significantly reduced compared to that for the BFO & fixed gain model, in 37% of the tested cases no significant difference is found, and in 11% of the cases the inclusion of the variable gain model is found to increase the size of the cumulative density function.

Examples of each of these different cases are shown below. The very first test in the sequence is an example of where the null hypothesis (i.e. that the two cdfs are equal) is accepted at an $\alpha = 0.05$ level of significance, with a p-value of 0.36.

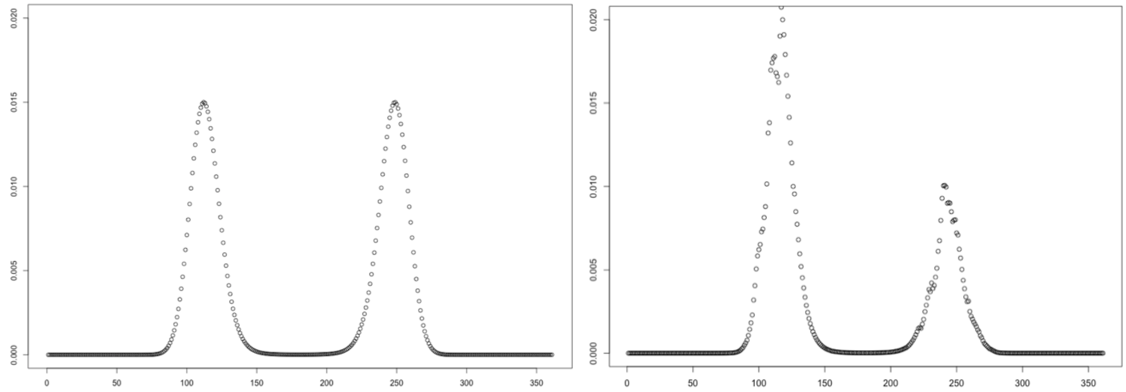

Figure 71. Example of Ho Rejected H_A: BFO&12dBi > BFO&Variable Gain, 04:04Z 14N

In this case, the addition of the variable gain model (right panel) changes the relative probability of one of the two solutions in the bimodal distribution (the desired effect in fact), however the change in cumulative density is not sufficiently discernable from that of the bimodal pdf for the BFO and fixed gain model (left-hand panel), where the densities for the two modes are equal.

An example of where the Kolmolgorov-Smirnov test indicates an increase in the cdf as a result of the inclusion of the variable gain model is shown below. Although the bimodal peaks are apparent in both cases (BFO & 12dBic Fixed left-hand panel), the inclusion of the variable gain model in this case has increased the dispersion, and thus the estimated cumulative density function (not the desired effect).

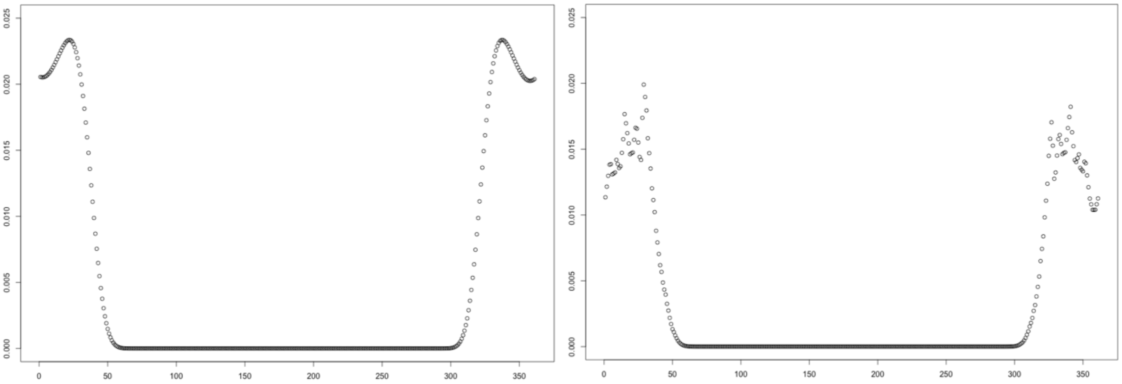

Figure 72. Example of Ho Rejected H$_A$: BFO&12dBi < BFO&Variable Gain, 17:07Z 14N

The figure below shows the 17:07Z estimated pdfs for the known latitude at that time, where the heading is known to be 027(T); the inclusion of the variable gain model increases the estimated probability density of the bimodal peak corresponding to the correct heading and decreases that of the (incorrect) second peak, i.e. the desired result, however the cdf of the latter increases, hence the Kolmolgorov-Smirnov test result.

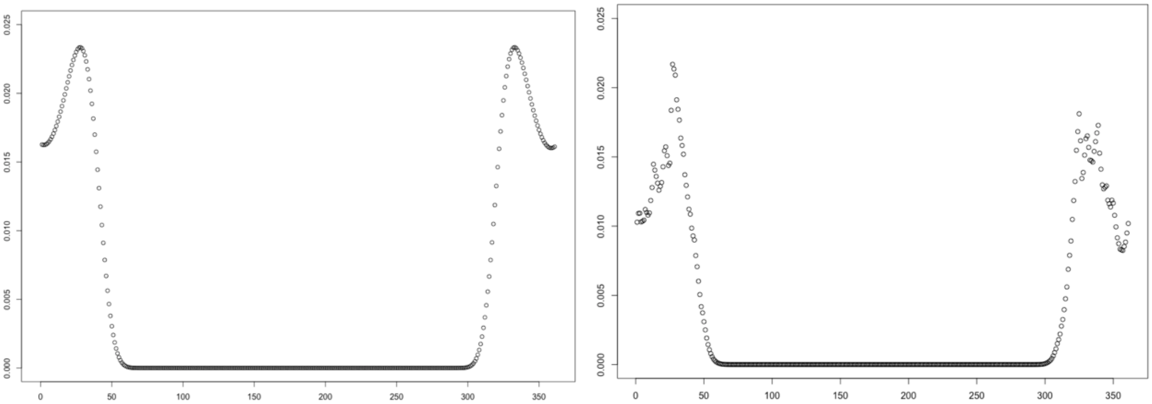

Figure 73. Example of Ho Rejected H$_A$: BFO&12dBi < BFO&Variable Gain, 17:07Z 5.4N (Known Heading = 027T)

These results suggest that a test on the change in degree of bimodality may be more appropriate to the question in hand, as the desired effect manifests itself as the emphasis of the peak in the bimodal probability density function which contains the true heading, over that for the mode which does not. The dip test in the following section tests for the degree of bimodality or multimodality, which can be subsequently compared for each case.

Hartigan's Dip Test Results on Estimated Probability Density Functions

The results of Hartigan's Dip Test for the multimodal probability density functions estimated at 04:04Z, 06:11Z, 06:48Z, 17:07Z and 18:28Z are shown below. In all cases, the BFO & variable gain model can be observed to decrease the degree of multimodality in the estimated pdfs, indicating the desired effect of reducing the number of solutions, although the degree of difference varies with the relative geometry at different locations.

Table 22

Hartigan's Dip Test D-Statistic for Fixed and Variable Gain Estimated PDFs

Model	04:04Z	06:11Z	06:48Z	17:07Z	18:28Z
BFO & 12dBi Fixed	0.014	0.020	0.016	0.027	0.009
BFO & Variable Gain	0.006	0.016	0.014	0.012	0.003

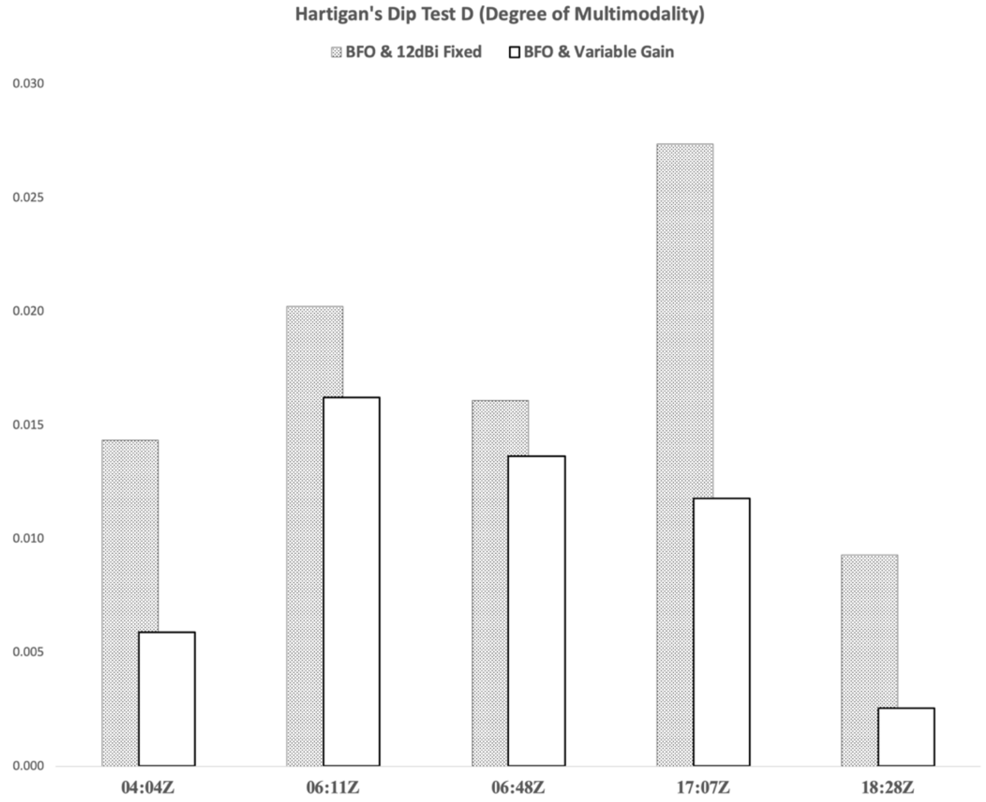

Figure 74. Hartigan's Dip Test D-Statistic for Fixed and Variable Gain Estimated PDFs

Trajectory Analysis at Probability Density Function Estimation Points 18:28Z-00:11Z

The following charts provide a summary of the indicated track possibilities for the flight after the 18:25Z restart up until the 6th arc at 00:11Z, along with a summary of the estimated probability densities for the meta-analysis subset both at the 6th arc and cumulatively along the respective trajectory estimates.

From the 18:22Z position and track indicated at the final point of primary surveillance radar contact, the pdf at the time of subsequent restart of the terminal at 18:28Z indicates a true track solution (true heading adjusted for the wind correction angle) broadly consistent with the 296 degree track of airway N571. For both the 18:40Z telephony attempt and the 19:41Z BTO arc, the pdfs are bimodal when sampled at velocities corresponding to typical cruise Mach numbers, and unimodal around a 180(T) heading when sampled at lower velocities (350-400kts over ground). When combined with the fact that the indicated latitude for the 18:38Z observation is higher (~7.5N) when sampled at higher velocity and lower (~4-5N) when sampled at lower velocity, either of the solutions is plausible from an aircraft performance standpoint. In either case, the general direction of the aircraft at 18:38Z is southerly, between 151 and 221 degrees.

Although unimodal solutions around a 180(T) due south heading are found for both the 18:38Z and 19:41Z observations, a consistent heading of 180(T) through both observations times is not consistent with the displacement of the 19:41Z arc to the west of the feasible range limit arc for the 18:38Z telephony attempt. The bimodal pdfs for the 18:38Z and 19:41Z observations both indicate a possible ~220(T) degree heading; given the displacement of the 19:41Z arc, the trajectory requiring the least number of turns would be one with a 180(T) heading at 18:38Z and ~220(T) heading at 19:41Z.

Figure 75 provides an indicative geographical context for these possible solutions.

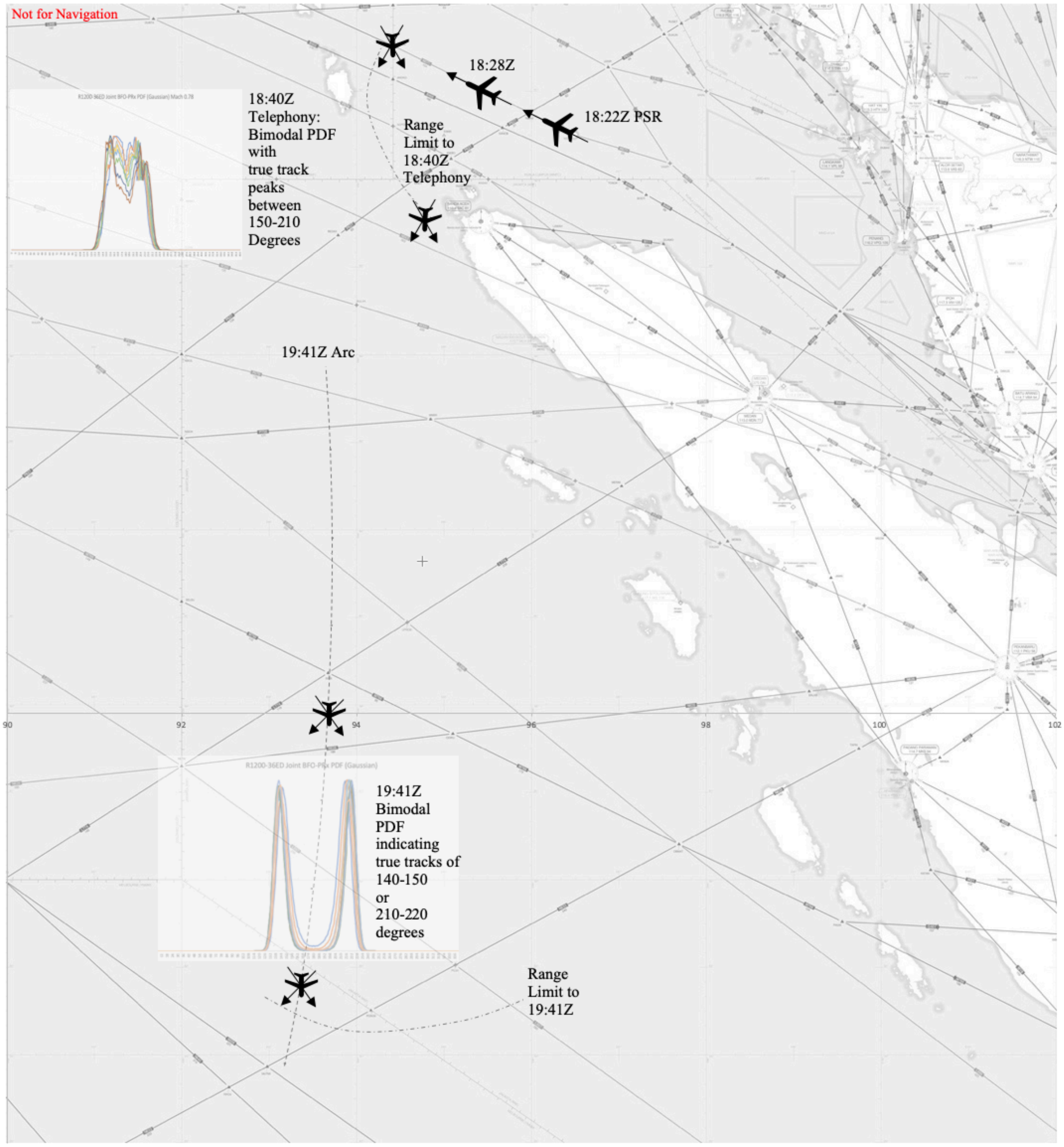

Figure 75. Bimodal PDFs at 18:40Z and 19:41Z with indicated track solutions

It is worth noting that the alternative, ~145(T) track, in the bimodal pdf toward the southerly end of the feasible range limit for the 19:41Z location, would be broadly consistent with flight parallel to and just outside of the Indonesian FIR, as would the northerly solution for the 18:40Z telephony attempt. However, the location of the 19:41Z arc and the feasible range limit for the aircraft at that time render extremely unlikely the necessary excursion west of 92E to remain entirely clear of that FIR.

The 20:41Z pdf indicates an approximately southerly heading when sampled at M0.84 toward at 11.7S, with a more bimodal solution indicated at more northerly locations which would correspond to lower velocity tracks, as shown in Figure 76.

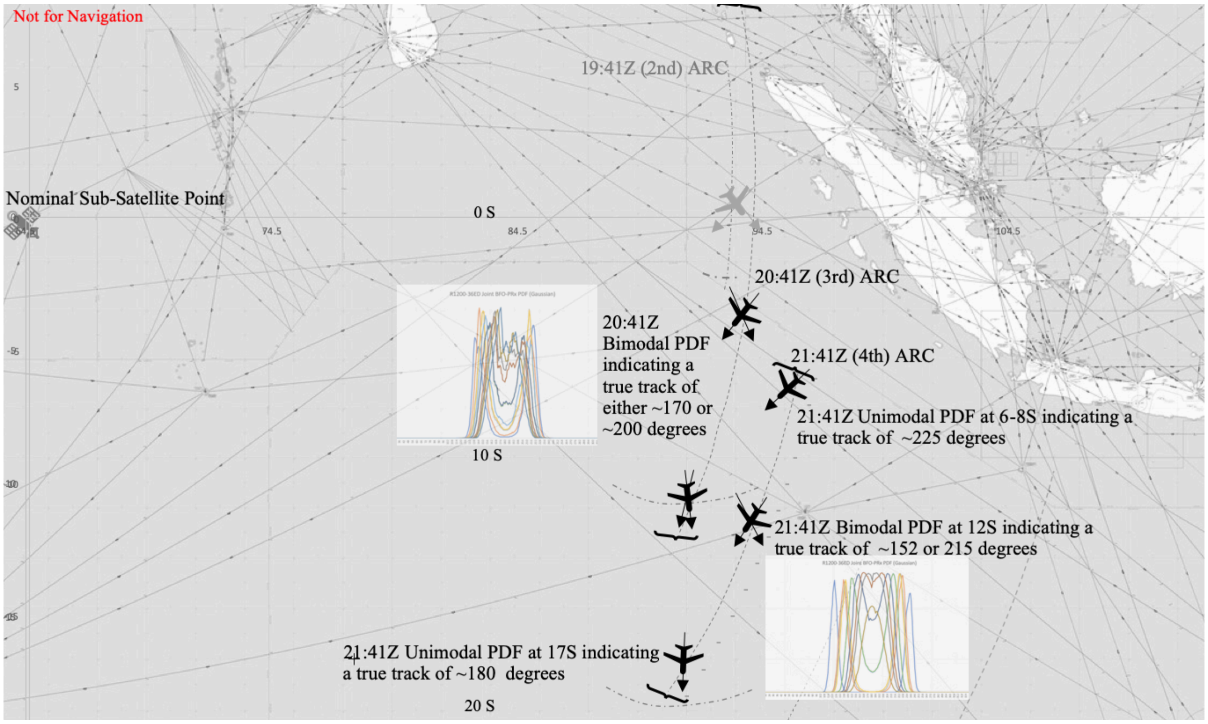

Figure 76. 20:41Z and 21:41Z PDFs with indicated track solutions (Background Skyvector)

The ~174-180(T) track solution toward the feasible range limit for the 20:41Z observation time can be seen in Figure 76 to be broadly consistent with the unimodal pdf solution one hour later at the 21:41Z arc, also toward the reasonable range limit, ~180(T) at 17-20S. For lower velocities, more northerly sample points on the 21:41Z arc exhibit a ~225(T) unimodal pdf. In all cases, the general direction is southerly or south-westerly.

The 22:41Z pdf (Figure 77) also indicates a southerly heading toward the southerly feasible extent, with solutions farther north along the 22:41Z arc drifting to ~242(T). In all cases the general direction at 22:41Z is southerly or southwesterly.

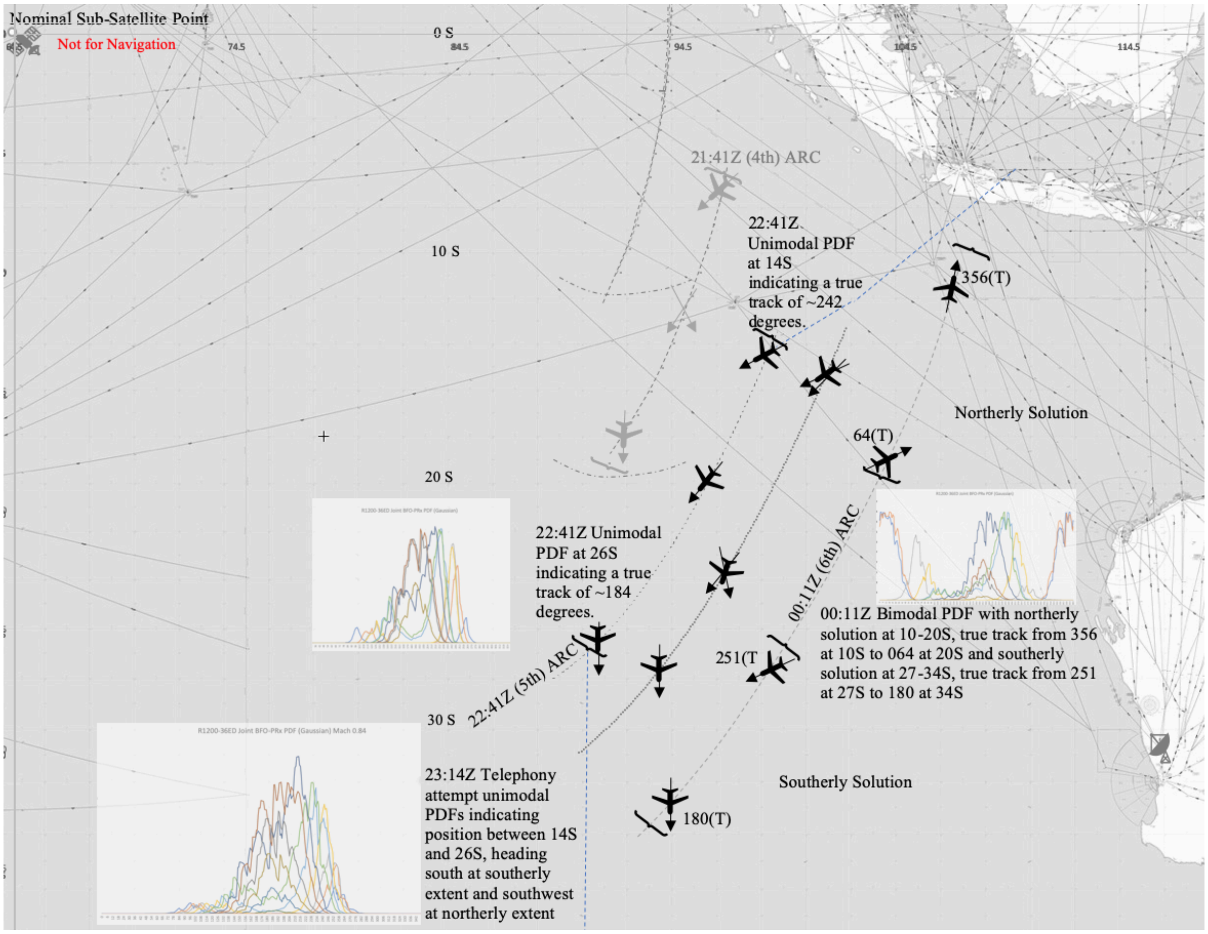

Figure 77. 22:41Z, 23:14Z and 00:11Z PDFs with indicated track solutions (Background Skyvector)

The 23:14Z pdf has the advantage of a much larger sample of observations than the BTO arcs (n=29 versus n=1), which were averaged in order to reduce the observational noise. The peaks at between 18S and 27S, with southerly (170-190T) headings at 27S and more southwesterly headings (210-240T) farther north (16-22S).

As is apparent in Figure 78, the 00:11Z probability density function on the 6th arc is pronouncedly bimodal across the range of arc-latitudes sampled. As can be observed in the charts, the two solutions are approximately symmetrical about the sub-satellite point, with the indicated aircraft heading ranges very approximately reflected. Neither the BFO nor the AES gain model, nor indeed the combination of the two, can resolve this fundamental ambiguity; however, the combination of the two can serve to reduce the size of the solution space for each solution, depending on the relative geometry. The 0.995 percentile range is 12-15S heading 347-044 (~016T) for the northerly solution, and for the southerly solution 29S-34S heading 199-245 (~222T). The 0.97 percentile ranges are 10-20S at 334-065 (~020T +/- 45), and 27-34S at 185-255T (220T +/- 35) for the northely and southerly solutions, respectively.

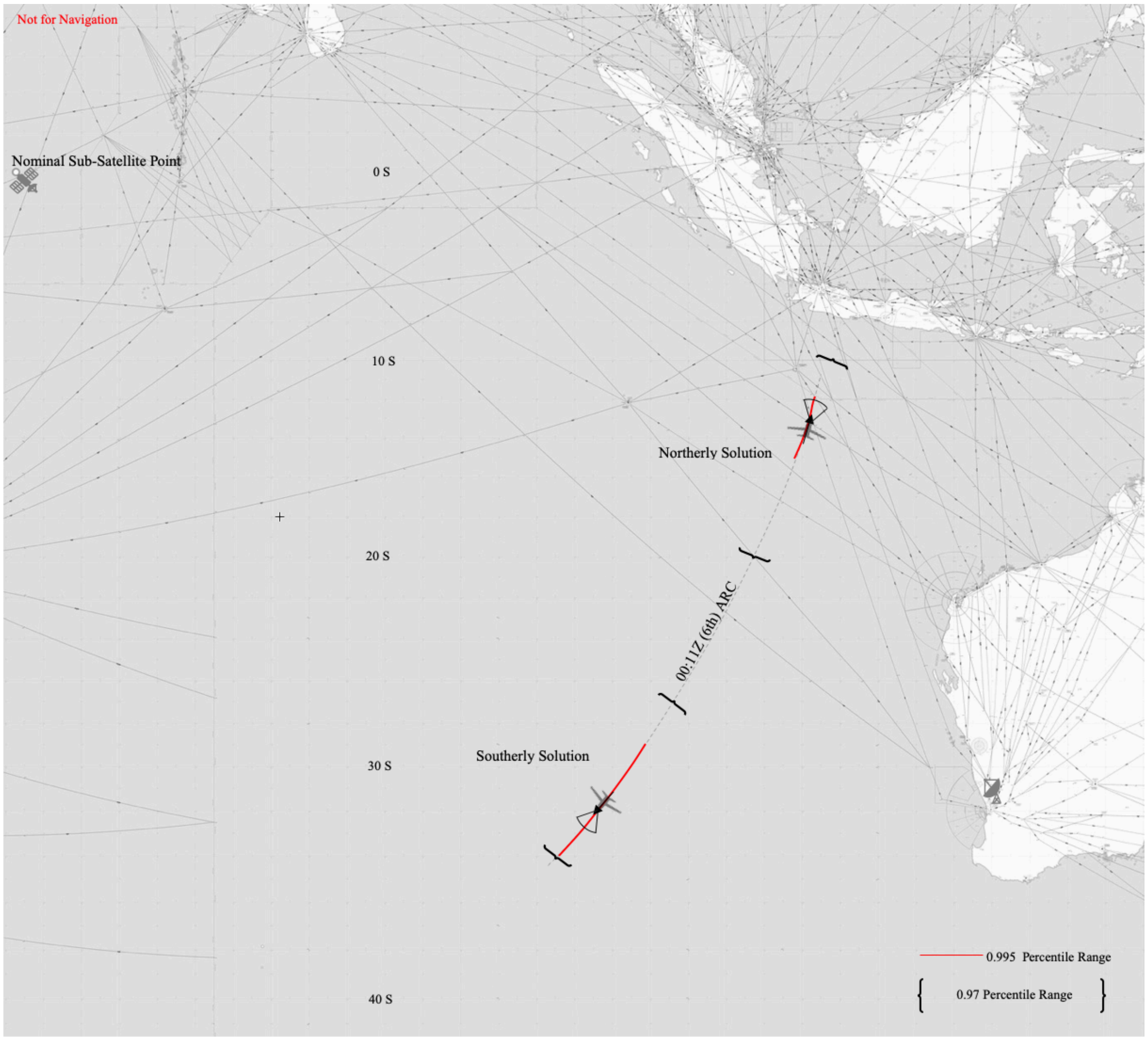

Figure 78. 00:11Z 6th Arc 0.97 and 0.995 Percentiles of Joint BFO & Received Power Probability Density Estimates (Background Chart Skyvector.com (2019))

Given the displacement of the subsequent (7th) arc, some headings are infeasible without multiple major turns. The headings which are more feasible in that regard are toward the south of each band (~34S, 185T), (~15S, 45T). When sampled across a wide range of feasible velocities, the southerly solution is more persistent in terms of the estimated density, while the northerly solution becomes much less pronounced at lower velocities.

Estimated probability densities at the 6th arc location 00:11Z for the subset of meta-analysis studies are shown in Figure 79, along with the three highest peak densities which correspond to approximately the 0.9999 percentile. Those with the higher densities tend to be in the vicinity of one or the other peaks, one far to the north at ~12S and the other in the 33-37S region. The existence of two possible solutions is strongly indicated.

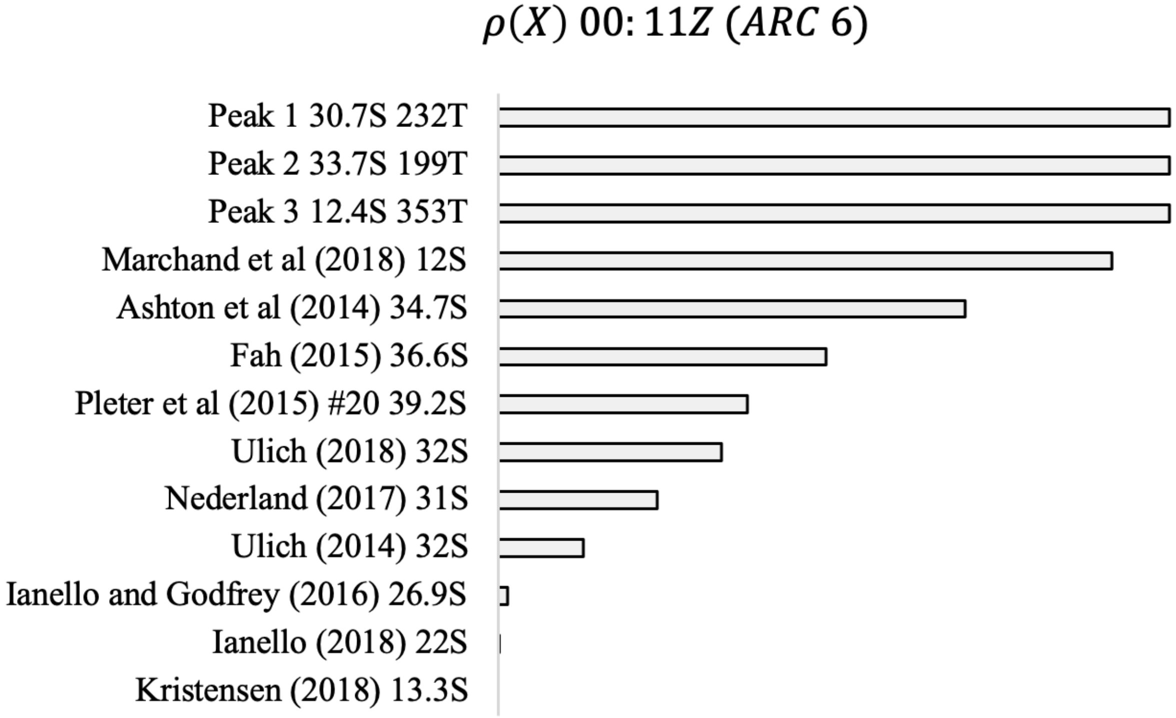

Figure 79. 00:11Z 6th Arc Estimated Probability Densities, Peaks & Meta-Analysis Subset

Figure 80 displays the sum of probability densities along each of the trajectories in the meta-analysis subset. Those with higher sums tend to pass through more points with higher estimated densities from the 2nd through to the 6th arc. However, the sum of the densities for the meta-analysis subset are relatively small in comparision to the sum of the peaks, through which a hypothetical optimal-fit trajectory would pass. In some cases, trajectories in the meta-analysis subset which pass through locations and headings with high probability density estimates earlier in the flight diverge from those areas at the 6th arc, as for example is the case with Pleter et al (2015) solution #20. Other cases, such as Marchand et al (2018), cross the 6th arc at a location and heading which for which the estimated probability density is high but diverge from such areas at multiple points earlier in the flight.

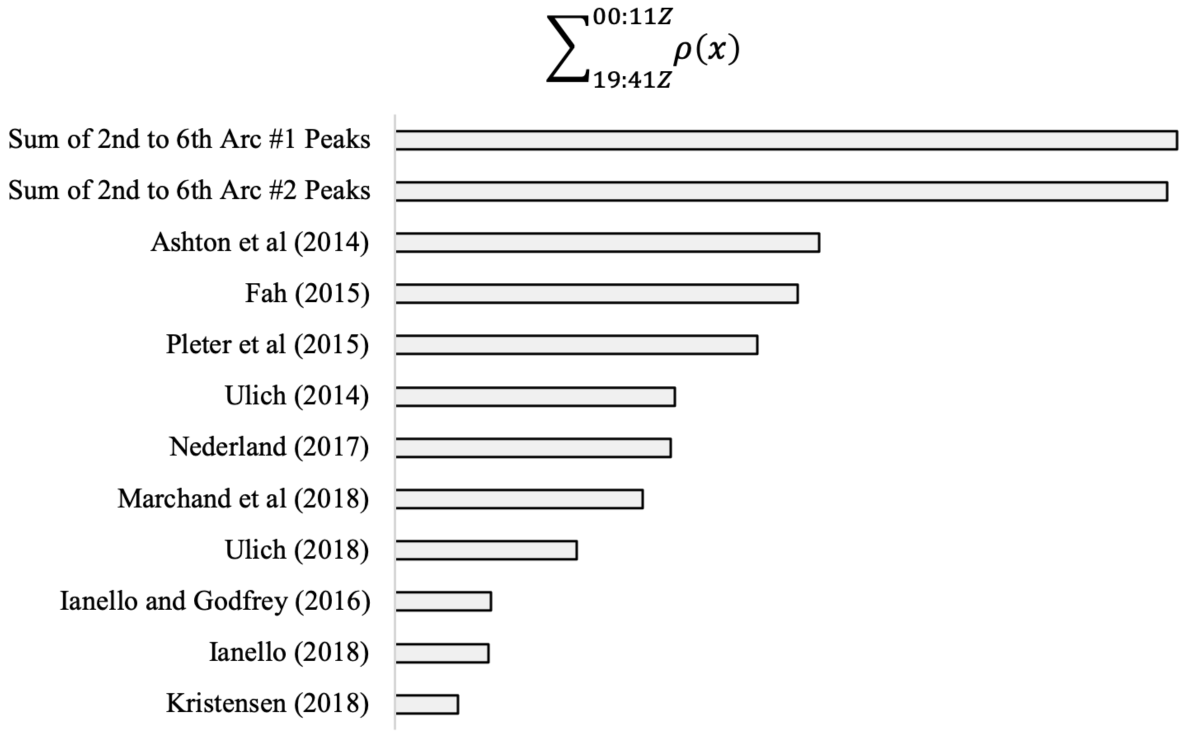

Figure 80. Sum of Probability Densities Along Trajectories

Figure 81 illustrates two examples (of many possible) trajectories which pass through headings and locations from the systematic sampling which correspond to peak or near-peak estimated probability density at each arc, such that the accumulated probability density along the trajectories is close to peak.

The generally southerly trajectory which passes through the southerly solution area at the 00:11Z arc is the more coherent in terms of general direction and required velocity. The alternative, which crosses the 00:11Z arc in the northerly solution area requires a series of 180-degree turns as well as significant velocity (and potentially altitude) changes along the track. However, trajectories can be defined which terminate in either the northerly or southerly 00:11Z solution areas, and which fit to the pass points along the way.

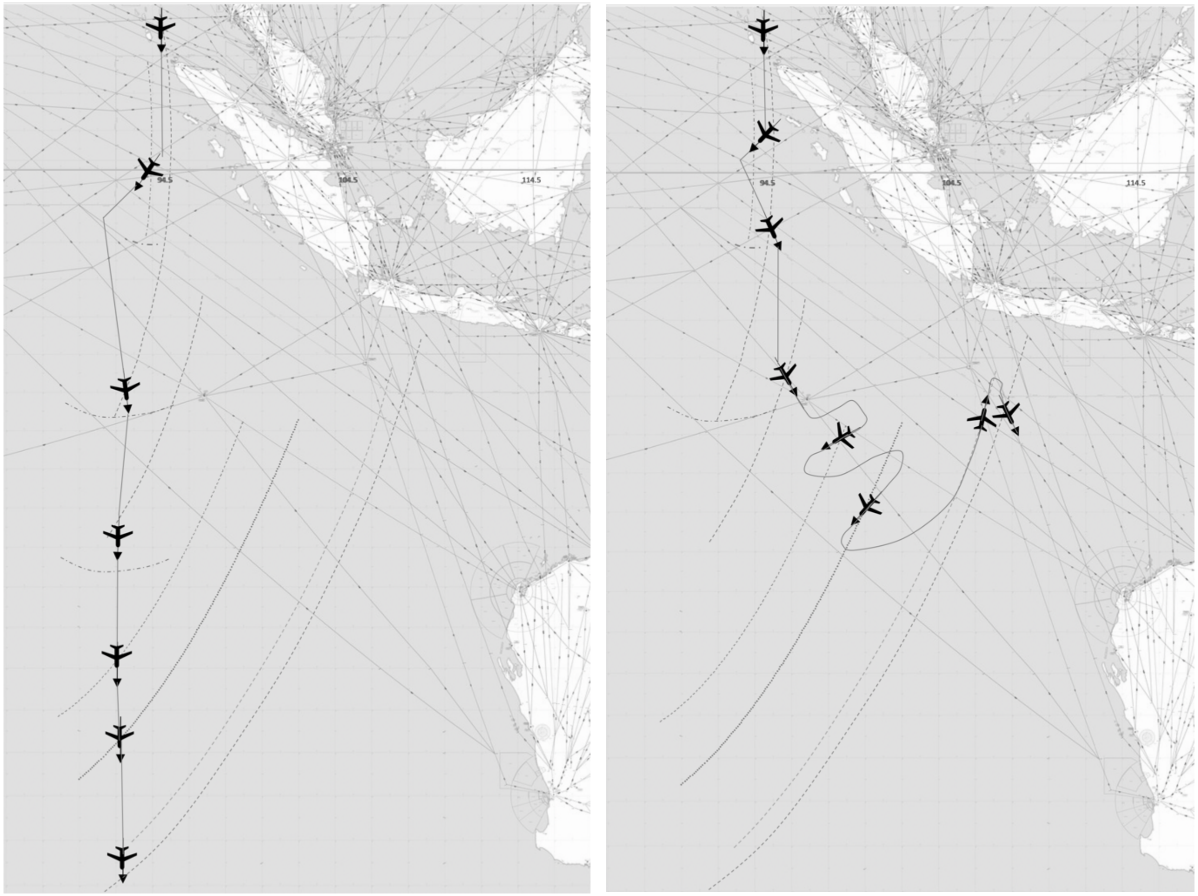

Figure 81. Indicative trajectories to northerly and southerly extents of 0.97 percentile region of 00:11Z arc, with high crossing-point cumulative probability densities.

RQ-3. Effect of GADSS on Future Occurrences.

RQ-2. In the absence of an adopted probable cause for the loss of MH370, what is an estimate of the probability of an oceanic hull loss with high spatial uncertainty (>5NM LKP) as a function of time, during the period 2020 to 2030?

Based on the methodology and assumptions described in Chapter III, the results of the Monte Carlo simulation (~20,000 samples in total) of oceanic hull loss incidents during the period 2020-2030 are provided below. The baseline fleet forecast, oceanic hours forecast and oceanic hull loss risk rates are summarized in Table 23. For GADSS measures, ADT stands for Autonomous Distress Tracking and FDR for Flight Data Recovery.

Table 23

Baseline Estimates Used for Monte Carlo Simulation

	2020	2021	2022	2023	2024	2025	2026	2027	2028	2029	2030
Oceanic Flight Hours Forecast (Millions)	5.6	5.8	6.0	6.3	6.5	6.7	7.0	7.3	7.5	7.8	8.1
n_{Dec}	4.0	4.1	4.2	4.3	4.4	4.5	4.6	4.7	4.8	4.9	5.0
$R_{HullLoss} = a \,.\, e^{b \,. n_{Dec}}$	0.07	0.06	0.06	0.06	0.05	0.05	0.05	0.04	0.04	0.04	0.04
$\mu_{Yr} = R_{HullLoss} \cdot \sum Oceanic\ Flight\ Hours_{Yr}$	0.39	0.38	0.37	0.36	0.35	0.34	0.33	0.32	0.31	0.30	0.29
Pre-GADSS ADT & FDR Fleet	26927	26231	25510	24764	23992	23193	22366	21510	20625	19708	18759
GADSS ADT Fleet (New Deliveries After 1/1/2021)	0	1656	3370	5144	6980	8880	10847	12483	14176	15928	17741
GADSS ADT & FDR Fleet (New Type Certs after 1/1/2021)	0	0	0	0	0	0	0	400	814	1242	1686
Forecast Total Air Transport Fleet	26927	27887	28880	29908	30972	32074	33213	34393	35614	36878	38186
% fleet pre-GADDS (mandatory adoption only)	100%	94%	88%	83%	77%	72%	67%	63%	58%	53%	49%
% fleet GADDS ADT (mandatory adoption only)	0%	6%	12%	17%	23%	28%	33%	36%	40%	43%	46%
% fleet GADDS ADT&FDR (mandatory adoption only)	0%	0%	0%	0%	0%	0%	0%	1%	2%	3%	4%

The probability ranges for the random variables used were: voluntary adoption, forward fit p=0.1 to p=0.7, retrofit p=0.05 to p=0.5; failure rates, ELT/UWB p=0.5 pre-GADSS and p=0.15 post-GADSS and for communications p=0.75 pre-GADSS and p=0.15 post-GADSS.

The baseline loss distribution, being a Poisson distributed sample of simulated cumulative offshore hull losses during the period, does not change under the different scenarios tested, as the primary purpose of the GADSS measures is to improve distress tracking, SAR efforts and flight data recovery, not to reduce the hull loss rate per se. However, it should be noted that there are potentially second order effects of the GADSS implementation which could impact the loss rate, however those are not explicitly modelled in this simulation, although they are considered to be implicitly modelled in the stepped reduction of the n_{Dec} parameter from 4.0 (the estimated current rate in the 2010-2018 period) to 5.0 at the end of the next decade which extends a decades long gradual reduction in the overall risk rate due to new technology and improved safety practices.

The Monte Carlo sampled baseline loss rate for the 2020-2030 period is shown in Figure 82; of the ~5,000 simulations the mean rate is 3.73 cumulative oceanic losses >12 NM offshore during the decade, with a range from 0 to 13. Based on historical ratios, the distribution for near-shore losses in water would be approximately equal.

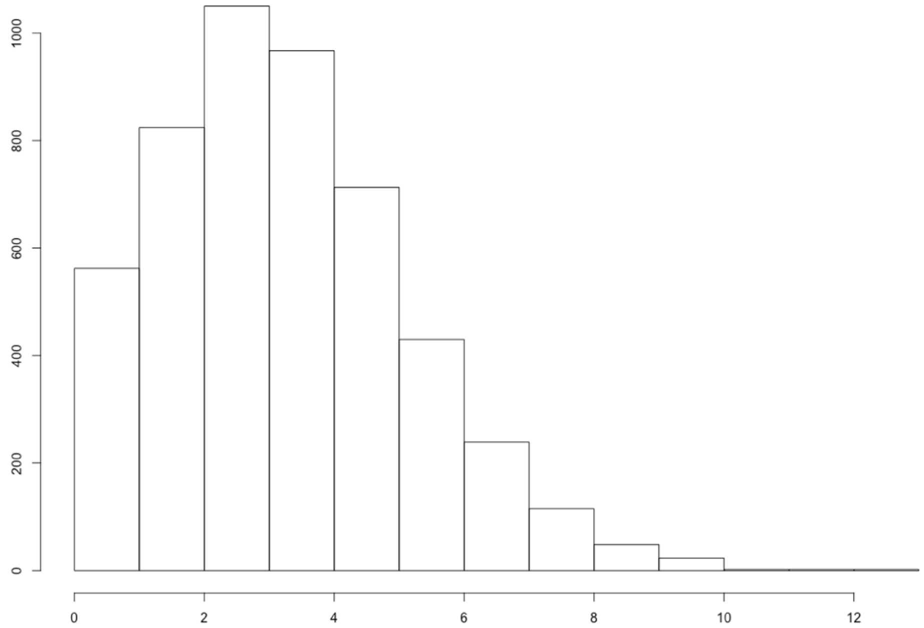

Figure 82. Baseline Distribution for Oceanic Hull Losses 2020-2030 >12NM Offshore

Of these, not all would be expected to be losses with high spatial uncertainty, depending on the success rate of the existing generation of ELTs and communications technologies during an emergency. A high spatial uncertainty condition is assumed to require both the failure of the ELT/UWB and of the communications. Based on the random variables shown above, the sampled distribution for oceanic hull losses with high spatial uncertainty in the absence of GADSS, i.e. assuming historical success rates and no GADSS implementation going forward, is shown Figure 83. The mean rate for cumulative losses during the decade is 1.4, with a range from 0 to 10.

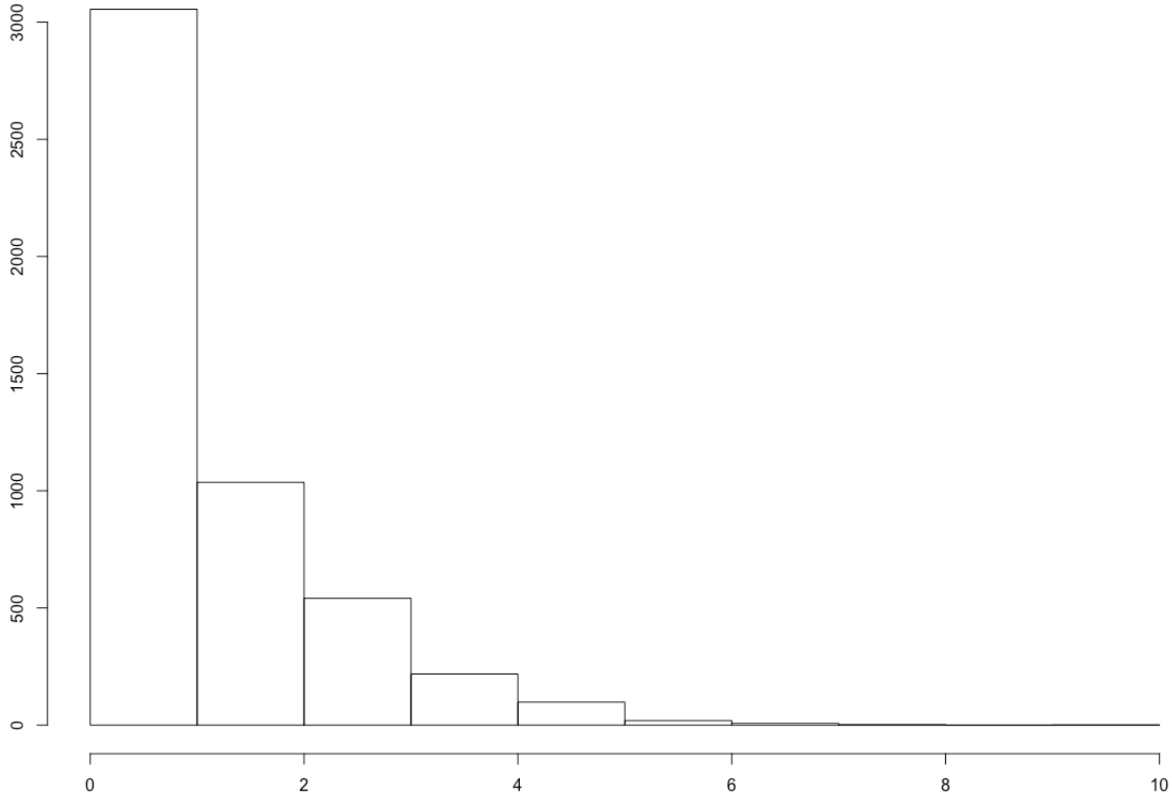

Figure 83. Simulated Oceanic Loss Distribution, High Spatial Uncertainty, No GADSS

The following estimated distributions with the implementation of GADSS were estimated under two scenarios, first under the mandatory adoption model and then with the addition of simulated voluntary adoption between the ranges specified above.

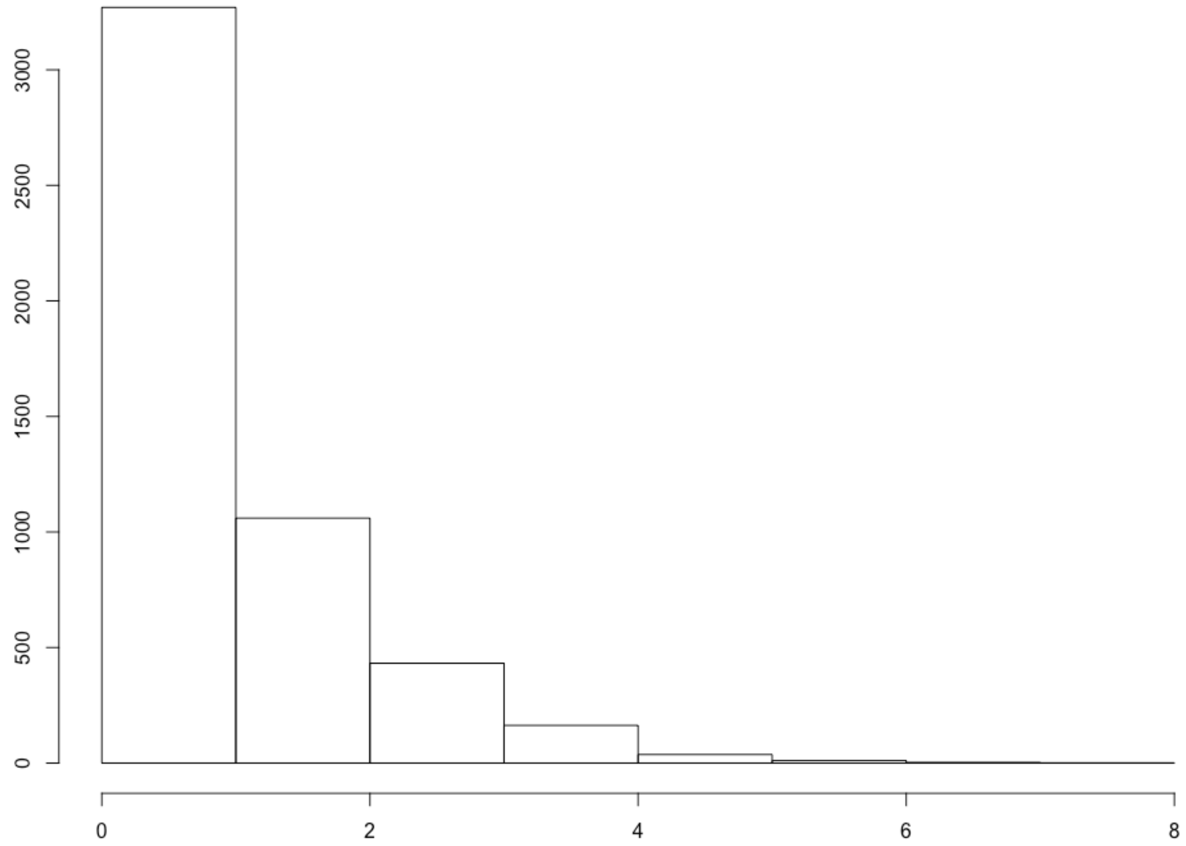

Figure 84. Simulated Oceanic Loss Distribution, High Spatial Uncertainty, Mandatory GADSS Adoption Only

Under the assumption of mandatory implementation only (above), the mean cumulative rate is 1.2 such losses during 2020-2030, with a range from 0 to 8. Under the assumption of additional voluntary adoption, at a rate randomly sampled between 0.1 and 0.7 for new deliveries after 1/1/21 and 0.05 to 0.5 for retrofit of the existing fleet with GADSS measures such as ADT or flight data streaming, the sampled rate (below) is a mean of 0.8 losses with high spatial uncertainty during the decade, with a range of 0 to 5.

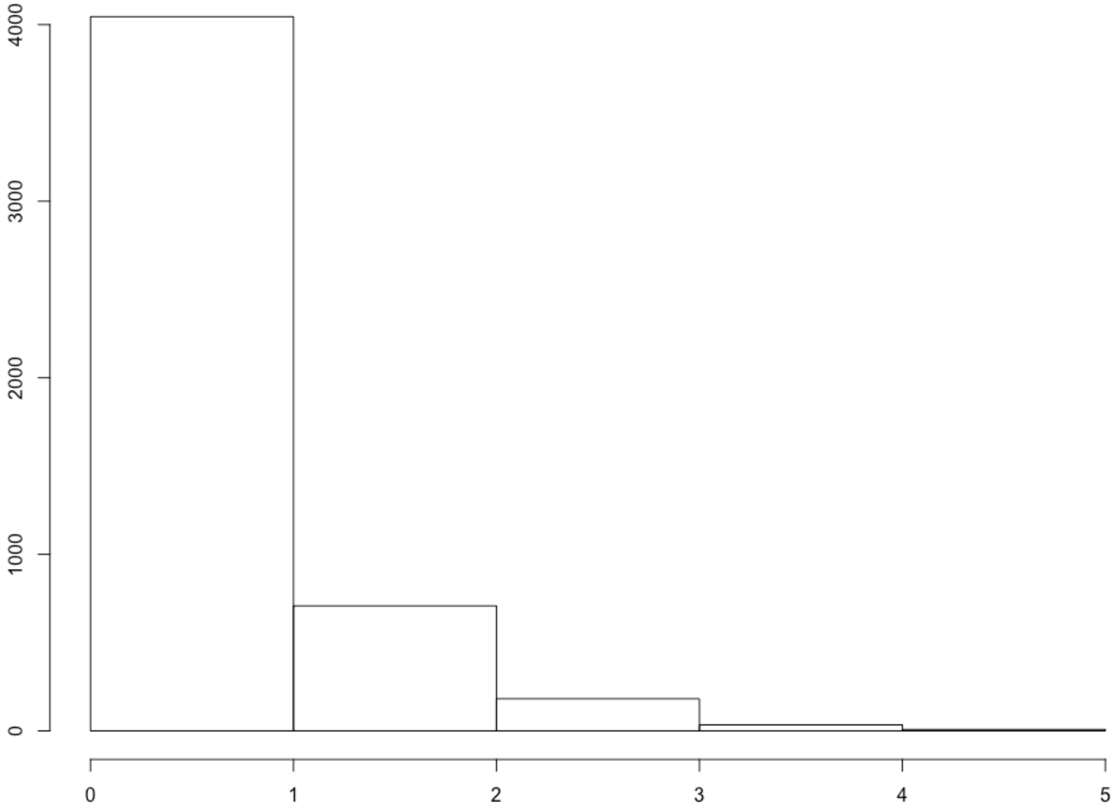

Figure 85. Simulated Oceanic Loss Distribution, High Spatial Uncertainty, Mandatory & Voluntary GADSS Adoption

The RQ2 hypothesis test results are shown below, both for the mandatory adoption model compared to the baseline no GADSS simulation, and for the combined mandatory and voluntary adoption model, also compared to the baseline no GADSS simulation.

H-2 $H_{2\text{-}0}$: No statistically significant reduction in the estimated probability of an oceanic hull loss with high spatial uncertainty (>5NM LKP) is forecast during the period 2020-2030 as a result of the GADSS measures.

$H_{2\text{-}A}$: A statistically significant reduction in the estimated probability of an oceanic hull loss with high spatial uncertainty (>5NM LKP) is forecast during the period 2020-2030 as a result of the GADSS measures.

The test results are shown below for the two cases. In both cases, the null hypothesis that the ratio of the rates = 1 is rejected at an $\alpha = 0.05$ level of significance and the alternative hypothesis that the ratio of the no GADSS estimated rate to the implemented GADSS rate is >1 is accepted.

Table 24

Comparison Test for Poisson Rates, No GADSS and Mandatory GADSS, No GADSS and Mandatory & Voluntary GADSS

			High Spatial Uncertainty Simulated Rates						95% CI	
Comparison Pair	Total simulated losses of 5000 iterations, cumulatively over 10 years	Time base (yrs)	No GADSS Poisson rate from simulation	Mandatory GADSS adoption (only) rate from simulation	Mandatory & voluntary GADSS adoption rate from simulation	Expected Rate 1	Rate Ratio	p-value	LL	UL
No GADSS and Mandatory GADSS Adoption (Only)	18585	10	6805	6029		6417	1.13	<0.0001	1.1	∞
No GADSS and Mandatory + Voluntary GADSS Adoption	18585	10	6805		3927	5366	1.73	<0.0001	1.7	∞

Based on these results and under the assumptions and methodology previously described, the simulations indicate that the estimated reduction in the probability of oceanic hull losses with high spatial uncertainty during the 2020-2030 period GADSS implementation statistically significant. However, the simulations do not suggest that the risk has been eliminated. In fact, the probability of no such losses during the period is estimated from the simulation to be 0.3 for the baseline case, 0.32 for the mandatory adoption model and 0.45 for the mandatory plus voluntary adoption model. Thus, we should expect at least one such loss during the decade, with the probability of 2 or more losses with high spatial uncertainty during the decade estimated as 0.39, 0.34 and 0.19 for the three scenarios, respectively, as shown in the table below.

Table 25

Estimated Probabilities of Cumulative Losses with High Spatial Uncertainty 2020-2030.

Number of Occurances (Cumulative 2020-2030)	Forecast Probability - No GADSS Scenario	Forecast Probability - GADSS Mandatory Adoption Only Scenario	Forecast Probability - GADSS Mandatory & Voluntary Adoption Scenario
0	0.30	0.32	0.45
1	0.31	0.34	0.36
2	0.21	0.21	0.14
3 or more	0.18	0.13	0.05

The greatest impact on risk reduction is forecast when voluntary adoption of the measures occurs beyond the mandatory implementation.

CHAPTER V

CONCLUSIONS

The purpose of this study was threefold. First, to provide a systematic review of multiple geospatial estimates for the final location of MH370 during the period 2014-2018, including investigation of the reasons why these studies reach such geospatially diverse conclusions from the same observed data, through meta-analysis of multiple independent estimates for location of the wreckage and through testing of key assumptions. This aspect was approached through meta-analysis of a set of studies in two groups, namely ocean drift and satellite communications, and a meta-regression on the second group. Testing was also performed on BFO bias assumptions.

Secondly, to evaluate a previously unused source of information, namely the spatial characteristics of antennas, combined with measurements made during the flight, as a potential source of additional useful spatial information. This aspect was approached through estimation of a linear model, sensitivity analysis and probability density function estimation on a physical model which incorporates both the BFO and received power observables, making use of a variable antenna gain model in the latter case.

Finally, to make an independent assessment of the impact of the GADSS implementation on the reduction of the probability of future occurrences of oceanic hull loss accidents with high spatial uncertainty. This aspect of the study was approached through Monte Carlo simulation of future scenarios of GADSS adoption.

Research Question 1

RQ-1(a) Conclusions

RQ-1. Meta-Analysis: For the studies identified in Tables 1 and 2, which provide geospatial estimates of the MH370 trajectory and/or end of flight vicinity:

(a): Is the observed variation in estimated probable impact location for MH370 across these studies likely due to random variation within the range of uncertainty of the observed data and propagated error, or do the studies exhibit statistical heterogeneity?

The meta-analysis was split into two subgroups, comprising of studies primarily making use of the satellite communications data and those making use of ocean drift analysis, respectively. The first hypothesis tested was that for statistical heterogeneity, for which the two groups yielded different results:

H-1(a): *For the satellite communications and ocean drift sub-groups:*

$H_{1a\text{-}0}$: There is no statistically significant heterogeneity across the studies.

$H_{1a\text{-}A}$: There is statistically significant heterogeneity across the studies.

Ocean Drift Studies Sub-Group. In the case of the ocean drift data, the null hypothesis was accepted and thus the conclusion is that the studies are statistically homogenous, with a distribution centered at ~30S in the vicinity of the 7th arc (Figure 24) and an estimated 95% range from 12S to 38S, under the assumptions and imputations previously described for the analysis in this study.

The relatively concentrated imputed means for the studies in this sub-group, from 23.5S to 34S and the generally large stated range of uncertainty, from 5 degrees to 25 degrees of latitude, are both broadly consistent with a meta-analysis sample with varying methodological approaches and varying assumptions, but which overall would be consistent with having been drawn from the same underlying population.

In regard to the fundamental ambiguity of the satellite data at the time of the 00:11Z arc, the ocean drift results are more consistent with the southerly solution, where for example the 28-34S range is a high probability estimated region in both cases. However, the possibility of selection bias has not been investigated within the scope of the present study – where for example some of the drift analysis studies may not have included origin locations as far as 11-12S in their analysis – a possibility which would be recommended for further research.

Satellite Communications Data Studies Sub-Group. In the case of this group, the null hypothesis was rejected, indicating statistical heterogeneity. The explanation offered for this heterogeneity as a result of the present study is the presence of pronounced bimodality and multimodality in the probability density functions estimated from a systematic sample of approximately 100,000 location and heading combinations.

Based on the physical models, assumptions and methodology as previously described, the BFO observable was found to produce bimodal results at the vast majority of sampled locations, exhibiting multiple points of ambiguity in terms of locations and tracks for which the observed and calculated BFO values are near-zero within the noise level of the data, presenting multiple solutions which, all other things being equal, are equiprobable or nearly so. The non-uniqueness of the error induced by the assumption of a fixed satellite location in the AES Doppler pre-compensation calculation is suggested as the underlying cause of the bimodality.

When sampled across multiple arc-latitude locations, these bimodal results accumulate into multimodal distributions with a large number of spatially dispersed potential solution points. Furthermore, as the satellite-aircraft distance increases as the flight progresses, the bimodal solutions tend to diverge spatially, leading to the significant north/south solution ambiguity at the 00:11Z (6th) arc. In the presence of these ambiguities, many of the studies in the meta-analysis have identified local solutions which correspond to one of these points of ambiguity – and the existence of manifold such points essentially explains the heterogeneity.

RQ-1(b) Conclusions

Sub-question (b) sought to investigate the question of to which factors the arc-latitude estimates are most sensitive. This was addressed through a meta-regression on the satellite communications sub-group studies, with the hypothesis tested as:

H-1(b): *For each regression coefficient (predictor) or set of coefficients:*

$H_{1b\text{-}1\text{-}0}$: The regression coefficient (predictor) is not significantly different to zero (zero slope).

$H_{1b\text{-}1\text{-}A}$: The regression coefficient (predictor) is significantly different to zero (zero slope).

When tested in isolation, the null hypothesis was rejected for all four predictors tested, namely the maximum time to turn south after the 18:28Z restart, the variation in altitude of the constituent trajectories used in the study estimation, the cumulative true track changes in the constituent trajectories used in the study estimation, and the variation in ground track velocity. When tested simultaneously, the null hypothesis was rejected for the latter two predictors only, these predictors also being those which produced the highest r^2

values in the single predictor regressions, at 71.3% for the cumulative true track changes predictor and 29.2% or the velocity predictor. In all regression combinations, the cumulative track changes predictor appears to exhibit the strongest linear relationship to the arc-latitude estimates.

Thus, it is concluded that the variation in arc-latitude estimates at the 7th arc is most sensitive to the cumulative changes in track in the constituent trajectories, followed by their variation in velocity. Studies which estimate a terminal location in the far north area naturally tend to have more turns and also tend to assume human control, while those which terminate at the other, southerly, extreme tend to assume fixed autopilot modes and/or the estimation models produce generally minor turns after the turn south just prior to 18:40Z.

Thus, resolution of the ambiguities presented by the bimodal and multimodal solutions across the feasible range of sampled values is key to resolving the question of direction at each of the crossing points, and thus likely trajectories.

As the BFO bias is critical to analysis of the data following the 18:25Z restart and as the BFO bias is known to be susceptible to significant changes over time, the following hypothesis was also tested for (a) significance in difference between the MH371 and MH370 flights, i.e. before and after a shutdown and restart, (b) significance in difference of the R-1200-0-36ED channel compared to other R-channels, (c) significance in difference for the MH370 flight before and after the 18:25Z restart, and (d) sensitivity to a slight change in return link transmission frequency within the 1645-1655MHz range:

> *For each bias BFO used in estimation, across time and across channels:*
>
> $H_{1b\text{-}2\text{-}0}$: There is no significant different in the bias over time or across channels.

$H_{1b\text{-}2\text{-}A}$: There is a significant different in the bias over time or across channels.

It was found that the bias on the R1200-0-36ED channel (i.e. the sole channel used for the majority of observations after the restart) changed significantly between the MH371 and MH370 flights (~21Hz), but no statistically significant change in the bias was detected for the MH370 flight before and after the 18:25Z restart, and where a residual amount of a rapidly decaying ephemeral bias is likely to be the reason for a ~3Hz difference in the bias to the pre-restart value, still apparent at end of the restart sequence of transmissions (but where the pre- and post-restart bias estimated were found not to be statistically significant). The R1200-0-36ED channel was found to have a significantly different BFO bias value to other channels, while an estimation of the post-restart value making use of these known differences appears to confirm the R1200-0-36ED bias value used in the prior (meta-analysis) studies (~150.1 Hz).

The R600 channel observations at 18:25Z and 00:19Z, when tested for significance of difference to the R1200 channel observations in the same sequences against known differences estimated from elsewhere in the dataset, were not found to be significantly different to those which would be expected for the BFO and received power in the 18:25Z case and for the received power in the 00:19Z case. The potential significance of these results is discussed further in the discussion section at the end of this chapter.

RQ-2 Conclusions

This research question sought to investigate the question of whether the spatial characteristics of antennas can be used to reduce the spatial uncertainty in the estimates of final location for the MH370 aircraft. Specifically, the analysis was performed using a spatial characteristic of the AES dual side-mounted antenna type used on the 9M-MRO aircraft, where the peak gain varies as a predictable function of the apparent azimuth and elevation of the satellite, based on a given aircraft location and heading. Given that the arc-latitude estimates were found to be most sensitive to the cumulative changes in track, the question of whether or not this coarse method of reverse direction finding could serve to reduce the uncertainty was pertinent to the study.

The presence and detectability of a component of the received power variations due to this variable antenna gain effect was tested through the comparison of two nested linear regression models, one using a physical functional model for received power including gains and losses across the entire communications chain and assuming a fixed 12dBic AES antenna gain, and the other being a modification of the same physical model but using a variable gain model for the AES antenna.

The following hypothesis was tested:

H-2 $H_{2\text{-}0}$: There is no significant difference in the sum of squared residuals for a linear model estimated using BFO data and a fixed gain model and that estimated using both BFO data and the peak gain variation model for the AES antenna.

$H_{2\text{-}A}$: A statistically significant difference is found in the sum of squared residuals for a linear model estimated using BFO data and a fixed gain model and that estimated using both BFO data and the peak gain variation model for the AES antenna

Based on the regression results, the null hypothesis was rejected in this case, from which it is inferred that the gain variation effect is present and detectable in the data, albeit in the presence of substantial noise, signal fading and unmodeled systematic effects.

Making use of this effect, a sensitivity analysis of both the BFO and received power residuals (observed – calculated) was conducted over ~100,000 systematic sample points, from which probability density functions were estimated at the same sample points. The joint probability density estimation combines the BFO and power residuals by estimating the conditional probability of observing both the BFO residual and the received power residual at any hypothetical (i.e. sampled) location and heading. In principle and assuming conditional independence, it is less likely on average to encounter two near-zero value residuals (i.e. for both the BFO and received power) at the same time, location and heading, than it is to encounter one such result. This has particular potential value in eliminating or reducing the estimated probability density of one of the BFO-only bimodal solutions at any given location and heading combination.

In practice, this was found in the results to depend on the relative geometry; in some cases both the BFO-only zero-value residuals and the received power zero-value residuals occur at approximately the same headings when systematically sampled across 360 degrees at a given location. In other cases, the two are not coincident, such that one of the BFO-only zero-value crossing points is revealed as the more likely one through inclusion of the received power residual. In the estimated probability density functions, this latter case manifests itself as a change in the bimodal distribution, where two approximately equal bimodal peaks in the BFO-only pdf are modified to a pair where the estimated density for one is significantly higher than for the other. Hartigan’s dip test as performed on the BFO-only and combined pdfs demonstrated this change in the degree of bimodality across all the samples tested.

For the period of flight after the 18:25Z restart until the 00:11Z arc, this change in bimodality due to inclusion of the variable gain antenna model is most apparent for the 18:40Z telephony attempt and at the 22:41Z BTO arc; in both cases the ambiguity of alternative headings present in the BFO-only pdfs at those times can be resolved with a high degree of confidence. For the remaining observations tested, at 19:41Z, 20:41Z, 21:41Z, 00:11Z and the 23:14Z telephony attempt, the effect is present but is insufficiently powerful under the present model to resolve the ambiguity decisively.

Based on the methodology, assumptions and analysis in the present study, the most coherent and consistent trajectory suggested by the combined BFO and received power results is one which takes a southerly track after 20:41Z and which crosses the 6th arc between 28S and 34S, with a sustained southerly heading most strongly indicated toward the southerly end of that range, which would indicate a similar range along the 7th arc given the 8 minute spacing between the two. It is also noteworthy that satellite imagery in which 70 objects were assessed to be non-natural in origin also corresponds to this general vicinity, where the majority of those objects are in the region of 34.5S 91.3E. The joint pdfs do not strongly indicate solutions south of 34S. Also, given that the region along the arc to the south of 29S has been searched to a distance of approximately 25NM orthogonally to the 7th arc, the most likely explanations for the failure of the search in this region, if in fact the southerly solution is the correct one, would either be the small ($p \sim 0.06$) chance of the search having covered the debris field but having missed the debris, or that the descent profile is significantly shallower than assumed.

However, it is important to note that feasible trajectories were found to exist for both the northerly (~12-15S) and southerly (28S-34S) solution areas at the 00:11Z arc, which pass through the high probability density solutions at all arcs. Given the observed multimodality, it is not sufficient for any given solution to fit the data, it is necessary to also demonstrate that alternative given solutions do not fit the data nearly as well. Thus, the fundamental ambiguity at the 00:11Z arc was not decisively resolved as a result of inclusion of the variable gain antenna model in the pdf estimation. It is possible that a more refined physical model for the received power residual, perhaps making use of more specific knowledge of the network in use and a larger than 24 hour data set, could serve to improve the estimation; this is suggested as an item for possible future research.

Research Question 3

RQ-3. Effect of GADSS on Future Occurrences: In the absence of an adopted probable cause for the loss of MH370, what is an estimate of the probability of an oceanic hull loss with high spatial uncertainty (>5NM LKP) as a function of time, during the period 2020 to 2030?

This question sought to estimate a distribution of offshore (>12NM) hull-loss scenarios with high spatial uncertainty during the coming decade, through Monte Carlo simulation based on alternative scenarios of (a) no GADSS implementation, (b) GADSS implementation strictly limited to that mandated in recent Annex 6 amendments and (c) additional voluntary GADSS adoption beyond the mandatory minimum. The following hypothesis was tested on the derived distributions:

H-3 $H_{3\text{-}0}$: No statistically significant reduction in the estimated probability of an oceanic hull loss is forecast during the period 2020-2030 as a result of the GADSS measures.

$H_{3\text{-}A}$: A statistically significant reduction in the estimated probability of an oceanic hull loss is forecast during the period 2020-2030 as a result of the GADSS measures.

The estimated distributions were found to be statistically significantly reduced for both the mandated adoption only GADSS scenario and the additional voluntary adoption GADSS scenario, over the baseline no GADSS scenario. Naturally, the most significant reduction is forecast for the additional voluntary adoption scenario, where a greater percentage of the global air transport fleet benefits from the reduced risk of a lost aircraft due to the improved reliability of tracking and location alerting and reporting. This is most likely to happen where there are potential operational benefits to be gained from voluntary adoption of GADSS-compliant solutions together with the safety benefits, for example as may be gained from the use of streamed data in near real-time.

Overall, it is concluded that the implementation of the GADSS will serve to reduce the risk of an oceanic hull loss with high spatial uncertainty, although not necessarily reducing the risk of a hull loss (which is not necessarily its purpose either). However, even with the GADSS implementation and even with a forecast continued reduction in the rate of such losses as has been seen over the past decades, under the assumptions, chosen variables and probabilities used in this simulation, the results indicate that we should expect around 2-4 (range from 0 to 10) hull losses more than 12 miles offshore during the 2020's, of which we should expect 1-2 (range from 0 to 6) with high spatial uncertainty, which could incur search costs in the order of $50-100m each, not to mention the diminished hope of recovering survivors in the immediate aftermath of a loss where SAR efforts do not benefit from a last known position of <5NM.

Discussion and Interpretation of the Results and Conclusions

The thirty-eight prior studies considered in this study exhibit a very broad geospatial distribution, from 12S to 40S in the vicinity of the 7th arc. The ocean drift subgroup indicates a mean value in the vicinity of 30S and the satellite communications subgroup in the vicinity of 33S, although in both cases the range of uncertainty extends hundreds of nautical miles from those mean points.

In the case of the satellite communications subgroup, the presence of local solutions in the BFO data creates multiple points of ambiguity. When tested on arcs on the earlier MH371 flight, the true location, heading and velocity creates a valid local solution, however multiple other solutions can be found on those same arcs which do not correspond to the true aircraft state but which are indistinguishable from the correct solution. Thus, it is likely that at least one of the studies in this subgroup does indeed identify the true state of the aircraft at 00:19Z, however no way has yet been identified to distinguish between that solution and others, which fit to the data but do not reflect the true aircraft state. Indeed, key to resolving this ambiguity is not only to identify a valid solution but also to identify why that solution is the correct one to the exclusion of other possible solutions. Toward the end of the flight, valid solutions in terms of the BTO and BFO observations exist as far apart as 12S and 40S.

Of the variables considered for the satellite communications subgroup of studies, the arc-latitude estimate on the 7th arc appears to be most sensitive to the cumulative changes in track along the trajectory after the last primary radar contact at 18:22Z. Intuitively, this makes sense, as a more northerly end point would require more turns, or larger turns, than a more southerly end point. This means that the sensing of direction at each BTO arc crossing point is an important factor in the analysis of potential trajectories which could terminate at any of the valid BTO/BFO end points. The inclusion in this study of an additional method of direction sensing based on the observed received power of each transmission combined with a known gain variation effect of the antenna as a function of direction between the aircraft and spacecraft was intended to aid in the estimation of direction at each arc. Although the combination of Doppler-based (BFO) and received power based direction sensing is shown to reduce the number of possible solutions, at most of the arc crossing times it does not reduce them sufficiently to isolate a single trajectory; at least not with the present model, which used 24 hours of data and details of the communication chain available in the public domain - it is possible that a refined model using a much larger data set and more detailed network information could improve on the technique substantially, certainly a recommendation for further work.

Under the present model, a fundamental ambiguity remains between a northerly solution (~12-15S) and a southerly solution (30-36S) the 6th and 7th arcs, even with the combined estimation technique. However, when considering trajectories through each arc where the estimated direction based on the combined technique is assessed, those which terminate in the 12-15S region require multiple 180 degree turns between successive arc crossings, while the most coherent trajectory is a southerly one which crosses the 6th arc in the vicinity of ~34S and the 7th arc near ~35S.

While this region has already been searched, the search area extended approximately 25NM from the 7th arc, under the assumption of no human control of the flight at that time, supported by an assessment that the recovered flaperon was likely retracted at the point of impact and separation, and by analysis of the final two BFO observations, which suggested a very high and increasing rate of descent.

The latter result was not replicated in this study, the key point of difference to prior work being the effect of a transient bias which occurs during restarts of the AES terminal on different channels, namely the R600 and R1200 channels. With regard to the 18:25Z in-flight restart, Holland (2018) discards the R600 channel data, while applying an estimated transient bias effect to the R600 channel observation in the case of the 00:19Z restart.

However, the results of this study suggest that the R600 channel may not in fact be affected by the transient bias; statistical testing on the R600 18:25Z observation suggests that it is not affected, and also that only the observed C/No value was anomalous at that time, and not the BFO or received power. In fact, when the latter two measurements are used in the combined direction estimation technique, a 296(T) heading consistent with flight along airway N571 is strongly indicated. When the raw observed R600 channel BFO and received power data is used in estimation for the 00:19Z 7th arc crossing, i.e. without application of the transient bias which may not in fact affect this channel, the implied rate of descent is much lower than has previously been estimated, more in the range of 1,600-2,000 fpm.

When combined with the fact that no physiological basis (i.e. exposure to very low pressure and temperature for certain periods of tine) was identified in the literature review for the present study upon which to discard the possibility of human control at the end of flight, particularly if the ~4,800 ft altitude during the period of primary radar contact is correct, the possibility of an impact farther than 25NM from the 7th arc deserves further consideration. Between the two extremes of an entirely uncontrolled descent after fuel exhaustion and a perfectly executed, flaps deployed, ocean ditching lies a broad continuum of possibilities for the true descent profile. The fact that the ~250,000 sq km search did not locate the flight recorders or other evidence is estimated at a probability p=0.94 to be due to the final location being outside of the searched area, based on the p=0.06 estimate of the survey having covered the wreckage but failing to detect it. This leaves the possibilities that (a) the impact was close to the 7th arc in an area not searched, for example the 12-15S area, (b) the impact was in the vicinity of an area of the 7th arc previously searched, but orthogonally displaced from it by more than 25NM, or (c) some other location, for example if the BTO bias changed substantially during the restarts.

As a result of the combined probability density function estimates of this study making use of the combined BFO/received power direction sensing method, the 12-15S possibility was not eliminated. However, the more coherent trajectory is clearly toward the 35S vicinity. While the ~30S vicinity suggested by a number of studies is a possibility, the indicated direction of the aircraft under the present (combined BFO/power) method is too far westerly at the 6th and 7th arcs to make this a peak probability density area (notwithstanding the possibility that the combined technique is inaccurate or could be improved upon).

Based on all these considerations, the region most strongly indicated by the combined direction sensing technique and the trajectories which pass through the highest joint probability density function estimates at all arc crossing points is that indicated in the blue box in Figure 86, in the region of 34-37S from 25-75NM from the 7th arc and approximately corresponding to boxes 12-15 B & D of the original ATSB defined search area. This region is to the south of the consensus high probability area of the ocean drift studies, although it is the peak density area estimated in some studies. Also noteworthy about this region is that it was not included in the surface searches conducted in 2014 shortly after the loss (dark shaded box), while it also contains the estimated most likely point of origin of a large number of objects in an apparent debris field recorded by French military intelligence satellite imagery and subsequently determined to be likely non-natural in origin, although none of those objects could be positively identified as being either aircraft segments or from the MH370 flight. Although this is the vicinity most strongly indicated as a result of the present study, it is also stressed that other solutions, even those far to the north, were not eliminated as a result of the analysis, and further work is recommended in improving and refining the techniques proposed herein, for example with the benefit of more data. Neither the opportunities for additional insights from the MH370 data, nor the opportunity to reduce the risk of future oceanic hull losses which result in prolonged searches, are exhausted.

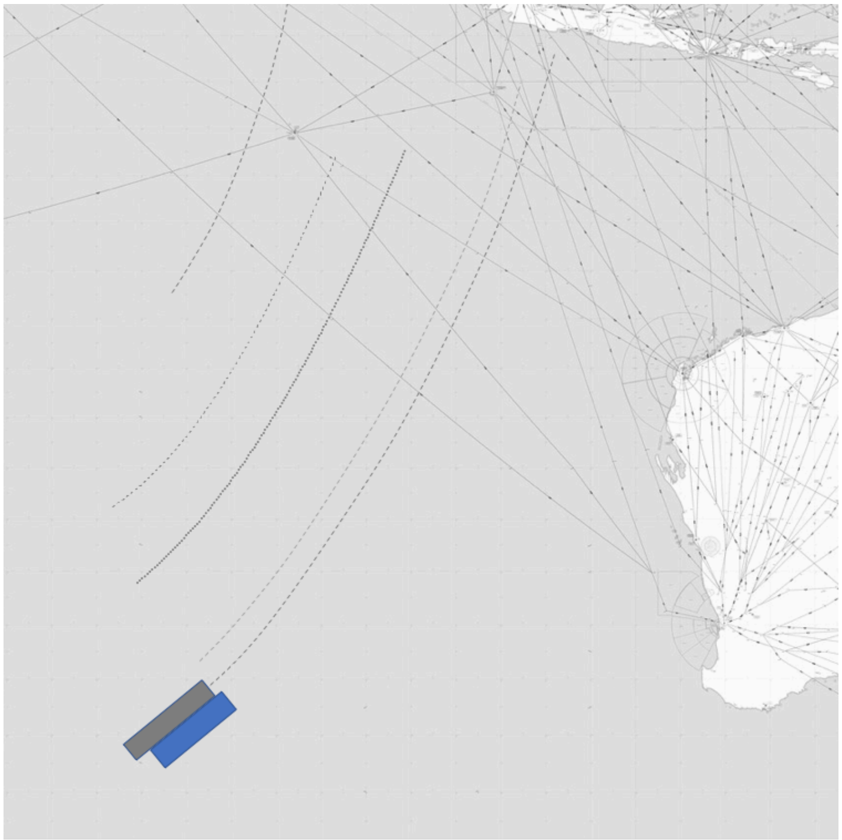

Figure 86. Most strongly indicated region from joint BFO and received power probability density function estimates with the most coherent trajectories.

REFERENCES

Airbus (2017). *Airbus launches new fixed and deployable flight recorders.* Retrieved from: https://www.airbus.com/newsroom/press-releases/en/2017/06/airbus-launches-new-fixed-and-deployable-flight-recorders-for-it.html

Anderson, B., Bennett, S., Davies, C., Exner, M., Farrar, T., Godfrey, R., Holland, B., Hyman, G., Ianello, V., Martin, B., Steel, D., Thompson, D., Wise, J.J. (2014a). *Further Progress Report from the Independent Group, and Updated MH370 Search Area Recommendation.* Retreived from http://tmfassociates.com/blog/wp-content/uploads/2014/09/MH370-IG-Further-Progress-Report.pdf

Anderson, P., & Tushman, M. (1990). Technological Discontinuities and Dominant Designs: A Cyclical Model of Technological Change. *Administrative Science Quarterly, 35*(4), 604-633. doi:10.2307/2393511

Antara News. (2014, March 19). Indonesian military radar did not detect missing airplane. *Antara News.* Retrieved from https://en.antaranews.com/news/93270/indonesian-military-radar-did-not-detect-missing-airplane

ARINC (1994). *Aviation Satellite Communications System (SatCom) Prt: 2 System Design and Equipment Functional Description*. (ARINC 741). Annapolis, MD: ARINC Industry Activities.

Ashton, C., Schuster Bruce, A., College, G., & Dickinson, M. (2015). The Search for MH370. *Journal of Navigation, 68*, 1-22.

ATSB. (2014). MH370 - *Definition of Underwater Search Areas*. Australian Transport Safety Bureau: Canberra

ATSB. (2014). *MH370 Flight Path Analysis & Update.* Australian Transport Safety Bureau: Canberra

ATSB. (2015). *MH370 – Definition of Underwater Search Areas.* Australian Transport Safety Bureau: Canberra

ATSB. (2016). MH370 *First Principles Review.* Australian Transport Safety Bureau: Canberra

ATSB. (2016). *MH370 Search and debris examination update.* Australian Transport Safety Bureau: Canberra

ATSB. (2016). *Debris examination reports 1, 2, 3, 4 and 5.* Australian Transport Safety Bureau: Canberra

ATSB. (2017). *The Operational Search for MH370.* Australian Transport Safety Bureau: Canberra

ARAIB, (2015) *Aircraft Accident Report Asiana Airways Boeing 747-400F, HL7604*. Aircraft and Railway Accident Investigation Board: Seoul.

Auten, J.D., Kuhne, M.A.; Walker, H.M., Porter, H.O. (2010). Neurologic Decompression Sickness Following Cabin Pressure Fluctuations at High Altitude. *Aviation, Space, and Environmental Medicine, 81*(4), 427-430. doi: https://doi.org/10.3357/ASEM.2406.2010

Barry, C. (2017, February 11). *Why We Need Data Withheld by Malaysia*. Retrieved from The Disappearance of MH370: http://mh370.radiantphysics.com/2017/02/04/why-we-need-data-withheld-by-malaysia/

Ball Aerospace (2017). *The Airlink® High-Gain Antenna System*. Ball Aerospace & Communications Corp: Broomfield, CO.

BEA (2011). *Triggered Transmission of Flight Data Working Group Report*. Paris: BEA.

Beccario, C. (2018). *Earth.* Retrieved from: https://earth.nullschool.net/#2014/03/08/0000Z/wind/isobaric/250hPa/overlay=temp/orthographic=92.05,4.75,1328/loc=96.037,5.169

Bellamy, W. (2015, June). United Seeks New Telemedicine Technology. *Avionics International*. Retrieved from https://www.aviationtoday.com/2015/06/15/united-seeks-new-telemedicine-technology/

Berzins, G., Ryan, F., & Smith, K. (2015). Initiation and early development of a worldwide satellite communications system for aviation . *Journal of Aeronautical History,* Paper No 2015/04. Retrieved from: https://www.aerosociety.com/media/4760/initiation-and-early-development-of-a-worldwide-satellite-communications-system-for-aviation.pdf

Bill HR 79, Bill HR 79 The No Missing Planes Act (2016).

Boeing. (2017). *Statistical Summary of Commercial Jet Airplane Accidents.* Seattle, WA: Boeing Commercial Airplanes.

Boeing. (2018). *Commercial Market Outlook 2018-2037.* Seattle, WA: Boeing Commercial Airplanes. Retrieved from: https://www.boeing.com/resources/boeingdotcom/commercial/market/commercial-market-outlook/assets/downloads/2018-cmo-09-11.pdf

Brabham, D. (2008). Crowdsourcing as a Model for Problem Solving: An Introduction and Cases. Convergence: *The International Journal of Research into New Media Technologies, 14*(1), 75-90. doi: 10.1177/1354856507084420

CANSO (2010). *Global Air Navigation Services Performance Report 2010*. Hoofddorp, Netherlands: Civil Air Navigation Services Organisation.

CANSO (2011). *Global Air Navigation Services Performance Report 2011*. Hoofddorp, Netherlands: Civil Air Navigation Services Organisation.

CANSO (2012). *Global Air Navigation Services Performance Report 2012*. Hoofddorp, Netherlands: Civil Air Navigation Services Organisation.

CANSO (2013). *Global Air Navigation Services Performance Report 2013*. Hoofddorp, Netherlands: Civil Air Navigation Services Organisation.

CANSO (2014). *Global Air Navigation Services Performance Report 2014.* Hoofddorp, Netherlands: Civil Air Navigation Services Organisation.

CANSO (2015). *Global Air Navigation Services Performance Report 2015*. Hoofddorp, Netherlands: Civil Air Navigation Services Organisation.

CANSO (2016). *Global Air Navigation Services Performance Report 2016*. Hoofddorp, Netherlands: Civil Air Navigation Services Organisation.

CANSO (2017). *Global Air Navigation Services Performance Report 2017*. Hoofddorp, Netherlands: Civil Air Navigation Services Organisation.

Chen, G., Gu, C., Morris, P. J., Paterson, E. G., Sergeev, A., Wang, Y.-C., and Wierzbicki, T. (2015). Malaysia Airlines Flight MH370: Water Entry of an Airliner, *Not. Am Math. Soc., 62*, 330–344.

Chilton, S. (2009). Crowdsourcing is Radically Changing the Geodata Landscape: Case Study of OpenStreetMap. *Proceedings of the International Cartographic Conference 2009.* Retrieved July 12 2018 from: https://icaci.org/files/documents/ICC_proceedings/ICC2009/html/nonref/22_6.pdf

Chillit, M. (2017). *The Plane at Batavia*. Seattle: Amazon

Clarke, A.C. (1945, October). Extra-Terrestrial Relays. *Wireless World*. Retrieved from: http://clarkeinstitute.org/wp-content/uploads/2010/04/ClarkeWirelessWorldArticle.pdf

Cochran, W.G. (1954). The Combination of Estimates from Different Experiments. *Biometrics, 10*(1), 101-129.

Cook, M. (2014). The Bioethics of the Search for MH370. *Australasian Science, 35*(5), 50.

Cook, T. D. (1985). Post-positivist critical multiplism. In W. R. Shadish, & C. S. Reichardt (Eds.), *Reproduced in Evaluation Studies Review Annual* (12). Beverly Hills, CA: Sage Publications.

Creswell, J.W. (2012). *Educational Research.* Boston: Pearson.

CSIRO. (2017). *The Search for MH370 and Ocean Surface Drift Parts I to IV.* Canberra: ATSB.

Daniel, P. (2016). *Rapport d'étude dérive à rebours de flaperon*. Paris: Meteo France.

Davey, S., Gordon, N., Holland, I., Rutten, M., & Williams, J. (2015). *Bayesian Methods in the Search for MH370.* Springer-Verlag.

DCA. (2008). *Radar Services and Procedures.* AIP Malaysia, Department of Civil Aviation Malaysia.

De Changy, F. (2018, May 29). MH370: mystery of private company behind renewed search

for missing plane. *Post Magazine.* Retrieved from https://www.scmp.com/topics/malaysia-airlines-flight-370

Diaconis, P. (1998). A Place for Philosophy? The Rise of Modeling in Statistical Science. *Quarterly of Applied Mathematics, LVI* (4), 797-805.

Diaconis, P. (2018, September). *Chance and Evidence.* Presented at the Oxford Mathematics Public Lectures, Oxford University.

Doksone, T. (2014, March 18). Thailand gives radar data 10 days after plane lost. *The Jakarta Post.* Retrieved from http://www.thejakartapost.com/news/2014/03/18/thailand-gives-radar-data-10-days-after-plane-lost.html

Doucet, A., de Freitas, N. & Gordon, N. (2001) *Sequential Monte Carlo in Practice.* Springer-Verlag: New York

Dunn, W. (2003). *Public Policy Analysis: An Introduction.*

Durgadoo, J.V., Siren, R., Biastoch, A., Nurser, A.J.G, New, A.L., Hirschi, J., Drillet, Y., Durand, E., Rodwell, M.J., Bidlot, J., Janssen, P.A.E.M. (2016). *Backtracking of the MH370 flaperon from La Réunion.* Kiel: Heimholtz Centre for Ocean Research; National Oceanography Centre; ECMWF.

European Commission (2015) COMMISSION REGULATION (EU) 2015/2338 of 11 December 2015

Flight Safety Foundation (2018). *Aviation Safety Network*. Retrieved from https://aviation-safety.net

Franzoni, C, & Sauermann, H. (2014). Crowd science: The organization of scientific research in open collaborative projects. *Research Policy, 43*(1), 1-20. doi: 10.1016/j.respol.2013.07.005

García-Garrido, V., Mancho, A.M., Wiggins, S., & Mendoza-Parra, C. A., (2015). A dynamical systems perspective on the absence of debris associated with the disappearance of flight

MH370. *Nonlinear Processes in Geophysics Discussions, 22*(6); 701-712. doi: https://doi.org/10.5194/npg-22-701-2015.

Geiger, D., Rosemann, M., & Fielt, E. (2011). Crowdsourcing information systems: a systems theory perspective. *Proceedings of the 22nd Australasian Conference on Information Systems.* Sydney 2011.

Gauss, C.F. (1857). *Theory of the Motion of the Heavenly Bodies Moving About the Sun in Conic Sections. Translated by Charles Henry Davis*. Little, Brown and Company: Boston.

Gilbert, M. (2017). *An Analysis of MH370's Flight Path Between Waypoint IGARI and the top of the Malacca Strait, a Review of Potential Vulnerabilities Specific to Airplane 9M-MRO and a Hypothesis Regarding Possible In Flight Events and an End-of-Flight Scenario*. Retrived from http://media.news.com.au/multimedia/2016/MH370/MH370ResearchV3.4.pdf

GlobusMax (2015, 2018). *The Waypoint Hypothesis.* Retrived from https://globusmax.wordpress.com

Godfrey, R. (2018). *Drift Analysis of MH370 Floating Debris*. Retrieved from https://www.dropbox.com/s/ifc2n5h0zoz1moo/Drift%20Analysis%20of%20MH370%20Floating%20Debris.pdf?dl=0

Golafshani, N. (2003). Understanding reliability and validity in qualitative research. *The Qualitative Report, 8*(4), 597-606. Retrieved from http://www.nova.edu/ssss/QR/QR8-4/golafshani.pdf

Griffin, D. (2017). MH370 - drift analysis [web log post]. Retrived from https://blogs.csiro.au/ecos/satellite-images-add-to-weight-of-evidence-locating-missing-mh370/

Griffin, D., Oke, P., & Jones, E.M. (2016). *The search for MH370 and ocean surface drift – Parts I-III*. Canberra: CSIRO. doi 10.4225/08/5892224dec08c

Griffin, D., Oke, P., (2017). *The search for MH370 and ocean surface drift – Part IV*. Canberra: CSIRO.

Guillot, C., (2013). The Wisdom of the Crowd. *The Internal Auditor, 70*(5), 44-50

Gunson, S. (2017). Where is MH370 [comment to web log post]. Retrived from http://mh370research.blogspot.com/2014/05/airplane-traffic-at-1822-utc-last-air.html

Hall, B (2015). Map of radar coverage. Retreived from https://www.dropbox.com/s/1qpkdf7yiu9n449/radar-FOV.JPG?dl=0

Hartigan, J., & Hartigan, P. (1985). The Dip Test of Unimodality. *The Annals of Statistics, 13*(1), 70-84. Retrieved from http://www.jstor.org/stable/2241144

Hoffmann-Wellenhoff, B., Lichtenegger, H., & Collins, J. (1992). *GPS Theory and Practice*. Vienna, Austria: Springer-Verlag.

Holland, I. D. (2017). *MH370 Burst Frequency Offset Analysis and Implications on Descent Rate at End-of-Flight.* Edinburgh, Australia: Commonwealth of Australia Defence Science and Technology Group.

Howe, J. (2006). *Crowdsourcing: A definition.* Retrieved from http://www.crowdsourcing.com/cs/2006/06/crowdsourcing_a.html

Ianello, V. (2015, August 18). *Some Observations on the Radar Data for MH370.* Retrieved from https://www.dropbox.com/s/zh9rfqa6rxy582m/2015-08-18%20Radar%20Data%20for%20MH370.pdf?dl=0

Ianello, V. (2017). *Why We Need Data Withheld by Malaysia.* Retrieved from http://mh370.radiantphysics.com/2017/02/04/why-we-need-data-withheld-by-malaysia/

Ianello, V. (2017, June 4). *MH370 End-of-Flight with Banked Descent and No Pilot.* Retrieved from The Disappearance of MH370: http://mh370.com/radiantphysics.com

Iannello, V. (2017, July 4). *Some Insights from the Unredacted Satellite Logs.* Retrieved from The Disappearance of MH370: www.mh370.radiantphysics.com

Ianello, V., & Godfrey, R. (2016). Possible Flight Path of MH370 towards McMurdo Station, Antarctica. Retrived from http://mh370.radiantphysics.com/papers

Ianello, V., & Guillaume, Y. (2016). Further Analysis of Simulator Data Related to MH370. Retrived from http://mh370.radiantphysics.com/papers

Ianello, V., (2018). An MH370 Flight Path Ending Further North on 7th Arc. Retrived from http://mh370.radiantphysics.com/papers

Ianello, Thompson & Workman, (2017, February 7). Re: Why we need the data withheld by Malaysia. [Web log comments]. Retrieved from

http://mh370.radiantphysics.com/2017/02/04/why-we-need-data-withheld-by-malaysia/

IAU. (2006). IAU Planet Definition Committee. *Proceedings of the International Astronomical Union XXVI General Assembly,* Prague.

IMO, (2016). *International Aeronautical Search and Maritime Search and Rescue Manual.* International Maritime Organization: London.

ICAO. (1944). *Convention on International Civil Aviation.* Montreal: ICAO.

ICAO (2007) *Manual for Aeronautical Mobile Satellite (Route) Service. Part III.* Montreal: ICAO.

ICAO. (2012). *The Convention on International Civil Aviation Annexes 1 to 18 ('Annexes Booklet').* Montreal: ICAO.

ICAO (2016). *Procedures for Air Navigation Services, Air Traffic Management*, Doc 4444, 16th Edition. Montreal: ICAO.

ICAO. (2017). COVER SHEET TO AMENDMENT 42.

ICAO GADSS AG. (2017). *GADSS Concept of Operations.* ICAO GADSS Advisory Group.

Inmarsat (2007). Inmarsat-3 F3 Technical Description. Retrieved from https://licensing.fcc.gov/myibfs/download.do?attachment_key=-136047

IPFS (2016) List of Unrecovered Flight Recorders. Retrieved from https://ipfs.io/ipfs/QmXoypizjW3WknFiJnKLwHCnL72vedxjQkDDP1mXWo6uco/wiki/List_of_unrecovered_flight_recorders.html

ITU (2016). *International Telecommunications Union Statistics on Internet Use*. Retrieved July 12, 2018 from: https://www.itu.int/en/ITU-D/Statistics/Pages/stat/default.aspx

Jacques, H. & Gantan, J. (2014, March 19). Indonesian Bureaucracy Grounded MH370 Search Flights, Military Pledges 'Fullest Support'. *Jakarta Globe.* Retrieved from https://jakartaglobe.id/news/indonesian-bureaucracy-grounded-mh370-search-flights-military-pledges-fullest-support/

Jansen, E., Coppini, G., and Pinardi, N. (2016). Drift simulation of MH370 debris using superensemble techniques, *Nat. Hazards Earth Syst. Sci., 16*, 1623-1628, doi: 10.5194/nhess-16-1623-2016

Kristensen, M. (2018). *How to find MH370?* Retrived from https://arxiv.org/abs/1811.09315

Lee, M.D., Zhang, S., Shi, J. (2011). The wisdom of the crowd playing The Price Is Right. *Memory & Cognition, 39*. 914-923. doi: 10.3758/s13421-010-0059-7

Lin, Y. (1999). *General Systems Theory: A Mathematical Approach*. Kluwer Academic / Plenum Publishers, New York.

Lumsden, K. (2003). *Economics.* Pearson.

Malaysian Government. (2015). *Interim Safety Investigation for MH370 (9M-MRO).* The Malaysian ICAO Annex 13 Safety Investigation Team for MH370: Kuala Lumpur.

Malaysian Government. (2016). *2nd Interim Safety Investigation for MH370 (9M-MRO).* The Malaysian ICAO Annex 13 Safety Investigation Team for MH370: Kuala Lumpur.

Malaysian Government. (2017). *3rd Interim Safety Investigation for MH370 (9M-MRO).* The Malaysian ICAO Annex 13 Safety Investigation Team for MH370: Kuala Lumpur.

Malaysian Government. (2018a). *4th Interim Safety Investigation for MH370 (9M-MRO).* The Malaysian ICAO Annex 13 Safety Investigation Team for MH370: Kuala Lumpur.

Malaysian Government. (2018). *Safety Investigation Report Malaysia Airlines Boeing 777-200ER (9M-MRO) 08 March 2014.* The Malaysian ICAO Annex 13 Safety Investigation Team for MH370. Publication MH370/01/2018..

Marchand, J., Gasser, P., Delarche, M., & Garot, J. (2018). A plausible trajectory for MH370. Retrived from http://mh370-captio.net/wp-content/uploads/2018/01/MH370-PlausibleTrajectory-3.4.pdf

Marjanovic, S.,Fry, C., & Chataway, J. (2012). Crowdsourcing based business models: In search of evidence for innovation 2.0. *Science and Public Policy 39*(3), 318-332. doi: 10.1093/scipol/scs009

Marks, A. (2000). When planes crash in water, recovery gets complicated. *Christian Science Monitor*. Retrieved from https://www.csmonitor.com/2000/0202/p2s2.html

Mele, C., Pels, J., & Polese, F. (2010). A Brief Review of Systems Theories and Their Managerial Applications. *Service Science, 2*(1-2):126-135.

Milgram, S. (1963). Behavioral Study of obedience. *The Journal of Abnormal and Social Psychology*, 67(4), 371-378.

Minchin, S., Mueller, N., Lewis, A., Byrne, G., Tran, M., (2017). *Summary of imagery analyses for non-natural objects in support of the search for Flight MH370: Results from the analysis of imagery from the PLEIADES 1A satellite undertaken by Geoscience Australia*. Record 2017/13. Canberra: Geoscience Australia. doi: http://dx.doi.org/10.11636/Record.2017.013

Miron, P., Beron-Vera, F.J., Olascoaga, M.J., & Koltai, P. (2019). Markov-chain inspired search for MH370. Retrieved from https://arxiv.org/pdf/1903.06165.pdf

Mohney, G. (2014, March 13). Long Search for Missing Plane Could Cost 'Hundreds of Millions of Dollars. *ABC News*. Retrieved from https://abcnews.go.com/International/long-search-missing-plane-cost-hundreds-millions-dollars/story?id=22899690

National Safety Council. (2016). *Odds of Dying*. Retrieved from NSC Injury Facts: http://injuryfacts.nsc.org/all-injuries/preventable-death-overview/odds-of-dying/

Nederland, (2017). *MH370 northerly flight path – waypoint approach (v. 3.0).* Retrived from https://www.docdroid.net/GvlrLaV/mh370-waypoint-30.pdf

Nesterov, O. (2018). Consideration of various aspects in a drift study of MH370 debris, *Ocean Science, 14*, 387-402. doi: https://doi.org/10.5194/os-14-387-2018, 2018.

Nickerson, J.A., Wuebker, R., & Zenger, T. (2017). Problems, theories, and governing the crowd. *Strategic Organization,15*(2), 275-288. doi: 10.1177/1476127016649943

O'Donnell, R. (2010, Jan 1). *Radar Systems Engineering Lecture 5 Propagation through the Atmosphere.* Retrieved from University of New Hampshire: http://aess.cs.unh.edu/Radar%202010%20PDFs/Radar%202009%20A_5%20Propagation%20Effects.pdf

Parfitt, C. (2016, March). *GADSS Overview and FAA Position.* Presented to MRO & Flight Ops IT Conference.

Passig, D., Cohen, N., & Bareket-Bojmel (2015). Crowd-deliberation as an organizational problem solving tool. *International Journal of Manpower, 36*(7), 1124-1143. doi: 10.1108/IJM-03-2014-0075

Patton, M.Q. (2015). *Qualitative Research & Evaluation Methods: Integrating Theory and Practice* (4th ed.). Thousand Oaks, CA: Sage.

Pattiaratchi, C., & Wijeratne, S. (2016). The search for MH370 is over: what we learnt and where to now. *The Conversation*.

Pichavant, C. (2016, April). *Aircraft Tracking & Flight Data Recovery – The Aircraft Manufacturer View.* Presented at the meeting of the Royal Aeronautical Society, London.

Pleter, O., Constantinescu, C., & Jakab, B. (2016). Reconstructing the Malaysian 370 Flight Trajectory by Optimal Search. *The Journal of Navigation*, 1-23.

R Core Team (2018). R: A language and environment for statistical computing. R Foundation for Statistical Computing, Vienna, Austria. URL https://www.R-project.org/.

RMP (2014). Royal Malaysia Police Team Task Force CID Reports on MH370. Retrieved from https://www.reddit.com/r/Solving41818/comments/85lf8g/rmp_report_from_mh370_and_leaked_files_that_may/

Roddy, D. (1989). *Satellite Communications*. New York: McGraw-Hill

Rodzi, N.H. (2018, January 10). Malaysia to pay US firm up to $93 million if it finds MH370 in 90 days The Straits Times. Retrieved from https://www.straitstimes.com/asia/se-asia/malaysian-govt-appoints-us-based-exploration-firm-ocean-infinity-to-hunt-for-malaysia

RStudio Team (2016). RStudio: Integrated Development for R. RStudio, Inc., Boston, MA URL http://www.rstudio.com/.

Rydberg, H. (2015). *MH370: Finding the Debris Origin.* Retrived from http://bitmath.org/mh370/debris-origin.pdf

Schuster-Bruce, A. (2017). Data Streaming by Satellite for Air Accident Investigation and Airlines Operations and Maintenance. *Flight Location and Data Recovery Conference, .* Hamburg.

Sheather, S.J. (2009). *A Modern Approach to Regression with R*. New York: Springer.

Singer, P. (2010). *The life you can save: How to do your part to end world poverty.* New York: Random House.

SK999 (2016). Notes on the Flight Path of MH370. Retrieved from https-//drive.google.com/file/d/0B7YQpAH4JIN5amtWUURLZV9JNk0/view.pdf

SK999 (2018). MH370 Radar Path Compared with Numerical Integration of Bayesian Methods Velocity and Track Angle Figures (Updated for ADS-B).

Skolnik, M. (1962). *Introduction to Radar Systems.* New York: McGraw Hill.

SkyVector (2018). SkyVector. Retrieved from Skyvector.com

Smithson, P. (2016). Head for Home. Retrieved from http://www.findmh370.com

Snedecor, G.W. (1934). *Calculation and interpretation of analysis of variance and covariance* (Iowa. State college of agriculture and mechanic arts, Ames. Division of industrial science. Monograph no. l). Ames, Ia.: Collegiate Press.

Sobel, D. (1995). *Longitude: The True Story of a Lone Genius Who Solved the Greatest Scientific Problem of His Time.* New York: Bloomsbury.

Spinor (2014). My take on the MH370 Inmarsat “raw” data. [web log comment]. Retrieved from https://spinor.info/weblog/?p=5985

SSIG. (2014). No Signs of Flight Mh370 Detected By Indonesian Military Radar In East Aceh. South-South Information Gateway. Retrieved from http://www.ssig.gov.my/blog/2014/03/21/no-signs-of-flight-mh370-detected-by-indonesian-military-radar-in-east-aceh/

Surowiecki, J. (2005). *The wisdom of crowds.* New York: Anchor Books.

Schwarzer, G., Carpenter, J.R., & Rücker, G. (2015). *Meta-Analysis in R.* Heidelberg: Springer.

The Nation. (2014). Thai Air Force radar may have detected Malaysia's MH370: Thai Air Force Chief. *The Nation.* Retrieved from https://www.thaivisa.com/forum/topic/712004-thai-air-force-radar-may-have-picked-up-mh370/

Thomas, G. (2018). MH370: What has been left out of the flawed investigation. Airline Ratings. Retrieved from https://www.airlineratings.com/news/mh370-left-flawed-investigation/

Thompson, D. (2017, February 11). *The Disappearance of MH370*. Retrieved from Why We Need Data Withheld by Malaysia: http://mh370.radiantphysics.com/2017/02/04/why-we-need-data-withheld-by-malaysia/

Tikuisis, P. (1995). Predicting survival time for cold exposure. *International Journal of Biometeorology 39*(94). doi: https://doi.org/10.1007/BF01212587

Trinanes, J.A., Olascoaga, M.J., Goni, G.J, Maximenko, N.A., Griffin, D.A. & Hafner, J. (2016). Analysis of flight MH370 potential debris trajectories using ocean observations and numerical model results, *Journal of Operational Oceanography, 9*(2), 126138. doi: 10.1080/1755876X.2016.1248149

Tripathi , A. (2017). *Myth or Reality? Crowdsourcing as a Complex Problem-Solving Model: Evidence from Software Developed by the Crowd and Professionals* (Thesis). Nebraska.

Tushman, M., & Anderson. (1986). Technological discontinuities and organizational environments. *Administrative science quarterly, 31*(3) 439-465. doi: 10.2307/2392832

Twombly. (2018, Mar). *Flight Training*, p. 6.

Ulich, B. (2014). *The Location of MH370*. Retrieved from http://vocasupport.com/wp-content/uploads/2015/01/The-Location-of-MH370-by-Dr.-Bobby-Ulich-2014.09.25.pdf

Ulich, B. (2018). *Identification of MH370 Route into the Southern Indian Ocean*. Retrieved from http://vocasupport.com/wp-content/uploads/2015/01/The-Location-of-MH370-by-Dr.-Bobby-Ulich-2014.09.25.pdf

Ulich, B. (2018). *Should a search for 9M-MRO be carried out north of latitude 25S?*. Retrieved from http://vocasupport.com/wp-content/uploads/2015/01/The-Location-of-MH370-by-Dr.-Bobby-Ulich-2014.09.25.pdf

USCG, (2016). United States Coast Guard, U.S. Aeronautical Search and Rescue Regions. Retrieved from https://www.navcen.uscg.gov/images/GMDSS/SARAreas/23_US_Aeronautical_SRR_Overview.jpg

Utterback, J. (1996). Invasion of a Stable Business by Radical Innovation. In J. Utterback, *Mastering the Dynamics of Innovation*. Cambridge MA: Harvard Business School Press.

Viechtbauer, W. (2017). Metafor: A Meta-Analysis Package for R, retrieved from: https://cran.r-project.org/web/packages/metafor/metafor.pdf

Von Bertalanffy, L. (1972). The history and status of general systems theory. Academy of Management Journal, 407.

Von Bertanallfy, L. (1968). *General System Theory*. New York: Braziller.

Wells, D.E. (1974). Doppler Satellite Control. Technical Report No. 29. New Brunswick: University of New Brunswick Geodesy and Geomatics Engineering.

Wardell, J. (2014). Search for MH370 to be most expensive in aviation history. *Reuters.* Retrieved from https://www.reuters.com/article/us-malaysia-airlines-costs/search-for-mh370-to-be-most-expensive-in-aviation-history-idUSBREA3709520140408

Westfeldt, P., & Konrad, J. (1992). The Airlink® High Gain Antenna System. In Mayes, P. et al, *Proceedings of the 1993 Antenna Applications Symposium.* Symposium conducted at Hanscom AFB, MA.

Wichman, B.A. and Hill, I.D. (1982). Algorithm AS 183: An Efficient and Portable Pseudo-Random Number Generator, Applied Statistics, 31, 188-190.

Wise, J. (2016, May 16). The SDU Re-logon: A Small Detail That Tells Us So Much About the Fate of MH370. Retrieved from Jeff Wise: www.jeffwise.net/category/aviation

Wise, J. (2017) http://jeffwise.net/2017/01/18/were-mh370-searchers-unlucky-or-duped/comment-page-7/

Workman, D. (2017). Re: Why we need the data withheld by Malaysia. [Web log comment]. Retrieved from http://mh370.radiantphysics.com/2017/02/04/why-we-need-data-withheld-by-malaysia/

Yap, F.F. (2015). Autopilot Flight Path BFO Error Analysis. Retrieved from http://www.duncansteel.com/archives/1366

Yap, F.F. (2015). BFO and BTO Calculator. Retrieved from https://drive.google.com/file/d/0B6gvsOWO81hTTGJDVklRX3BCa1E/view

APPENDIX

GSM Phone Link Budget Analysis. The mobile phone belonging to the first officer is reported to have made a brief connection with sector 2 of the BBFARLIM2 GSM base transceiver station on the island of Penang, although only enabling the location based service (LBS) to operate, no attempted call or text message was recorded. Given the highly directional nature of GSM BTS antennas, this raises the question of whether any inference can be made about the aircraft altitude from this brief connection. With reference to a typical vertical gain pattern of a GSM antenna, the connection is almost certain to have been made via a sidelobe in the antenna pattern, given the typical vertical pattern of the boresight, which in the suburban setting in which this particular base station is located, is very likely to have had a downtilt of a few degrees. This is supported by the fact that the terrain profile of the line of sight between the location of the GSM BS and the estimated position of the aircraft at the time of connection is such that the line of sight would have been terrain shielded below ~10 degrees. As can be seen from the figure below, the terrain rises approximately 1,200ft at 1.2 miles from the GSM BS along the line of sight, which as a first order approximation creates a terrain mask below 10 degrees of elevation. At 12 miles, this equates to approximately 12,000 ft.

At the time of the incident, Celcom's spectrum assets consisted of 34MHz at 900MHz, 50MHz at 1800MHz and 20MHz at 2600MHz bands (ABI Research, 2014; Celcom, 2012; Malaysian Wireless, 2016), although the latter was for LTE service and, even if the mobile station was 2.6Ghz capable, the base station in question is very unlikely to have been upgraded to LTE at that time; Oxford Business Group (2014) reported that Celcom had deployed 700 LTE sites as of March, 2014, less than 10% of the company's reported number of over 9,000 sites (Celcom, 2011), where such early deployment would normally be expected in very high density traffic areas and not in the suburban location of the BBFARLIM2 site.

ITU-R Recommendation F.1336-4 (ITU, 2014) provides average and peak measured gain patterns for an unspecified number of representative antennas, covering both the 900MHz and 1800MHz bands. As can be seen from the charts, the 900MHz antennas typically exhibit a side lobe peak at approximately 20 degrees above the boresight angle of -15dB to the boresight gain, followed by a sharp drop off to -20dB, while antennas in the 1700-2700MHz range typically exhibit a peak in the -15dB to -17dB range over a broader range of elevation angles from 10 to 40 degrees. In the horizontal plane it is assumed that the connection was close to peak.

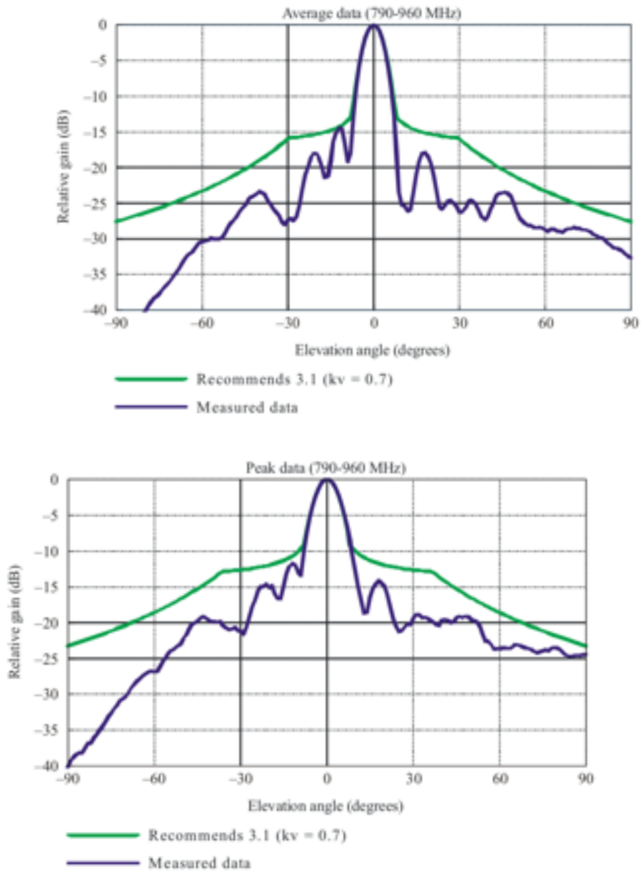

Figure 87: 900MHz GSM Average and Peak Gain in Elevation (ITU, 2014)

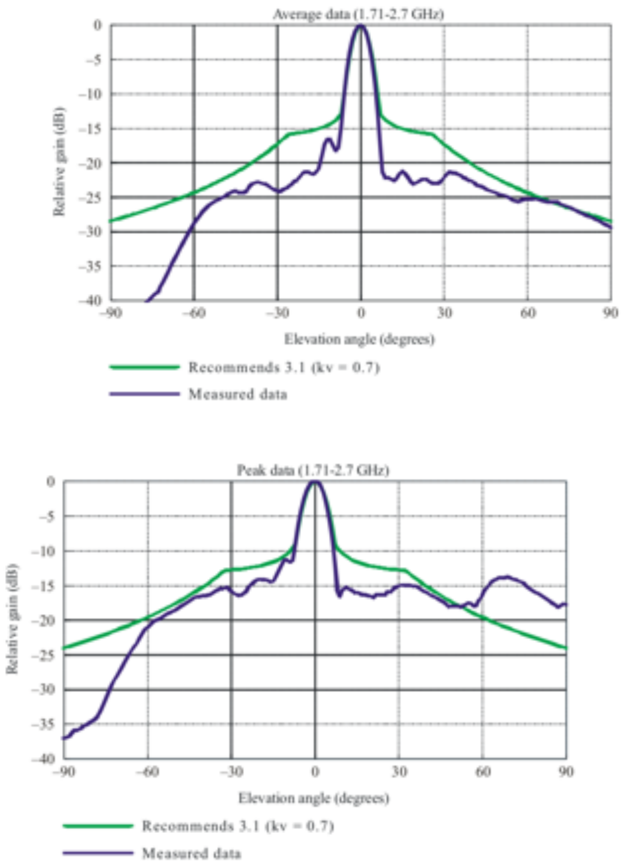

Figure 88: 1800MHz GSM Average and Peak Gain in Elevation (ITU, 2014)

The 3G standard for GSM900 and GSM1800 quotes a base station receiver sensitivity of -104 dBm, however typical operator values are around -108 dBm (ECC, 2008) Assuming that the BS receiver sensitivity is in the range of -104 to -108 dBm, with a system noise level in the order of -109dBm to -114 dBm at 900 MHz and a physical limit at the antenna connector of -121dBm, given the brief connection we might assume that the received power from the on-board device at the GSM BS antenna connector would likely have been in the range of -105 to -120dBm. If the peak EIRP of the mobile device is assumed to be 32dBm for the class of GSM handset used (ETSI, 2005) this would imply that the sum of the insertion loss of the aircraft frame or window, plus the free space path loss, plus the base station antenna gain in the assumed side lobe to be in the range of -137 to -152 dBm.

The free space path loss at 10NM range equates to 116.9dB and 122.9dB at 900MHz and 1800MHz, respectively. The effect of aircraft altitude on the slope distance would equate to less than 2dB of difference to these free space path loss estimates. Moriaitis and Panagopoulos (2011) measured insertion losses of an aircraft hull in the range of 15.5 to 21.4 dB at 1800MHz, while others have derived a 21.5dB attenuation at 1.9GHz for an aircraft window. The CEPT ECC (ECC, 2008) provides a summary of ten studies of effective aircraft attenuation on GSM mobile phones in the 900 and 1800MHz bands, conducted by Airbus, Boeing, OnAir, Ericsson, Telenor and Qualcomm, which range from 5dB of gain to 32dB of attenuation, with an overall average of 12dB of insertion loss. The FAA (2014) provides guidance of a 12dB attenuation assumption for a metal fuselage for areas such as flight decks, near windows or doors without EMI gaskets, or 20-32 dB for progressively more shielded areas.

For the -104dBm base station receiver sensitivity case as per the GSM900/1800 standard, establishment of the link is theoretically possible at the -15dB point in the normalized elevation plane gain pattern for the GSM BS in both the 900 and 1800 MHz bands. At 900MHz: 32dBm EIRP – 12 dB attenuation – 116.9 path loss = 96.9 dBm, a 7 dB margin to -104dBm at the 0 dBi point (roughly equivalent to the -15 dB normalized point for a typical 15 dBi GSM antenna) which would render the link theoretically viable even at 20dB insertion loss for the aircraft. At 1800MHz: 32dBm – 12 – 122.9 = -102.0 dBm, leaving a smaller margin for higher insertion losses but still theoretically possible, up to 40 degrees elevation. It has also been noted that the registration on the network occurred at a time when the Doppler shift on the uplink would have been reduced due to the relative geometry, however that would have changed quickly as a function of the rapidly changing geometry and the limit of the GSM system to track Doppler shifted signals is around 150Hz, which could explain the very brief connection (Workman, 2017).

In terms of altitude discrimination, in the 900 MHz case the -15dB sidelobe peak at approximately 20 degrees would imply an altitude at 10 NM in the 20-25,000ft range, depending on the base station antenna downtilt, and where the possibility of contact below 10,000ft for the edges of the main lobe is considered negligible due to the aforementioned terrain shielding. In the 1800 MHz case, the broad distribution of the -15dB point means that altitude could range anywhere from 12,000 to 50,000 ft. Therefore it is concluded that it is not possible to make an altitude inference or estimate for this connection based on the information available. With specific knowledge of the exact model of base station antenna used, its measured gain pattern in the vertical plane, the frequency used for the specific uplink transmission and the base station receive specifications, ideally with other information such as the received power of the recorded signal, it may be possible to make a more refined estimate or inference, a recommendation for further work, although the typical existence of multiple sidelobes and the wide range of possible insertion losses due to the airframe may result in high uncertainty in any such inference, even if these details were known.

Error Propagation Analysis BTO

The functional model relating the BTO observed values to the distance from the spacecraft to the aircraft is given by:

$$R_{AES}^{SC} = \frac{c.(BTO_t - \beta)}{2} - R_{GES}^{SC}$$

Where the variables $\mathrm{BTO_t}$, β and R_{GES}^{SC} each contain measurement noise or uncertainty, expressed by their standard deviations σ_{BTO}, σ_{β}, σ_{R}, respectively. The uncertainty in the derived spacecraft-aircraft range R_{AES}^{SC} is a function of the uncertainty in the variables used in its estimation and the sensitivity of the function to each of those variables, such that the uncertainty in the derived parameter can be found by application of the Gaussian error propagation function:

$$\sigma_{R_{AES}^{SC}}^2 = \sigma_{BTO}^2 \cdot \left(\frac{\partial f}{\partial BTO}\right)^2 + \sigma_{\beta}^2 \cdot \left(\frac{\partial f}{\partial \beta}\right)^2 + \sigma_{R_{GES}^{SC}}^2 \cdot \left(\frac{\partial f}{\partial R_{GES}^{SC}}\right)^2 + \cdots$$

Where the ellipsis refers to the higher order terms which in this application are assumed to be zero, that is the independent variables are assumed to be uncorrelated in this case. The partial derivates express the rate of change of the function with respect to each of the variables and are evaluated for the BTO function as follows:

$$\left(\frac{\partial f}{\partial BTO}\right)^2 = \left(\frac{c}{2}\right)^2 ; \ \left(\frac{\partial f}{\partial \beta}\right)^2 = \left(-\frac{c}{2}\right)^2 ; \ \left(\frac{\partial f}{\partial R_{GES}^{SC}}\right)^2 = (-1)^2$$

Ashton et al. (2014) estimated the bias β using 17 BTO measurements, i.e. n=17, taken while the aircraft was at the gate at Kuala Lumpur airport, thus at a known position and where the satellite-aircraft range R_{AES}^{SC} could be estimated independently of the BTO measurements, and where the standard deviation of the BTO measurements was estimated as 31.3 µsec, equivalent to 9.38km. From this, we can estimate the standard deviation of the bias estimate β, as the standard deviation of the mean, $\sigma_{\beta} = \frac{\sigma_{BTO}}{\sqrt{n}}$, a function which itself can be derived from the Gaussian error propagation law above, which for n=17 yields an estimate of σ_{β}= 7.59 µsec, equivalent to 2.275km. The uncertainty in the range from the Ground Earth Station to the spacecraft, $\sigma_{R_{GES}^{SC}}$, at the time of a given BTO observation is a function of the measurement precision of the Tracking, Telemetry & Command system used for the spacecraft and any accumulated error in the orbit determination function. Rodriguez, Krier, Thill and Vincente (2014) show that the ranging precision of the tone-ranging technique typically used for this purpose is less than 3m at 95% for a geosynchronous orbit, however the radial position error can accumulate in the orbit determination function to around 100m over several days, therefore a conservative estimate of $\sigma_{R_{GES}^{SC}}$ = 0.1km is used for this study, especially given the low sensitivity of the overall function to this specific parameter as given by the partial derivates above.

Using these previously estimated standard deviations together with the partial derivates above, the standard deviation of any given satellite to aircraft range estimated using the BTO function is given, to first order, by:

$$\sigma^2_{R_{AES}^{SC}} = \sigma^2_{BTO} \,.\, \left(\frac{c}{2}\right)^2 + \sigma^2_{\beta} \,.\, \left(-\frac{c}{2}\right)^2 + \sigma^2_{R_{GES}^{SC}} \,.\, (-1)^2 + \cdots$$

$$= \sigma^2_{R_{AES}^{SC}} = 31.3\ \mu\text{sec}^2 \,.\, \left(\frac{c}{2}\right)^2 + 7.59\ \mu\text{sec}^2 \,.\, \left(-\frac{c}{2}\right)^2 + 0.1 km^2 \,.\, (-1)^2 + \cdots$$

$= \sigma^2_{R_{AES}^{SC}}$ = 23,316.926km, therefore $\sigma_{R_{AES}^{SC}}$ = (23,316.926)$^{1/2}$ = 4.83km

Which suggests that the uncertainty of any given BTO derived range is 4.83km at 1-sigma, or 9.7km at 2-sigma or approximately 95% confidence assuming the distribution is Gaussian (hmmm ‘distinctly nonGaussian”). The propagation of this range uncertainty to the ocean surface depends upon the apparent elevation angle θ of the spacecraft from the aircraft location and can be approximated to first order as $\sigma_{R_{AES}^{SC}}$. Cos θ, so for θ= 30^{O} the horizontal uncertainty on the ocean surface would be estimated at 4.2km 1-sigma or 8.4km 2-sigma.

A key assumption in this error propagation analysis is that the mean value of the bias β as estimated on the ground prior to departure remained constant over a period of more than

8 hours and, moreover, that it remained constant through an apparent power cycle of the AES at approximately 1625Z and, in the case of the 7th BTO arc, through a second apparent power cycle between 0011Z and 0019Z.

Pulau Perak Eyewitness. The RMP report contains a handwritten note that there was an eyewitness on Pulau Perak who saw the aircraft. This island is uninhabited except for a military installation. Resolution of whether or not there was such an eyewitness and whether the aircraft was seen flying at an unusually low altitude could be valuable in determination of the vertical trajectory at that point in time.

Oklahoma State University Institutional Review Board

Date: 01/10/2019
Application Number: ED-19-6
Proposal Title: A META-ANALYSIS OF SPATIAL ESTIMATES IN THE CASE OF MALAYSIAN AIRLINES FLIGHT MH370 WITH ANALYSIS OF KEY ASSUMPTIONS AND ASSESSMENT OF THE PROBABILITY OF FUTURE OCEANIC HULL LOSSES

Principal Investigator: Pete Large
Co-Investigator(s):
Faculty Adviser: Jon Loffi
Project Coordinator:
Research Assistant(s):

Processed as: Not Human Subjects Research

Status Recommended by Reviewer(s): Closed

Based on the information provided in this application, the OSU-Stillwater IRB has determined that your project does not qualify as human subject research as defined in 45 CFR 46.102 (d) and (f) and is not subject to oversight by the OSU IRB. Should you have any questions or concerns, please do not hesitate to contact the IRB office at 405-744-3377 or irb@okstate.edu.

Sincerely,
Oklahoma State University IRB

VITA

Peter Oliver Large

Candidate for the Degree of

Doctor of Education

Thesis: A META-ANALYSIS OF GEOSPATIAL ESTIMATES IN THE CASE OF MALAYSIAN AIRLINES FLIGHT MH370

Major Field: Applied Educational Studies, with the Aviation and Space specialization.

Biographical:

Education:

Completed the requirements for the Doctor of Education in Aviation and Space at Oklahoma State University, Stillwater, Oklahoma in May, 2019.

Completed the requirements for the Master of Science in Management at Stanford University, Stanford, CA in 2008.

Completed the requirements for the Bachelor of Science in Surveying & Mapping Science at The University of Newcastle Upon Type, Newcastle, UK, 1994.

Experience:

2015-2019, AirSpatial LLC

2016-2018, Inmarsat Aviation.

1996-2014, Trimble Navigation Ltd.

Professional Memberships:

Member of the Academy of Management

Member of the Strategic Management Society

Member of the American Institute of Aeronautics and Astronautics

IATA Certified Aviation Management Professional

Associate Fellow of the Royal Institute of Navigation.